

**Design of Catalyst Interfaces for Heterogeneous Dihydrogen Production Manifolds and
Incorporation into Photocathode Systems**

By

Shawn C. Eady

**A dissertation submitted in partial fulfillment
of the requirements for the degree of
Doctor of Philosophy
(Chemistry)
in the University of Michigan
2016**

Doctoral Committee:

**Associate Professor Nicolai Lehnert, Chair
Professor Mark M. Banaszak-Holl
Associate Professor Bart Bartlett
Professor Levi T. Thompson**

© Shawn C. Eady 2016

This thesis is dedicated to my mother, Barbara, whose bravery in the face of psychological illness encourages me to be mindful of what burdens others may carry; to my father, Vincent, whose unwavering persistence despite occupational and economic difficulties has inspired me to work tirelessly towards my goals despite frequent setbacks and barriers; to my brother, Gregory, whose determination and success living with chronic illness has made me realize the capacity of human spirit and the preciousness of life; to my sister, Joelle, who has brought so much joy into all of our lives; and to my wife, Heather, who accepts the extent of my virtues and even loves the depth of my flaws.

Acknowledgements

Lehnert Group, thanks for the comradery and support through all of the ups and downs over these 5+ years, whoever they may be, there can only ever be one true lab family.

Nicolai, I find it near impossible that a version of myself five years prior could believe such personal and professional development was possible. This development could not have been attained without your mentorship and scientific guidance through the challenging projects and exciting results they yielded.

Heather, your love and support through these (at times difficult) years has been an invaluable resource and I often question how I could have finished the program without you. The likely answer is by using a variety of legal and illegal substances, but I am so much happier I have you.

My collaborators Sabrina Peczonczyk, Betsy Brown and Tanya Breault, your assistance was critical to my thesis development and always given with a smile.

My colleagues, especially Kayla Pyper, Ben Klepser, Charles Lhermitte, Eli Fahrenkrug, Junsi Gu, and Sudarat Lee, thanks for help in guiding me through the sometimes winding road to becoming a more proficient materials and electrochemical scientist.

The chemistry teaching faculty, especially Amy Gottfried and Kathleen Nolta, the time spent teaching with you was never a chore, but rather gave a unique perspective on teaching methods and modes of learning that I will always cherish.

The chemistry department staff, especially Roy Wentz, Jeff Kampf, and Jim Windak, but including all 1500 staff, without your personal assistance my research could not have been developed to the extent that it was.

Table of Contents

Dedication.....	ii
Acknowledgements.....	iii
List of Tables.....	vii
List of Figures.....	viii
List of Schemes.....	xix
List of Charts.....	xx
Abstract.....	xxi
Chapter	
1	1
Introduction	1
1.1. Sustainable and Renewable Energy Production	1
1.2. Dihydrogen as an Energy Source: Benefits and Challenges	3
1.3. Photocatalytic Systems for Hydrogen Production	5
1.4. Scope of Thesis	15
Chapter 2	25
Hydrogenase Inspired Design of Hydrogen Production Catalysts	25
2.1. Structural, Spectroscopic and Electrochemical Characterization of Pentacoordinate Iron Hydrogen Production Catalysts as Models for the Distal Iron of [FeFe] hydrogenase	26

2.2. Comparison to Analogous Pentacoordinate Iron Catalysts: Effect of Diphosphine Ligand Structure on Overpotential and Catalytic Performance	44
2.3. Electrocatalytic Activity of Hydrogenase Model Catalysts Electrostatically Adsorbed to Reduced Graphene Oxide Surfaces	51
Chapter 3	71
Investigation of Graphitic Supports as Interfaces for Catalyst Heterogenization	71
3.1. Adsorption of Cobalt Bis(dithiolene) Hydrogen Production Catalysts on Graphitic Supports: Initial Testing of Heterogeneous Catalyst Systems	73
3.2. Electrocatalytic Analysis of Cobalt Bis(dithiolene) Derivatives: Effect of Ring Size and Substitution on Catalyst Loading, Activity and Overpotential	93
3.3. A Smorgasbord of Carbon: Comparison of Catalyst Loading and Performance Across a Variety of Graphitic Supports	137
Chapter 4	167
Application of Catalyst Interfaces on Semiconductor Surfaces	167
4.1. Construction and Characterization of Cobalt Bis(dithiolene)-Adsorbed CH₃-GaP/Graphene Surfaces	167
4.2. Click Chemistry as a Versatile Interface for Catalyst Binding on GaP	179
Chapter 5	203
Conclusions and Future Work	203
5.1. Conclusions	203
5.2. Future Work	209

List of Tables

Table 2.1: Pentacoordinate iron compounds and selected properties.	28
Table 2.2: Comparison of selected bond lengths [\AA] and angles [$^{\circ}$] for selected pentacoordinate iron complexes, and Co complex 10	30
Table 2.3: Select bond lengths [\AA] and angles [$^{\circ}$] for penta-coordinate iron species 1 as predicted by DFT calculations and comparison to crystal structure values. Calculations were performed with BP86/TZVP.	39
Table 3.1: Redox potentials (vs. SHE) and select catalytic properties of cobalt complexes.	99
Table 4.1: IR spectra peak comparison of $(\text{TBA})[\text{Co}(\text{S}_2\text{C}_6\text{Cl}_2\text{H}_2)_2]$ (1) adsorbed on $\text{CH}_3\text{-GaP/graphene}$, solid bulk material of 1 , and the simulated IR spectrum of 1	173
Table 4.2. Monolayer Coverage Calculation Parameters for Various Reactants.	195

List of Figures

Figure 1.1: Comparison of observed and simulated climate change based on three large-scale indicators in the atmosphere.	2
Figure 1.2: Allocation of hydrogen produced in 2007 to production method from National Energy Institute report.	6
Figure 1.3: Production and utilization paths of solar hydrogen.	7
Figure 1.4: Ribbon representation of Clostridium pasteurianum (CpI) [FeFe] hydrogenase with the FeS clusters and H cluster shown as space filling models, and zoom of the H cluster as ball and stick representation.	10
Figure 1.5. Cartoon representation of a hybrid (enzyme-TiO ₂) nanoparticle system showing aspects that are desirable for efficient and practical H ₂ production.	14
Figure 2.1: Crystal structures of [Fe(S ₂ C ₆ H ₄)((C ₆ H ₅) ₂ PN(ⁱ Pr)P(C ₆ H ₅) ₂)(CO)] (1) (<i>left</i>) and [Fe(S ₂ C ₆ H ₄)((C ₆ H ₅) ₂ PN(<i>p</i> -fluorobenzyl)P(C ₆ H ₅) ₂)(CO)] (5) (<i>right</i>) with ellipsoids shown at 50% probability.	29
Figure 2.2: Structural comparison of the FePXP unit for several pentacoordinate iron hydrogen production catalysts.	30

Figure 2.3: Cyclic voltammetry of a 2mM solution of 1 in acetonitrile at various scan rates and of 1 at a scan rate of 100 mV/s with the addition of increasing equivalents of acetic acid.	31
Figure 2.4: Peak anodic:cathodic current ratios and variation in peak cathodic/anodic currents as a function of the square root of scan rate for selected pentacoordinate iron complexes.	32
Figure 2.5: Peak catalytic current for with respect to catalyst concentration at acid saturation conditions for complexes 2 and 6	33
Figure 2.6: Peak catalytic current for selected pentacoordinate iron catalysts as a function of [AcOH] and [AcOH] ^{1/2}	34
Figure 2.7: Gas chromatography dihydrogen production measurement for bulk electrolysis at -1.7 V vs. Fc ^{0/+} of 5 (1 mM) with acetic acid (40 mM) in a 0.2 M (TBA)PF ₆ acetonitrile solution; charge passed during the electrolysis experiment.	35
Figure 2.8: Variation of $\nu(\text{C-O})$ for [Fe(S ₂ C ₆ H ₄)((C ₆ H ₅) ₂ PN(^{<i>i</i>} Pr)P(C ₆ H ₅) ₂)(CO)] (1) in acetonitrile solution upon the addition of acetic acid and toluene sulfonic acid monitored by solution IR spectroscopy.	37
Figure 2.9: Bulk electrolysis at -1.8 V vs. Fc ⁺⁰ of a 4 mM solution of 1 in acetonitrile with 0.1 M (TBA)PF ₆ monitored by solution IR spectroscopy.	38
Figure 2.10: Crystal structure of [Co(S ₂ C ₆ H ₄)((C ₆ H ₅) ₂ PN(^{<i>i</i>} Pr)P(C ₆ H ₅) ₂)(CO)] (10) with ellipsoids shown at 50% probability.	40

Figure 2.11: Cyclic voltammogram of [Co(S ₂ C ₆ H ₄)((C ₆ H ₅) ₂ PN(ⁱ Pr)P(C ₆ H ₅) ₂)CO] (10) in acetonitrile solution.	41
Figure 2.12: Cyclic voltammetry of 10 (2 mM) at a scan rate of 100 mV/s with the addition of increasing equivalents of (Bu ₃ NH)BF ₄	42
Figure 2.13: Monitoring of ν(C-O) for the crude product of [Co((C ₆ H ₅) ₂ PN(ⁱ Pr)P(C ₆ H ₅) ₂)(S ₂ C ₆ H ₄)(CO)] (10) in acetonitrile (5 mM) with addition of triethylammonium hexafluorophosphate using IR spectroscopy.	43
Figure 2.14: Cyclic voltammetry of [Fe(S ₂ C ₆ H ₄)((C ₆ H ₅) ₂ PN(CH ₂ (p-C ₆ H ₄ F))P(C ₆ H ₅) ₂)CO] (5) adsorbed on a FTO/RGO working electrode.	52
Figure 2.15: ¹ H NMR of [Fe(S ₂ C ₆ H ₄)((C ₆ H ₅) ₂ PN(p-fluorobenzyl)P(C ₆ H ₅) ₂)CO] (5).	64
Figure 2.16: ³¹ P NMR of [Fe(S ₂ C ₆ H ₄)((C ₆ H ₅) ₂ PN(p-fluorobenzyl)P(C ₆ H ₅) ₂)CO] (5).	64
Figure 2.17: ¹⁹ F NMR of [Fe(S ₂ C ₆ H ₄)((C ₆ H ₅) ₂ PN(p-fluorobenzyl)P(C ₆ H ₅) ₂)CO] (5).	65
Figure 2.18: IR of [Fe(S ₂ C ₆ H ₄)((C ₆ H ₅) ₂ PN(p-fluorobenzyl)P(C ₆ H ₅) ₂)CO] (5) embedded in a KBr matrix.	65
Figure 2.19: IR of [Co(S ₂ C ₆ H ₄)((C ₆ H ₅) ₂ PN(ⁱ Pr)P(C ₆ H ₅) ₂)CO] (10) embedded in a KBr matrix.	66
Figure 3.1: Electrochemical RGO deposition on a FTO-coated glass surface and cathodic window in aqueous solution.	74
Figure 3.2: Cyclic voltammetry of (TBA)[Co(S ₂ C ₆ Cl ₂ H ₂) ₂] (1) adsorbed on a FTO/RGO working electrode at various scan rates.	75

Figure 3.3: Cyclic voltammetry of (TBA)[Co(S ₂ C ₆ Cl ₂ H ₂) ₂] (1) adsorbed on a FTO/RGO working electrode with addition of TFA.	76
Figure 3.4: Cyclic voltammograms of (TBA)[Co(S ₂ C ₆ Cl ₂ H ₂) ₂] (1) adsorbed on a FTO/RGO in consecutively applied solutions in absence and presence of acid.	77
Figure 3.5: Cyclic voltammetry of (TBA)[Co(S ₂ C ₆ Cl ₂ H ₂) ₂] (1) adsorbed on a FTO/RGO working electrode with addition of HCl.	78
Figure 3.6: Cyclic voltammetry of (TBA)[Co(S ₂ C ₆ Cl ₂ H ₂) ₂] (1) adsorbed on a HOPG working electrode.	79
Figure 3.7: Cyclic voltammetry of (TBA)[Co(S ₂ C ₆ Cl ₂ H ₂) ₂] (1) adsorbed on a HOPG working electrode with addition of TFA.	80
Figure 3.8: Cyclic voltammograms of (TBA)[Co(S ₂ C ₆ Cl ₂ H ₂) ₂] (1) adsorbed on a HOPG working electrode in consecutively applied solutions in absence and presence of acid.	81
Figure 3.9: Hydrogen evolution and charge accumulation monitoring for electrolysis of (TBA)[Co(S ₂ C ₆ H ₂ Cl ₂) ₂] (1) adsorbed on a HOPG working electrode in the presence of TFA.	83
Figure 3.10: Foot-of-the-wave analysis of (TBA)[Co(S ₂ C ₆ Cl ₂ H ₂) ₂] (1) on FTO/RGO in the presence of 1.3 mM HCl.	89
Figure 3.11: Foot-of-the-wave analysis of (TBA)[Co(S ₂ C ₆ Cl ₂ H ₂) ₂] (1) on FTO/RGO in the presence of 2 mM TFA.	89
Figure 3.12: Foot-of-the-wave analysis of (TBA)[Co(S ₂ C ₆ Cl ₂ H ₂) ₂] (1) on HOPG in the presence of 12 mM TFA.	90
Figure 3.13: XPS of (TBA)[Co(S ₂ C ₆ Cl ₂ H ₂) ₂] (1) adsorbed on a FTO/RGO electrode.	90

Figure 3.14: XPS of (TBA)[Co(S ₂ C ₆ Cl ₂ H ₂) ₂] (1) adsorbed on a FTO/RGO electrode after electrochemical analysis.	91
Figure 3.15: UV-Visible spectrum of (TBA)[Co(S ₂ C ₆ Cl ₂ H ₂) ₂] (1) in dichloromethane solution.	91
Figure 3.16: Proton reduction overpotential comparison (TBA)[Co(S ₂ C ₆ Cl ₂ H ₂) ₂] (1) adsorbed on a FTO/RGO with platinum equilibrium potential in identical 1.1 mM HCl solutions under 1 atm H ₂ gas flow.	92
Figure 3.17: Cyclic voltammetry of (TBA)[Co(S ₂ C ₆ Cl ₂ H ₂) ₂] (1) adsorbed on a HOPG working electrode in the presence of high concentrations of TFA.	92
Figure 3.18: Crystal structure of TBA[Co(S ₂ C ₁₀ H ₇) ₂] (6) with ellipsoids shown at 50% probability.	95
Figure 3.19: XPS of TBA[Co(S ₂ C ₆ Cl ₄) ₂] (3) on a FTO/RGO electrode.	96
Figure 3.20: Cyclic voltammetry of (TBA)[Co(S ₂ C ₆ Cl ₄) ₂] (3) adsorbed on a FTO/RGO working electrode at various scan rates.	98
Figure 3.21: Cyclic voltammetry of (TBA)[Co(S ₂ C ₆ Cl ₂ H ₂) ₂] (2) adsorbed on a HOPG working electrode at various scan rates.	99
Figure 3.22: Cyclic voltammetry of (TBA)[Co(S ₂ C ₆ H ₄) ₂] (1) and (TBA)[Co(S ₂ C ₁₀ H ₆) ₂] (6) adsorbed on a HOPG working electrode in an aqueous 0.1 M KPF ₆ solution at varying scan rates.	100
Figure 3.23: Cyclic voltammetry of (TBA)[Co(S ₂ C ₆ Cl ₄) ₂] (3) adsorbed on a FTO/RGO working electrode with addition of TFA.	101

Figure 3.24: Cyclic voltammetry of (TBA)[Co(S ₂ C ₇ H ₆) ₂] (5) and (TBA)[Co(S ₂ C ₁₀ H ₆) ₂] (6) adsorbed FTO/RGO working electrodes with addition of TFA.	102
Figure 3.25: Cyclic voltammetry of (TBA)[Co(S ₂ C ₆ H ₄) ₂] (1) and (TBA)[Co(S ₂ C ₆ Cl ₄) ₂] (3) adsorbed on a HOPG working electrode in an with the addition of TFA.	103
Figure 3.26: Cyclic voltammetry of (TBA)[Co(S ₂ C ₁₀ H ₆) ₂] (6) adsorbed on a HOPG working electrode with addition of TFA.	104
Figure 3.27: Cyclic voltammograms of active cobalt bis(dithiolene) catalyst derivatives adsorbed on the same HOPG working electrode in an aqueous 0.1 M KPF ₆ solution with 4 mM TFA (pH 2.4).	105
Figure 3.28: Controlled Potential Electrolysis at -0.5 V vs. SHE of several cobalt bis(dithiolene) catalyst derivatives adsorbed to the same HOPG electrode in an aqueous 0.1 M KPF ₆ solution with 0.5 M H ₂ SO ₄ (pH 0.3).	107
Figure 3.29: Controlled Potential Electrolysis at -0.5 V vs. SHE of (TBA)[Co(S ₂ C ₆ Cl ₄) ₂] (3) adsorbed to a HOPG electrode in an aqueous 0.1 M KPF ₆ solution with 0.5 M H ₂ SO ₄ (pH 0.3) and cyclic voltammetry analysis after experiment completion.	108
Figure 3.30: Cyclic voltammogram of (TBA)[Co(S ₂ C ₆ Cl ₄) ₂] (3) adsorbed to a HOPG electrode after CPE experiment in a new (pH 7) aqueous solution before and after the addition of sulfuric acid to pH 1.5.	109
Figure 3.31: Polarization curves of active cobalt bis(dithiolene) catalyst derivatives adsorbed on the same HOPG working electrode in an aqueous soltuion with 50 mM TFA (pH 1.3).	117

Figure 3.32: UV-Visible spectrum in dichloromethane solution of cobalt bis(dithiolene) complexes.	133
Figure 3.33: XPS of TBA[Co(S ₂ C ₁₀ H ₆) ₂] (6) on a FTO/RGO electrode.	134
Figure 3.34: Cathodic window and background signal observed for FTO/RGO electrodes by cyclic voltammetry.	135
Figure 3.35: Proton reduction overpotential comparison (TBA)[Co(S ₂ C ₆ Cl ₄) ₂] (3) adsorbed on a FTO/RGO and HOPG with platinum equilibrium potential in identical 1 mM TFA solution under 1 atm H ₂ gas flow.	135
Figure 3.36: Foot-of-the-wave analysis of (TBA)[Co(S ₂ C ₆ Cl ₄) ₂] (3) on HOPG in the presence of 32 mM TFA (pH 1.5).	136
Figure 3.37: Foot-of-the-wave analysis of (TBA)[Co(S ₂ C ₁₀ H ₆) ₂] (6) on HOPG in the presence of 32 mM TFA (pH 1.5).	136
Figure 3.38: Cyclic voltammetry of (TBA)[Co(S ₂ C ₆ Cl ₂ H ₂) ₂] (1) adsorbed on a bulk graphite working electrode at various scan rates.	138
Figure 3.39: Cyclic voltammetry of (TBA)[Co(S ₂ C ₆ Cl ₂ H ₂) ₂] (1) adsorbed on a bulk graphite working electrode with addition of TFA.	139
Figure 3.40: Polarization curves of (TBA)[Co(S ₂ C ₆ Cl ₂ H ₂) ₂] (1) adsorbed on a bulk graphite working electrode and adsorbed in a GPEN film on a glassy carbon working electrode with 0.05 M TFA (pH 1.3).	141
Figure 3.41: Cyclic voltammetry of (TBA)[Co(S ₂ C ₆ Cl ₂ H ₂) ₂] (1) adsorbed on a pencil graphite working electrode at various scan rates.	142

Figure 3.42: Cyclic voltammetry of (TBA)[Co(S ₂ C ₆ Cl ₂ H ₂) ₂] (1) adsorbed on a pencil graphite working electrode with addition of TFA.	143
Figure 3.43: Cyclic voltammetry of (TBA)[Co(S ₂ C ₆ Cl ₂ H ₂) ₂] (1) adsorbed on a glassy carbon working electrode with the addition of low and high TFA concentrations.	144
Figure 3.44: Cyclic voltammetry of (TBA)[Co(S ₂ C ₆ Cl ₂ H ₂) ₂] (1) adsorbed on a graphene-coated glassy carbon working electrode at various scan rates and with the addition of TFA.	145
Figure 3.45: Cyclic voltammetry of (TBA)[Co(S ₂ C ₆ H ₂ Cl ₂) ₂] (1) adsorbed in a GPEN film at various scan rates.	146
Figure 3.46: Cyclic voltammetry of (TBA)[Co(S ₂ C ₆ H ₂ Cl ₂) ₂] (1) adsorbed in a GPEN film on a glassy carbon working electrode with addition of TFA.	147
Figure 3.47: XPS of TBA[Co(S ₂ C ₆ Cl ₂ H ₂) ₂] (1) on bulk graphite.	148
Figure 3.48: XPS monitoring of TBA[Co(S ₂ C ₆ Cl ₂ H ₂) ₂] (1) on bulk graphite over the course of argon ion sputtering experiments.	149
Figure 3.49: Titration of graphite powder into a solution of TBA[Co(S ₂ C ₆ Cl ₂ H ₂) ₂] (1) monitored by UV-Visible spectroscopy; XRD of bulk graphite powder before and after adsorption of 1	150
Figure 3.50: Charge accumulation over time for the controlled potential electrolysis of (TBA)[Co(S ₂ C ₆ Cl ₂ H ₂) ₂] (1) adsorbed on a bulk graphite working electrode; picture of hydrogen formation at the bulk graphite electrode during the electrolysis.	151

Figure 3.51: Charge accumulation over time for the controlled potential electrolysis of (TBA)[Co(S ₂ C ₆ Cl ₂ H ₂) ₂] (1) adsorbed in a GPEN film on glassy carbon; picture of hydrogen formation at the GPEN electrode during the electrolysis.	152
Figure 3.52: Proton reduction overpotential comparison (TBA)[Co(S ₂ C ₆ Cl ₂ H ₂) ₂] (1) adsorbed on a FTO/RGO with platinum equilibrium potential in identical 1.1 mM HCl solutions under 1 atm H ₂ gas flow.	157
Figure 3.53: Foot-of-the-wave analysis of (TBA)[Co(S ₂ C ₆ Cl ₂ H ₂) ₂] (1) on bulk graphite in the presence of 32 mM TFA.	157
Figure 3.54: Foot-of-the-wave analysis of (TBA)[Co(S ₂ C ₆ H ₂ Cl ₂) ₂] (1) adsorbed on bulk graphite powder embedded in nafion (50 mg/mL) in the presence of 32 mM TFA.	158
Figure 3.55: XPS of TBA[Co(S ₂ C ₆ Cl ₂ H ₂) ₂] (1) on FTO/graphene electrode.	159
Figure 3.56: XPS of TBA[Co(S ₂ C ₆ Cl ₂ H ₂) ₂] (1) on bulk graphite powder used in GPEN films.	160
Figure 4.1: XPS of a gallium phosphide surface before and after electrodeposition of RGO.	168
Figure 4.2: SEM image of a bare gallium phosphide surface, gallium phosphide with RGO electrodeposited on the surface, and a FTO electrode with RGO electrodeposited on the surface.	169
Figure 4.3: SEM image of a methylated gallium phosphide surface with RGO and predominantly single layer graphene on the surface.	169

Figure 4.4: XPS Co 2p core spectra of GaP/RGO surface before and after adsorption of (TBA)[Co(S ₂ C ₆ Cl ₂ H ₂) ₂] (1).	170
Figure 4.5: GATR of (TBA)[Co(S ₂ C ₆ Cl ₂ H ₂) ₂] (1) adsorbed on CH ₃ -GaP/graphene, IR of solid bulk material of 1 by ATR, and simulated IR spectrum of (1).	171
Figure 4.6: Resonance Raman at 647 nm of (TBA)[Co(S ₂ C ₆ Cl ₂ H ₂) ₂] (1) adsorbed on CH ₃ -GaP/graphene and in a 1:1 propionitrile:butyronitrile solution.	172
Figure 4.7: XPS of (TBA)[Co(S ₂ C ₆ Cl ₂ H ₂) ₂] (1) adsorbed on CH ₃ -GaP/graphene.	174
Figure 4.8: High-resolution Br 3d XP spectra of pentenyl-GaP(111)A after bromination step and after subsequent azide exchange.	180
Figure 4.9: XP spectra of N 1s region of azide-terminated GaP(111).	181
Figure 4.10: XPS of [Fe(S ₂ C ₆ H ₄)((C ₆ H ₅) ₂ PN((CH ₂) ₂ C≡CH)P(C ₆ H ₅) ₂)CO] (1) modified GaP(111)A through a pentenyl-linker.	182
Figure 4.10: Cyclic voltammetry of GaP(111)A with covalently attached [Fe(S ₂ C ₆ H ₄)((C ₆ H ₅) ₂ PN((CH ₂) ₂ C≡CH)P(C ₆ H ₅) ₂)CO] (1) under illumination before and after the addition of acetic acid.	183
Figure 4.11: Co 2p XP spectra of cobaloxime-modified GaP(111) through the conversion of an allyl and pentenyl linkers.	183
Figure 4.12: GATR-FTIR of azide-terminated and cobaloxime-modified GaP(111)A through a pentenyl-linker.	184

Figure 4.13: XP Co 2p and P 2p core spectra of pristine cobaloxime-GaP(111)A covalently bound through a pentenyl-linker; XPS of the same surfaces after two months in ambient conditions.185

Figure 4.14: Cyclic voltammetry of cobaloxime modified GaP(111)A electrode and a pentenyl-modified GaP(111)A control in a pH 7 aqueous solution with 1 M potassium phosphate buffer and illuminated with white light at an intensity of 100 mW/cm².186

List of Schemes

Scheme 1.1: Anode and cathode reaction components for the production of hydrogen from water.	9
Scheme 2.1: Preparation of penta-coordinate iron dihydrogen production catalysts.	27
Scheme 2.2: Illustration of the delocalization of the nitrogen lone pair of the PNP ligand, leading to a planar FePNP ring.	45
Scheme 2.3: Proposed hydrogen production mechanism for pentacoordinate iron catalysts.	50
Scheme 4.1. Schematic representation of photocatalytic hydrogen production at the surface of a graphene-covered gallium phosphide electrode with a cobalt bis(dithiolene) catalyst adsorbed.	168
Scheme 4.2. Functionalization of gallium phosphide surfaces with a terminal azide and subsequent click reaction to covalently attach cobaloxime catalysts.	179

List of Charts

Chart 1.1. Nickel bis(diphosphine) hydrogen production catalysts with a PN ^R P pendant amine ligand.	12
Chart 2.1: Pentacoordinate iron complexes as models of distal iron in [FeFe] hydrogenase active site.	26
Chart 3.1. Co bis(dithiolene) compound (1) used for RGO adsorption, (left), schematic representation of π -stacking interactions (right).	73
Chart 3.2. Cobalt-bis(benzenedithiolene) derivatives.	93
Chart 3.3 Cobalt bis(dithiolate) complex (1) used for graphite adsorption (right), schematic representation of the catalyst in graphitic materials (left).	137
Chart 4.1. Cobaloxime-modified GaP(111)A surface labeled with t_1 and t_2	194

Abstract

Engineering solar-powered catalyst systems for fuel production is of critical importance to the advancement of the global energy economy. Heterogeneous catalyst manifolds most promising for photocatalysis are those that boast versatile and cheap, stable components. Huisgen's 1,3-dipolar cycloaddition ('click' chemistry) and π -stacking graphene adsorption systems provide a range of facile methods for electrode-surface modification and catalyst binding to build stable photocathode systems. Prior to this work, Co^{III} bis(benzenedithiolate) catalysts had been reported as active proton reduction catalysts in homogeneous phase. Due to the novelty of these complexes for use as proton reduction catalysts, no work prior to that reported in this thesis has attempted to heterogenize cobalt bis(dithiolene) catalysts and attach them to semiconductor surfaces. While several hydrogen production catalyst systems had been reported electrostatically adsorbed to graphitic supports, these studies lacked in-depth analysis of the ligand and graphitic support's effects on catalyst adsorption, activity and retention on the surface. Previous studies have succeeded in functionalizing several semiconductor surfaces (such as silicon) with alkyne or azide groups; however, such modification of gallium-based 3,5-semiconductor systems containing an inherently strong driving force for proton reduction was previously unreported. Finally, previous literature examples of hydrogen production catalysts electrostatically adsorbed on graphene-coated semiconductors were relatively scarce, and were severely outweighed by work on covalent catalyst tethered systems. This work has for the first time heterogenized cobalt bis(dithiolene) complexes, a new class of H_2 production catalysts, on graphitic supports and further attached the catalysts to the surface of GaP by means of the graphitic interface. These studies have provided

insight into how the catalyst ligand structure and even the type of carbon in the interface can affect catalyst loading, activity and retention on the surface of the support. Initial studies of graphene- and Click-catalyst interfaces on gallium phosphide surfaces reported here represent some of the first examples of such interface development on these materials. These results push the edge of knowledge in solar-to-fuel conversion by expanding possibilities in the design of inexpensive, robust and easily modifiable photocathode systems with interchangeable catalyst and semiconductor components. With modifications, these interface methods could give access to a nearly unlimited variety of photocatalytic systems beyond the solar-to-hydrogen manifolds proposed in this work, making graphene and Click manifolds the template for a solar-fueled future.

Chapter 1

Introduction

1.1. Sustainable and Renewable Energy Production

In the advent of the 21st century, over two millennia since the first known use of fossil fuels and after several centuries of primary dependence on these fuel sources, initiatives to introduce renewable energy sources into the global energy economy have developed substantially from initial conceptualization nearly a century ago. The driving force behind this movement stems from the variety of limitations to fossil fuel dependence, most notably the inadequacy of depending on a naturally limited resource with an exponentially increasing global energy demand. In 2010, approximately 14 TW of energy was consumed globally, a value that is estimated to double to 28 TW by 2050.¹⁻³ While newly discovered sources and methods of retrieving fossil fuels (e.g., fracking for shale-bound natural gas) are expected to meet this increased demand at least until 2050, the increasing global energy demand of the world's growing population will eventually outweigh the ever-decreasing fossil fuel supply.⁴

In addition, with advances in technology for climate study in the 20th century, researchers realized gaseous emissions from fossil fuel use were causing detriment to the environment, as evidenced by climate change observations over the last few decades (**Figure 1.1**).⁵ These emissions, which reached a higher atmospheric concentration in 2007 than has been seen in nearly seven centuries (380 ppm), are intrinsically tethered to the combustion of fossil fuels, further

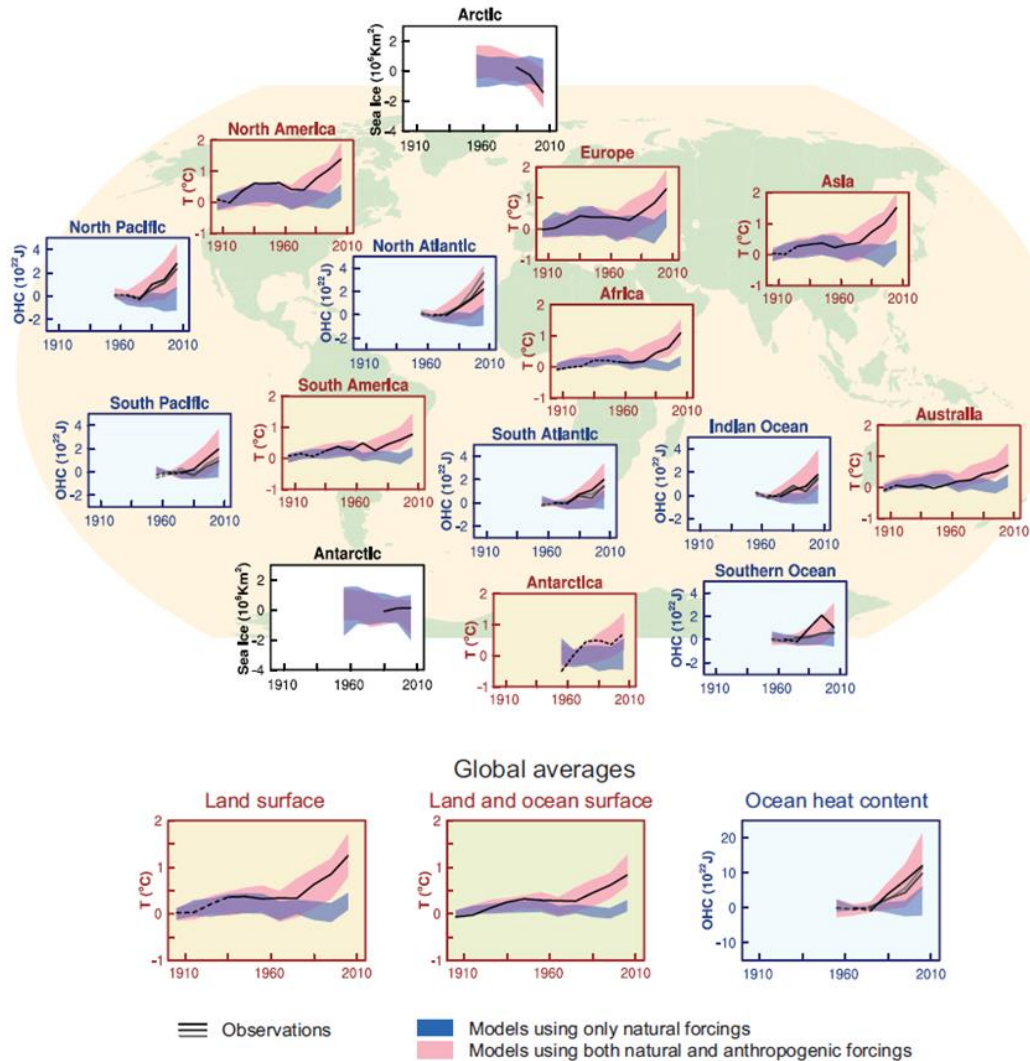


Figure 1.1. Comparison of observed and simulated climate change based on three large-scale indicators in the atmosphere, the cryosphere and the ocean: change in continental land surface air temperatures (yellow panels), Arctic and Antarctic September sea ice extent (white panels), and upper ocean heat content in the major ocean basins (blue panels). Global average changes are also given. Anomalies are given relative to 1880–1919 for surface temperatures, 1960–1980 for ocean heat content and 1979–1999 for sea ice. All time-series are decadal averages, plotted at the center of the decade. For temperature panels, observations are dashed lines if the spatial coverage of areas being examined is below 50%. For ocean heat content and sea ice panels, the solid line is where the coverage of data is good and higher in quality, and the dashed line is where the data coverage is only adequate, and thus, uncertainty is larger. Reprinted from *Climate Change 2013: The Physical Science Basis*, IPCC working group I contribution to the AR5, Figure SPM.6, Page 18, Copyright (2013) by Cambridge University Press.

motivating efforts to phase out these fuels as a primary energy source.^{6,7} To this end, decades of research has focused on developing relatively scarcely used renewable energy sources such as wind, hydroelectric and solar to facilitate their incorporation into a demanding industrialized energy economy, in addition to making this energy an economically viable alternative to fossil

fuels. Realization of these goals has provided a significant scientific challenge. Efficient harvesting of natural energy is complicated by both obvious restrictions, such as limited geological availability of hydroelectric energy, and technological limitations, most notably the difficulty of collecting and utilizing solar energy with affordable materials.

Another barrier to replacing fossil fuels with natural energy sources is the challenge of distributing and utilizing the harvested energy, when infrastructure has been designed largely for petroleum and coal in our fossil fuel-dependent energy economy. Several fuel alternatives to petroleum have been proposed and implemented for use in vehicles and generators, most commonly short chain alcohols such as ethanol.⁸⁻¹⁰ While use of these fuels provides a step away from dependence on petroleum, the energy densities of the short chain alcohols are lower than gasoline, and energy is still attained by combustion, which produces carbon emissions. Further, while ethanol is a renewable resource that can be produced from plant material such as corn, harvesting sufficient amounts of plant material for ethanol to completely replace fossil fuels may not be possible, or at the very least would place a strain on farming resources in some countries.¹¹⁻

13

1.2. Dihydrogen as an Energy Source: Benefits and Challenges

One viable energy carrier with well-documented merits is dihydrogen gas. The use of hydrogen provides several advantages not realized with petroleum-based fuel. One such benefit is the energy density of hydrogen; it has the highest energy density per mass of any fuel at 120 MJ/kg, approximately three times higher than that of gasoline (44.4 MJ/kg) and nearly five times higher than ethanol (26.6 MJ/kg) and methanol (19.9 MJ/kg). Along with its high energy density for use in internal combustion engines, hydrogen has the highest possible electron density of any material

as two electrons can be extracted per molecule. This highlights another advantage of hydrogen over gasoline; while use of the latter is restricted to combustion engines with efficiencies typically not exceeding 30–40% due to loss of energy as heat, electrical energy extraction from hydrogen can be performed at near-quantitative efficiencies in fuel cells. Lastly, while cost has traditionally provided a barrier for gasoline fuel substitution, more recent analyses of hydrogen fuel produced in the latest alkaline and proton polymer exchange membrane electrolyzers and used in fuel cell electric vehicles give costs as low as approximately \$6/kg, the equivalent of \$3-\$5/gallon in gasoline prices. These competitive costs, which have the possibility of decreasing further with additional infrastructure and technology advances, make hydrogen an increasingly viable alternative as a carbon-free energy carrier for development in the 21st century.¹⁴

While hydrogen is known for its explosive nature and involvement in such tragedies as the Hindenburg disaster, hydrogen actually provides several safety advantages compared to gasoline. First and foremost, as noted above, use in a fuel cell-based power source avoids combustion of the material, meaning ignition of the fuel in a hydrogen fuel cell-powered vehicle is unlikely. In the event the hydrogen is ignited, the gas's propensity to burn quickly and rise make hydrogen-related fires end relatively quickly and leave the immediate area generally unmarred, as demonstrated in simulated fuel leak fires comparing gasoline and hydrogen fuels.¹⁵

Implementing hydrogen as an energy carrier is by no means an initiative without challenges or drawbacks. The most obvious of these is the inherent difficulty of incorporating a gaseous fuel in a society so accustomed to liquid fuel transport and storage. In addition, pressurization or cryogenic temperatures are required to store hydrogen as a liquid (which is preferable due to the low energy density per volume of hydrogen gas under standard temperature conditions). Not only does this require changes in commercial and private sector fuel infrastructure, but pressurized or

cryogenic containment presents safety concerns. Alternative means of storage, such as use of chemicals for physisorption (e.g., zeolites, metal organic frameworks)¹⁶⁻¹⁸ and chemisorption (e.g., metal hydrides)¹⁹⁻²¹, are currently under development. However, previous research has shown these storage methods have difficulty meeting the weight percent standards set by Department of Energy application guidelines. Finally, one of the most significant challenges in implementing a hydrogen fuel economy is renewably producing sufficient amounts of clean hydrogen, as outlined in section **1.3** below. This is a key barrier to the economically viable production of a variety of alternative fuels, such as for the hydrogenation of CO₂ to methanol, a liquid fuel that can more easily be implemented as a gasoline alternative in the current fuel infrastructure.

1.3. Development of Photocatalytic Systems for Hydrogen Production

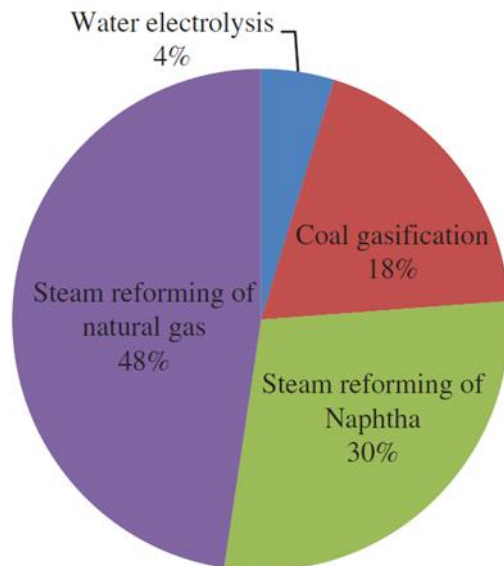


Figure 1.2. Allocation of hydrogen produced in 2007 by production method from National Energy Institute report. Reprinted from ‘Techno-Economic Study of Hydrogen Production via Steam Reforming of Methanol, Ethanol, and Diesel’, Volume 1, Seyyed Mohsen Mousavi Ehteshami and Siew Hwa Chan, Page 16, Copyright (2014) by Taylor & Francis Group.

Production of hydrogen has been an industrial focus for decades; however, the predominant applications driving this production have not been renewable energy. Rather, the majority of industrially produced hydrogen has been used for petroleum refinement, food processing, the synthesis of ammonia (via the Haber-Bosch process) to produce fertilizer; and as a feedstock to produce a variety of chemical compounds such as methanol. More than 50 million tons of hydrogen is produced and consumed every year, and only a small fraction of this amount is used as a carbon-free fuel alternative to petroleum. Of greater concern is the current means of hydrogen production, since use of hydrogen as a carbon-free energy carrier is only effective if the production method does not generate carbon emissions in turn. To date, more than 90% of hydrogen produced globally is sourced from fossil fuels, most commonly via steam reformation of methane and coal gasification, generating CO_x waste and effecting a negative environmental impact (**Figure 1.2**).²² Thus a means of renewably producing hydrogen while minimizing carbon emissions is vital to

continue meeting the global demand for industrial and farming applications, while making hydrogen a truly clean energy carrier from production to utilization.¹⁴

Solar energy provides a viable fossil fuel alternative for hydrogen production, as outlined in **Figure 1.3**, and has the potential to provide the most energy of any natural resource, far surpassing our global energy demands.²³ The challenge to effectively utilize this energy has been met by scientists across the globe with impressive results, arguably starting with the introduction of the first functional patented solar cell in 1940 by Russel Ohl, a semiconductor researcher at Bell Labs who discovered the device as a silicon piece with an accidental yet fortuitous crack to provide the p-n junction basis of a solar cell. By 1954, three scientists at Bell Labs — a chemist named Calvin Fuller, a physicist named Gerald Pearson, and an engineer named Daryl Chapin — together designed the first practical arsenic- and boron-doped silicon solar cell connected in series to provide a ‘solar battery,’ whose functionality was demonstrated by successfully powering a radio transmitter. Low solar cell efficiencies (defined as the percentage of solar energy converted to

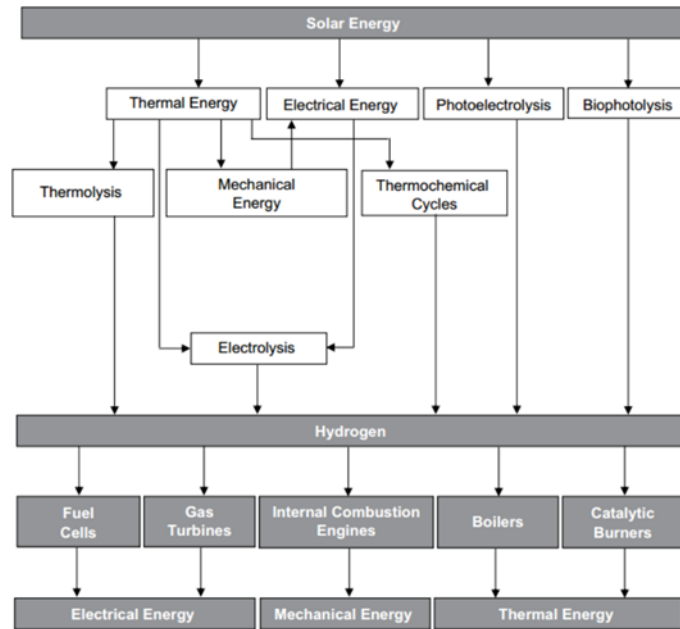


Figure 1.3. Production and utilization paths of solar hydrogen. Reprinted from ‘A review on solar-hydrogen/fuel cell hybrid energy systems for stationary applications’, Volume 35, A. Yilanci, I. Dincer, H.K. Ozturk, Page 233, Copyright 2008, with permission from Elsevier.

electrical energy) of these early designs and the high cost of the cells, particularly compared to the cheap and well-instituted fossil fuels primarily used at this time, did not provide ideal conditions for immediate commercialization. However, within a decade of initial development solar energy harvesting devices began to find their way into various applications, most famously perhaps for use in powering satellites.

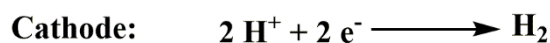
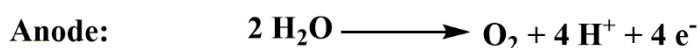
Since these early models, designing more efficient solar cells with more affordable materials has been the primary focus of solar research.²³ Several core strategies have been developed to utilize inexpensive semiconductor materials. One of these is the development of thin film semiconductor materials, which have been furthered modified since initial introduction in the late 1970s to be as thin as a few nanometers in thickness. They also can be easily coated on glass or devices and have recently attained efficiencies of over 15%, in some cases even outperforming multicrystalline silicon cells.^{24,25} Another method for more efficient solar cell production is the dye sensitization of semiconductor materials. In 1988, Brian O'Regan and Michael Gratzel at UC Berkeley modernized this method by developing a device composed of a porous electron accepting material, most commonly titanium dioxide, coated with a light-harvesting organic dye. These cells are now commonly referred to as Gratzel cells.²⁶ These cells are not as competitive as thin film cells in terms of efficiency, and they are more difficult to construct due to the necessity of an electrolyte solution (e.g., I_3/I^- in water) for electron transport to complete the circuit. However, they display reasonable maximum solar conversion efficiencies of ~10–15% while costing a fraction of the price in materials compared to traditional silicon solar cells, allowing them more potential for scalable applications.^{27,28} More recent 'third generation' solar cell technology utilizing tandem cells overcomes efficiency limits of single band-gap solar cells, and when coupled

to thin cell and dye sensitizing innovations, provides exciting prospects for the design of affordable, highly efficient solar cells.^{29,30}

As scientists have known for decades, the most abundant potential source of hydrogen is a substance which covers more than two-thirds of the earth's surface. The oxidation of water, a readily available resource, provides four electrons and protons in addition to a molecule of dioxygen for every two water molecules, which in turn can be used to generate two molecules of hydrogen gas. Yet extracting hydrogen from water is non-trivial, as water oxidation requires a minimum applied potential of 1.23 V (237 kJ/mol) to meet the thermodynamic requirements for oxygen production. Further, additional energy (overpotential) is typically required to overcome activation barriers for the oxidation of water and to achieve high efficiencies, and an appropriate catalyst is necessary to lower overpotentials as much as possible. The catalysts observed to display the lowest overpotentials for water oxidation generally include precious metals such as platinum. Such materials incur high costs for application in water electrolyzers, and their limited abundance in the earth's crust provide obvious limitations for common use on a global scale.^{31,32}

Nature is able to facilitate the anodic reaction of water splitting (**Scheme 1.1**), i.e. the extraction of energy (electrons) and protons from water, using only sunlight in photosynthesis. This impressive feat has been thoroughly studied. One of the core components of this finely tuned system is a cube-like structure able to catalyze the 4-electron oxidation of water, while only comprising the inexpensive metals manganese and calcium. Research on these systems has

Hydrogen Production From Water (Water Splitting)



Scheme 1.1. Anode and cathode reaction components for the production of hydrogen from water.

allowed further elucidation of the electronic structure of these manganese clusters, and even for the production of functional models for water oxidation. These models complexes, in addition to a variety of other molecular and solid state materials composed of inexpensive materials, have been developed to provide viable substitutions for platinum as water oxidation catalysts. The design of such catalysts, and their incorporation into photoanode systems allowing for the direct utilization of solar energy to extract protons and electrons from water (as seen for photosystem II in nature), has an immense impact for prospects for the carbon-free production of hydrogen.

While water oxidation is the most naturally abundant source of the protons and electrons to make hydrogen, and thus an important focus of research, the cathodic reaction in water splitting, i.e. the combination of protons and electrons from any source to evolve hydrogen, is inevitably another important focus for clean hydrogen production. Hydrogen production can only be facilitated at reasonable energy levels by using a catalyst capable of efficiently combining the

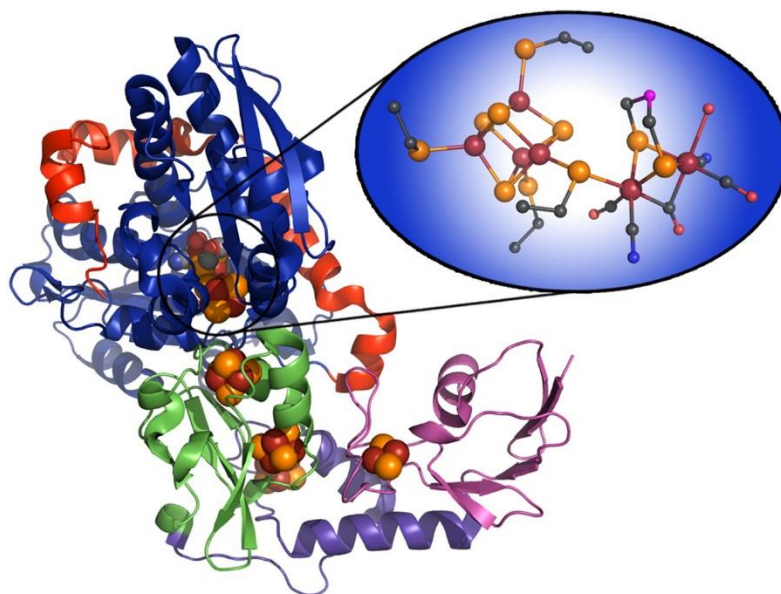


Figure 1.4. Ribbon representation of *Clostridium pasteurianum* (CpI) [FeFe] hydrogenase with the FeS clusters and H cluster shown as space filling models, and zoom of the H cluster as ball and stick representation. Reprinted from PNAS, Synthesis of the 2Fe subcluster of the [FeFe]-hydrogenase H cluster on the HydF scaffold, Eric M. Shepard et al., Volume 107, pg. 10448, Copyright (2010) by National Academy of Sciences.

electrons and protons, and has been observed to be most efficient with the use of platinum and similar precious metals. Nature, however, is observed to reversibly catalyze the combination of protons and electrons for hydrogen production or oxidation in enzymes known as hydrogenases at negligible overpotentials using only inexpensive metals such as iron and nickel. These enzymes are categorized into the classes [FeFe], [NiFe] and [Fe] hydrogenases based on the metals present in the active site, and in nature their primary function is the production of hydrogen as an energy carrier or to safely dispose of excess electron equivalents. One of the most active [FeFe] enzymes, from *Clostridium pasteurianum* (**Figure 1.4**), is capable of reaching turnover frequencies of $10,000\text{ s}^{-1}$ for hydrogen production in pH neutral aqueous solutions.³³ Even without precious metals, these enzymes are able to function at nearly negligible overpotentials even lower than those attained by platinum, are functional in neutral pH ranges, and often show nearly indefinite stability in their native state.^{34,35} This impressive activity profile is the reason hydrogenases have been the focus of intensive study since their initial discovery in the 1930s. After more than a half century of fervent analysis, the structure, reactivity, and even mechanisms of hydrogenases have been largely elucidated, allowing insight into how we might utilize similarly inexpensive materials for electron/proton and hydrogen interconversion.³⁶⁻⁵⁵

Efforts to model the active sites of hydrogenases to create inexpensive early transition metal catalysts with incredible hydrogen production activities have been ongoing for nearly as long as hydrogenase enzyme studies. While the enzyme remains uncontested in overall performance, individual aspects such as turnover frequency (TOF), overpotential, and catalyst durability expressed as turnover number (TON) have been very nearly matched by a variety of molecular and solid state catalysts.^{46,56-108} One of the most prominent of these model systems, developed by Daniel Dubois and coworkers, exhibits TOF as high as 10^5 s^{-1} and is composed of a



Chart 1.1. Nickel bis(diphosphine) hydrogen production catalysts with a PN^RP pendant amine ligand.

nickel metal center with two bidentate phosphine ligands, each with pendant amines in a ‘PCN^RCP’ motif (**Chart 1.1**).^{67,109} This ligand system is essential to the high level of activity, as the flexible ligand ‘arm’ allows for combination of formed Ni-H species with the protonated pendant amines for facile H₂ formation and activation.¹¹⁰⁻¹¹² The advantages of this ligand system are further demonstrated by its use in iron and cobalt systems capable of hydrogen production.^{113,114} Unlike in the case of hydrogenases, these catalyst systems are typically observed in acetonitrile solutions due to solubility restrictions, and require the addition of an acid (typically protonated dimethylformamide with a triflate anion, [(DMF)H]⁺OTf⁻) for H₂ production with and overpotentials of approximately 300 mV (± ~80 mV, depending on the catalyst derivative) for catalyst activation.¹¹⁵ Despite these limitations, the activity displayed by these catalysts even beyond the impressive rates observed for native hydrogenases, rank them as one of the fastest known hydrogen production catalysts and highlight their potential use in devices for hydrogen generation.¹⁰⁹

The harvesting of solar energy and utilization of that energy to produce fuel are each significant scientific challenges, as outlined above. However, to produce efficient technology capable of directly converting sunlight into fuel, another challenge must be overcome: the integration of semiconductor and catalyst systems. In the most simple scenario for the production

of hydrogen fuel from an acidic solution, a photosensitizer (such as a p-type semiconductor or an organometallic complex) would absorb a photon, exciting an electron from the valence band (or highest occupied molecular orbital for the complex) to the conduction band (or higher energy unoccupied orbital for the complex, most commonly a metal-to-ligand charge transfer). This excited state is energetically positioned above the lowest unoccupied (or singularly occupied) molecular orbital of the catalyst, allowing for energetically favorable electron transfer to and reduction of the catalyst. The catalyst would in turn combine two of the received electrons and protons from solution to produce a molecule of hydrogen.

Despite the apparent simplicity of this design, it is easy to overlook key design factors, which, if not properly addressed, will result in low solar-fuel conversion efficiencies or a completely inactive system altogether. Perhaps the most obvious of these is the manner in which the catalyst and semiconductor are combined. In the most basic photocatalytic systems, the catalyst is often not directly attached to the photosensitizer. Rather, the catalyst and photosensitizer are often simply dissolved in the same solution, or in the case of a solid semiconductor, the catalyst interfaces with the photosensitizer only at the material's surface. This design is simple to facilitate, and thus is one of the most commonly seen in literature, particularly for preliminary studies of photocatalytic systems to test the compatibility of a catalyst and photosensitizer.^{13,93,116-121} However, the drawbacks to such a system are many, the most substantial of which involves the outer-sphere electron transfer between the photosensitizer and the catalyst that is typically required for function in these systems, which is limited by the collision of the two materials and thus diffusion. As in the case of all systems for photocatalysis, recombination of the electron-hole pair in the photosensitizer is an inevitable side reaction, and delays to electron transfer such as in these diffusion-limited systems often serve to increase recombination rates which decrease the overall

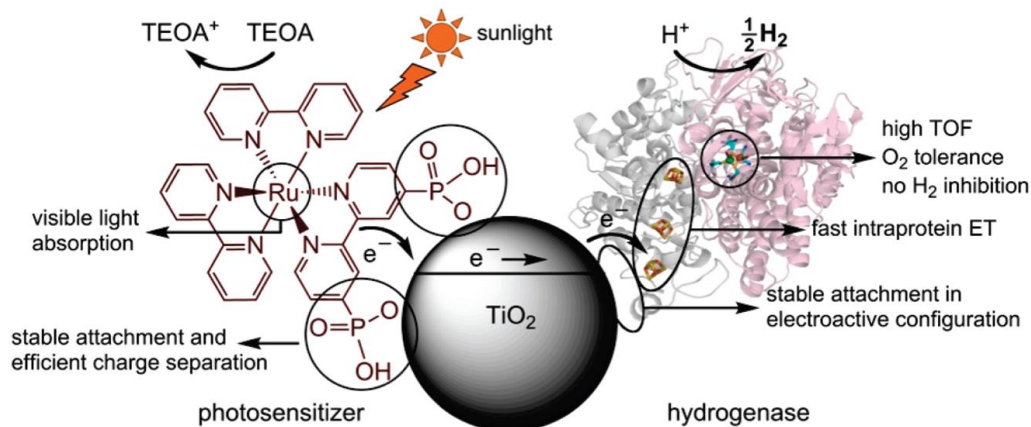


Figure 1.5. Cartoon representation of a hybrid (enzyme-TiO₂) nanoparticle system showing aspects that are desirable for efficient and practical H₂ production from sunlight shown a hydrogenase (*Db* [NiFeSe]-H) as catalyst and the complex (RuP) that proved to be the most suitable photosensitizer. Reprinted with permission from Reisner, E.; Powell, D. J.; Cavazza, C.; Fontecilla-Camps, J. C.; Armstrong, F. A. *J. Am. Chem. Soc.* 2009, *131*, 18457. Copyright (2009) American Chemical Society.

solar-to-fuel efficiency. Other problems with this design include the possibility for recombination via the interaction of two photosensitizers in solution, the limited stability that is often observed for molecular catalysts and photosensitizers in solution, and the difficulty of inclusion in an industrially scaled device for fuel production.

Modifications to this design strive to eliminate the diffusion-dependence for outer-sphere electron transfer by attaching the photosensitizer and catalyst, most commonly via covalent bond formation. This strategy has been employed in a variety of photosensitizer-catalyst combinations, ranging from covalent binding of two molecular components to the introduction of molecular or semiconductor photosensitizers into the periphery of enzymes.^{93,122-127} In particular, a couple of recent studies have been reported that modify semiconductors with hydrogenases (**Figure 1.5**) or the aforementioned nickel bis(diphosphine) model systems for hydrogen production.^{127,128} While these systems do not observe TOF values as high as the enzyme or molecular catalyst in solution (TOF of 50 s⁻¹ and 285⁻¹ observed in each system, respectively), they provide functional examples of photocatalytic systems for solar-to-fuel conversion via heterogenization of molecular (or

supramolecular) hydrogen production catalysts. Based on the performance of these catalysts in homogeneous solutions, further modification of the photocatalytic interface is likely the key to unleashing the full potential of these light-driven H₂ production manifolds.

Frequently, one of the major disadvantages of such covalently bound photocatalytic systems are the synthetic efforts required to facilitate the covalent bond formation between the photosensitizer and catalyst pair. This often requires modification of the ligand framework for the catalyst as well as modification of the ligand (for a molecular photosensitizer) or semiconductor surface. While this has been shown to be an effective method, it is often a lock-and-key situation, where the synthetic modifications are specific to a particular photosensitizer and catalyst combination. This limits the ability to test and interchange a wide variety of catalyst and photosensitizer combinations, as can be beneficial in optimizing such systems. Thus a semiconductor-catalyst interface allowing for facile interchange of the components would be an effective tool in the creation of photocathode systems that are functional at scale.

1.4. Scope of Thesis

The scope of this thesis is the development, testing and incorporation of an interface method to attach a catalyst for the production of hydrogen fuel to a semiconductor capable of harvesting the required energy to drive catalysis. A three-aim approach was utilized for the efficient design of a photocathode system for hydrogen production. The first aim focuses on the design of molecular catalysts functional for hydrogen production with customizable ligand structures capable of modification for electrode surface attachment. My catalyst design targeted hydrogenase models in an attempt to replicate the low overpotentials and incredible activities displayed by these biological systems. The characterization and electrocatalytic analysis of these

complexes is discussed in section 2.1, while further analysis of the results and comparison with similar catalysts in the literature is presented in section 2.2. Finally, preliminary results for testing the catalysts, adsorbed to reduced graphene oxide electrodes, are discussed in section 2.3. This work is in part reproduced from a manuscript published in Dalton Transactions: Eady, S. C.; Breault, T.; Thompson, L.; Lehnert, N. *Dalton Transactions* **2016**, 45, 1138.⁶⁰

The second aim of this thesis focuses directly on the development of methods for interfacing molecular catalysts with semiconductor surfaces. These studies concentrate on the heterogenized catalyst systems electrostatically adsorbed on graphitic supports that are inert to proton reduction, so characteristics of the heterogeneous system, including catalytic activity and durability, can be assessed without the added complication of semiconductor coupling. Section 3.1 describes initial testing of a cobalt bis(dithiolene) complex adsorbed onto graphitic supports as heterogeneous catalyst for hydrogen production. This section is partially reproduced from a publication in Chemical Communications: Eady, S. C.; Peczonczyk, S. L.; Maldonado, S.; Lehnert, N. *Chem. Commun.* **2014**, 50, 8065.¹²⁹ In the remainder of the chapter, a thorough assessment is provided detailing how tuning the catalyst ligand structure (section 3.2) and the use of various types of graphitic supports (section 3.3) affect the performance of the heterogeneous system for hydrogen production. These two sections represent two full manuscripts slated for submission to by February 2016.¹²⁹

The final aim focuses applying on actualizing the previously studied interface methods to the attachment of molecular catalysts to semiconductor surfaces. The preliminary work accomplished on this final step is presented in chapter 4, and confirms the presence of electrostatically adsorbed cobalt bis(dithiolene) (section 4.1) and covalently tethered cobaloxime (section 4.2) catalyst species on gallium phosphide surfaces, assuring the success of both interface

methods and providing evidence that the same interactions and catalyst species observed in the initial interface development (see chapter 3) are present on the semiconductor surface. Work in this chapter has been conducted in collaboration with Betsy Brown and Sabrina Peczonczyk from the Maldonado group.

References

- (1) Lewis, N. S.; Nocera, D. G. *Proceedings of the National Academy of Sciences* **2006**, *103*, 15729.
- (2) Nocera, D. G. *Energy & Environmental Science* **2010**, *3*, 993.
- (3) Hoffert, M. I.; Caldeira, K.; Jain, A. K.; Haites, E. F.; Harvey, L. D. D.; Potter, S. D.; Schlesinger, M. E.; Schneider, S. H.; Watts, R. G.; Wigley, T. M. L.; Wuebbles, D. J. *Nature* **1998**, *395*, 881.
- (4) *World Energy Assessment Report: Energy and the Challenge of Sustainability*, United Nations, 2003.
- (5) *IPCC, 2013: Summary for Policymakers*, 2013.
- (6) Petit, J. R.; Jouzel, J.; Raynaud, D.; Barkov, N. I.; Barnola, J. M.; Basile, I.; Bender, M.; Chappellaz, J.; Davis, M.; Delaygue, G.; Delmotte, M.; Kotlyakov, V. M.; Legrand, M.; Lipenkov, V. Y.; Lorius, C.; Pepin, L.; Ritz, C.; Saltzman, E.; Stievenard, M. *Nature* **1999**, *399*, 429.
- (7) Siegenthaler, U.; Stocker, T. F.; Monnin, E.; Lüthi, D.; Schwander, J.; Stauffer, B.; Raynaud, D.; Barnola, J.-M.; Fischer, H.; Masson-Delmotte, V.; Jouzel, J. *Science* **2005**, *310*, 1313.
- (8) Akia, M.; Yazdani, F.; Motaeae, E.; Han, D.; Arandiyan, H. *Biofuel Research Journal* **2014**, *1*, 16.
- (9) Tanger, P.; Field, J. L.; Jahn, C. E.; DeFoort, M. W.; Leach, J. E. *Frontiers in Plant Science* **2013**, *4*, 218.
- (10) Dionisi, D.; Anderson, J. A.; Aulenta, F.; McCue, A.; Paton, G. *Journal of Chemical Technology & Biotechnology* **2015**, *90*, 366.
- (11) Nwachukwu, C. C.; Lewis, C. *Biomass* **1986**, *11*, 271.
- (12) Huang, W.-D.; Zhang, Y. H. P. *PLoS ONE* **2011**, *6*, e22113.

- (13) Kumar, B.; Beyler, M.; Kubiak, C. P.; Ott, S. *Chemistry – A European Journal* **2012**, *18*, 1295.
- (14) Thompson, L.; Barbier, F.; Burns, L.; Friedland, R.; Kiczek, E.; Nozik, A.; Richmond, G.; Robert Shaw, J.; Wilson, D. *Report of the Hydrogen Production Expert Panel: A Subcommittee of the Hydrogen & Fuel Cell Technical Advisory Committee*, 2013.
- (15) Swain, M. R. *Fuel Leak Simulation*, 2001.
- (16) Dong, J.; Wang, X.; Xu, H.; Zhao, Q.; Li, J. *Int. J. Hydrogen Energy* **2007**, *32*, 4998.
- (17) Masika, E.; Mokaya, R. *Energy & Environmental Science* **2014**, *7*, 427.
- (18) Langmi, H. W.; Ren, J.; North, B.; Mathe, M.; Bessarabov, D. *Electrochim. Acta* **2014**, *128*, 368.
- (19) Sakintuna, B.; Lamari-Darkrim, F.; Hirscher, M. *Int. J. Hydrogen Energy* **2007**, *32*, 1121.
- (20) Khan, J.; Jain, I. P. *Int. J. Hydrogen Energy*.
- (21) Xiao, X.; Fan, X.; Yu, K.; Li, S.; Chen, C.; Wang, Q.; Chen, L. *The Journal of Physical Chemistry C* **2009**, *113*, 20745.
- (22) Mousavi Ehteshami, S. M.; Chan, S. H. *Energy Technology & Policy* **2014**, *1*, 15.
- (23) Yilanci, A.; Dincer, I.; Ozturk, H. K. *Prog. Energy Combust. Sci.* **2009**, *35*, 231.
- (24) Duan, X.; Niu, C.; Sahi, V.; Chen, J.; Parce, J. W.; Empedocles, S.; Goldman, J. L. *Nature* **2003**, *425*, 274.
- (25) Chopra, K. L.; Paulson, P. D.; Dutta, V. *Progress in Photovoltaics: Research and Applications* **2004**, *12*, 69.
- (26) O'Regan, B.; Gratzel, M. *Nature* **1991**, *353*, 737.
- (27) Gratzel, M. *Nature* **2001**, *414*, 338.
- (28) Burschka, J.; Pellet, N.; Moon, S.-J.; Humphry-Baker, R.; Gao, P.; Nazeeruddin, M. K.; Gratzel, M. *Nature* **2013**, *499*, 316.
- (29) Conibeer, G.; Green, M.; Corkish, R.; Cho, Y.; Cho, E.-C.; Jiang, C.-W.; Fangsuwannarak, T.; Pink, E.; Huang, Y.; Puzzer, T.; Trupke, T.; Richards, B.; Shalav, A.; Lin, K.-l. *Thin Solid Films* **2006**, *511–512*, 654.

- (30) Green, M. A. *Physica E: Low-dimensional Systems and Nanostructures* **2002**, *14*, 65.
- (31) Ni, M.; Leung, M. K. H.; Leung, D. Y. C.; Sumathy, K. *Renewable and Sustainable Energy Reviews* **2007**, *11*, 401.
- (32) Hisatomi, T.; Kubota, J.; Domen, K. *Chem. Soc. Rev.* **2014**, *43*, 7520.
- (33) Madden, C.; Vaughn, M. D.; Díez-Pérez, I.; Brown, K. A.; King, P. W.; Gust, D.; Moore, A. L.; Moore, T. A. *J. Am. Chem. Soc.* **2012**, *134*, 1577.
- (34) Hinnemann, B.; Moses, P. G.; Bonde, J.; Jørgensen, K. P.; Nielsen, J. H.; Horch, S.; Chorkendorff, I.; Nørskov, J. K. *J. Am. Chem. Soc.* **2005**, *127*, 5308.
- (35) Shafaat, H. S.; Rüdiger, O.; Ogata, H.; Lubitz, W. *Biochimica et Biophysica Acta (BBA) - Bioenergetics* **2013**, *1827*, 986.
- (36) Cammack, R. *Nature* **1999**, *397*, 214.
- (37) Nicolet, Y.; De Lacey, A. L.; Vernede, X.; Fernandez, V. M.; Hatchikian, E. C.; Fontecilla-Camps, J. C. *J. Am. Chem. Soc.* **2001**, *123*, 1596.
- (38) Greco, C.; Bruschi, M.; De Gioia, L.; Ryde, U. *Inorg. Chem.* **2007**, *46*, 5911.
- (39) Volbeda, A.; Charon, M.-H.; Piras, C.; Hatchikian, E. C.; Frey, M.; Fontecilla-Camps, J. C. *Nature* **1995**, *373*, 580.
- (40) Nicolet, Y.; Piras, C.; Legrand, P.; Hatchikian, C. E.; Fontecilla-Camps, J. C. *Structure* **1999**, *7*, 13.
- (41) Shima, S.; Pilak, O.; Vogt, S.; Schick, M.; Stagni, M. S.; Meyer-Klaucke, W.; Warkentin, E.; Thauer, R. K.; Ermler, U. *Science* **2008**, *321*, 572.
- (42) Volbeda, A.; Fontecilla-Camps, J. C. *J. Chem. Soc. Dalton Trans.* **2003**, 4030.
- (43) Gordon, J. C.; Kubas, G. J. *Organometallics* **2010**, *29*, 4682.
- (44) Hatchikian, E. C.; Forget, N.; Fernandez, V. M.; Williams, R.; Cammack, R. *Eur. J. Biochem.* **1992**, *209*, 357.
- (45) Volbeda, A.; Martin, L.; Cavazza, C.; Matho, M.; Faber, B. W.; Roseboom, W.; Albracht, S. P. J.; Garcin, E.; Rousset, M.; Fontecilla-Camps, J. C. *J. Biol. Inorg. Chem.* **2005**, *10*, 239.
- (46) Adam, F. I.; Hogarth, G.; Richards, I.; Sanchez, B. E. *J. Chem. Soc. Dalton Trans.* **2007**, 2495.
- (47) Lubitz, W.; Reijerse, E.; van Gestel, M. *Chem. Rev.* **2007**, *107*, 4331.

- (48) Ogata, H.; Lubitz, W.; Higuchi, Y. *J. Chem. Soc. Dalton Trans.* **2009**, 7577.
- (49) Pereira, A. S.; Tavares, P.; Moura, I.; Moura, J. J. G.; Huynh, B. H. *J. Am. Chem. Soc.* **2001**, *123*, 2771.
- (50) Peters, J. W.; Lanzilotta, W. N.; Lemon, B. J.; Seefeldt, L. C. *Science* **1998**, *282*, 1853.
- (51) Popescu, C. V.; Münck, E. *J. Am. Chem. Soc.* **1999**, *121*, 7877.
- (52) Schwab, D. E.; Tard, C.; Brecht, E.; Peters, J. W.; Pickett, C. J.; Szilagy, R. K. *Chem. Commun.* **2006**, 3696.
- (53) Vignais, P. M.; Billoud, B. *Chem. Rev.* **2007**, *107*, 4206.
- (54) Kubas, G. J. *Chem. Rev.* **2007**, *107*, 4152.
- (55) Bennett, B.; Lemon, B. J.; Peters, J. W. *Biochemistry* **2000**, *39*, 7455.
- (56) Baffert, C.; Artero, V.; Fontecave, M. *Inorg. Chem.* **2007**, *46*, 1817.
- (57) Barton, B. E.; Olsen, M. T.; Rauchfuss, T. B. *J. Am. Chem. Soc.* **2008**, *130*, 16834.
- (58) Barton, B. E.; Rauchfuss, T. B. *Inorg. Chem.* **2008**, *47*, 2261.
- (59) Beyler, M.; Ezzaher, S.; Karnahl, M.; Santoni, M.-P.; Lomoth, R.; Ott, S. *Chem. Commun.* **2011**, *47*, 11662.
- (60) Eady, S. C.; Breault, T.; Thompson, L.; Lehnert, N. *Dalton Transactions* **2016**.
- (61) Boyke, C. A.; van der Vlugt, J. I.; Rauchfuss, T. B.; Wilson, S. R.; Zampella, G.; De Gioia, L. *J. Am. Chem. Soc.* **2005**, *127*, 11010.
- (62) Canaguier, S.; Artero, V.; Fontecave, M. *J. Chem. Soc. Dalton Trans.* **2008**, 315.
- (63) Capon, J.-F.; Ezzaher, S.; Gloaguen, F.; Pétilion, F. Y.; Schollhammer, P.; Talarmin, J. *Chem. Eur. J.* **2008**, *14*, 1954.
- (64) Carroll, M. E.; Barton, B. E.; Gray, D. L.; Mack, A. E.; Rauchfuss, T. B. *Inorg. Chem.* **2011**, *50*, 9554.
- (65) Carroll, M. E.; Barton, B. E.; Rauchfuss, T. B.; Carroll, P. J. *J. Am. Chem. Soc.* **2012**, *134*, 18843.
- (66) Cheah, M. H.; Tard, C.; Borg, S. J.; Liu, X.; Ibrahim, S. K.; Pickett, C. J.; Best, S. *P. J. Am. Chem. Soc.* **2007**, *129*, 11085.

- (67) Curtis, C. J.; Miedaner, A.; Ciancanelli, R.; Ellis, W. W.; Noll, B. C.; Rakowski DuBois, M.; DuBois, D. L. *Inorg. Chem.* **2003**, *42*, 216.
- (68) Darensbourg, M. Y.; Lyon, E. J.; Zhao, X.; Georgakaki, I. P. *Proc. Natl. Acad. Sci. USA* **2003**, *100*, 3683.
- (69) de Hatten, X.; Bothe, E.; Merz, K.; Huc, I.; Metzler-Nolte, N. *Eur. J. Inorg. Chem.* **2008**, 4530.
- (70) Duan, L.; Wang, M.; Li, P.; Na, Y.; Wang, N.; Sun, L. *J. Chem. Soc. Dalton Trans.* **2007**, 1277.
- (71) Eckenhoff, W. T.; McNamara, W. R.; Du, P.; Eisenberg, R. *Biochimica et Biophysica Acta (BBA) - Bioenergetics* **2013**, *1827*, 958.
- (72) Eilers, G.; Schwartz, L.; Stein, M.; Zampella, G.; de Gioia, L.; Ott, S.; Lomoth, R. *Chem. Eur. J.* **2007**, *13*, 7075
- (73) Ezzaher, S.; Capon, J.-F.; Gloaguen, F.; Petillon, F. Y.; Schollhammer, P.; Talarmin, J. *Inorg. Chem.* **2007**, *46*, 9863.
- (74) Felton, G. A. N.; Glass, R. S.; Lichtenberger, D. L.; Evans, D. H. *Inorg. Chem.* **2006**, *45*, 9181.
- (75) Felton, G. A. N.; Vannucci, A. K.; Chen, J.; Lockett, L. T.; Okumura, N.; Petro, B. J.; Zakai, U. I.; Evans, D. H.; Glass, R. S.; Lichtenberger, D. L. *J. Am. Chem. Soc.* **2007**, *129*, 12521.
- (76) Galinato, M. G. I.; Whaley, C. M.; Roberts, D.; Wang, P.; Lehnert, N. *Eur. J. Inorg. Chem.* **2011**, 1147.
- (77) Gao, W.; Ekström, J.; Liu, J.; Chen, C.; Eriksson, L.; Weng, L.; Åkermark, B.; Sun, L. *Inorg. Chem.* **2007**, *46*, 1981.
- (78) Gao, W.; Sun, J.; Åkermark, T.; Li, M.; Eriksson, L.; Sun, L.; Åkermark, B. *Chem. Eur. J.* **2010**, *16*, 2537.
- (79) Georgakaki, I. P.; Miller, M. L.; Darensbourg, M. Y. *Inorg. Chem.* **2003**, *42*, 2489.
- (80) Gloaguen, F.; Lawrence, J. D.; Schmidt, M.; Wilson, S. R.; Rauchfuss, T. B. *J. Am. Chem. Soc.* **2001**, *123*, 12518.
- (81) Ibrahim, S. K.; Liu, X.; Tard, C.; Pickett, C. J. *Chem. Commun.* **2007**, 1535.
- (82) Jiang, S.; Liu, J.; Shi, Y.; Wang, Z.; Åkermark, B.; Sun, L. *J. Chem. Soc. Dalton Trans.* **2007**, 896.

- (83) Justice, A. K.; De Gioia, L.; Nilges, M. J.; Rauchfuss, T. B.; Wilson, S. R.; Zampella, G. *Inorg. Chem.* **2008**, *47*, 7405.
- (84) Justice, A. K.; Zampella, G.; De Gioia, L.; Rauchfuss, T. B.; van der Vlugt, J. I.; Wilson, S. R. *Inorg. Chem.* **2007**, *46*, 1655.
- (85) Le Cloirec, A.; Best, S. P.; Borg, S.; Davies, S. C.; Evans, D. J.; Hughes, D. L.; Pickett, C. J. *Chem. Commun.* **1999**, 2285.
- (86) Lomoth, R.; Ott, S. *Dalton Trans.* **2009**, 9952.
- (87) Lyon, E. J.; Georgakaki, I. P.; Reibenspies, J. H.; Darensbourg, M. Y. *Angew. Chem. Int. Ed. Engl.* **1999**, *38*, 3178.
- (88) Morvan, D.; Capon, J.-F.; Gloaguen, F.; Le Goff, A.; Marchivie, M.; Michaud, F.; Schollhammer, P.; Talarmin, J.; Yaouanc, J.-J. *Organometallics* **2007**, *26*, 2042.
- (89) Morvan, D.; Capon, J.-F.; Gloaguen, F.; Schollhammer, P.; Talarmin, J. *Eur. J. Inorg. Chem.* **2007**, 5062.
- (90) Nehring, J. L.; Heinekey, D. M. *Inorg. Chem.* **2003**, *42*, 4288.
- (91) Ohki, Y.; Tatsumi, K. *Eur. J. Inorg. Chem.* **2011**, *2011*, 973.
- (92) Ohki, Y.; Yasumura, K.; Kuge, K.; Tanino, S.; Ando, M.; Li, Z.; Tatsumi, K. *Proc. Natl. Acad. Sci. USA* **2008**, *105*, 7652.
- (93) Ott, S.; Kritikos, M.; Åkermark, B.; Sun, L. *Angew. Chem. Int. Ed. Engl.* **2003**, *42*, 3285.
- (94) Ott, S.; Kritikos, M.; Åkermark, B.; Sun, L.; Lomoth, R. *Angew. Chem. Int. Ed. Engl.* **2004**, *43*, 1006.
- (95) Quentel, F.; Passard, G.; Gloaguen, F. *Energy & Environmental Science* **2012**, *5*, 7757.
- (96) Schmidt, M.; Contakes, S. M.; Rauchfuss, T. B. *J. Am. Chem. Soc.* **1999**, *121*, 9736.
- (97) Schwartz, L.; Eilers, G.; Eriksson, L.; Gogoll, A.; Lomoth, R.; Ott, S. *Chem. Commun.* **2006**, 520.
- (98) Song, L.-C.; Ge, J.-H.; Yan, J.; Wang, H.-T.; Luo, X.; Hu, Q.-M. *Eur. J. Inorg. Chem.* **2008**, 164.
- (99) Song, L.-C.; Li, C.-G.; Gao, J.; Yin, B.-S.; Luo, X.; Zhang, X.-G.; Bao, H.-L.; Hu, Q.-H. *Inorg. Chem.* **2008**, *47*, 4545.

- (100) Song, L.-C.; Wang, H.-T.; Ge, J.-H.; Mei, S.-Z.; Gao, J.; Wang, L.-X.; Gai, B.; Zhao, L.-Q.; Yan, J.; Wang, Y.-Z. *Organometallics* **2008**, *27*, 1409.
- (101) Song, L.-C.; Wang, L.-X.; Tang, M.-Y.; Li, C.-G.; Song, H.-B.; Hu, Q.-M. *Organometallics* **2009**, *28*, 3834.
- (102) Tard, C.; Pickett, C. J. *Chem. Rev.* **2009**, *109*, 2245.
- (103) Thomas, C. M.; Liu, T.; Hall, M. B.; Darensbourg, M. Y. *Inorg. Chem.* **2008**, *47*, 7009.
- (104) Wang, F.; Wang, M.; Liu, X.; Jin, K.; Dong, W.; Sun, L. *J. Chem. Soc. Dalton Trans.* **2007**, 3812.
- (105) Wang, M.; Chen, L.; Sun, L. *Energy & Environmental Science* **2012**, *5*, 6763.
- (106) Wang, N.; Wang, M.; Zhang, T.; Li, P.; Liu, J.; Sun, L. *Chem. Commun.* **2008**, 5800.
- (107) Yu, Z.; Wang, M.; Li, P.; Dong, W.; Wang, F.; Sun, L. *J. Chem. Soc. Dalton Trans.* **2008**, 2400.
- (108) Zhao, X.; Georgakaki, I. P.; Miller, M. L.; Mejia-Rodriguez, R.; C.-Y., C.; Darensbourg, M. Y. *Inorg. Chem.* **2002**, *41*, 3917.
- (109) Helm, M. L.; Stewart, M. P.; Bullock, R. M.; DuBois, M. R.; DuBois, D. L. *Science* **2011**, *333*, 863.
- (110) Raugei, S.; Chen, S.; Ho, M.-H.; Ginovska-Pangovska, B.; Rousseau, R. J.; Dupuis, M.; DuBois, D. L.; Bullock, R. M. *Chemistry – A European Journal* **2012**, *18*, 6493.
- (111) Rakowski DuBois, M.; DuBois, D. L. *Chem. Soc. Rev.* **2009**, *38*, 62.
- (112) Wilson, A. D.; Shoemaker, R. K.; Miedaner, A.; Muckerman, J. T.; DuBois, D. L.; DuBois, M. R. *Proceedings of the National Academy of Sciences* **2007**, *104*, 6951.
- (113) Wiedner, E. S.; Yang, J. Y.; Dougherty, W. G.; Kassel, W. S.; Bullock, R. M.; DuBois, M. R.; DuBois, D. L. *Organometallics* **2010**, *29*, 5390.
- (114) Liu, T.; DuBois, D. L.; Bullock, R. M. *Nat Chem* **2013**, *5*, 228.
- (115) Kilgore, U. J.; Roberts, J. A. S.; Pool, D. H.; Appel, A. M.; Stewart, M. P.; DuBois, M. R.; Dougherty, W. G.; Kassel, W. S.; Bullock, R. M.; DuBois, D. L. *J. Am. Chem. Soc.* **2011**, *133*, 5861.
- (116) McNamara, W. R.; Han, Z.; Alperin, P. J.; Brennessel, W. W.; Holland, P. L.; Eisenberg, R. *J. Am. Chem. Soc.* **2011**, *133*, 15368.

- (117) McNamara, W. R.; Han, Z.; Yin, C. J.; Brennessel, W. W.; Holland, P. L.; Eisenberg, R. *Proc Natl Acad Sci U S A* **2012**, *109*, 15594.
- (118) Wang, X.; Goeb, S.; Ji, Z.; Pogulaichenko, N. A.; Castellano, F. N. *Inorg. Chem.* **2011**, *50*, 705.
- (119) Lazarides, T.; McCormick, T.; Du, P.; Luo, G.; Lindley, B.; Eisenberg, R. *J. Am. Chem. Soc.* **2009**, *131*, 9192.
- (120) Probst, B.; Kolano, C.; Hamm, P.; Alberto, R. *Inorg. Chem.* **2009**, *48*, 1836.
- (121) Wang, M.; Na, Y.; Gorlov, M.; Sun, L. *J. Chem. Soc. Dalton Trans.* **2009**, 6458.
- (122) Ford, W. E.; Rodgers, M. A. J. *The Journal of Physical Chemistry* **1994**, *98*, 3822.
- (123) Ghosh, P.; Spiro, T. G. *J. Am. Chem. Soc.* **1980**, *102*, 5543.
- (124) Zadvornyy, O. A.; Lucon, J. E.; Gerlach, R.; Zorin, N. A.; Douglas, T.; Elgren, T. E.; Peters, J. W. *J. Inorg. Biochem.* **2012**, *106*, 151.
- (125) Gao, W.; Liu, J.; Jiang, W.; Wang, M.; Weng, L.; Åkermark, B.; Sun, L. *Comptes Rendus Chimie* **2008**, *11*, 915.
- (126) Sano, Y.; Onoda, A.; Hayashi, T. *Chem. Commun.* **2011**, *47*, 8229.
- (127) Reisner, E.; Powell, D. J.; Cavazza, C.; Fontecilla-Camps, J. C.; Armstrong, F. A. *J. Am. Chem. Soc.* **2009**, *131*, 18457.
- (128) Seo, J.; Pekarek, R. T.; Rose, M. J. *Chem. Commun.* **2015**, *51*, 13264.
- (129) Eady, S. C.; Peczonczyk, S. L.; Maldonado, S.; Lehnert, N. *Chem. Commun.* **2014**, *50*, 8065.

Chapter 2

Hydrogenase Inspired Design of Dihydrogen Production Catalysts

Introduction

The search for sustainable dihydrogen production systems has been an ongoing focus of global research efforts for nearly half a century.¹⁻³ Incorporation of non-precious metal catalysts to yield efficient dihydrogen production manifolds in aqueous systems is an ever-growing area in the field of electrocatalysis.^{4,5} Major discoveries in proton reduction electrochemistry have been made in the past few decades, which suggests that non-precious metals such as iron, nickel and cobalt with selected ligand manifolds and the correct environment may provide activities and stabilities competitive to platinum and similar rare metal catalysts.^{6-23 11,24-41}

A major challenge in the design of industrially viable electrocatalysts is minimizing the wasted input energy, i.e. overpotential, required for catalyst activation. A number of iron- and nickel-centered electrocatalysts for dihydrogen production with incredible activities ($>10,000 \text{ s}^{-1}$) have been reported in the literature; however, many of these are only active in strongly acidic conditions or have moderate to high overpotentials, typically in excess of 200 mV.^{6,42} It is therefore the focus of this study, which has been reproduced in part from a manuscript published in *Dalton Transactions* (Eady, S. C.; Breault, T.; Thompson, L.; Lehnert, N. *Dalton Transactions* **2016**, **45**, 1138), to investigate catalytic systems capable of functioning in weakly acidic media with minimal overpotentials.⁴³

In addition, to transition from basic scientific research in catalyst development to application-driven research, easy access to a variety of functionalities in the ligand periphery of a catalyst is desirable.⁴⁴⁻⁴⁶ One such application is the heterogenization of catalysts via immobilization on electrode surfaces, especially in light-driven proton reduction systems that couple water oxidation with proton reduction for efficient water splitting.^{12,29,41,45-52} Realization of such systems is met with formidable obstacles, including a means of providing a versatile ligand system that will not impact catalyst ‘core’ structure and function upon derivatization and surface immobilization. Thus it can be reasoned that the development of suitable strategies and ligand systems for catalyst immobilization is as important as the catalyst design itself, and having a catalyst system with an easily customizable ligand periphery is critical for future applications.

2.1. Structural, Spectroscopic and Electrochemical Characterization of pentacoordinate iron complexes as models for the distal iron of [FeFe] hydrogenase

Previously, penta-coordinate iron catalysts that are active for proton reduction have been reported by Ott and coworkers.³⁷ These compounds display impressive activity ($\text{TOF} > 500 \text{ s}^{-1}$ with modest overpotentials (0.17-0.24 V vs. Pt for acetic acid concentrations of 0.1-0.5 M, respectively) and were obtained in high yields in a single synthetic step from diphosphine and dithiolate ligands under atmospheric CO pressure. However, these complexes utilize a

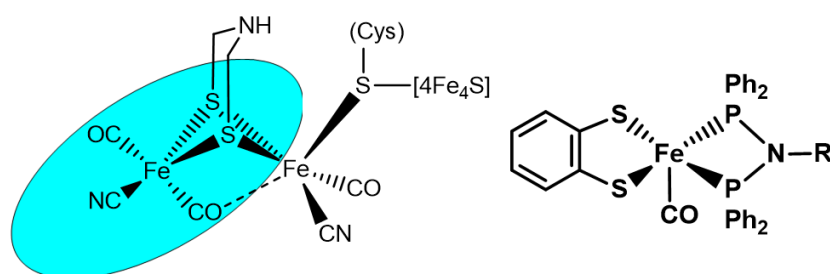
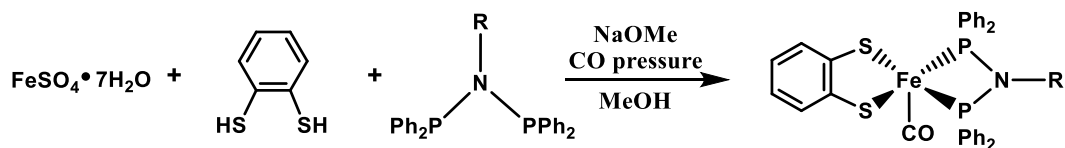


Chart 2.1. Pentacoordinate iron complexes (*right*) as models of distal iron in [FeFe] hydrogenase active site (*left*)

conformationally flexible diphosphine ligand, which, when locked into a fixed conformation in the surface-bound state, might become less active.⁴⁵ Herein we report catalytically active derivatives with a much more rigid, conjugated ‘PNP’ ligand structure, leading to iron complexes that contain a very rigid, Fe-P-N-P four-membered ring. Several derivatives of these complexes are presented and are characterized structurally as well as spectroscopically. Electrochemical properties of the complexes are further investigated, in addition to their activities for proton reduction as catalytically active models for the distal iron in [FeFe] hydrogenases (**Chart 2.1**). These systems provide a versatile, yet simple ‘toolbox’ for ligand derivatization which can be tailored to a variety of applications.

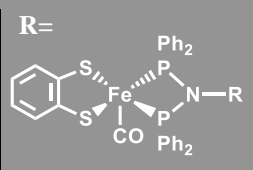
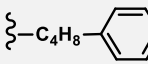
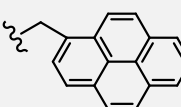
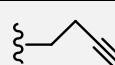


Scheme 2.1. Preparation of penta-coordinate iron dihydrogen production catalysts.

Characterization

In all cases, dropwise addition of the deprotonated dithiolate ligand in methanol to a suspension of ferrous sulfate and the respective PNP diphosphines in methanol under a carbon monoxide atmosphere led to a distinct color change of the solution to deep reddish-brown. Removal of solvent after 5 hours and subsequent extraction of the products into methylene chloride provided the corresponding iron species in crude yields of 60-90%.⁵³ Flash chromatography over neutral silica generally gave the compounds in high purity as assessed by ¹H, ³¹P and ¹⁹F NMR infrared spectroscopy (IR), and mass spectrometry (MS) (see experimental section). IR spectra of the iron complexes consistently show a single $\nu(\text{C-O})$ stretch at frequencies of 1927-1939 cm^{-1} , indicative

Table 2.1. Penta-coordinate iron compounds prepared here and selected properties

	#	$\nu(\text{C-O})$ ν_{max} (cm^{-1})	^{31}P NMR δ_{P} (ppm)	^{19}F NMR δ_{F} (ppm)	$E_{1/2}$ (V) [*]	η (V) [◇]	$i_{\text{cat}}/i_{\text{p}}$	TOF (s^{-1}) [†]	k_{cat} ($\text{M}^{-1} \text{s}^{-1}$) [‡]
	1	1932	105.4	N/A	-1.69	0.21	2.7	1.38	120
	2	1935	112.7	N/A	-1.62	0.14	2.9	1.58	235
	3	1934	113.5	N/A	-1.57	0.09	2.26	0.96	144
	4	1935	113.5	-120	-1.61	0.13	2.61	1.28	301
	5	1931	111.4	-115	-1.66	0.18	4.28	3.46	1243
	6	1932	109.4	N/A	-1.63	0.15	4.32	3.51	1375
	7	1931	110.8	N/A	-1.68	0.20	2.45	1.13	197
	8	1939	113.4	N/A	-1.6	0.12	1.22	0.28	8
	9	1927	109.2	N/A	-1.63	0.15	2.61	1.28	109

* Potentials are reported versus a ferrocene/ferrocenium internal standard (0.64 V vs. NHE)

◇ Overpotentials reported are lower-end estimates vs. Pt with 0.1 M acetic acid in acetonitrile.

† Turnover frequencies were calculated using **equation 1** at the $E_{1/2}$ potential for the corresponding complex with an [AcOH] of 0.1 M and a catalyst concentration of 1 mM.

‡ Bimolecular rate constants calculated from the slope of the i_{cat} vs. [AcOH]^{1/2} plot.

of species containing a single carbonyl ligand. Two intense bands are also present at energies of 1434 and 694 cm^{-1} that are characteristic of the phenyl groups of the diphosphine ligand, and that vary by a minimal amount ($\sim 1\text{-}2 \text{ cm}^{-1}$) with substitution at the amine position. The ^{31}P NMR spectra of the iron complexes show a single sharp resonance at 105-113 ppm depending on the substituents at the PNP amine group (**Table 2.1**).

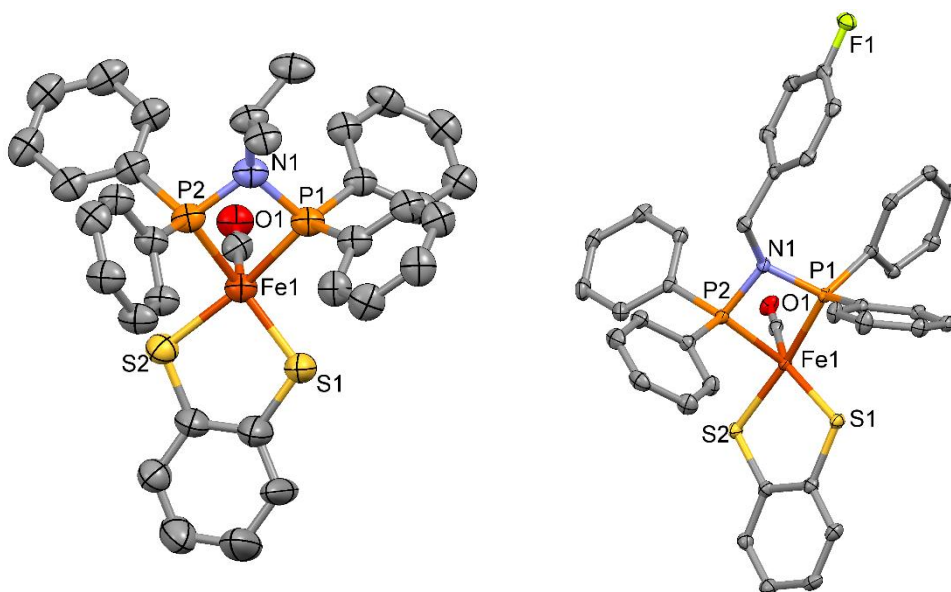


Figure 2.1. Crystal structures of $[\text{Fe}(\text{S}_2\text{C}_6\text{H}_4)((\text{C}_6\text{H}_5)_2\text{PN}(i\text{Pr})\text{P}(\text{C}_6\text{H}_5)_2)(\text{CO})]$ (**1**) (*left*) and $[\text{Fe}(\text{S}_2\text{C}_6\text{H}_4)((\text{C}_6\text{H}_5)_2\text{PN}(\text{p-fluorobenzyl})\text{P}(\text{C}_6\text{H}_5)_2)(\text{CO})]$ (**5**) (*right*) with ellipsoids shown at 50% probability. Hydrogen atoms and dichloromethane solvent molecules are omitted for clarity. Selected bond distances [\AA] and angles [degrees]: (**1**) Fe1-P1 2.203(15), Fe1-P2 2.2(13), Fe1-S1 2.161(13), Fe1-S2 2.189(14), P1-N1 1.71(4), P2-N1 1.703(4), P1---P2 2.577(17), S1---S2 3.082, S1-Fe1-S2 90.25(5), P1-Fe1-P2 71.65(5), Fe-P-N-P torsion 6.74. (**5**) Fe1-P1 2.215(6), Fe1-P2 2.144(6), Fe1-S1 2.166(6), Fe1-S2 2.21(6), P1-N1 1.718(16), P2-N1 1.708(17), P1---P2 2.583(7), S1---S2 3.096, S1-Fe1-S2 90.03(2), P1-Fe1-P2 72.65(2), Fe-P-N-P torsion 8.19.

The molecular structures of **1** and **5** have been confirmed by X-ray crystallography, showing penta-coordinate complexes with distorted square-pyramidal geometries and an axial carbonyl ligand (**Figure 2.1**). The Fe-P and Fe-S bond lengths observed for **1** and **5** are nearly identical to the ‘PCNCP’ ligated iron complex, $[\text{Fe}(\text{S}_2\text{C}_6\text{H}_4)((\text{C}_6\text{H}_5)_2\text{PCH}_2\text{N}(\text{dep})\text{CH}_2\text{P}(\text{C}_6\text{H}_5)_2)(\text{CO})]$, reported by Ott and coworkers, as well as to the $\text{P}(\text{FeCp}_2)\text{P}$ ligated iron complex, $[\text{Fe}(\text{S}_2\text{C}_6\text{H}_4)((\text{C}_6\text{H}_5)_2\text{P}(\text{FeCp}_2)\text{P}(\text{C}_6\text{H}_5)_2)(\text{CO})]$, reported by Jones and coworkers (**Table 2.2**).^{28,37} The S-Fe-S bond angles also show strong similarities across these compounds, as expected for the identical dithiolate ligand. In contrast, the P-Fe-P bond angle is significantly larger (by over 15°) in the complex reported by Jones, and even more so (over 17°) in Ott’s compound. Most notably, the torsion angles of the Fe-P-N-P ring in the complexes reported here are very small ($< 9^\circ$), showing a nearly planar ring structure. In

Table 2.2. Comparison of selected bond lengths [Å] and angles [°] for selected penta-coordinate iron compounds.

Complex (#)	M-S1	M-S2	M-P1	M-P2	P-M-P	S-M-S	MPNP torsion	τ (0-1)
1	2.161(13)	2.189(14)	2.203(15)	2.2(13)	71.65(5)	90.25(5)	6.74	0.26
5	2.166(6)	2.21(6)	2.215(6)	2.144(6)	72.65(2)	90.03(2)	8.19	0.73
10	2.194(9)	2.202(8)	2.188(9)	2.187(8)	72.13(3)	91.16(3)	3.77	0.03
Fe(S₂C₆H₄)((C₆H₅)₂PCH₂N(dep)CH₂P(C₆H₅)₂)(CO) ^{37 a}	2.187(6)	2.187(6)	2.208(6)	2.212(6)	89.59(2)	89.32(2)	14.01	0.13
Fe(S₂C₆H₄)((C₆H₅)₂P(CH₂N^{Ph}CH₂)₂P(C₆H₅)₂)(CO) ^{40 a}	2.21(6)	2.17(6)	2.14(6)	2.17(6)	81.73(2)	88.7(2)	29/58	0.22
Fe(S₂C₆H₄)((C₆H₅)₂P(FeCp₂)P(C₆H₅)₂)(CO) ^{28 a}	2.2(12)	2.177(12)	2.222(12)	2.225(12)	87.49(4)	89.31(4)	18.2 (FePFeP)	0.72

^adep: 1,1-diethoxypropane; FeCp₂: bis(cyclopentadienyl)iron or ferrocene; N^{Ph}: N(C₆H₅).

comparison, the Fe-P-N-P unit of Ott's complex has a torsion angle of 14°, and shows a distinctly non-planar chair conformation for the whole Fe-P-C-N-C-P unit (**Figure 2.2**). Jones' compound exhibits a similarly large torsion angle of 18° for its Fe-P-Fe-P unit. These differences highlight the more rigid, conjugated structure of the FePNP ring in the complexes reported here. Comparison of C-O stretching frequencies shows strong similarity for **1** and **5** ($\nu(\text{C-O})_{\text{MeCN}} = 1933$ and 1931 cm^{-1} , respectively) compared to the compound reported by Ott and coworkers ($\nu(\text{C-O})_{\text{MeCN}} = 1932$

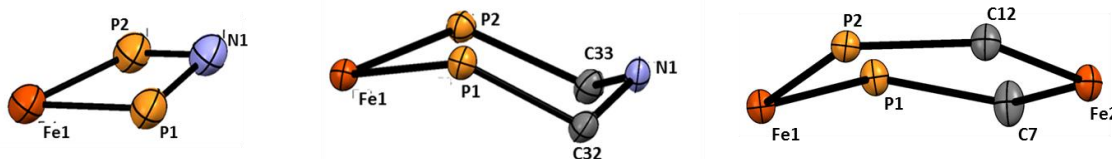


Figure 2.2. Structural comparison of the FePXP unit for [Fe(S₂C₆H₄)((C₆H₅)₂PN(ⁱPr)P(C₆H₅)₂)CO] (**1**) (left), Fe(S₂C₆H₄)((C₆H₅)₂PCH₂N(dep)CH₂P(C₆H₅)₂)(CO)¹ (center), and [Fe(S₂C₆H₄)((C₆H₅)₂P(FeCp₂)P(C₆H₅)₂)(CO)] (right.)

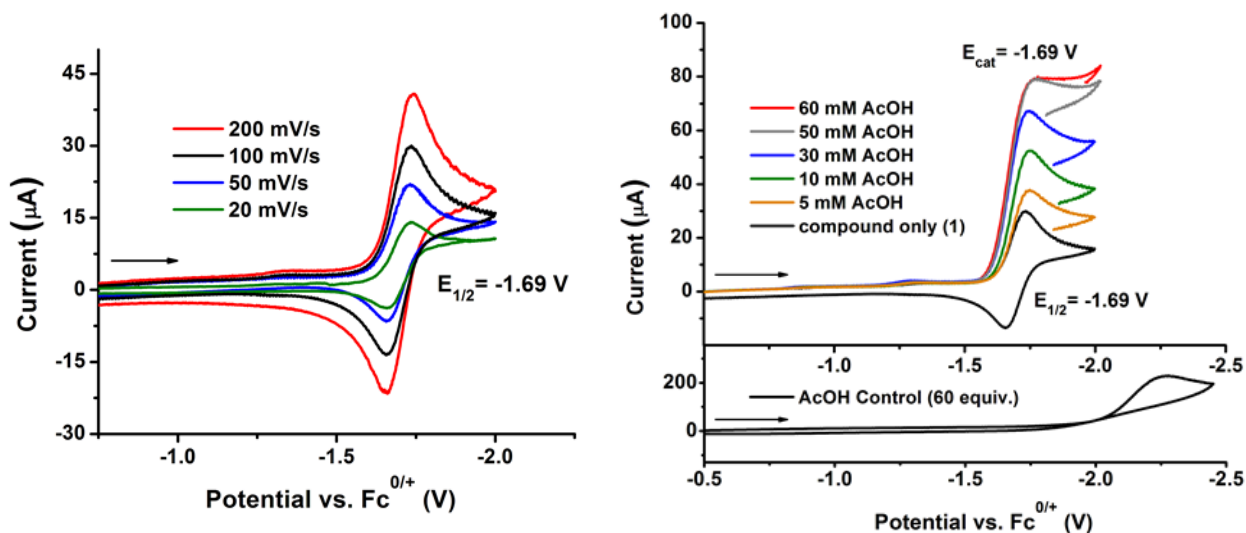


Figure 2.3. *Left:* Cyclic voltammetry of a 2mM solution of **1** in acetonitrile at various scan rates *Right:* Cyclic voltammetry of **1** at a scan rate of 100 mV/s with the addition of increasing equivalents of acetic acid. Solutions were 0.1 M (TBA)PF₆ and ferrocene was used as an internal standard. The working electrode was a glassy carbon disc, the reference was a non-aqueous Ag/AgNO₃ (0.01M) electrode, and the auxiliary electrode was a platinum disc.

cm⁻¹), while both sets of compounds show a somewhat higher $\nu(\text{C-O})$ than that reported by Jones and coworkers ($\nu(\text{C-O})_{\text{DCM}} = 1915 \text{ cm}^{-1}$). Addison's tau (τ) values (defined as $\tau = (\beta - \alpha)/60$)⁵⁴ were determined for the penta-coordinate iron complexes as a measure of distortion from an ideal square-pyramidal geometry ($\tau = 0$) or an ideal trigonal-bipyramidal geometry ($\tau = 1$) with S1-Fe1-P2 constituting α and S2-Fe1-P1 constituting β for $\tau = (\beta - \alpha)/60$. Tau values for compounds **1** and **5** are 0.26 and 0.73 respectively, showing a substantial change in solid state geometry despite a minimal change in the overall PNP structure. While the compounds reported by Ott and coworkers have a square-pyramidal structure more closely related to **1**, the ferrocene derivatives reported by Jones and coworkers are observed to have a nearly identical tau value to **5**.

Cyclic voltammograms of the penta-coordinate iron compounds in acetonitrile solution show reversible redox waves, assigned to the Fe^{II/I} couple, at potentials ranging from -1.57 to -1.69 V versus Fc^{0/+} (**Figure 2.3**). All compounds are observed to have $i_{\text{pa}}/i_{\text{pc}}$ separations of approximately 0.07 V, as is observed for the ferrocene internal standard under identical conditions. For most compounds, the $i_{\text{pa}}/i_{\text{pc}}$ ratio consistently gave values of 1 (± 0.1) at all scan rates,

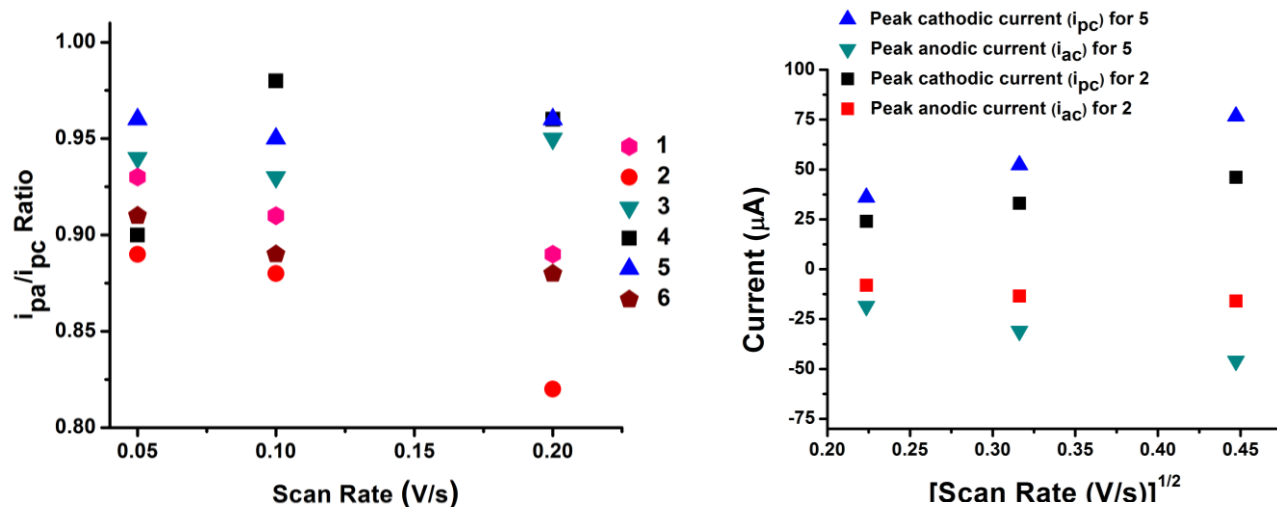


Figure 2.4. *Left:* peak anodic:cathodic current ratios for **1** (pink), **2** (red), **3** (grey), **4** (black), **5** (blue) and **6** (wine). *Right:* variation in peak cathodic/anodic currents as a function of the square root of scan rate for **5** (square) and **2** (circle). Compound **5** is presented as an example of a chemically reversible catalyst ($i_{pa}/i_{pc} \sim 1$), in contrast to compound **2** ($i_{pa}/i_{pc} < 0.9$ at higher scan rates).

suggesting chemical reversibility with no decomposition occurring after reduction on the voltammogram time scale (**Figure 2.4**). Complexes **2** and **8** have disproportionately smaller anodic peaks compared to cathodic peaks ($i_{pa}/i_{pc} < 0.9$). For several of the compounds, a small decrease in the i_{pa}/i_{pc} ratio with increasing scan rates is observed, most noticeably for **2** and **8**. As it is more significant at higher scan rates, this decrease in i_{pa}/i_{pc} is likely due to a somewhat slow geometric reorganization step for these compounds (see DFT results below), resulting in a mixture of conformations with slightly offset oxidation potentials and a slightly lower i_a overall at higher scan rates. With the exceptions of these complexes, all i_c and i_a values are seen to increase proportionally to $[\text{scan rate}]^{1/2}$ (**Figure 2.4**), and no significant change in peak potentials (E_{pa} and E_{pc}) is observed upon varying the scan rate.

Electrocatalytic Studies

Upon addition of acetic acid ($\text{pK}_{a_{\text{MeCN}}} = 22.3$), the cathodic waves of the iron species increased approximately linearly with acid concentration, which simultaneously occurred with the

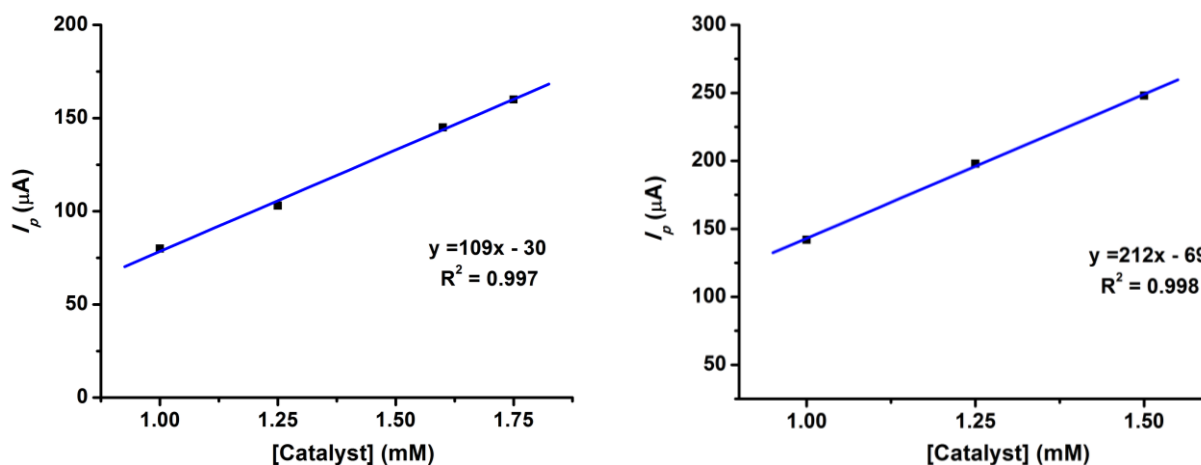


Figure 2.5. Peak catalytic current for **2** (left) and **6** (right) with respect to catalyst concentration at acid saturation conditions. All experiments performed in acetonitrile with 0.1 M (TBA)PF₆ as supporting electrolyte. The working electrode was a glassy carbon disc, the reference was a non-aqueous Ag/AgNO₃ (0.01M) electrode, and the auxiliary electrode was a platinum disc electrode.

subsiding of the corresponding anodic waves. This behavior is indicative of electrocatalytic proton reduction from acetic acid, and consistently gave half-maximum wave potential (E_{cat}) values that directly coincide with the $E_{1/2}$ of each iron species. Background reduction of acetic acid protons by glassy carbon at these potentials and acid concentrations is negligible as shown in **Figure 2.3**. Importantly, activity occurs at potentials that correspond to only very slight overpotentials for proton reduction, as compared to the same process (acetic acid reduction, 0.1M) by platinum under identical conditions (see Experimental Section).³⁷ A half-wave potential (E_{cat}) of only -1.57 V vs. Fc^{0/+} is displayed by the compound with the 4-bromophenyl substituent at the PNP amine (**3**), corresponding to an overpotential of only 0.09 V vs. platinum, the lowest for all of the compounds reported here. The overpotentials of all compounds are listed in **Table 2.1**. It is worth noting that the current increase for **8** is significantly lower than that for all other compounds, low enough that **8** could be considered inactive for proton reduction (within error).

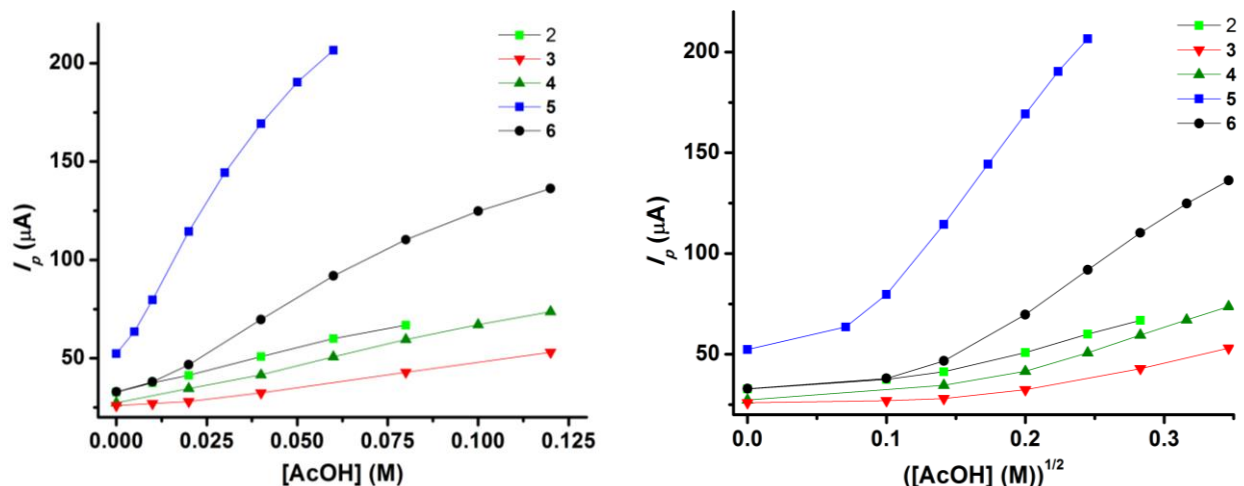


Figure 2.6. Peak current for **2** (1 mM, light green trace), **3** (1 mM, red trace), **4** (1 mM, green trace), **5** (2 mM, blue trace) and **6** (1 mM, black trace) as a function of [AcOH] (**a**) and [AcOH]^{1/2} (**b**). All experiments were performed in acetonitrile with 0.1 M (TBA)PF₆ as supporting electrolyte. The working electrode was a glassy carbon disc, the reference was a non-aqueous Ag/AgNO₃ (0.01M) electrode, and the auxiliary electrode was a platinum disc electrode.

The catalytic current increases linearly with catalyst concentration over the investigated range of catalysts [1.0-1.75 mM] at acid saturation conditions, indicative of a first order dependence of the rate on catalyst concentration (**Figure 2.5**). With lower acid concentrations, total catalysis is observed, where activity is limited only by diffusion of substrate (acid) to the electrode and catalytic activity increases linearly with acid concentration.⁵⁵ At higher acid concentrations (exact number of equivalents is dependent on the ligand substitution), catalytic plateau currents are approximately linear with [AcOH]^{1/2} (**Figure 2.6**) until activity saturation behavior is observed. Bimolecular rate constants are calculated from the slopes of these plots with **equation 1** analogous to the methods used by Ott and coworkers to provide a direct comparison to their similar catalyst systems:

$$(1) I_p = FAC_{cat}^0 \sqrt{D} \sqrt{2kC_S^0}$$

Here, D is the diffusion coefficient as determined by the Randles Sevcik equation (**Equation S3**) to be 1 x 10⁵ (+/- 0.2) cm²/s, and A is the electrode area (0.031 cm²). Rate constants from Equation 1 give a range of activities from 8 to 1375 M⁻¹ s⁻¹ (**Table 2.1**).³⁷ At the activity saturation point

where the peak catalytic current (i_{cat}) is seen to be independent of acid concentration, rate estimates for each species can also be obtained from the ratio of the peak catalytic current to the cathodic current in the absence of acid (**equation 2**).⁵⁶

$$(2) \quad \frac{i_{cat}}{i_p} = \frac{2}{0.446} \sqrt{\frac{RTk_{obs}}{Fv}}$$

Here, F = Faraday's constant and v = scan rate (V/s). This method is used to calculate TOF for the penta-coordinate species, varying from 0.28 to 3.51 s^{-1} , depending on the ligand substitution pattern as listed in **Table 2.1** (see Table for TOF measurement conditions).

Bulk electrolysis coupled with gas chromatography (GC) was used to monitor electrocatalytic dihydrogen production by **5** (1 mM) in acetonitrile solution from 0.04 M acetic acid (**Figure 2.7**). GC confirmed continued catalytic activity for 2 hours to produce a total of 87 micromoles of dihydrogen with 73% Faradaic efficiency. From this electrolysis data a turnover number (TON) of 6 has been calculated for **5**. After initial activity subsided ($t = 2$ hours), a second

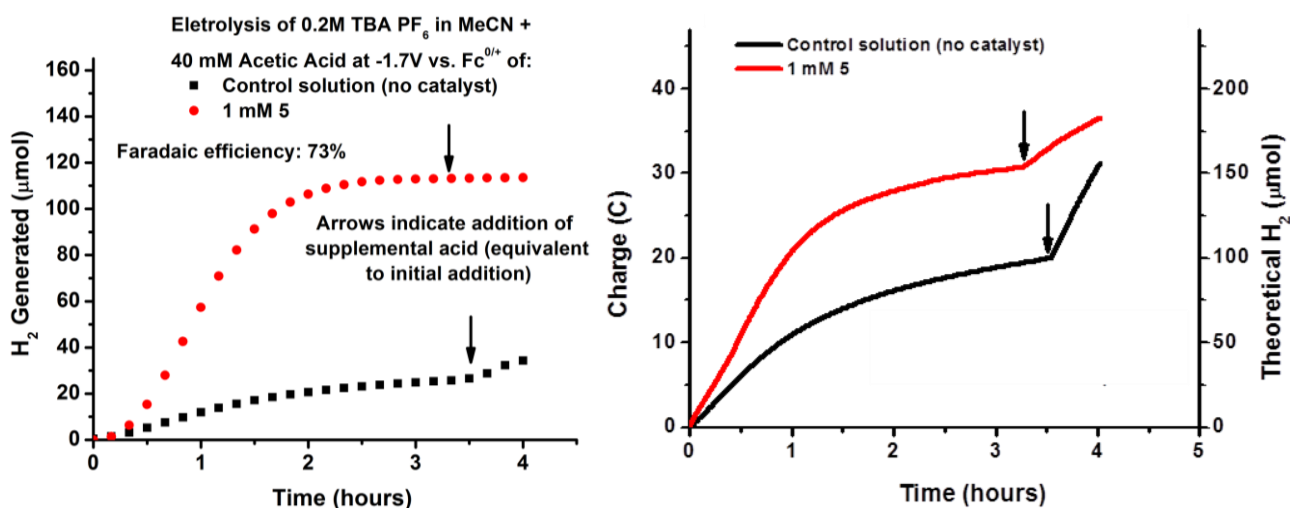


Figure 2.7. *Left:* Gas chromatography dihydrogen production measurement for bulk electrolysis at -1.7 V vs. Fc^{0/+} of **5** (1 mM) with acetic acid (40 mM) in a 0.2 M (TBA)PF₆ acetonitrile solution. *Right:* Charge passed during the electrolysis experiment. 0.1 M (TBA)PF₆ and ferrocene was used as an internal standard. The working and auxiliary electrodes were carbon felt (4 cm²), and the reference was a non-aqueous Ag/AgNO₃ (0.01M) electrode. Ferrocene (0.1 M) was used in the counter compartment as a sacrificial reductant. Arrows indicate addition of supplemental acid, equivalent to the initial addition.

aliquot of acid was added; however, no significant resurgence in dihydrogen production was observed beyond control levels, confirming the compound's activity had not ceased due to acid depletion. Significant bleaching of the solution had occurred within the initial 2 hours of electrolysis. Solution IR analysis of the electrolysis solution at this time showed negligible signal intensity at the carbonyl ligand stretching frequency for **5** (1931 cm^{-1}), indicating the complex had degraded including loss of CO. ^{31}P NMR confirmed the degradation of **5** with complete loss of the resonance at 111.4 ppm, and decomposition was further evidenced by a change in solution color from reddish-brown to yellow.

The less than quantitative efficiency is likely due to trace amounts of ferrocenium hexafluorophosphate (the oxidized form of the sacrificial reductant) leaking through the glass frit and being reduced at the working electrode. This phenomenon is also observed in the control experiments, confirming that substantial non-faradaic charge is being passed in the absence of catalyst. Additional charge loss could be attributed to a possible reductive decomposition pathway for these catalyst species.

Mechanistic Studies

Monitoring of the C-O stretching frequency of **1** in acetonitrile solution by IR spectroscopy upon the addition of acetic acid ($\text{pK}_{\text{aMeCN}} = 22.3$) shows no significant shift of the $\nu(\text{C-O})$ band under these conditions (**Figure 2.8**). This result rules out chemical alteration of the catalyst by acetic acid prior to the reduction of the complexes, and is further supported by the fact that the catalytic onset potential for each iron complex with this acid is nearly identical to its $E_{1/2}$ value ($\text{Fe}^{\text{II}}/\text{Fe}^{\text{I}}$ potential). These observations are consistent for all complexes investigated here (**1-9**) that differ in the PNP substitution pattern. The same results were obtained using the significantly

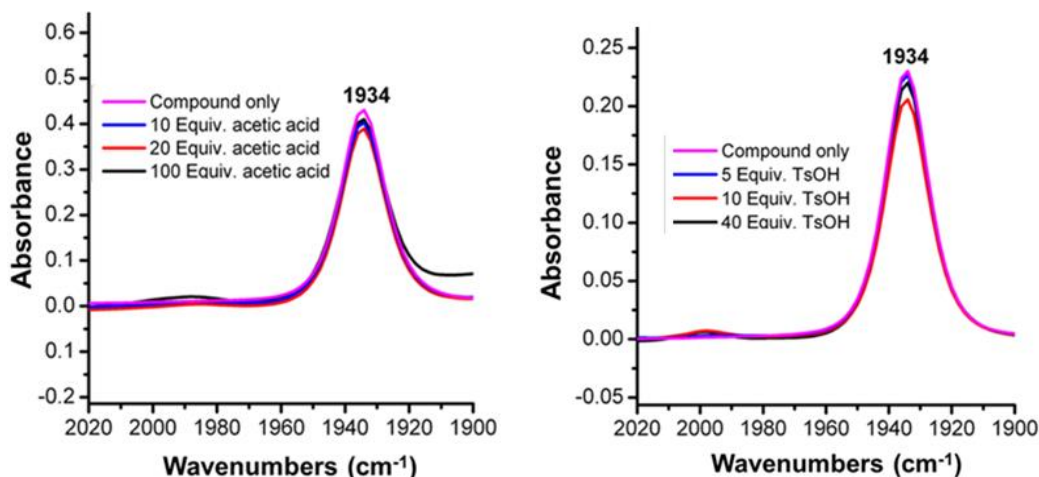


Figure 2.8. Variation of $\nu(\text{C-O})$ for $[\text{Fe}(\text{S}_2\text{C}_6\text{H}_4)((\text{C}_6\text{H}_5)_2\text{PN}(\text{iPr})\text{P}(\text{C}_6\text{H}_5)_2)(\text{CO})]$ (**1**) in acetonitrile solution upon the addition of acetic acid (*left*) and toluene sulfonic acid (*right*), monitored by solution IR spectroscopy.

stronger toluenesulfonic acid (TsOH, $\text{pK}_{\text{aMeCN}} = 8.3$). These results suggest that the Fe^{II} complexes cannot be protonated by the acids used for the electrocatalytic studies performed here, and that the initial mechanistic step for our penta-coordinate iron catalysts is a one-electron reduction. To observe intermediates after initial reduction, bulk electrolysis of species **1** was performed, and the reaction was monitored by solution IR spectroscopy (**Figure 2.8**). Upon applying a potential of -1.7 vs. $\text{Fc}^{+/0}$, a red shift in the carbonyl ligand stretching frequency of nearly 100 cm^{-1} was observed, showing a slightly broader and less intense signal at 1836 cm^{-1} . This shift is indicative of the formation of a reduced $\text{Fe}^{\text{I}}\text{-CO}$ species, and correlates well with the reduced $[\text{Fe}(\text{S}_2\text{C}_6\text{H}_4)((\text{C}_6\text{H}_5)_2\text{P}(\text{CH}_2\text{N}^{\text{Ph}}\text{CH}_2)_2\text{P}(\text{C}_6\text{H}_5)_2)(\text{CO})]$ species observed by Ott and coworkers with a $\nu(\text{C-O})$ band at 1850 cm^{-1} .⁴⁰ This species is assumed to be the reactive intermediate for hydride formation as no further reduction events are evident at this applied potential (no further carbonyl band shifting is observed with additional electrolysis time). Loss of the $\nu(\text{C-O})$ signal at 1836 cm^{-1} for **1**⁻ was observed only several minutes after the applied potential was removed, and no

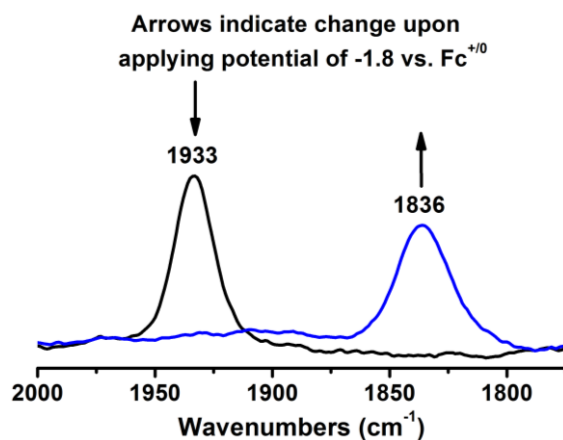


Figure 2.9. Bulk electrolysis at -1.8 V vs. $\text{Fc}^{+/0}$ of a 4 mM solution of **1** in acetonitrile with 0.1 M (TBA)PF₆ monitored by solution IR spectroscopy. The black trace is the spectrum of the compound prior to passing charge; the blue trace corresponds to the species formed during bulk electrolysis.

substantial recovery of **1** as indicated by the $\nu(\text{C-O})$ band at 1933 cm^{-1} was observed, suggesting decomposition including CO loss.

Density Functional Calculations

Given the similarity in overall structure for all $[\text{Fe}(\text{S}_2\text{C}_6\text{H}_4)(\text{PNP})(\text{CO})]$ derivatives reported here, full geometry optimizations of **1** ($S = 0$) with the BP86 functional and the TZVP basis set were performed as a representation of all the complexes investigated here. The optimized structure of **1** overall matched reasonably well with the crystal structure as shown in **Table 2.3**, with an average offset of 0.03 \AA for iron-ligand bond lengths and 0.3 degrees for iron-ligand bond angles. In contrast, both the FePNP torsion and τ values are somewhat underestimated, with a predicted torsion angle that is 4 degrees lower than that in the crystal structure and an estimated τ value of 0.01 . Frequency calculations of **1** produce a single carbonyl stretch with $\nu(\text{C-O})$ of 1951 cm^{-1} , which is close to the experimental value of 1933 cm^{-1} and reflects the normal error reported for DFT/experimental comparisons in literature.

Table 2.3. Select bond lengths [\AA] and angles [$^\circ$] for penta-coordinate iron species **1** as predicted by DFT calculations and comparison to crystal structure values. Calculations were performed with BP86/TZVP.

Structure source	Fe-S1	Fe-S2	Fe-P1	Fe-P2	P-Fe-P	S-Fe-S	FePNP torsion	τ (0-1)
Crystal structure of 1	2.161(13)	2.189(14)	2.203(15)	2.2(13)	72.66(5)	90.03(5)	6.74	0.26
DFT structure of 1	2.198	2.198	2.226	2.238	73.02	90.28	2.71	0.01
DFT structure of 1⁻	2.255	2.286	2.206	2.24	72.93	88.38	6.26	0.7
DFT structure of 1⁻ - (CO)	2.216	2.226	2.152	2.164	73.35	91.06	0.01	0.19
DFT structure of 1⁻ (MeCN)	2.272	2.272	2.183	2.194	73.17	88.73	2.94	0.03

Calculations on the reduced Fe^I species **1⁻** ($S = 1/2$) show a relatively small change in bond lengths compared to **1**, with an increase of 0.06 and 0.08 \AA for Fe-S1 and Fe-S2, respectively, and a decrease of only 0.02 \AA for Fe-P1. The P1-Fe1-P2 bond angle has a similar change of approximately 2 degrees. Far more substantial changes in FePNP torsion angle and τ value are predicted upon reduction, with a 4 degree increase in torsion angle and an increase of τ from 0.01 to 0.7. This represents a substantial change in complex geometry upon reduction from an essentially ideal square pyramidal structure to a more closely trigonal bipyramidal geometry. Frequency calculations of **1⁻** produce a single carbonyl stretch with $\nu(\text{C-O})$ of 1886 cm^{-1} , substantially higher than the $\nu(\text{C-O})$ value of 1836 cm^{-1} observed experimentally upon reduction of **1**. Loss of the $\nu(\text{C-O})$ signal for **1⁻** after several minutes, as evidenced by IR spectroscopy, prompted DFT investigations of the reduced structure after the loss of CO (**1⁻ - (CO)**, $S = 1/2$). The ΔE for CO loss from the low-spin Fe^I complex was calculated to be unfavorable by 45.6 kcal/mol, a substantial value for a process seen to be experimentally credible. While this value supports the slow timeframe of CO loss after reduction observed by IR spectroscopy, it likely also

suggests an alternative chemical transformation prior to CO loss to promote this reaction and avoid such an energetically unfavorable pathway as direct loss from the reduced, five-coordinate complex.

Cobalt Analogs

The cobalt compound analogous to **1** was prepared following the same synthetic procedure as in the case of iron, but using a cobaltous sulfate reagent as the metal source. IR spectroscopic analysis of this compound (crude product) shows a single $\nu(\text{C-O})$ band at 1988 cm^{-1} (see experimental section), suggesting the corresponding cobalt penta-coordinate compound had been formed with an analogous ligand environment as in the case of **1**. Mass spectrometry confirmed the presence of a species with m/z of 627, corresponding to the cobalt dithiolate diphosphine complex after the loss of the carbonyl ligand (as was seen by mass spectrometry analysis for the iron analog). Single crystals of **10** suitable for diffraction were afforded with some difficulty, and analysis confirmed the expected five-coordinate structure displaying a square pyramidal geometry with an axial carbonyl ligand, completely analogous to the iron complex (**Figure 2.10**).

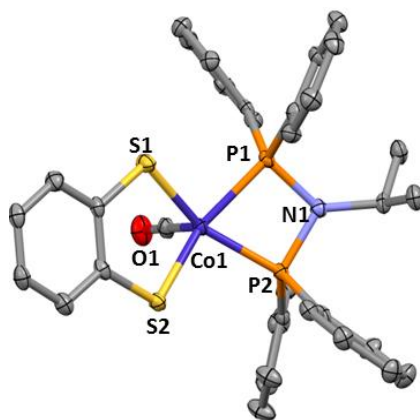


Figure 2.10. Crystal structure of $[\text{Co}(\text{S}_2\text{C}_6\text{H}_4)((\text{C}_6\text{H}_5)_2\text{PN}(\text{Pr})\text{P}(\text{C}_6\text{H}_5)_2)(\text{CO})]$ (**10**) with ellipsoids shown at 50% probability. Hydrogen atoms are omitted for clarity. Selected bond distances [\AA] and angles [degrees]: Co1-P1 2.188(9), Co1-P2 2.187(8), Co1-S1 2.194(9), Co1-S2 2.202(8), P1-N1 1.695(2), P2-N1 1.708(2), P1---P2 2.576(10), S1---S2 3.140, S1-Co1-S2 91.16(3), P1-Co1-P2 72.13(3), Co-P-N-P torsion 3.77

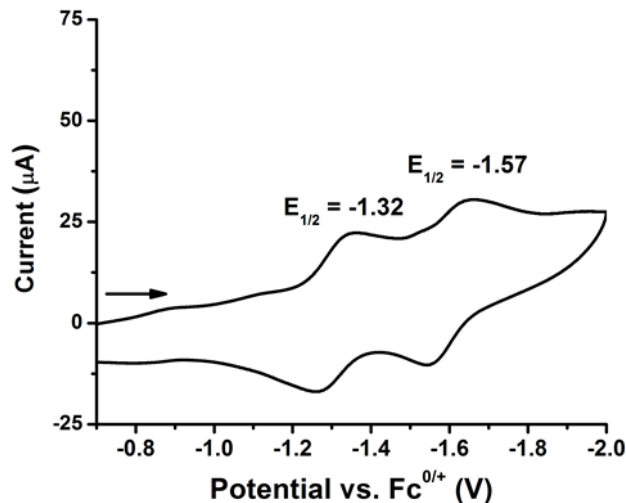


Figure 2.11. Cyclic voltammogram of $[\text{Co}(\text{S}_2\text{C}_6\text{H}_4)((\text{C}_6\text{H}_5)_2\text{PN}(\text{Pr})\text{P}(\text{C}_6\text{H}_5)_2)\text{CO}]$ (**10**) in acetonitrile solution with 0.1 M $(\text{TBA})\text{PF}_6$ supporting electrolyte. The working electrode was a glassy carbon disc, the reference was a non-aqueous Ag/AgNO_3 (0.01M) electrode, and the auxiliary electrode was a platinum disc electrode. The redox couple with $E_{1/2} = -1.32$ V was seen to vary in concentration for each batch of compound. Typically the feature was significantly lower in current response than the redox couple with $E_{1/2} = -1.57$ V and was originally considered an impurity, for better visibility a batch with a larger signal at $E_{1/2} = -1.32$ V is shown here.

Given the difficulty in obtaining pure product for **10**, electrochemical analysis was performed on the crude product. Cyclic voltammetry of this mixture showed a main redox feature at -1.57 V vs. $\text{Fc}^{0/+}$, while a minor feature attributed to an impurity was evident with an $E_{1/2}$ of -1.32 V (**Figure 2.11**). Upon the addition of tributylammonium hexafluorophosphate ($\text{Bu}_3\text{NH PF}_6$), an increasing cathodic current was observed at -1.63 V, corresponding to the $E_{1/2}$ of the more prominent redox feature in the CV of crude **10** (**Figure 2.12**). Increasing acid concentrations showed a linear increase in catalytic current; however, multiple features were apparent upon close analysis of the catalytic wave, suggesting the presence of multiple active species in the crude product or the availability of multiple mechanistic pathways at more negative potentials. A substantial cathodic shift of the E_{cat} was also evident with increasing acid concentration, indicating the species or mechanistic pathway giving rise to the more anodic portion of the wave was being altered with additional acid.

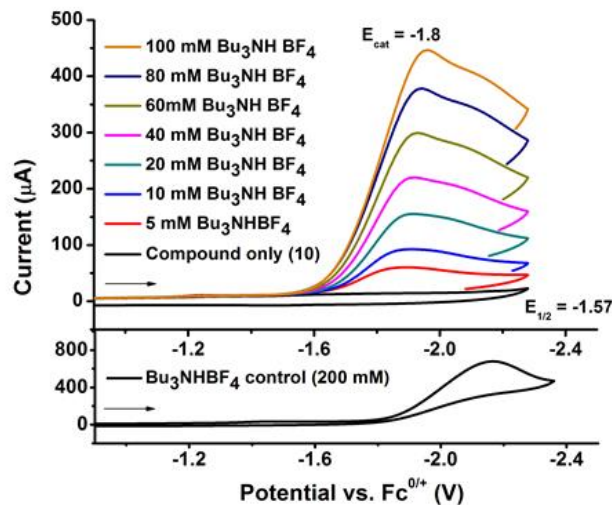


Figure 2.12. Cyclic voltammetry of **10** (2 mM) at a scan rate of 100 mV/s with the addition of increasing equivalents of $(\text{Bu}_3\text{NH})\text{BF}_4$. Solutions contained 0.1 M $(\text{TBA})\text{PF}_6$ as a supporting electrolyte and ferrocene was used as an internal standard. The working electrode was a glassy carbon disc, the reference was a non-aqueous Ag/AgNO_3 (0.01M) electrode, and the auxiliary electrode was a platinum disc electrode.

In order to obtain further insight into the mechanism and fate of $[\text{Co}(\text{S}_2\text{C}_6\text{H}_4)((\text{C}_6\text{H}_5)_2\text{PN}(\text{tPr})\text{P}(\text{C}_6\text{H}_5)_2)\text{CO}]$, the crude product of **10** was monitored by solution IR spectroscopy upon addition of increasing equivalents of triethylammonium hexafluorophosphate ($\text{Et}_3\text{NH PF}_6$, $\text{pK}_{\text{aMeCN}} = 18.5$)⁵⁷ (**Figure 2.13**). The observed depletion of the $\nu(\text{C-O})$ band at 1993 cm^{-1} at higher acid concentrations with no new signal in the carbonyl range confirmed the decomposition of **10** during electrochemical analysis. These results indicate that the observed catalytic current must in fact correspond to at least two active species in the crude product, and that the shifting of the E_{cat} is due to the decomposition and subsided activity of **10** at higher acid concentrations. This hypothesis is also supported by the two redox signals typically observed in the crude of **10** (**Figure 2.11**).

These results prompted us to investigate the second active species in the crude product, which remains active at high acid concentrations, and which has a very high catalytic activity ($\text{TOF} > 1000\text{ s}^{-1}$) as estimated with **equation 1**. To determine the identity of this elusive species,

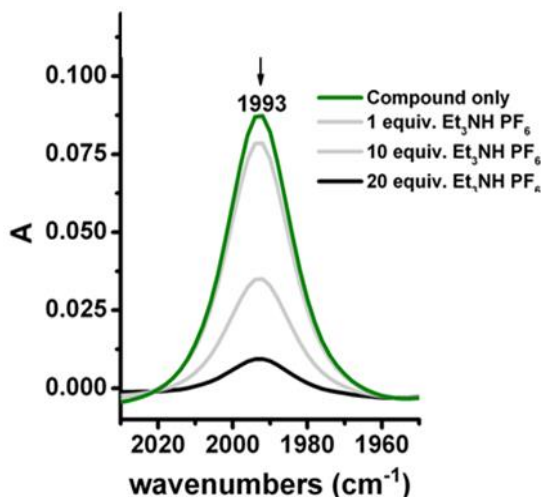


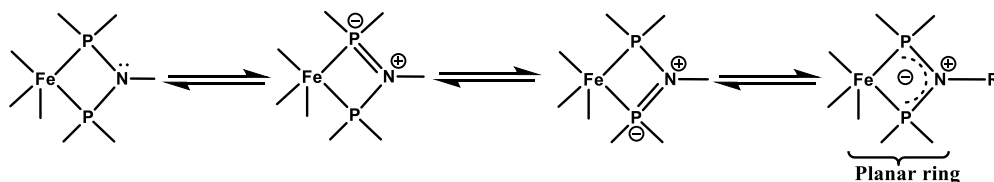
Figure 2.13. Monitoring of $\nu(\text{C-O})$ for the crude product of $[\text{Co}((\text{C}_6\text{H}_5)_2\text{PN}(\text{iPr})\text{P}(\text{C}_6\text{H}_5)_2)(\text{S}_2\text{C}_6\text{H}_4)(\text{CO})]$ (**10**) in acetonitrile (5 mM) with addition of triethylammonium hexafluorophosphate using IR spectroscopy. Under these conditions, decomposition of the Co complex is observed.

extensive column chromatography using various stationary phases and techniques was utilized. Chromatography was found to be generally inefficient for the complete isolation of the second active species; however, electrochemical analysis of all column fractions in the presence of acid allowed for the identification of fractions containing the highest activity levels per fraction mass. In this way, the unknown active species could be concentrated, and subsequently analyzed by ^{31}P NMR and UV-Visible spectroscopy. Surprisingly, the ^{31}P NMR results clearly showed that the major species present in these fractions did not contain the phosphine ligand. Reproduction of the original synthesis in the absence of diphosphine and CO yielded deep blue cobalt dithiolate compounds. Suspiciously, the UV-Visible spectrum of this compound matches those of the most active column fractions of the crude product of **10**. Electrochemical testing of these cobalt dithiolate compounds under the same conditions as **10** showed a redox wave corresponding to the unknown active species in **Figure 2.11**, and the same catalytic current response was observed at high acid concentrations as was seen with the crude product of **10** (after the depletion of the penta-coordinate cobalt complex).

At that time, analogous reactivity and synthetic details were reported by McNamara and coworkers regarding cobalt bis(dithiolate) H₂ production catalysts.¹⁷ Based on these considerations, it is evident that the unknown active species in our preparations is the cobalt bis(dithiolate) complex [Co(S₂C₆H₄)₂]⁻. This evidence suggests that these Co(S₂C₆H₄)₂-type species are consistent impurities in the crude product of **10** and similar preparations, and that these species are responsible for the sustained catalytic activity observed at high acid concentrations. In conclusion, pentacoordinate cobalt complexes of formula [Co(S₂C₆H₄)((C₆H₅)₂PN(ⁱPr)P(C₆H₅)₂)CO] displayed electrochemical responses indicative of hydrogen production catalysis, but instability in acid and under turnover conditions and difficulty in purification discouraged further investigation. Notably, the unstable nature of these complexes was contrasted by the incredible stability of the unintended [Co(S₂C₆H₄)₂]⁻ byproduct, which remained capable of turnover after long-term air exposure and extensive chromatography. In summary, through rigorous chromatography and mechanistic studies detailed above, it was determined that the component of the crude product responsible for the sustained current response at high acid concentrations was not the pentacoordinate cobalt analog, but rather a cobalt bis(dithiolate) by-product similar to those reported independently by McNamara et al.¹⁷

2.2. Comparison to Analogous Pentacoordinate Iron Catalysts: Effect of Diphosphine Ligand Structure on Overpotential and Catalytic Performance

In this chapter, a new series of five-coordinate Fe^{II}-CO complexes that serve as H₂ production catalysts with weak acids at very low overpotentials (relative to the thermodynamic activation potential for acetic acid) is reported. Our penta-coordinate iron compounds all contain a rigid Fe(S₂C₆H₄)(PNP) ligand structure and show very similar $\nu(\text{C-O})$ frequencies, ³¹P NMR



Scheme 2.2. Illustration of the delocalization of the nitrogen lone pair of the PNP ligand, leading to a planar FePNP ring.

resonances, and $E_{1/2}$ values. These results generally suggest that modification of the secondary ligand sphere of the PNP ligand has a limited effect on the geometrical structure and electron density at the metal center in the resulting complexes.

The penta-coordinate iron compound **1** exhibits a distorted square-pyramidal geometry with an Addison τ value (defined as $\tau = (\beta - \alpha)/60$)⁵⁴ of 0.26. The Fe-P-N-P- ring is nearly perfectly planar, confirming the rigid nature of the ligand moiety. This planar geometry around the nitrogen atom is surprising and is indicative of a conjugated ring structure (see **Scheme 2.2**). In comparison, the structures of the related complexes by Ott and coworkers, $[\text{Fe}(\text{S}_2\text{C}_6\text{H}_4)((\text{C}_6\text{H}_5)_2\text{PCH}_2\text{N}(\text{dep})\text{CH}_2\text{P}(\text{C}_6\text{H}_5)_2)(\text{CO})]$, and Jones and coworkers, $[\text{Fe}(\text{S}_2\text{C}_6\text{H}_4)((\text{C}_6\text{H}_5)_2\text{P}(\text{FeCp}_2)\text{P}(\text{C}_6\text{H}_5)_2)(\text{CO})]$, show very similar core structures, but non-planar rings in the Fe-P-C-N-C-P and Fe-P-C-Fe-C-P units, respectively (**Figure 2.2**). As identical dithiolate and CO ligands are used in all three types of compounds, the reduced activity and lower overpotentials seen in the compounds reported here can be exclusively attributed to the structural differences from the ‘PNP’ diphosphine ligand used here.^{28,37}

Electrochemical analysis of compounds **1-9** shows that all penta-coordinate iron complexes have chemically reversible $\text{Fe}^{\text{II}}/\text{Fe}^{\text{I}}$ couples, with the exception of some irreversible behavior ($i_{\text{pa}}/i_{\text{pc}} < 1 \pm 0.1$) observed for complexes **2** and **8** when cycling at higher scan rates (>100 mV/s). This result indicates that there is a relatively slow geometric reorganization prior to reoxidation for these complexes. Interestingly, DFT calculations on complex **1** indicate that the approximately

square-planar Fe(II) complex undergoes a rearrangement to a trigonal-bipyramidal structure upon reduction. Hence, there might be a more hindered (hence slower) rearrangement from square-pyramidal to trigonal-bipyramidal for **2** and **8** compared to the other catalysts investigated here, which would explain the somewhat irreducible behavior of these complexes at higher scan rates. Overpotential values, as determined by comparison to the potential for proton reduction from acetic acid at a platinum electrode (under identical conditions), are observed to vary significantly between different amine substitutions for complexes **1-9**. The most notable differences are seen with more electron donating ($R = ^i\text{Pr}$, $\eta = 0.21 - 0.28$ V) aliphatic amine substituents and those with more electron withdrawing substituents ($R = p\text{-BrC}_6\text{H}_4$, $\eta = 0.09 - 0.16$ V), showing a definitive effect of the PNP ligand properties on the metal's redox potential. However, comparison among the complexes with more similar PNP amine substitutions does not show conclusive trends, such as those for $R = \text{C}_6\text{H}_4$, $p\text{-BrC}_6\text{H}_4$, and $p\text{-FC}_6\text{H}_4$, with lower-estimate η values of 0.14, 0.09, and 0.13 V, respectively. In comparison, the 'PCNCP'-type complexes reported by Ott and coworkers have overpotential values ranging from 0.17 to 0.25 V for proton reduction from acetic acid (lower end estimates).³⁷ Similarly, the 'PCFeCP'-type complex prepared by Jones and coworkers has a reported overpotential range of 0.17 - 0.2 V.²⁸ The higher overpotentials seen in the 'PCNCP'- and 'PCFeCP'-type complexes suggest that the more rigid, conjugated 'PNP'-type ligand structure used here is advantageous for lowering the overpotential for proton reduction, and also allows for a stronger amine substituent effect of the phosphine ligand on the metal's redox potential.

Variation in electrocatalytic activity for proton reduction is also seen across our series of compounds, spanning a range of roughly an order of magnitude in TOF with the lowest rate of 0.28 s^{-1} for **8** and the highest TOF of 3.51 s^{-1} for **6**. Direct comparison of similar substituents shows

substantial differences, such as the nearly 300% increase in TOF from fluorophenyl (**4**) to fluorobenzyl (**5**), in this example with only the addition of a methylene moiety before the phenyl ring substituent. Similarly, comparing the complexes with the phenyl substituent (**2**) and the butylphenyl substituent (**6**) at the PNP amine shows an increase of more than 200% in TOF (1.58 s^{-1} for (**2**) and 3.51 s^{-1} for (**6**)), which is again thought to be caused by the aliphatic butyl moiety. While this effect could be due to the more electron-donating character of the aliphatic substituent versus the aromatic substituent, the relatively low activity seen in the isopropyl derivative (**1**, 1.38 s^{-1}) does not follow this trend. Alternatively, this might be better attributed to the steric flexibility allowed by the alkyl groups and the geometric structures of the Fe^{II} complexes, as the reduction from Fe^{II} to Fe^{I} very likely causes a change in the geometry of the complexes towards trigonal-bipyramidal (see DFT results above). In this regard, it is interesting to note that complex **1**, which is approximately square planar, shows one of the lowest TOF (and k_{cat}) values, whereas complex **5**, which is already close to trigonal-bipyramidal in its $\text{Fe}(\text{II})$ form, has one of the highest catalytic activities. This indicates that the structural rearrangement of the complexes after reduction might be a key factor that determines the electrocatalytic activities of our catalysts. For comparison, ‘PCFeCP’-type complex reported by Jones and coworkers, $[\text{Fe}(\text{S}_2\text{C}_6\text{H}_4)((\text{C}_6\text{H}_5)_2\text{P}(\text{FeCp}_2)\text{P}(\text{C}_6\text{H}_5)_2)(\text{CO})]$, was not seen to reach activity saturation up to a $[\text{AcOH}]$ concentration of 1.6 M in THF, with an estimated TOF of 241 s^{-1} , determined by the same method used here (**equation 1**; catalyst concentration 0.6 mM) at the peak catalytic potential of approximately -1.8 V. Notably, this maximum TOF is nearly two orders of magnitude larger than that of the most active of our compounds (3.51 s^{-1} for **6**), which reach their maximum TOF at much lower acid concentrations.²⁸

Bimolecular catalytic rate constants were calculated for **1-9** based on cyclic voltammetry data using equation **2** in an analogous manner to Ott and coworkers. These calculated values also vary widely across the catalyst series by roughly two orders of magnitude, from $8 \text{ M}^{-1} \text{ s}^{-1}$ to $1375 \text{ M}^{-1} \text{ s}^{-1}$. As expected, the general trend in activity across the series of compounds reported here is preserved in both TOF and rate constant estimates. Interestingly, at peak acid concentrations (0.1 M), a TOF of 137 s^{-1} can be calculated for **6** (equation **1**), which is over an order of magnitude higher than the TOF calculated for **6** by equation **2** (3.51 s^{-1}). It is also of interest that the estimated TOFs and the bimolecular rate constants do not correlate with the overpotential in these complexes. The bimolecular rate constants estimated for the corresponding ‘PCNCP’-type complex $[\text{Fe}(\text{S}_2\text{C}_6\text{H}_4)((\text{C}_6\text{H}_5)_2\text{PCH}_2\text{N}(\text{dep})\text{CH}_2\text{P}(\text{C}_6\text{H}_5)_2)(\text{CO})]$ by Ott and coworkers is nearly an order of magnitude higher ($1000 \text{ M}^{-1} \text{ s}^{-1}$) as compared to the average k_{cat} value in our series (Table **2.1**).³⁷ The exceptions to this trend are compounds **5** and **6**, which both show exceptional k_{cat} values (1243 and $1375 \text{ M}^{-1} \text{ s}^{-1}$, respectively) compared to our other complexes. While these k_{cat} values exceed those estimated by Ott and coworkers, comparison of the acid titration CV data shows that our complexes reach activity saturation at much lower acid concentrations (below 0.1 M, with a maximum i_c/i_p of only about 5), whereas for Ott’s compound no activity saturation is observed up to an $[\text{AcOH}]$ concentration of 0.5 M (resulting in i_c/i_p of approximately 20, and $\text{TOF} = 77 \text{ s}^{-1}$ from equation **1**). These results show that the bimolecular rate constants are not an accurate predictor of *maximum catalyst activity*, since acid-independent steps in the mechanism can lead to activity saturation for different catalysts at different acid concentrations, causing substantial differences in maximum TOF values that can be accomplished. The most reasonable explanation for this difference (supported by the DFT results) is that the flexibility afforded from the diphosphines with larger rings may allow for necessary conformational changes to occur more rapidly upon

turnover, leading to faster rates for Ott's compounds. The geometric strain observed in the FePNP system is extreme and likely leads to reduced rates and increased ligand lability. In addition, the availability of pendant amines in Ott's complexes that can serve as proton shuttles could contribute to their faster rates. In this regard, DuBois and others have shown that pendant amines can facilitate M-H/H⁺ and M/H-H interactions during catalysis, leading to faster catalyst turnover.^{9,58-60} On the other hand, comparison of overpotentials shows a distinct advantage of the FePNP unit in our complexes, causing a distinct drop in overpotential as discussed above. This is most pronounced in compound **3** with an E_{cat} of -1.57 V vs. Fe^{0/+}, giving an overpotential of only 0.09 V versus platinum. The substantial difference in catalyst stability under turnover, when considered along with the stability of our original catalysts **1-9** in solution and in the presence of acid, indicates that the reduced and/or protonated forms of **1-9** are significantly less stable than the corresponding intermediates of Ott's catalysts, which are reported to undergo insignificant decomposition over the course of 30 turnovers in slightly over one hour.

Acid titration studies provide insight into the initial steps of catalysis. For all penta-coordinate iron catalysts (**1-9**) reported here, protonation did not occur prior to reduction with either acetic or toluenesulfonic acid, as evidenced by solution IR spectroscopy. These results are in contrast to those of Ott and coworkers, who observed blue shifting of the C-O stretching frequency upon addition of TsOH, indicative of ligand protonation as discussed above.³⁷ This difference, despite using the same dithiolate ligand as in Ott's complexes, suggests that the PNP ligand structure reported here is structurally unique, and that the amine is generally insufficiently basic to protonate under these conditions (due to resonance stabilization of the amine's lone pair; see **Scheme 2.2**). This is further supported by the fact that the potential for electrocatalytic H₂ production is identical to the E_{1/2}, the Fe^{II}/Fe^I potential in the absence of acid. The mechanism

mildly acidic conditions) upon alteration of the second coordination sphere of the ligand framework. The compounds show some of the lowest overpotentials for proton reduction with mononuclear iron catalysts reported to date. However, this improvement comes at a price of a reduced catalytic rate for the compounds and, unfortunately, a decrease in stability compared to analogous monoiron complexes reported in the literature. The contrast observed here between activity estimates by cyclic voltammetry data and electrolysis illustrates the limitation of activity estimates that are derived under non-turnover conditions. Efforts to stabilize catalyst derivatives via use of alternative dithiolate ligands are currently underway. In addition, studies are in progress exploiting the highly functionalizable ligand framework in our catalysts for use in a variety of applications, including surface probes and easily modifiable sensors.

2.3. Electrocatalytic Activity of Hydrogenase Model Catalysts Electrostatically Adsorbed to Reduced Graphene Oxide Surfaces.

In order to test the functionalizable iron catalysts for applications on heterogeneous surfaces, the derivatives functionalized with aromatic moieties attached at the amine positions, specifically **5**, **6** and **7**, were adsorbed on reduced graphene oxide (RGO)-deposited fluorine doped tin oxide (FTO) electrodes prepared as outline in the experimental section and described in detail in **Chapter 3**. Analysis of these electrodes in acetonitrile solution in some cases showed a new irreversible redox response with an E_{pc} at approximately -1.7 V vs. $Fc^{0/+}$; however, typically only responses consistent with background signal were observed, and under repeated scan conditions any samples with signals at -1.7 V were seen to decrease to background (**Figure 2.14**, left). Analysis of the catalyst-adsorbed FTO/RGO electrodes for electrocatalytic behavior in acetonitrile solution with the addition of acetic acid, unlike in the case of the homogeneous systems, showed

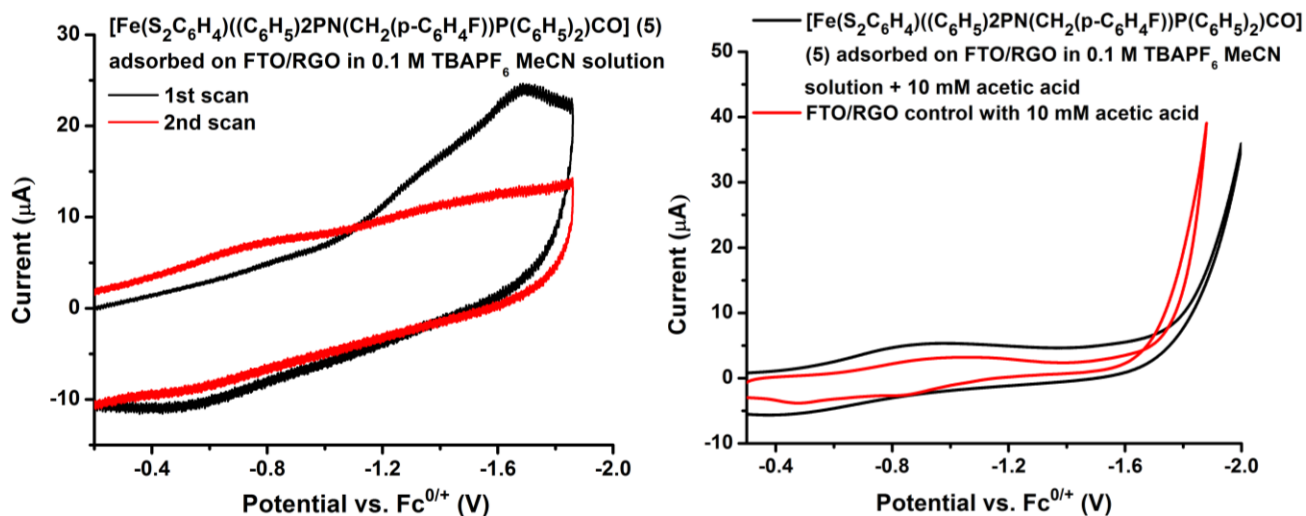


Figure 2.14. Cyclic voltammetry of $[\text{Fe}(\text{S}_2\text{C}_6\text{H}_4)((\text{C}_6\text{H}_5)_2\text{PN}(\text{CH}_2(\text{p}\text{-C}_6\text{H}_4\text{F}))\text{P}(\text{C}_6\text{H}_5)_2)\text{CO}]$ (**5**) adsorbed on a FTO/RGO working electrode in 0.1 M TBAPF₆ MeCN solution before (*left*) and after (*right*) the addition of acetic acid. Counter electrode is a platinum disc and reference electrode is Ag/AgNO₃ (0.01M).

no significant increase in cathodic current. Further acid addition effects only a minute change in current which has been associated with background current at FTO/RGO (**Figure 2.14**, right). Analysis of the current response in aqueous solutions with acetic acid also showed no increased current response. Due to failure to perform as heterogeneous electrocatalysts under these conditions, further assessment of catalyst binding and activity on FTO/RGO was not pursued.

In summary, the electrochemical data suggests that the iron catalysts with diphosphine ligands modified to contain aromatic moieties may adsorb to FTO/RGO surfaces; however no significant change above background current is observed with the addition of acetic acid in acetonitrile or aqueous solutions. The results indicate that the catalysts either desorb in acidic conditions or upon electrochemically cycling in acidic solutions, in either case suggesting the catalysts do not have potential for use as heterogeneous hydrogen production catalysts with this particular interface design. However, due to the highly customizable ligand framework and low overpotentials for these complexes, further investigation of these catalysts attached to

semiconductors using an alternative interface is still of interest for study, and is explored in **Section 4.2**.

Experimental Section

General Procedures

Unless otherwise stated, all syntheses were performed under a dinitrogen atmosphere with distilled and degassed solvents.

Materials.

Isopropylamine (99%), triethylamine (>99%), 1-amino-3-aminobutyne (95%), 1-pyrenemethylamine hydrochloride (95%), 1-pyrenebutanol (99%), aniline (99%), 4-bromoaniline (97%), 4-fluoroaniline (99%), 4-fluorobenzylamine (97%), 4-phenylbutylamine (97%), benzene-1,2-dithiol (97%), and Fe(II) sulfate heptahydrate (>99%) were all purchased from Sigma Aldrich and used as received. Methylene chloride, acetonitrile and hexane were all purchased from Fisher (ACS grade), distilled over calcium hydride, and degassed with a dinitrogen purge before use. Methanol was purchased from Fisher (ACS grade), distilled over magnesium sulfate (Fisher), and degassed with dinitrogen prior to use.

Physical Measurements

¹H NMR spectra at 400 MHz, ³¹P NMR spectra at 170 and ¹⁹F NMR spectra at 348 MHz were obtained on a Varian MR400 spectrometer. All ¹H chemical shifts were measured relative to residual protons in the lock solvents and are referenced to Me₄Si (0.00 ppm). ³¹P NMR chemical shifts are referenced to the corresponding proton experiment conducted directly prior to the ³¹P measurement. ¹⁹F chemical shifts were referenced to a CCl₃F internal standard set to 0 ppm. All mass spectra collected using electrospray ionization (ESI) techniques were recorded on a

Micromass LCT Time-of-Flight Spectrometer. Solid state infrared (IR) spectra were recorded on a Perkin Elmer Spectrum 100 FT-IR spectrometer by embedding the compounds in a KBr matrix. Solution IR studies were conducted in acetonitrile (purified as described above) and measurements were performed between NaCl plates. Elemental analyses were performed by Atlantic Microlab, Inc, Norcross, GA.

Electrochemistry

Cyclic voltammetry (CV) was performed in a 3-electrode cell under an argon atmosphere with a glassy carbon working electrode ($A = 0.031 \text{ cm}^2$), platinum counter electrode, and Ag/AgNO₃ (0.01 M, MeCN) reference electrode. Acetonitrile used for electrochemical measurements was purchased from Fisher (ACS grade), distilled over calcium hydride, and degassed with a dinitrogen purge before use. Ferrocene (Fc, 99%) used as an internal standard was purchased from Sigma and recrystallized from hexane. All potentials are reported vs. the Fc^{0/+} redox couple. Bulk electrolysis studies were performed in a two-compartment cell separated by a glass frit. The working and counter electrodes were carbon felt, and the reference electrode was Ag/AgNO₃ (0.01 M, MeCN). Ferrocene was used in the counter electrode compartment as a sacrificial reductant. Working electrodes for all experiments were polished with alumina and diamond polish (1 μM), followed by electrochemical stripping in a 0.1 M (TBA)PF₆ acetonitrile solution (500 scans, 1 V/s, 0 to -2 V vs. Fc^{0/+}).

Graphene Oxide Preparation

Graphene oxide for RGO depositions was prepared via Hummer's method:⁶² sodium nitrate (0.5 g) was added to 23 mL of sulfuric acid in a large beaker and stirred until dissolved. Next, 1 g of graphite powder was added and stirred. After cooling in an ice bath, potassium permanganate (3 g) was slowly added to the suspension, instigating gas formation. The

ice-bath was then removed and the temperature of the suspension was brought up to room temperature. The reaction beaker was then placed in an oil bath at 40°C and stirred for 1 hour. The reaction was quenched with the slow addition of 40 mL DI water, causing a gas production of brown vapors. After gas production ceased, the suspension was then further diluted with 40 mL of 10% H₂O₂ solution to convert remaining manganese oxides to inert sulfates, causing a change of the solution to a brown color. The solids were centrifuged and washed extensively with a mixture of 5% H₂SO₄ and 5% H₂O₂. The remaining powders were then washed with DI water until neutral pH was reached. The resulting graphene oxide powder was dried in a vacuum oven at 40 °C to give 1.76 g of graphene oxide.

Reduced Graphene Oxide Depositions

0.5 g of graphene oxide (prepared as described above) was added to 30 mL of a 0.1 M sodium carbonate/bicarbonate buffered solution (pH= 9.2) in Millipore water. The solution was stirred extensively for a long time to allow for better graphene oxide sheet separation, becoming more viscous over time. Before deposition, fluorine-doped tin oxide (FTO) coated glass was cleaned by sonication in acetone, ethanol and water. The graphene oxide solution was degassed by a purge with argon gas prior to deposition. For all depositions, the cleaned FTO-glass piece was used as the working electrode in the graphene oxide solution, with a platinum auxiliary electrode and Ag/AgCl reference electrode. In a typical deposition, a CV would be initiated at the open circuit potential (~0 V) and scanned cathodically to -1.4 V, with two cathodic scans for all RGO surfaces used for analysis here. After deposition the surfaces were extensively rinsed with deionized water and briefly sonicated to remove any loose graphene (oxide) from the surface.

Overpotential Determination

Overpotential was determined by the exact method used by Ott and coworkers,³⁷ and is given relative to the corresponding $E_{1/2}^{Pt}$ obtained on a freshly polished Pt electrode under exactly the same conditions. The data reported in ref. 1 are directly relevant to the complexes reported here since our electrochemical experiments utilized the same solvent and acids (in nearly identical concentration ranges), as well as overall similar catalysts. Specifically, since all catalysts reported here reach activity saturation within roughly 100 equivalents of acetic acid, using 1 mM catalyst concentrations (i.e. acid concentrations do not exceed 0.2 M), the half-wave potential (E_{cat}) observed for platinum at [AcOH] of 0.2 M by Ott and coworkers, -1.48 V vs. $Fe^{0/+}$, was used to calibrate overpotentials for all catalysts reported here.

Gas Chromatography

Gas chromatography (GC) experiments in combination with bulk electrolysis studies for the measurement of dihydrogen gas were performed with a SRI 8610C gas chromatograph equipped with a thermal conductivity detector (TCD) and a flame ionization detector (FID), as well as MS13X (6') and Hayesep-D (6') columns using dinitrogen (99.999% pure) as the electrochemical cell carrier gas with a flow rate of 3 mL/min. For the bulk electrolysis experiments, injections into the detector were made every ten minutes and dihydrogen evolution volumes were quantified for these times. To calculate the amount of hydrogen produced between the 10 minutes intervals, the rate of hydrogen produced per minute at the two intervals was averaged ($(R_{x \text{ min}} + R_{x+10 \text{ min}})/2$), and this average rate was used for an estimate of the produced H_2 volume over the ten minute interval ($V_{\text{interval}} = R_{x-(x+10) \text{ avg}} (\text{V/min}) * 10 \text{ min}$). Cumulative volumes were obtained by taking the sum of the aforementioned volumes from each time span. Faradaic efficiency was calculated as the molar sum of the evolved dihydrogen divided by half of the total electron charge passed in the same time frame.

X-Ray Crystallography

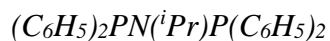
All structural data was collected on a Rigaku AFC10K Saturn 944+ CCD-based X-ray diffractometer equipped with a low temperature device and a Micromax-007HF Cu-target micro-focus rotating anode ($\lambda = 1.54187 \text{ \AA}$) operated at 1.2 kW power (40 kV, 30 mA). The X-ray intensities were measured at 85(1) K with the detector placed at a distance of 42.00 mm from the crystal. Analysis of the data showed negligible decay during data collection; the data were processed with CrystalClear 2.0 and corrected for absorption. The structures were solved and refined with the Bruker SHELXTL (version 2008/4) software package. Details about the structure determinations are provided in the Supporting Information.

Computational Methods

All geometry optimizations and frequency calculations were performed with the Gaussian 09 program package⁶³ with the BP86 functional and the TZVP basis set (as implemented in Gaussian 09).

General Preparation of diphosphine amine ligands:

Our method is a modification of a similar diphosphine synthesis reported by Imhoff et. al.⁶⁴ Chlorodiphenylphosphine (1.08 mL, 2 mmol) was added dropwise to a stirring solution of the selected primary amine (1 mmol) and triethylamine (1.4 mL, 10 mmol) in methylene chloride, causing a fine white precipitate to form. The mixture was allowed to stir overnight, after which time solvent was removed in vacuo. The solids were thoroughly washed with methanol (5x, 20 mL) and the filtered white product was dried by vacuum. The product was recrystallized from a dichloromethane/hexane solution at room temperature.



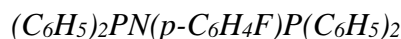
Recrystallization afforded the product as a white solid with a yield of 89%. $^1\text{H-NMR}$ (400 MHz, CDCl_3): $\delta_{\text{H}} = 7.23\text{-}7.42$ (m, 20H, $(\text{P}(\text{C}_6\text{H}_5)_2)_2$), 3.2 (m, 1H, $i\text{Pr}$), 0.63 (d, 6H, $i\text{Pr}$) ppm. $^{31}\text{P}\{^1\text{H}\}$ -NMR (202 MHz, CDCl_3): $\delta_{\text{P}} = 40$ ppm (broad).



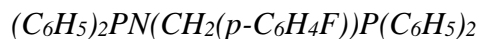
Recrystallization afforded the product as a white solid with a yield of 85%. $^1\text{H-NMR}$ (400 MHz, CD_2Cl_2): $\delta_{\text{H}} = 7.23\text{-}7.4$ (m, 20H, $(\text{P}(\text{C}_6\text{H}_5)_2)_2$), 6.94 (m, 3H, NC_6H_5), 6.64 (d, 2H, NC_6H_5) ppm. $^{31}\text{P}\{^1\text{H}\}$ -NMR (202 MHz, CD_2Cl_2): $\delta_{\text{P}} = 68.5$ ppm.



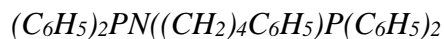
Recrystallization afforded the product as a white solid with a yield of 80%. $^1\text{H-NMR}$ (500 MHz, CD_2Cl_2): $\delta_{\text{H}} = 7.2\text{-}7.55$ (m, 20H, $(\text{P}(\text{C}_6\text{H}_5)_2)_2$), 6.74 (d, 2H, $\text{NC}_6\text{H}_4\text{Br}$), 6.5 (d, 2H, $\text{NC}_6\text{H}_4\text{Br}$) ppm. $^{31}\text{P}\{^1\text{H}\}$ -NMR (202 MHz, CD_2Cl_2): $\delta_{\text{P}} = 69.2$ ppm.



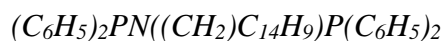
Recrystallization afforded the product as a white solid with a yield of 87%. $^1\text{H-NMR}$ (500 MHz, CD_2Cl_2): $\delta_{\text{H}} = 7.26\text{-}7.53$ (m, 20H, $(\text{P}(\text{C}_6\text{H}_5)_2)_2$), 6.58 (m, 2H, $\text{NC}_6\text{H}_4\text{F}$), 6.45 (m, 2H, $\text{NC}_6\text{H}_4\text{F}$) ppm. $^{31}\text{P}\{^1\text{H}\}$ -NMR (202 MHz, CD_2Cl_2): $\delta_{\text{P}} = 70.3$ ppm. $^{19}\text{F-NMR}$ (348 MHz, CD_2Cl_2): $\delta_{\text{F}} = -117.4$ ppm.



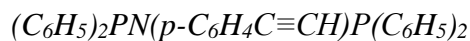
Recrystallization afforded the product as a white solid with a yield of 90%. $^1\text{H-NMR}$ (500 MHz, CD_2Cl_2): $\delta_{\text{H}} = 7.51\text{-}7.91$ (m, 20H, $(\text{P}(\text{C}_6\text{H}_5)_2)_2$), 6.6 (m, 2H, $\text{N}(\text{CH}_2)\text{C}_6\text{H}_4\text{F}$), 6.4 (m, 2H, $\text{N}(\text{CH}_2)\text{C}_6\text{H}_4\text{F}$), 4.0 (m, 2H, $\text{N}(\text{CH}_2)\text{C}_6\text{H}_4\text{F}$) ppm. $^{31}\text{P}\{^1\text{H}\}$ -NMR (202 MHz, CD_2Cl_2): $\delta_{\text{P}} = 72.5$ ppm. $^{19}\text{F-NMR}$ (348 MHz, CD_2Cl_2): $\delta_{\text{F}} = -112.4$ ppm.



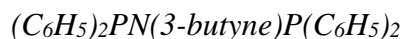
Recrystallization afforded the product as a colorless oil with a yield of 78%. 1H -NMR (500 MHz, CD_2Cl_2): $\delta_H = 7.0$ -8.2 (m, 25H, $(P(C_6H_5)_2)_2$ and $N((CH_2)_4C_6H_5)$), 2.98 (m, 2H, $N((CH_2)_4C_6H_5)$), 2.6 (m, 2H, $N((CH_2)_4C_6H_5)$), 1.54 (m, 2H, $N((CH_2)_4C_6H_5)$), 1.13 (m, 2H, $N((CH_2)_4C_6H_5)$) ppm. $^{31}P\{^1H\}$ -NMR (202 MHz, CD_2Cl_2): $\delta_P = 42.9$ ppm.



Recrystallization afforded the product as a white solid with a yield of 86%. 1H NMR (400 MHz, CD_2Cl_2): $\delta_H = 7.47$ -8.75 (m, 9H, $N(CH_2)C_{14}H_9$), 7.2-7.4 (m, 20H, $(P(C_6H_5)_2)_2$), 5.1 (m, 2H, $(N(CH_2)C_{14}H_9)$) ppm. $^{31}P\{^1H\}$ -NMR (202 MHz, CD_2Cl_2): $\delta_P = 58.9$ ppm.



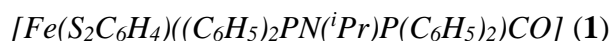
Recrystallization afforded the product as a beige solid with a yield of 60%. 1H -NMR (500 MHz, CD_2Cl_2): $\delta_H = 7.24$ -7.39 (m, 20H, $(P(C_6H_5)_2)_2$), 7.0 (d, 2H, (p- $HC\equiv CC_6H_4$)), 6.5 (d, 2H, (p- $HC\equiv CC_6H_4$)), 3.1 (s, 1H, (p- $HC\equiv CC_6H_4$)) ppm. $^{31}P\{^1H\}$ -NMR (202 MHz, CD_2Cl_2): $\delta_P = 64.3$ ppm.



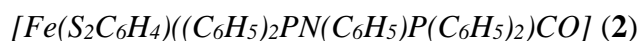
Recrystallization afforded the product as a white solid with a yield of 76%. 1H NMR (400 MHz, CD_2Cl_2): $\delta_H = 7.2$ -7.39 (m, 20H, $(P(C_6H_5)_2)_2$), 1.93 (m, 2H, $N((CH_2)_2C\equiv CH)$), 1.89 (s, 1H, $N((CH_2)_2C\equiv CH)$), 1.51 (m, 2H, $N((CH_2)_2C\equiv CH)$) ppm. $^{31}P\{^1H\}$ NMR (170 MHz, CD_2Cl_2): $\delta_P = 42.9$ ppm.

General preparation of penta-coordinate iron and cobalt complexes:

Metal compounds were prepared following a procedure initially reported by Takács et al. (see Scheme 1 above):⁵³ In a large vial, 1,2-benzenedithiol (0.14 g, 1 mmol) and sodium methoxide (0.11 g, 2 mmol) were dissolved in 10 mL of methanol. In a Schlenk flask the selected diphosphine ligand (1 mmol) and ferrous sulfate heptahydrate (0.280 g, 1 mmol) were combined in methanol (30 mL). The Schlenk flask was charged with 1 atm CO pressure, and the benzenedithiol solution was added dropwise via addition funnel to the mixture while stirring. Addition of this solution caused an immediate change in color from light yellow to reddish-brown. The mixture was allowed to stir under CO pressure for 5 hours, after which time the solvent was removed in vacuo. The resulting solid was washed with methylene chloride and filtered, the filtrate being collected and reduced in vacuo to a dark red-black solid. Flash column chromatography of the crude product over neutral silica gel in a 1:1 dichloromethane/hexane solvent mixture yielded complexes determined to be pure by ³¹P and ¹H NMR in most cases (exceptions are noted below).



Column chromatography of the product afforded a reddish-brown solid of **1** in 60% yield. Single crystals suitable for X-ray diffraction were obtained by recrystallization in CH₂Cl₂/hexane layered solutions with slow evaporation at -32°C. EA calc (x0.75 CH₂Cl₂): C 58.35, H 4.55, N 1.95; found: C 59.42, H 4.77, N 2.09. ¹H-NMR (400 MHz, CDCl₃): δ_H = 7.13-8.2 (m, 24H, (P(C₆H₅)₂)₂) and S₂C₆H₄), 3.47 (m, 1H, ⁱPr), 0.62 (d, 6H, ⁱPr) ppm. ³¹P{¹H}-NMR (202 MHz, CDCl₃): δ = 105.4 ppm; IR (KBr): ν_{max}/cm⁻¹ 1932 ν(C-O). APSI mass spectrum (positive mode): *m/z* = 623.9 (M – CO + H)⁺.



Column chromatography of the product afforded a reddish-brown solid of **2** in 65% yield. Recrystallization of this product in CH₂Cl₂/hexane layered solutions was required to remove residual impurities and provide pure compound. EA calc: C 64.82, H 4.26, N 2.04; found: C 64.25, H 5.05, N 1.93. ¹H-NMR (400 MHz, CD₂Cl₂): δ_H = 7.05-8.16 (m, 24H, (P(C₆H₅)₂)₂ and S₂C₆H₄), 7 (m, 2H, N(C₆H₅)), 6.6 (m, 2H, N(C₆H₅)) ppm. ³¹P{¹H}-NMR (170 MHz, CD₂Cl₂): δ_P = 112.7 ppm. IR (KBr): ν_{max}/cm⁻¹ 1935 ν(C-O).

*[Fe(S₂C₆H₄)((C₆H₅)₂PN(*p*-C₆H₄Br)P(C₆H₅)₂)CO] (3)*

Column chromatography of the product afforded a reddish-brown solid of **3** in 40% yield. Recrystallization of this product in CH₂Cl₂/hexane layered solutions was required to remove residual impurities and provide pure compound. ¹H-NMR (500 MHz, CD₂Cl₂): δ_H = 7.15-8.18 (m, 24H, (P(C₆H₅)₂)₂ and S₂C₆H₄), 7.1 (m, 2H, N(*p*-BrC₆H₅)), 6.4 (m, 2H, N(*p*-BrC₆H₅)) ppm. ³¹P{¹H}-NMR (202 MHz, CD₂Cl₂): δ_P = 113.5 ppm. IR (KBr): ν_{max}/cm⁻¹ 1934 ν(C-O).

*[Fe(S₂C₆H₄)((C₆H₅)₂PN(*p*-C₆H₄F)P(C₆H₅)₂)CO] (4)*

Column chromatography of the product afforded a reddish-brown solid of **4** in 60% yield. EA calc: C 63.17, H 4.01, N 1.99; found: C 62.19, H 4.22, N 1.95. ¹H-NMR (500 MHz, CD₂Cl₂): δ_H = 7.1-8.2 (m, 24H, (P(C₆H₅)₂)₂ and S₂C₆H₄), 6.74 (m, 2H, N(*p*-FC₆H₅)), 6.5 (m, 2H, N(*p*-FC₆H₅)) ppm. ³¹P{¹H}-NMR (202 MHz, CD₂Cl₂): δ_P = 113.5 ppm. ¹⁹F- NMR (348 MHz, CD₂Cl₂): δ_F = -114.2 ppm. IR (KBr): ν_{max}/cm⁻¹ 1935 ν(C-O).

*[Fe(S₂C₆H₄)((C₆H₅)₂PN(CH₂(*p*-C₆H₄F))P(C₆H₅)₂)CO] (5)*

Column chromatography of the product afforded a reddish-brown solid of **5** in 55% yield. Single crystals suitable for X-ray diffraction were obtained by recrystallization in CH₂Cl₂/hexane layered solutions with slow evaporation at -32°C. EA calc: C 63.61, H 4.21, N 1.95; found: C 63.19, H 4.18, N 1.97. ¹H-NMR (500 MHz, CD₂Cl₂): δ_H = 7.13-8.55 (m, 24H, (P(C₆H₅)₂)₂) and S₂C₆H₄), 6.55 (m, 2, N(CH₂)C₆H₄F), 6.45 (m, 2, N(CH₂)C₆H₄F), 4.5 (m, 2, N(CH₂)C₆H₄F); ³¹P{¹H}-NMR (202 MHz, CD₂Cl₂): δ_P = 111.4 ppm. ¹⁹F-NMR (348 MHz, CD₂Cl₂): δ_F = -115.1 ppm. IR (KBr): ν_{max}/cm⁻¹ 1931 ν(C-O).



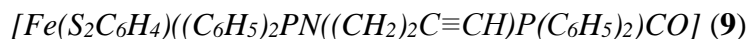
Column chromatography of the product afforded a reddish-brown solid of **6** in 67% yield. ¹H-NMR (500 MHz, CD₂Cl₂): δ_H = 7.1-8.1 (m, 27H, (P(C₆H₅)₂)₂), N((CH₂)₄C₆H₅) and S₂C₆H₄), 6.88 (d, 2H, N((CH₂)₄C₆H₅)), 2.94 (m, 2H, N((CH₂)₄C₆H₅)), 2.3 (d, 2H, N((CH₂)₄C₆H₅)), 2.15 (d, 2H, N((CH₂)₄C₆H₅)), 1.19 (d, 2H, N((CH₂)₄C₆H₅)) ppm. ³¹P{¹H}-NMR (202 MHz, CDCl₃): δ_P = 109.4 ppm. IR (KBr): ν_{max}/cm⁻¹ 1932 ν(C-O).



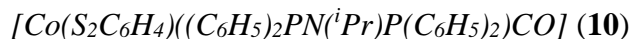
Column chromatography of the product afforded a reddish-brown solid of **7** in 63% yield. ¹H-NMR (400 MHz, CD₂Cl₂): δ_H = 6.8-8.2 (m, 33H, N(CH₂)C₁₄H₉), (P(C₆H₅)₂)₂) and S₂C₆H₄), 5.3 (m, 2H, N(CH₂)C₁₄H₉) ppm. ³¹P{¹H}-NMR (202 MHz, CD₂Cl₂): δ_P = 110.8 ppm. IR (KBr): ν_{max}/cm⁻¹ 1931 ν(C-O).



Column chromatography of the product afforded a reddish-brown solid of **8** in 66% yield. ^1H -NMR (500 MHz, CD_2Cl_2): $\delta_{\text{H}} = 7.0\text{-}8.2$ (m, 24H, $(\text{P}(\text{C}_6\text{H}_5)_2)_2$ and $\text{S}_2\text{C}_6\text{H}_4$), 6.9 (d, 2H, $\text{N}(\text{p-HC}\equiv\text{CC}_6\text{H}_4)$), 6.4 (d, 2H, $\text{N}(\text{p-HC}\equiv\text{CC}_6\text{H}_4)$), 3.2 (d, 1H, $\text{N}(\text{p-HC}\equiv\text{CC}_6\text{H}_4)$) ppm. $^{31}\text{P}\{^1\text{H}\}$ -NMR (202 MHz, CD_2Cl_2): $\delta_{\text{P}} = 113.4$ ppm. IR (KBr): $\nu_{\text{max}}/\text{cm}^{-1}$ 1939 $\nu(\text{C-O})$.



Column chromatography of the product afforded a reddish-brown solid of **9** in 45% yield. ^1H -NMR (400 MHz, CDCl_3): $\delta_{\text{H}} = 7.12\text{-}8.1$ (m, 24H, $(\text{P}(\text{C}_6\text{H}_5)_2)_2$ and $\text{S}_2\text{C}_6\text{H}_4$), 1.93 (m, 2H, $\text{N}((\text{CH}_2)_2\text{C}\equiv\text{CH})$), 1.89 (s, 1H, $\text{N}((\text{CH}_2)_2\text{C}\equiv\text{CH})$), 1.51 (m, 2H, $\text{N}((\text{CH}_2)_2\text{C}\equiv\text{CH})$) ppm. $^{31}\text{P}\{^1\text{H}\}$ -NMR (202 MHz, CD_2Cl_2): $\delta_{\text{P}} = 109.2$ ppm; IR (KBr): $\nu_{\text{max}}/\text{cm}^{-1}$ 1927 $\nu(\text{C-O})$.



A reddish-brown solid with high luster was collected with a crude yield of 70%. Single reddish-brown crystals confirmed as pure product and suitable for X-ray diffraction were obtained by recrystallization in CH_2Cl_2 /hexane layered solution with slow evaporation at room temperature. $^{31}\text{P}\{^1\text{H}\}$ NMR (202 MHz, CD_2Cl_2): $\delta_{\text{P}} = 80.9$ ppm; IR (KBr): $\nu_{\text{max}}/\text{cm}^{-1}$ 1988 $\nu(\text{C-O})$. APSI mass spectrum (positive mode): $m/z = 627.0$ ($\text{M} - \text{CO} + \text{H}$) $^+$.

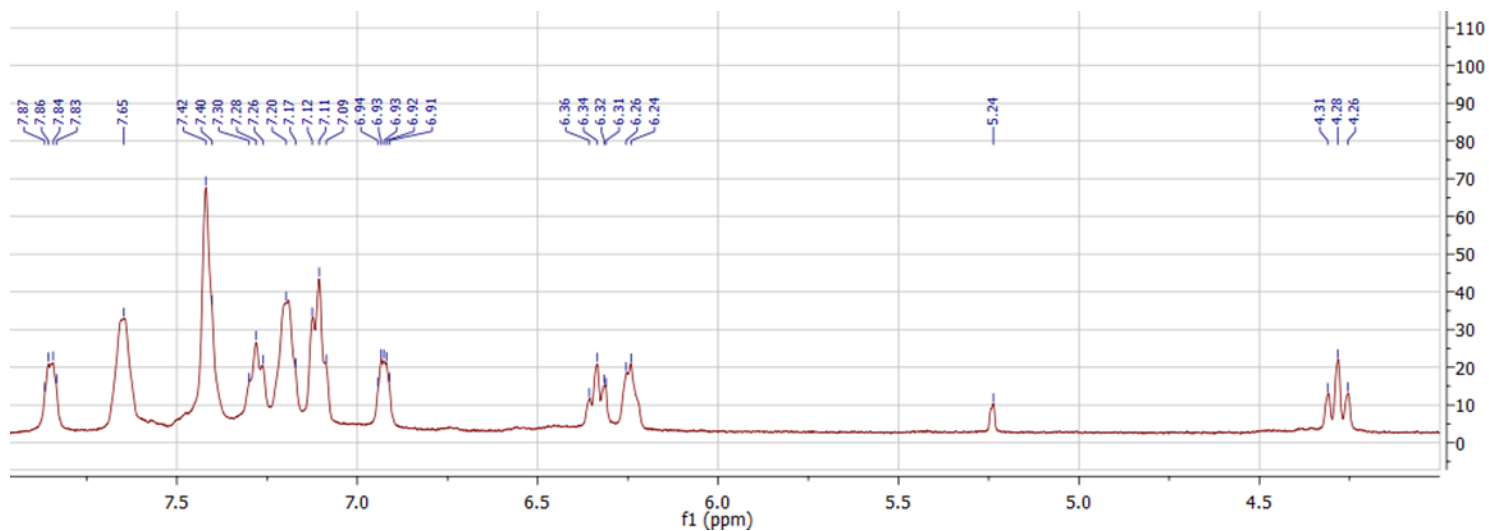


Figure 2.15. ^1H NMR spectra of $[\text{Fe}(\text{S}_2\text{C}_6\text{H}_4)((\text{C}_6\text{H}_5)_2\text{PN}(\text{p}\text{-fluorobenzyl})\text{P}(\text{C}_6\text{H}_5)_2)\text{CO}]$ (**5**) in CD_2Cl_2 .

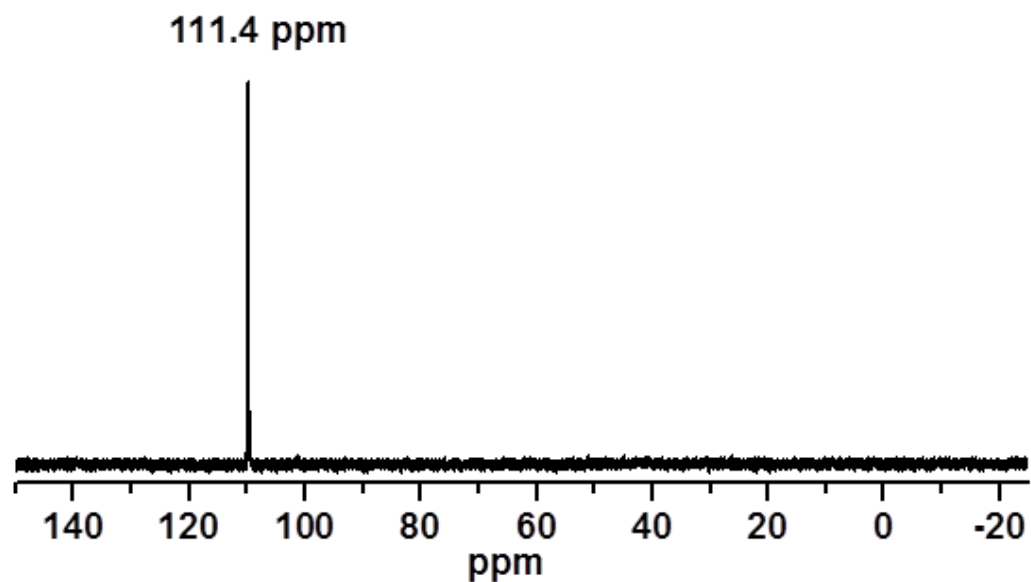


Figure 2.16. ^{31}P NMR spectra of $[\text{Fe}(\text{S}_2\text{C}_6\text{H}_4)((\text{C}_6\text{H}_5)_2\text{PN}(\text{p}\text{-fluorobenzyl})\text{P}(\text{C}_6\text{H}_5)_2)\text{CO}]$ (**5**) in CD_2Cl_2 .

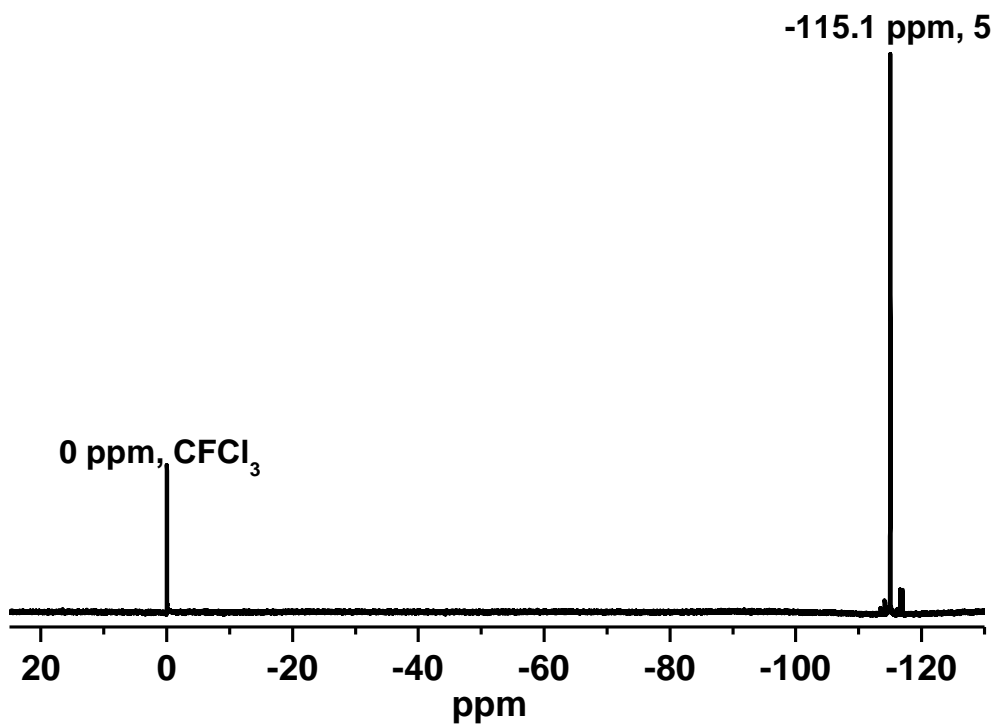


Figure 2.17. ^{19}F NMR spectra of $[\text{Fe}(\text{S}_2\text{C}_6\text{H}_4)((\text{C}_6\text{H}_5)_2\text{PN}(\text{p}\text{-fluorobenzyl})\text{P}(\text{C}_6\text{H}_5)_2)\text{CO}]$ (**5**) in CD_2Cl_2 .

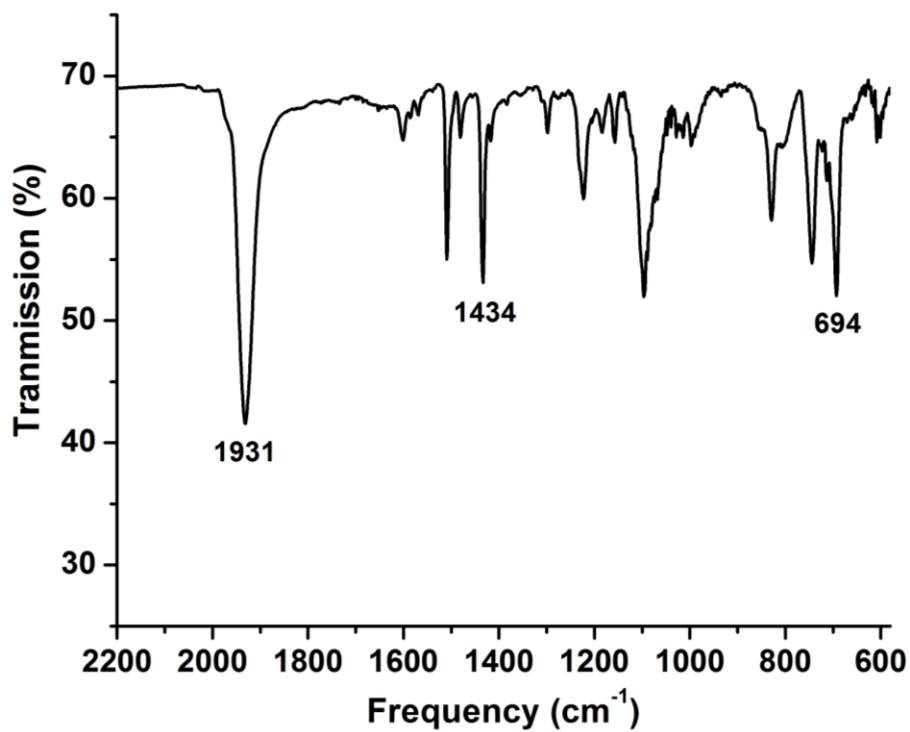


Figure 2.18. IR spectra of $[\text{Fe}(\text{S}_2\text{C}_6\text{H}_4)((\text{C}_6\text{H}_5)_2\text{PN}(\text{p}\text{-fluorobenzyl})\text{P}(\text{C}_6\text{H}_5)_2)\text{CO}]$ (**5**) embedded in KBr matrix.

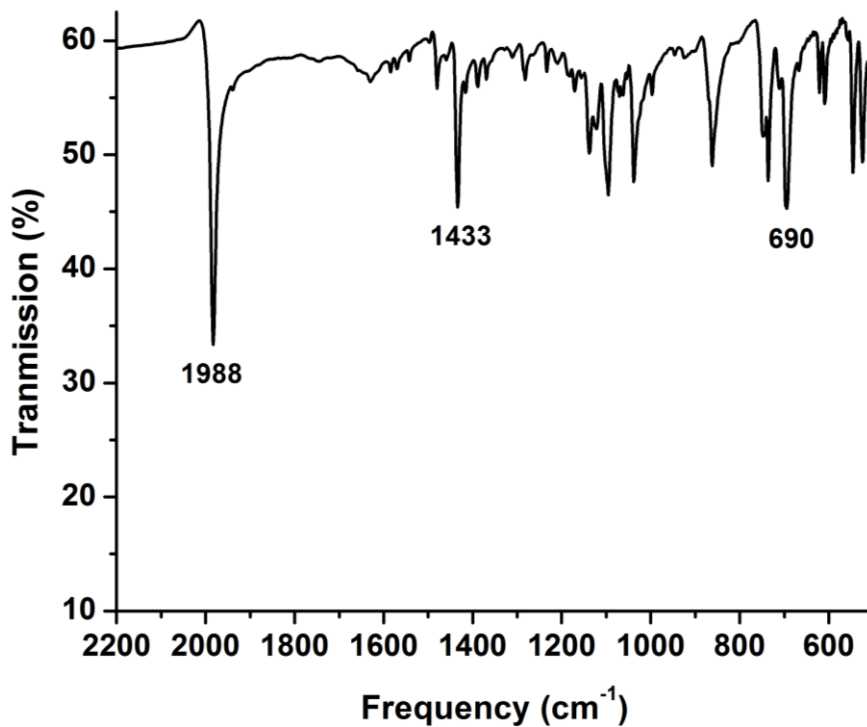


Figure 2.19. IR spectra of $[\text{Co}(\text{S}_2\text{C}_6\text{H}_4)((\text{C}_6\text{H}_5)_2\text{PN}(\text{iPr})\text{P}(\text{C}_6\text{H}_5)_2)\text{CO}]$ (**10**) embedded in KBr matrix.

References

- (1) Turner, J. A. *Science* **2004**, *305*, 972.
- (2) Cammack, R.; Frey, M.; Robson, R. *Hydrogen as a Fuel: Learning from Nature*; Taylor & Francis: London and New York, 2001.
- (3) Penner, S. S. *Energy* **2006**, *31*, 33.
- (4) McKone, J. R.; Marinescu, S. C.; Brunshwig, B. S.; Winkler, J. R.; Gray, H. B. *Chem. Sci.* **2014**, *5*, 865.
- (5) Wang, M.; Chen, L.; Sun, L. *Energy & Environmental Science* **2012**, *5*, 6763.
- (6) Helm, M. L.; Stewart, M. P.; Bullock, R. M.; DuBois, M. R.; DuBois, D. L. *Science* **2011**, *333*, 863.
- (7) Losse, S.; Vos, J. G.; Rau, S. *Coord. Chem. Rev.* **2010**, *254*, 2492.
- (8) Tard, C.; Pickett, C. J. *Chem. Rev.* **2009**, *109*, 2245.

- (9) Stewart, M. P.; Ho, M.-H.; Wiese, S.; Lindstrom, M. L.; Thogerson, C. E.; Raugei, S.; Bullock, R. M.; Helm, M. L. *J. Am. Chem. Soc.* **2013**, *135*, 6033.
- (10) Eckenhoff, W. T.; Eisenberg, R. *Dalton Trans.* **2012**, *2012*, 13004.
- (11) Merki, D.; Fierro, S.; Vrabel, H.; Hu, X. *Chem. Sci.* **2011**, *2*, 1262.
- (12) Dey, S.; Rana, A.; Dey, S. G.; Dey, A. *ACS Catalysis* **2013**, *3*, 429.
- (13) Canaguier, S.; Artero, V.; Fontecave, M. *J. Chem. Soc. Dalton Trans.* **2008**, 315.
- (14) Barton, B. E.; Rauchfuss, T. B. *Inorg. Chem.* **2008**, *47*, 2261.
- (15) Zampella, G.; Greco, C.; Fantucci, P.; de Gioia, L. *Inorg. Chem.* **2006**, *45*, 4109.
- (16) Yu, Z.; Wang, M.; Li, P.; Dong, W.; Wang, F.; Sun, L. *J. Chem. Soc. Dalton Trans.* **2008**, 2400.
- (17) McNamara, W. R.; Han, Z.; Yin, C.-J.; Brennessel, W. W.; Holland, P. L.; Eisenberg, R. *Proc. Natl. Acad. Sci. USA* **2012**, *109*, 15594.
- (18) Lakadamyali, F.; Kato, M.; Muresan, N. M.; Reisner, E. *Angew. Chem. Int. Ed.* **2012**, *51*, 9381.
- (19) Gao, W.; Ekström, J.; Liu, J.; Chen, C.; Eriksson, L.; Weng, L.; Åkermark, B.; Sun, L. *Inorg. Chem.* **2007**, *46*, 1981.
- (20) Duan, L.; Wang, M.; Li, P.; Na, Y.; Wang, N.; Sun, L. *J. Chem. Soc. Dalton Trans.* **2007**, 1277.
- (21) Cheah, M. H.; Tard, C.; Borg, S. J.; Liu, X.; Ibrahim, S. K.; Pickett, C. J.; Best, S. P. *J. Am. Chem. Soc.* **2007**, *129*, 11085.
- (22) Bigi, J. P.; Hanna, T. E.; Harman, W. H.; Chang, A.; Chang, C. J. *Chem. Commun.* **2010**, *46*, 958.
- (23) Baffert, C.; Artero, V.; Fontecave, M. *Inorg. Chem.* **2007**, *46*, 1817.
- (24) Pantani, O.; Naskar, S.; Guillot, R.; Millet, P.; Anxolabéhère-Mallart, E.; Aukauloo, A. *Angew. Chem. Int. Ed. Engl.* **2008**, *47*, 9948.
- (25) McCrory, C. C. L.; Uyeda, C.; Peters, J. C. *J. Am. Chem. Soc.* **2012**, *134*, 3164.

- (26) Hu, X.; Brunschwig, B. S.; Peters, J. C. *J. Am. Chem. Soc.* **2007**, *129*, 8988.
- (27) Dempsey, J. L.; Brunschwig, B. S.; Winkler, J. R.; Gray, H. B. *Acc. Chem. Res.* **2009**, *42*, 1995.
- (28) Roy, S.; Mazinani, S. K. S.; Groy, T. L.; Gan, L.; Tarakeshwar, P.; Mujica, V.; Jones, A. K. *Inorg. Chem.* **2014**, *53*, 8919.
- (29) Berben, L. A.; Peters, J. C. *Chem. Commun.* **2010**, *46*, 398.
- (30) Andreiadis, E. S.; Jacques, P.-A.; Tran, P. D.; Leyris, A.; Chavarot-Kerlidou, M.; Jousseme, B.; Matheron, M.; Pecaut, J.; Palacin, S.; Fontecave, M.; Artero, V. *Nat. Chem.* **2013**, *5*, 48.
- (31) Carroll, M. E.; Barton, B. E.; Gray, D. L.; Mack, A. E.; Rauchfuss, T. B. *Inorg. Chem.* **2011**, *50*, 9554.
- (32) Gärtner, F.; Boddien, A.; Barsch, E.; Fumino, K.; Losse, S.; Junge, H.; Hollmann, D.; Brückner, A.; Ludwig, R.; Beller, M. *Chemistry – A European Journal* **2011**, *17*, 6425.
- (33) Rakowski DuBois, M.; DuBois, D. L. *Acc. Chem. Res.* **2009**, *42*, 1974.
- (34) Yan, Y.; Xia, B.; Ge, X.; Liu, Z.; Wang, J.-Y.; Wang, X. *ACS Appl. Mater. Interfaces* **2013**, *5*, 12794.
- (35) Wouter Maijenburg, A.; Regis, M.; Hattori, A. N.; Tanaka, H.; Choi, K.-S.; ten Elshof, J. E. *ACS Appl. Mater. Interfaces* **2014**, *6*, asap (available online).
- (36) Ott, S.; Kritikos, M.; Åkermark, B.; Sun, L.; Lomoth, R. *Angew. Chem. Int. Ed. Engl.* **2004**, *43*, 1006.
- (37) Beyler, M.; Ezzaher, S.; Karnahl, M.; Santoni, M.-P.; Lomoth, R.; Ott, S. *Chem. Commun.* **2011**, *47*, 11662.
- (38) Wiedner, E. S.; Yang, J. Y.; Dougherty, W. G.; Kassel, W. S.; Bullock, R. M.; DuBois, M. R.; DuBois, D. L. *Organometallics* **2010**, *29*, 5390.
- (39) Appel, A. M.; DuBois, D. L.; Rakowski DuBois, M. *J. Am. Chem. Soc.* **2005**, *127*, 12717.
- (40) Orthaber, A.; Karnahl, M.; Tschierlei, S.; Streich, D.; Stein, M.; Ott, S. *Dalton Transactions* **2014**, *43*, 4537.

- (41) Eady, S. C.; Peczonczyk, S. L.; Maldonado, S.; Lehnert, N. *Chem. Commun.* **2014**, *50*, 8065.
- (42) Carroll, M. E.; Barton, B. E.; Rauchfuss, T. B.; Carroll, P. J. *J. Am. Chem. Soc.* **2012**, *134*, 18843.
- (43) Eady, S. C.; Breault, T.; Thompson, L.; Lehnert, N. *Dalton Transactions* **2016**.
- (44) Stolley, R. M.; Helm, M. L. *Nat Chem* **2014**, *6*, 949.
- (45) Le Goff, A.; Artero, V.; Jusselme, B.; Tran, P. D.; Guillet, N.; Métayé, R.; Fihri, A.; Palacin, S.; Fontecave, M. *Science* **2009**, *326*, 1384.
- (46) Tran, P. D.; Le Goff, A.; Heidkamp, J.; Jusselme, B.; Guillet, N.; Palacin, S.; Dau, H.; Fontecave, M.; Artero, V. *Angew. Chem. Int. Ed.* **2011**, *50*, 1371.
- (47) Blakemore, J. D.; Gupta, A.; Warren, J. J.; Brunshwig, B. S.; Gray, H. B. *J. Am. Chem. Soc.* **2013**, *135*, 18288.
- (48) Ibrahim, S. K.; Liu, X.; Tard, C.; Pickett, C. J. *Chem. Commun.* **2007**, 1535.
- (49) Liu, G.; Wu, B.; Zhang, J.; Wang, X.; Shao, M.; Wang, J. *Inorg. Chem.* **2009**, *48*, 2383.
- (50) Krawicz, A.; Yang, J.; Anzenberg, E.; Yano, J.; Sharp, I. D.; Moore, G. F. *J. Am. Chem. Soc.* **2013**, *135*, 11861.
- (51) Nocera, D. G. *Acc. Chem. Res.* **2012**, *45*, 767.
- (52) Seo, J.; Pekarek, R. T.; Rose, M. J. *Chem. Commun.* **2015**, *51*, 13264.
- (53) Takács, J.; Markó, L.; Párkányi, L. *J. Organomet. Chem.* **1989**, *361*, 109.
- (54) Addison, A. W.; Rao, T. N.; Reedijk, J.; van Rijn, J.; Verschoor, G. C. *J. Chem. Soc., Dalton Trans.* **1984**, 1349.
- (55) Costentin, C.; Drouet, S.; Robert, M.; Savéant, J.-M. *J. Am. Chem. Soc.* **2012**, *134*, 11235.
- (56) Bard, A. J.; Faulkner, L. R. *Electrochemical Methods: Fundamentals and Applications*; 2nd edition ed., 2000.

- (57) Coetzee, J. F. In *Progress in Physical Organic Chemistry*; John Wiley & Sons, Inc.: 2007, p 45.
- (58) Rakowski DuBois, M.; DuBois, D. L. *Chem. Soc. Rev.* **2009**, *38*, 62.
- (59) Raugei, S.; Chen, S.; Ho, M.-H.; Ginovska-Pangovska, B.; Rousseau, R. J.; Dupuis, M.; DuBois, D. L.; Bullock, R. M. *Chemistry – A European Journal* **2012**, *18*, 6493.
- (60) Ezzaher, S.; Capon, J.-F.; Gloaguen, F.; Petillon, F. Y.; Schollhammer, P.; Talarmin, J. *Inorg. Chem.* **2007**, *46*, 9863.
- (61) Rose, M. J.; Gray, H. B.; Winkler, J. R. *J. Am. Chem. Soc.* **2012**, *134*, 8310.
- (62) Hummers, W. S.; Offeman, R. E. *J. Am. Chem. Soc.* **1958**, *80*, 1339.
- (63) Frisch, M. J.; Trucks, G. W.; Schlegel, H. B.; Scuseria, G. E.; Robb, M. A.; Cheeseman, J. R.; Scalmani, G.; Barone, V.; Mennucci, B.; Petersson, G. A.; Nakatsuji, H.; Caricato, M.; Li, X.; Hratchian, H. P.; Izmaylov, A. F.; Bloino, J.; Zheng, G.; Sonnenberg, J. L.; Hada, M.; Ehara, M.; Toyota, K.; Fukuda, R.; Hasegawa, J.; Ishida, M.; Nakajima, T.; Honda, Y.; Kitao, O.; Nakai, H.; Vreven, T.; Montgomery Jr., J. A.; Peralta, J. E.; Ogliaro, F.; Bearpark, M. J.; Heyd, J.; Brothers, E. N.; Kudin, K. N.; Staroverov, V. N.; Kobayashi, R.; Normand, J.; Raghavachari, K.; Rendell, A. P.; Burant, J. C.; Iyengar, S. S.; Tomasi, J.; Cossi, M.; Rega, N.; Millam, N. J.; Klene, M.; Knox, J. E.; Cross, J. B.; Bakken, V.; Adamo, C.; Jaramillo, J.; Gomperts, R.; Stratmann, R. E.; Yazyev, O.; Austin, A. J.; Cammi, R.; Pomelli, C.; Ochterski, J. W.; Martin, R. L.; Morokuma, K.; Zakrzewski, V. G.; Voth, G. A.; Salvador, P.; Dannenberg, J. J.; Dapprich, S.; Daniels, A. D.; Farkas, Ö.; Foresman, J. B.; Ortiz, J. V.; Cioslowski, J.; Fox, D. J.; Gaussian, Inc.: Wallingford, CT, USA, 2009.
- (64) Imhoff, P.; Elsevier, C. J. *J. Organomet. Chem.* **1989**, *361*, C61.

Chapter 3

Investigation of Graphitic Supports as Interfaces for Catalyst Heterogenization

Introduction

Devices capable of generating dihydrogen from a renewable energy source are crucial for meeting the global dihydrogen consumption demand and for efforts to replace carbon-based fuel technologies. Large-scale dihydrogen production from protons and electrons, whether directly coupled to water oxidation photoanodes or to electrolyzers powered by renewable energy sources, must inevitably be facilitated by heterogeneous catalysts to allow for application of the catalysts in large-scale flow reactors. To this end, electrocatalysts for dihydrogen production must be designed to meet the demanding standards of these systems. These electrocatalysts could either be built from catalytically active electrode materials, or from molecular catalysts immobilized on the electrode surfaces. The latter approach has the advantage that the molecular catalysts can be improved in a systematic manner and derivatized to meet given application needs. However, a substantial challenge in this regard is to design suitable interfaces that allow for the easy, yet stable and affordable, attachment of the catalysts to the electrode surfaces. In this chapter, which is reproduced in part from a manuscript published in *Chemical Communications* (Eady, S. C.; Peczonczyk, S. L.; Maldonado, S.; Lehnert, N. *Chem. Commun.* **2014**, *50*, 8065.), we demonstrate that reduced graphene oxide

films can serve as inexpensive, yet extremely versatile interfaces to adsorb dihydrogen production catalysts to a variety of electrode materials such as semiconductor surfaces.

In addition to the interface, fast, efficient, and inexpensive electrocatalysts are necessary to obtain platinum-free manifolds for dihydrogen production. Previous research in the renewable energy field has ‘unearthed’ a number of abundant and inexpensive iron, nickel and cobalt electrocatalysts for dihydrogen production.¹⁻⁴³ Solid state and molecular catalysts alike have displayed impressive proton reduction activity, rivaling platinum in overpotential (η), turnover frequency (TOF), and turnover number (TON).^{38,39,44-47} In some cases these systems have nearly matched or even exceeded platinum with regards to stability in poisoning conditions or for dual catalysis applications, a milestone that should be held in high regard, considering the decades of catalyst development spent towards platinum substitution.^{38,39,48,49} Still, design of versatile and inexpensive heterogeneous catalyst manifolds remains a major challenge for the development of cost-efficient dihydrogen production systems.

Cobalt bis(dithiolene) complexes, discovered nearly five decades ago, have historically been researched for various applications spanning from their strong absorption features to unique electronic structures.^{17,18,42,50-61} Recently, these complexes have been found to be active for dihydrogen production in acidic organic solutions by McNamara and coworkers, with a maximum TOF of 3,400 h⁻¹ and TON of 9,000 in 12 hours in solution.^{17,18} These catalyst systems have also been investigated as 2-dimensional polymer materials on graphitic supports, as well as one-dimensional light-permeable materials on silicon surfaces for photoelectrocatalysis.^{52,53} Curiously, these heterogeneous catalyst manifolds designed from a polymer material transferred to an electrode surface show substantially higher turnover frequencies than the corresponding catalysts in homogeneous phase. Their reported activity

even rivals the catalytic activities of nickel-bis(diphosphine) systems (albeit under different conditions), which have become the gold standard for homogeneous and heterogeneous dihydrogen production systems in a number of applications.^{10,38,39,41,62}

In this chapter, electrostatically adsorption of cobalt bis(dithiolene) catalysts to graphitic supports is studied as potential heterogeneous electrocatalysts for incorporation into photocathode systems. The core focus of these studies was to determine the effect of ligand modification and graphitic support selection on the overall performance of the electrocatalytic system for hydrogen production. The results of this analysis were then used to design photocathode manifolds (described in **Section 4.1**), incorporating both the RGO interface method and the cobalt bis(dithiolene) catalyst derivatives developed here.

3.1. Adsorption of Cobalt Bis(dithiolene) Hydrogen Production Catalysts on Graphitic Supports: Initial Testing of Heterogeneous Catalyst Systems

In this study we report a facile means of designing a graphene-interfaced heterogeneous catalyst system using widely available, inexpensive materials. The catalyst, RGO surfaces, and method of combination reported here require minimal synthetic effort and time to prepare. Resulting catalyst-adsorbed RGO surfaces indicate activity for H₂ formation at reasonable overpotentials in weakly acidic aqueous media. Most enticingly, this system shows resilience to O₂ exposure and resistance to catalyst leaching.

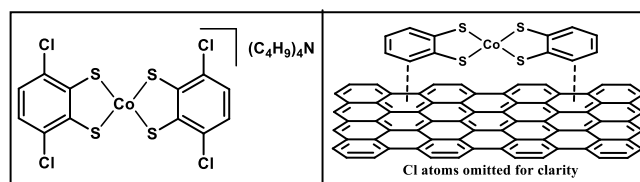


Chart 3.1. Co bis(dithiolene) compound (**1**) used for RGO adsorption, (left), schematic representation of π -stacking interactions (right).

Graphene oxide was prepared from flake graphite via Hummer's method⁶³, and an aqueous suspension was prepared in a weakly alkaline carbonate-buffered system. Reduced graphene oxide (RGO)-coated substrates were accessible by cyclic voltammetry (CV) in the graphene oxide suspension, using the substrate (here: metal oxide-coated glass) as the working electrode (**Figure 3.1**). For ease of study, initial testing was performed on glass coated fluorine-doped tin oxide (FTO) electrodes, which provide a very generous cathodic window (0.4 to -1.3 V vs. SCE) in aqueous solutions at a very low cost.⁹ To afford the catalyst-adsorbed surfaces, the RGO-coated FTO surfaces were soaked in a 5 mM solution of catalyst in acetonitrile for 12 hours. Keeping simplicity in design, the H₂ production catalyst selected for use here is a simple cobalt bis(dithiolene) complex that is afforded in high yield from a one-pot reaction with inexpensive materials (**Chart 3.1**).¹⁸

This compound has been shown by McNamara et al. to display impressive activity (TOF = 1,400 h⁻¹) and exemplary stability (TON = 6000) at low overpotentials for both electro-

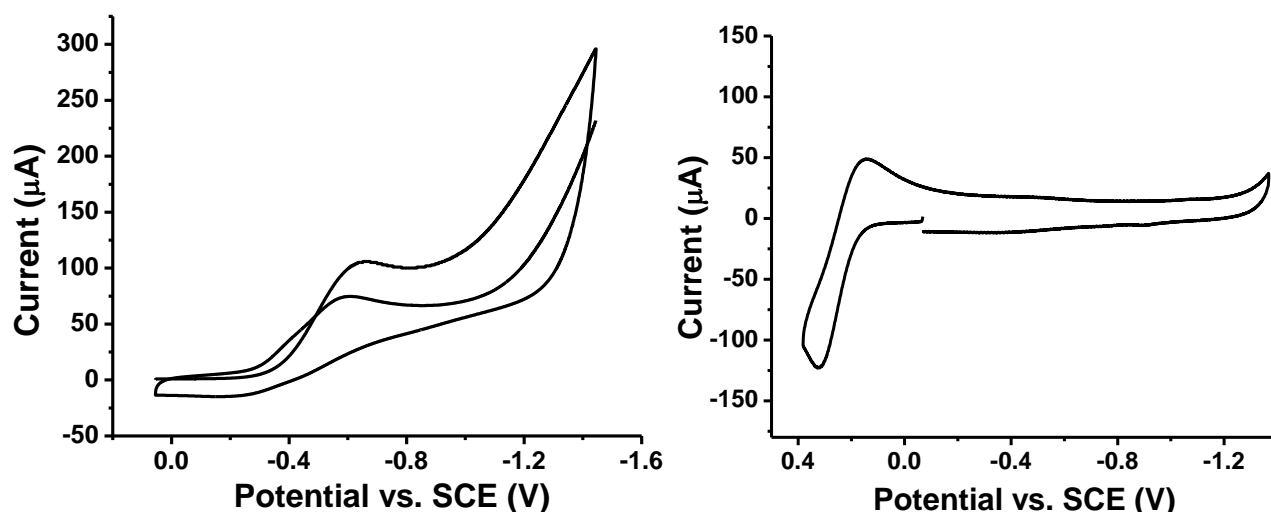


Figure 3.1. *Left:* Cyclic voltammogram showing RGO deposition on the FTO working electrode surface performed in a 0.1 M sodium carbonate/bicarbonate aqueous buffered solution (pH= 9.2) as described above. *Right:* Electrochemical window of RGO-coated FTO in aqueous 0.1 M potassium hexafluorophosphate with potassium ferricyanide/ferrocyanide (0.5 mM total) as the internal reference. Platinum was used as a counter electrode with a Ag/AgCl reference electrode. The scan rate was 100 mV/s. Potentials reported are vs. the saturated calomel electrode (SCE).

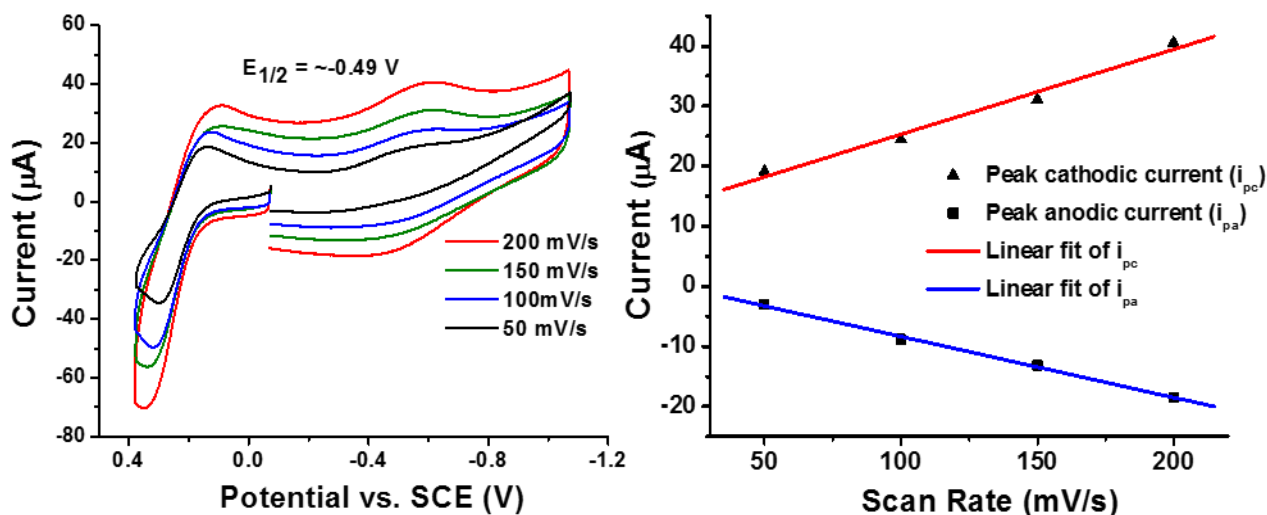


Figure 3.2. *Left:* Cyclic voltammetry of (TBA)[Co(S₂C₆Cl₂H₂)₂] (**1**) adsorbed on a FTO/RGO working electrode at various scan rates. The solution was 0.1 M aqueous potassium hexafluorophosphate, the counter electrode was a platinum wire, and the reference electrode was Ag/AgCl (saturated KCl solution). An equimolar solution of potassium ferricyanide/ferrocyanide (0.5 mM total) was used as an internal reference. Potentials are reported vs. the saturated calomel electrode. *Right:* Linear fit of the peak cathodic and anodic current vs. the scan rate.

and photocatalytic (using Ru-bpy) dihydrogen generation in homogeneous phase.¹⁸ It is notable that no synthetic manipulation is required for RGO adsorption of this compound, which is ideal for applications at scale, in comparison with other catalyst designs which often require custom introduction of aromatic moieties for surface attachment (via involved synthetic pathways).¹⁵

CV analysis of catalyst-soaked FTO/RGO surfaces (after extensive rinsing and sonication regimens) in aqueous solutions indicates that the compound is bound, showing quasi-reversible redox couples at an average potential of -0.49 V. It is noteworthy that the redox couple of **1** is roughly similar to that observed in solution (**Figure 3.2**).¹⁸ Importantly, upon addition of trifluoroacetic acid (TFA, pK_a= 0.23), CVs of the FTO/RGO/**1** system show a sharp increase in current during cathodic scanning at -0.73 V, a behaviour indicative of electrocatalytic reduction of protons from TFA (**Figure 3.3**, left). This activity is observed with an onset

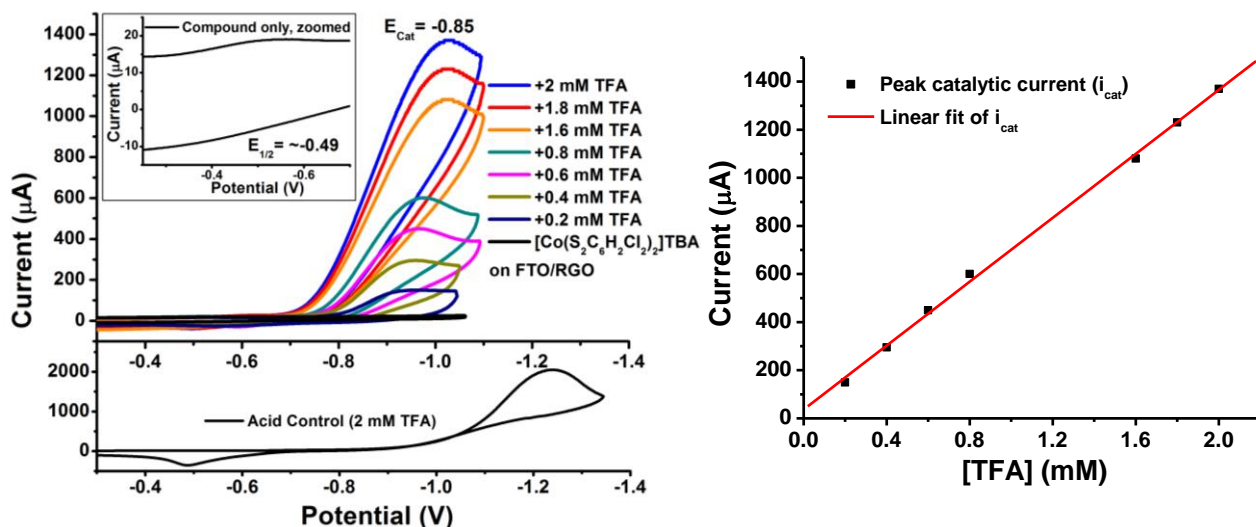


Figure 3.3. *Left:* Cyclic voltammetry of $(\text{TBA})[\text{Co}(\text{S}_2\text{C}_6\text{Cl}_2\text{H}_2)_2]$ (**1**) adsorbed on a FTO/RGO working electrode with addition of TFA at a scan rate of 100 mV/s. The solution was 0.1 M aqueous potassium hexafluorophosphate, the counter electrode was a platinum wire, and the reference electrode was Ag/AgCl (saturated KCl solution). An equimolar solution of potassium ferricyanide/ferrocyanide (0.5 mM total) was used as an internal reference. Potentials are reported vs. the saturated calomel electrode. *Right:* Linear fit of the peak catalytic current vs. increasing TFA concentrations, indicating an acid-diffusion controlled process under these conditions.

overpotential of only 0.37 V as compared to the reduction of TFA at a platinum electrode under the same conditions (see experimental section). Testing of the same FTO/RGO electrode in identical conditions prior to catalyst adsorption showed minimal background current, confirming this activity as being directly a result of the catalyst's presence. The half-wave potential ($E_{\text{cat}} = -0.85$ V) and catalytic peak potential ($E_{\text{pc}} = -1.0$ V) are both nearly identical to those reported in homogeneous phase, suggesting the catalyst is unaltered upon adsorption to RGO.¹⁸

Analysis of activity with increasing TFA addition shows a linear correlation (**Figure 3.3**, right) with no activity saturation observed at the acid concentrations used. Replacing the acidic solution after electrochemical analysis with a new electrolyte-only solution (pH \sim 7) shows the same redox couple seen in the first solution. Addition of TFA to the second solution shows the same activity as observed in the preceding run, and repetition of this process shows

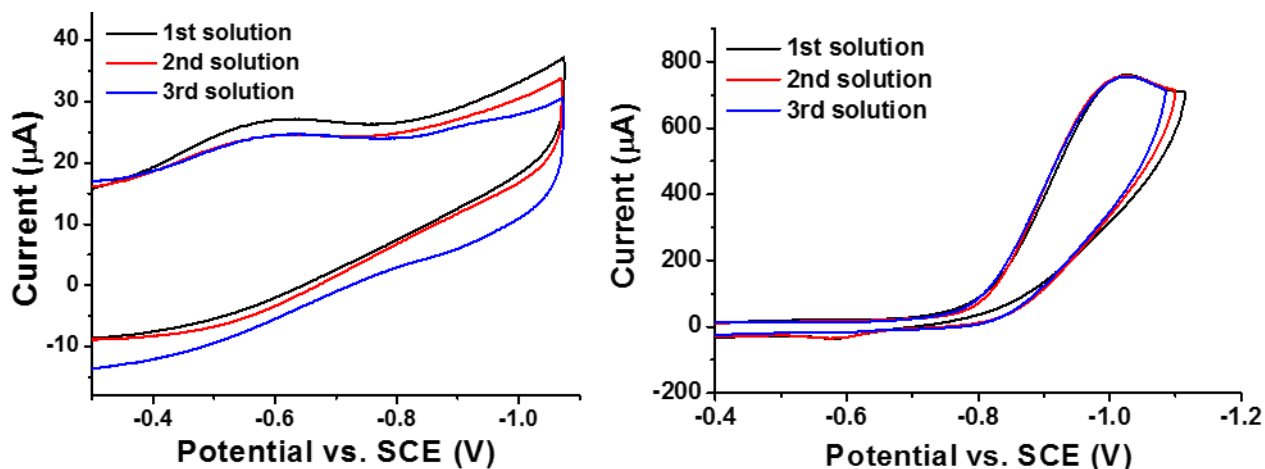


Figure 3.4. *Left:* overlay of cyclic voltammograms of (TBA)[Co(S₂C₆Cl₂H₂)₂] (**1**) adsorbed on a FTO/RGO working electrode in different (consecutively applied) solutions at a scan rate of 100 mV/s. *Right:* Cyclic voltammetry of **1** adsorbed on FTO/graphene with addition of TFA in renewed acidic solutions at a scan rate of 100 mV/s. Each solution was 0.1 M aqueous potassium hexafluorophosphate and 1 mM TFA, with an equimolar solution of potassium ferricyanide/ferrocyanide (0.5 mM total) used as an internal reference. The same electrodes were rinsed and reused for analysis of each solution, with a platinum wire counter electrode and a Ag/AgCl (saturated KCl) reference electrode. The FTO/RGO working electrode was rinsed thoroughly and sonicated briefly in water before analysis in each new solution. Potentials are reported vs. the saturated calomel electrode.

no significant decrease of catalyst activity (**Figure 3.4**, right). These results indicate the catalyst-adsorbed surfaces are O₂ stable and resistant to leeching under the experimental conditions (all manipulations done in air). XPS analysis of FTO/RGO/**1** surfaces after electrochemical testing confirms these findings (see experimental section). To assure these responses are not specific to just TFA, electrochemical analyses of the catalyst-adsorbed RGO surfaces with dilute hydrochloric acid solutions were also performed. These tests elicit identical responses in electrocatalytic behaviour (**Figure 3.5**).

The proton reduction mechanism of **1** on the RGO surface appears to correspond to that reported in solution by McNamara and coworkers. Upon addition of acid, no significant change is seen in the reduction event at approximately -0.5 V (although it is difficult to tell with the low intensity of the redox event), however a new wave appears at a potential roughly 0.25 V more cathodic than the original wave (**Figure 3.3**). This is indicative of an initial reduction of

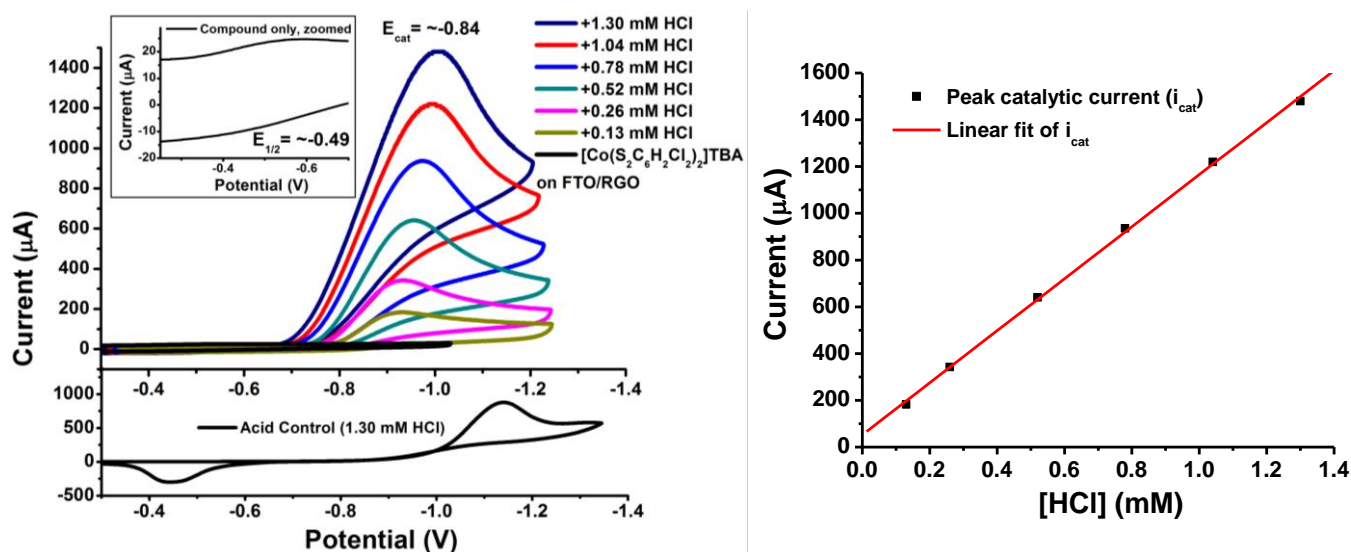


Figure 3.5. *Left:* Cyclic voltammetry of $[\text{Co}(\text{S}_2\text{C}_6\text{H}_2\text{Cl}_2)_2]$ (**1**) adsorbed on a FTO/RGO working electrode with addition of HCl at a scan rate of 100 mV/s. The solution was 0.1 M aqueous potassium hexafluorophosphate, the counter electrode was a platinum wire, and the reference electrode was Ag/AgCl (saturated KCl solution). An equimolar solution of potassium ferricyanide/ferrocyanide (0.5 mM total) was used as an internal reference. Potentials are reported vs. the saturated calomel electrode. *Right:* Linear fit of the peak catalytic current vs. increasing TFA concentrations, indicating an acid-diffusion controlled process under these conditions.

the cobalt anion to the dianion preceding rapid protonation of the dianion. This protonation event allows for a subsequent reduction unobserved in the absence of acid. While the final protonation event was not observed directly, these data suggest either an ECEC or ECCE type mechanism. These results show that the activity profile for **1** on RGO closely mirrors that reported for **1** in homogenous solution. These findings are indicative of the direct adsorption of **1** on the RGO surface and indicate a mechanism analogous to the homogeneous catalyst.

The bare FTO, FTO/RGO, and FTO/RGO/**1** surfaces were analysed by X-ray photoelectron spectroscopy (XPS) as described in the experimental section. The high-resolution C 1s XPS data of a bare FTO surface exhibit only features consistent with adventitious carbon.⁶⁴ After RGO deposition, signatures indicative of C-O (hydroxyl, epoxy) groups at 286.7 eV and C=O (carbonyl groups) at 288.4 eV are prominent. These signatures are consistent with previous reports of reduced graphene oxide on surfaces.⁶⁵ After soaking the

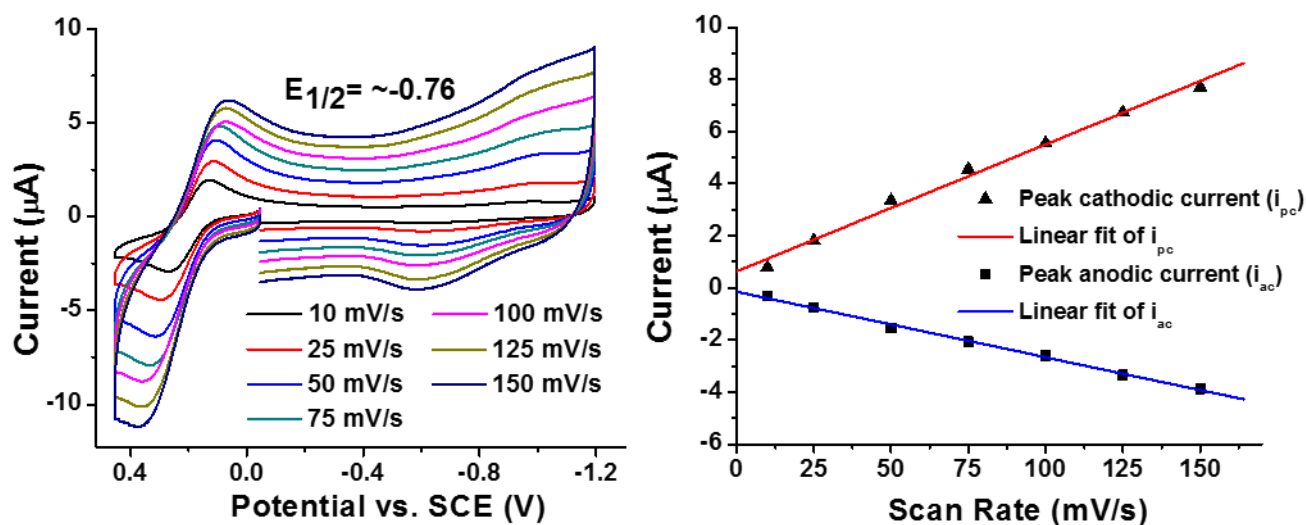


Figure 3.6. *Left:* Cyclic voltammetry of (TBA)[Co(S₂C₆Cl₂H₂)₂] (**1**) adsorbed on a HOPG working electrode at various scan rates. The solution was 0.1 M aqueous potassium hexafluorophosphate, the counter electrode was a platinum wire, and the reference electrode was Ag/AgCl (saturated KCl solution). An equimolar solution of potassium ferricyanide/ferrocyanide (0.5 mM total) was used as an internal reference. Potentials are reported vs. the saturated calomel electrode. *Right:* Linear fit of the peak cathodic and anodic currents versus the scan rate.

FTO/RGO electrode in a catalyst solution, a peak at 287.7 eV emerges in the C 1s spectra, corresponding to a C-S bonding energy which would be expected for **1**. This is further corroborated by the high-resolution Co 2p and S 2p spectra where features of Co and S are clearly present after exposure to catalyst. A feature corresponding to the Co-S energy is present in the Co 2p data; however it is difficult to distinguish above the background.

To confirm the facile heterogenization of compound **1** on a more controlled surface, adsorption on a highly-ordered pyrolytic graphite electrode (HOPG, Pine Instrument Co.) was also studied under the same conditions. For the purpose of these studies, the highly-ordered nature of the graphite surface was intended to simulate a sheet of graphene in terms of electrostatic interactions. Here, compound **1** is seen to exhibit a quasi-reversible redox couple at approximately -0.76 V (**Figure 3.6**). Addition of TFA to graphite/**1** shows catalytic current at an onset potential that approximately coincides with the observed redox couple (**Figure 3.7**, left). This current is absent at the same HOPG electrode prior to soaking in catalyst, and is

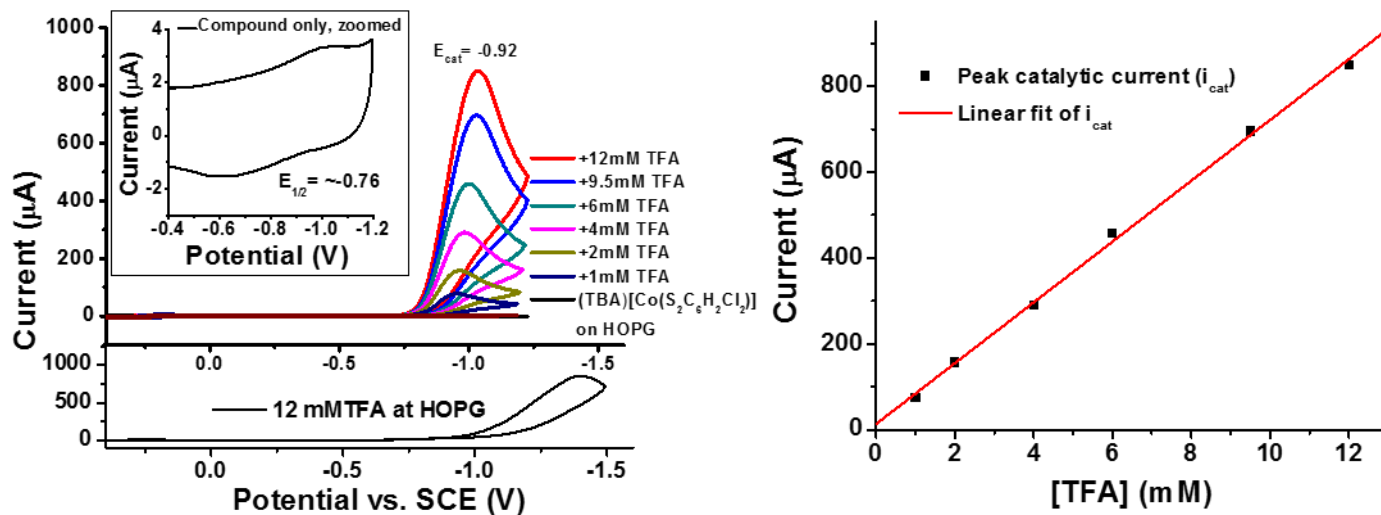


Figure 3.7. *Left:* Cyclic voltammetry of (TBA)[Co(S₂C₆H₂Cl₂)₂] (**1**) adsorbed on a HOPG working electrode with addition of TFA at a scan rate of 50 mV/s. The solution was 0.1 M aqueous potassium hexafluorophosphate, the counter electrode was a platinum wire, and the reference electrode was Ag/AgCl (saturated KCl solution). An equimolar solution of potassium ferricyanide/ferrocyanide (0.5 mM total) was used as an internal reference. Potentials are reported vs. the saturated calomel electrode. *Right:* Linear fit of the peak catalytic current versus increasing TFA concentrations, indicating an acid-diffusion controlled process under these conditions.

indicative of dihydrogen production from TFA, with a peak catalytic potential of -1 V and a current half-maximum potential of -0.92 V. Increasing acid concentrations lead to a linear increase in catalytic current, with no activity saturation observed at the acid concentrations studied (**Figure 3.7**, right). Excitingly, analysis of **1** on graphite at higher TFA concentrations (>20 mM) showed such high levels of dihydrogen production that peak catalytic currents were perturbed by gas bubbles at the graphite electrode, still without reaching activity-limited currents (see experimental section). As in the case of the FTO/RGO/**1** system, rinsing the HOPG electrode after acid titration CV studies and analysis in a fresh (pH ~ 7) aqueous solution still shows a redox signal with a conserved E_{1/2} value from the first analysis (**Figure 3.8**, left). Addition of equal amounts of TFA induce an increase in cathodic current approximately equal to what is observed in the first solution (**Figure 3.8**, right), showing that **1** is not prone to leaching for both RGO and HOPG supports under these conditions.

The similarity between the catalytic onset potential of **1** and its redox couple in the absence of acid on graphite suggests that reduction precedes protonation, possibly indicating an ECEC- or ECCE-type mechanism. It is therefore interesting to note that the overall mechanism is similar in the FTO/RGO/**1** and graphite/**1** systems, but that in the former case a ~ 0.2 V cathodic shift of the catalytic relative to the first redox wave is observed. This may indicate an inherent difference in the compound adsorption/interaction with RGO compared to graphite.

The turnover frequency (TOF) of the immobilized catalyst systems for dihydrogen production can be estimated using direct comparison of cathodic peaks in the presence and absence of acid (**equation 1**, experimental section). This method yields conservative estimates of 1007 s^{-1} and 701 s^{-1} for the FTO/RGO/**1** system in TFA and HCl, respectively at a 2 mM

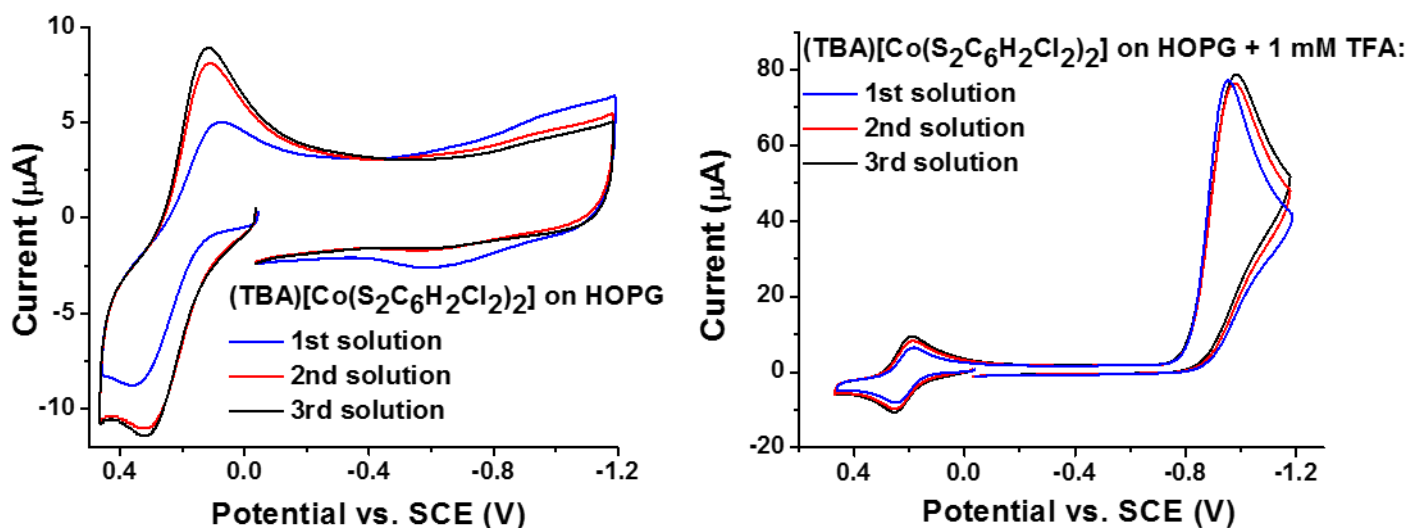


Figure 3.8. Cyclic voltammetry of $(\text{TBA})[\text{Co}(\text{S}_2\text{C}_6\text{H}_2\text{Cl}_2)_2]$ (**1**) adsorbed on a HOPG working electrode with addition of TFA in different (consecutively applied) solutions. Each solution was 0.1 M aqueous potassium hexafluorophosphate and 1 mM TFA, with an equimolar solution of potassium ferricyanide/ferrocyanide (0.5 mM total) used as an internal reference. The same electrodes were rinsed and reused for analysis of each solution, with a platinum wire counter electrode and a Ag/AgCl (saturated KCl) reference electrode. The HOPG working electrode was rinsed thoroughly and sonicated briefly in water before analysis in each new solution. Potentials are reported vs. the saturated calomel electrode.

acid concentration. It is noteworthy that these rates dramatically exceed those reported for the compound in homogeneous solution ($1,400 \text{ h}^{-1}$). One problem for the FTO/RGO/**1** system at high acid concentrations is background acid reduction as well as tin oxide reduction at the exposed FTO electrode surfaces (see acid controls, **Figures 3.3** and **3.5**). Hence, acid-saturation conditions could not be reached. Using the same method to calculate TOF for graphite/**1** systems gives a rate of $6,182 \text{ s}^{-1}$ at a 12 mM concentration of TFA. It is noteworthy that this level of activity is comparable to that of the renowned nickel bis(diphosphine) catalysts (although at a comparably higher overpotential), and is among the highest activities reported for cobalt-based hydrogen production systems.¹³ This rate was again determined in conditions where the catalyst activity was not saturated, this time due to disturbance of the voltammograms by H_2 production and background proton reduction by graphite at high acid concentrations. Therefore, catalytic rates for heterogeneous systems of **1** were also analysed by the ‘foot of the catalytic wave’ method (**equations 2 & 3**, experimental section). This method provides bimolecular rate constants of $5.77 \cdot 10^7 \text{ M}^{-1} \text{ s}^{-1}$ and $3.35 \cdot 10^7 \text{ M}^{-1} \text{ s}^{-1}$ for the FTO/RGO/**1** systems in HCl and TFA, respectively, and $3.68 \cdot 10^7 \text{ M}^{-1} \text{ s}^{-1}$ for the graphite/**1** system with TFA. While these estimates are exceptionally high (as expected since this method is less reliable in instances of substrate diffusion-limited activity), in combination with the results from **equation 1** this demonstrates that heterogeneous systems of **1** immobilized on graphitic surfaces have impressive dihydrogen production activities.

Electrolysis studies of **1** adsorbed on graphite were performed to assess our heterogeneous system under multiple turnover conditions, with dihydrogen production monitored by gas chromatography (**Figure 3.9**, left). After 12 hours of a -0.95 V applied potential in a 40 mM TFA solution, the graphite/**1** system had produced over 250 μmol of hydrogen and activity was still not seen to subside. The current observed correlated closely with the evolved hydrogen (**Figure 3.9**, right) and a Faradaic efficiency close to 100% was determined, indicating the exclusive use of injected electrons for proton reduction. An initial rate constant of $2.88 \cdot 10^{16}$ [molecules H_2] s^{-1} for H_2 production was calculated for a graphite/**1** electrode of 0.2 cm^2 surface area. Unfortunately, the attempt to calculate a molecular TOF was prevented due to difficulty in accurately quantifying the amount of **1** on the graphite surface. Future work to determine the molecular TOF and long-term electrolysis studies are underway.

In summary, our initial studies show that heterogeneous cobalt bis(dithiolene) electrocatalysts are easily afforded without the need of time consuming and costly

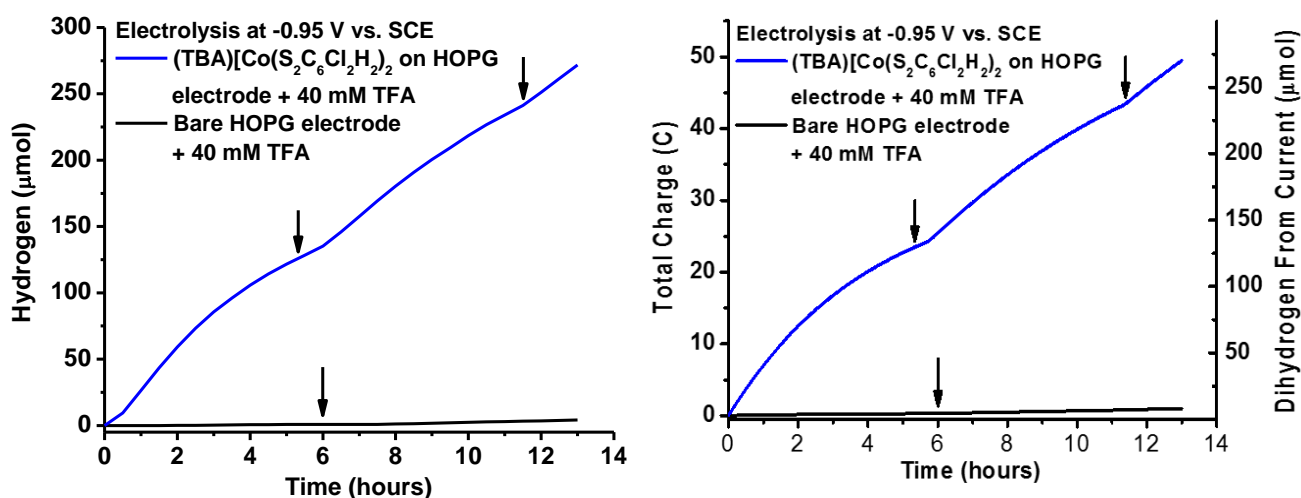


Figure 3.9. Electrolysis of HOPG electrodes at a potential of -0.95 vs. SCE with 40 mM TFA before and after soaking in a 5mM solution of (TBA)[Co(S₂C₆Cl₂H₂)₂] (**1**) for 12 hours. *Right:* dihydrogen evolution as directly measured by gas chromatography. Arrows on both plots indicate time points at which supplemental TFA was added (equal to initial aliquot). Electrolysis was performed in a two-compartment cell (split into working/reference electrode and counter electrode) with a 0.3 M aqueous potassium hexafluorophosphate solution in both compartments. Potassium ferrocyanide (0.3 M) was added as a sacrificial reductant in the counter electrode chamber. The reference electrode was a Ag/AgCl (saturated KCl) electrode, and a platinum mesh was used as the counter electrode. *Left:* Charge accumulation from the electrolysis over time.

functionalization of the ligand framework with large aromatic groups. These systems display total catalysis in practically relevant pH ranges (pH>3), and no substantial degradation or leeching is evident from either acidic conditions or O₂ exposure in the experiments conducted. With the wide range of substrates available for RGO deposition, this technique ensures that heterogeneous dihydrogen-generation catalysis is viable on a variety of materials, giving nearly limitless possibility for materials engineering. Applications in semiconductor systems are of particular interest, and corresponding studies are underway.

Experimental Section.

General Methods

Chemicals were of highest purity grade commercially available and used without further purification (unless mentioned). Methanol (anhydrous, ACS grade) was purchased from Fisher and distilled over calcium hydride, then degassed via extended nitrogen purges prior to use. Acetonitrile (ACS grade), sodium methoxide, trifluoroacetic acid, hydrochloric acid, potassium ferricyanide, and potassium ferrocyanide were purchased from Fisher. 3,6-dichloro-1,2-benzenedithiol was purchased from Sigma. Graphite powder was purchased from MTI Corp.

Synthesis

The preparation of the cobalt compound was performed by a method analogous to that reported by McNamara and coworkers:¹⁸

Tetrabutylammonium Co bis(3,6-dichlorophenyldithiolate) (1)

In an inert atmosphere box under N₂ pressure (Innovative Technologies), a solution of 3,6-dichloro-1,2-benzenedithiol (Cl₂bdt) (0.436 g, 2.05 mmol) and sodium methoxide (0.116 g, 2.10 mmol) was added dropwise to a suspension of cobalt(II) sulfate hexahydrate (0.281 g, 1 mmol) in 30 mL of dry methanol. The addition instigated a change in color to deep blue, and the resulting solution was stirred for 2 hours. A solution of tetrabutylammonium bromide (0.340 g, 1.05 mmol) in 5 mL methanol was added at this time, and the solution was stirred for an additional 2 hours. The solvent volume was reduced by vacuum to <10 mL, giving a dark blue precipitate which was filtered and dried. Recrystallization of the solid from dichloromethane/ether yielded (TBA)[Co(S₂C₆H₂Cl₂)₂] as a dark blue crystalline solid in 64% yield (0.462 g). Spectroscopic data of the product (see **Figure 3.15**) match those available in the literature.¹⁸

Graphene Oxide

Graphene oxide for graphene depositions was prepared as in previous studies outlined in the experimental details for chapter 2.

X-ray Photoelectron Spectroscopy (XPS, Maldonado laboratory)

All X-ray photoelectron spectra were acquired with a PHI 5400 analyzer using an Al K α (1486.6 eV) source without a monochromator. Spectra were recorded without charge neutralization at a base pressure of $<2.5 \cdot 10^{-9}$ Torr. A 6 mA emission current and 10 kV anode HT were used. Survey scans were acquired at a pass energy of 117.40 eV. High-resolution XP spectra of Sn 3d, C 1s, Co 2p and S 2p were recorded at a pass energy of 23.5 eV. The binding energies of all spectra were corrected by using the difference between the observed C 1s peak energy and the peak energy of adventitious carbon (284.6 eV).⁶⁶ Spectra were fit with a Shirley type background using CASAXPS version 2.313 software. C 1s spectra were fit with a singlet

using 45% Gaussian and 65% Lorentzian line shapes. The full width at half maximum (fwhm) was constrained between 0.6 and 2.0. Additional peaks using the same fitting parameters were used to fit the C-O and C-S signals.

UV-Visible Spectroscopy

Electronic absorption spectra were collected at room temperature using an Analytic Jena Specord-600 spectrometer with a WinASPECT (V2.2) interface.

Catalyst-Adsorbed Electrode Preparation

All catalyst-adsorbed electrode surfaces reported in this work were prepared by soaking the RGO or graphite surface in a 5 mM acetonitrile solution of **1** for 12 hours. After this period, surfaces were extensively rinsed with fresh acetonitrile and subsequently sonicated in a fresh acetonitrile solution for a minimum of 30 minutes to assure any loosely bound catalyst was sufficiently removed prior to electrochemical and XPS analysis.

Electrochemical Measurements

All electrochemical measurements were conducted in 18.2 Millipore water. Cyclic voltammetry and controlled potential coulometry were carried out using an Autolab potentiostat with a CHI electrochemical interface. For RGO measurements, the working electrode was a piece of fluorine-doped tin oxide-coated glass (purchased from Pilkington) with thin layers of RGO electrodeposited on the surface by the method described above. For graphite measurements, a highly-ordered edge plane graphite electrode (purchased from Pine instruments) was used. Platinum wire (CH Instrument) was used as the counter electrode in all experiments, and the reference was an aqueous Ag/AgCl electrode (CH Instruments, saturated AgCl and KCl fill solution). All solutions were prepared with 0.1 M potassium hexafluorophosphate supporting electrolyte as purchased from Fisher and subsequently

recrystallized. Argon gas was used to deoxygenate all solutions for a minimum of 30 minutes prior to data collection.

Reduced Graphene Oxide Depositions

RGO depositions were performed in an identical manner to the procedure outlined in the experimental details for chapter 2.

Determination of Catalytic Turnover Frequencies

The proton reduction activity rates for the FTO/graphene- and graphite-adsorbed catalyst systems were assessed both by methods reported by Bard and Faulkner (**equation 1**)⁶⁷ and by the ‘foot-of-the-wave’ method⁶⁸:

Bard and Faulkner Rate Estimate

For both FTO/graphene- and graphite-adsorbed systems acid concentrations used for analysis were below the maximum activity levels (activity saturation), in the FTO/graphene system due to the substantial tin oxide reduction seen at high acid concentrations, and in the graphite system due to disruption of the voltammogram signals by H₂ production at high acid concentrations as well as background acid reduction at graphite under these conditions. Rates predicted by this method are thus expected to be an underestimate of the true TOF under acid saturation.

$$(1) \frac{i_{cat}}{i_p} = \frac{2}{0.446} \sqrt{\frac{RTk_{obs}}{Fv}}$$

Here, i_{cat} and i_p are the peak cathodic current in the presence and absence of acid (respectively), v is the scan rate [V/s], F is Faraday’s constant, and k_{obs} is the observed catalytic rate.

For the FTO/graphene/**1** system, analysis in the presence of trifluoroacetic acid with a concentration of 2 mM gives an $i_{\text{cat}}/i_{\text{p}}$ ratio of 72.11, and is predicted by **equation 1** to have a rate of $1,007 \text{ s}^{-1}$. Analysis in the presence of hydrochloric acid with a concentration of 1.3 mM gives an $i_{\text{cat}}/i_{\text{p}}$ ratio of 60.16, and is predicted to have a rate of 701 s^{-1} . In the graphite/**1** system, activity with an acid concentration as high as 12 mM TFA can be observed without significant voltammogram distortion, giving an $i_{\text{cat}}/i_{\text{p}}$ ratio of 252.68, and is predicted to have a rate of $6,182 \text{ s}^{-1}$.

Activities obtained by this equation for the FTO/graphene/**1** and graphite/**1** systems in subsequent (fresh) acid solutions can be assumed to be very similar to this based on the consistent current responses observed with identical acid concentrations (**Figures 3.4 & 3.8**), thus giving a consistent $i_{\text{cat}}/i_{\text{p}}$ ratio and predicted TOF.

Foot-of-the-Wave Rate Analysis

Voltammetry data of the catalyst-soaked surfaces in the presence of acid were plotted according to methods reported by Saveant and coworkers⁶⁸, where E is the observed potential (reported vs. SCE), $E^0(\text{PQ})$ is the potential at the half-wave maximum for the catalytic wave, i is the observed current, and $i^0(\text{p})$ is the peak current of the cathodic wave for the catalyst-soaked surfaces in the absence of acid. Plotting the ratio of $(i/i^0(\text{p}))$ following **equation 2** afforded the curves seen below in **Figures 3.10-3.12**, the base of which was fitted linearly. The slope of this fit provides access to the bimolecular rate constant via **equation 3**.

$$(2) \frac{1}{1 + \exp\left[\frac{F}{RT}(E - E_{\text{PQ}}^0)\right]}$$

$$(3) M = 2.24 \sqrt{\frac{RT}{Fv}} \sqrt{2kC_A^0}$$

Here, M = slope, $C^0(a)$ is the substrate (acid) concentration [M], and v is the scan rate [V/s].

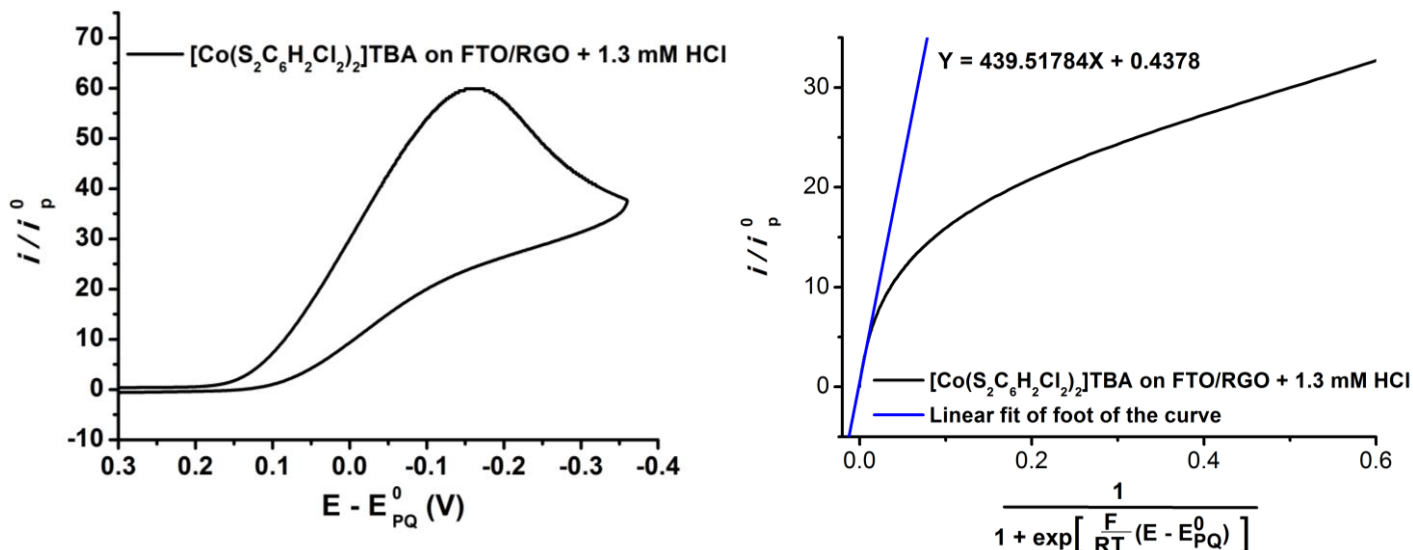


Figure 3.10. Foot-of-the-wave analysis of (TBA)[Co(S₂C₆H₂Cl₂)₂] (**1**) on FTO/graphene in the presence of 1.3 mM HCl. For **1** adsorbed on FTO/graphene with 1.3 mM HCl, foot-of-the-wave analysis gives a slope of 439.52, resulting in a rate constant of $5.77 \times 10^7 \text{ M}^{-1} \text{ s}^{-1}$ (from **equation 3**).

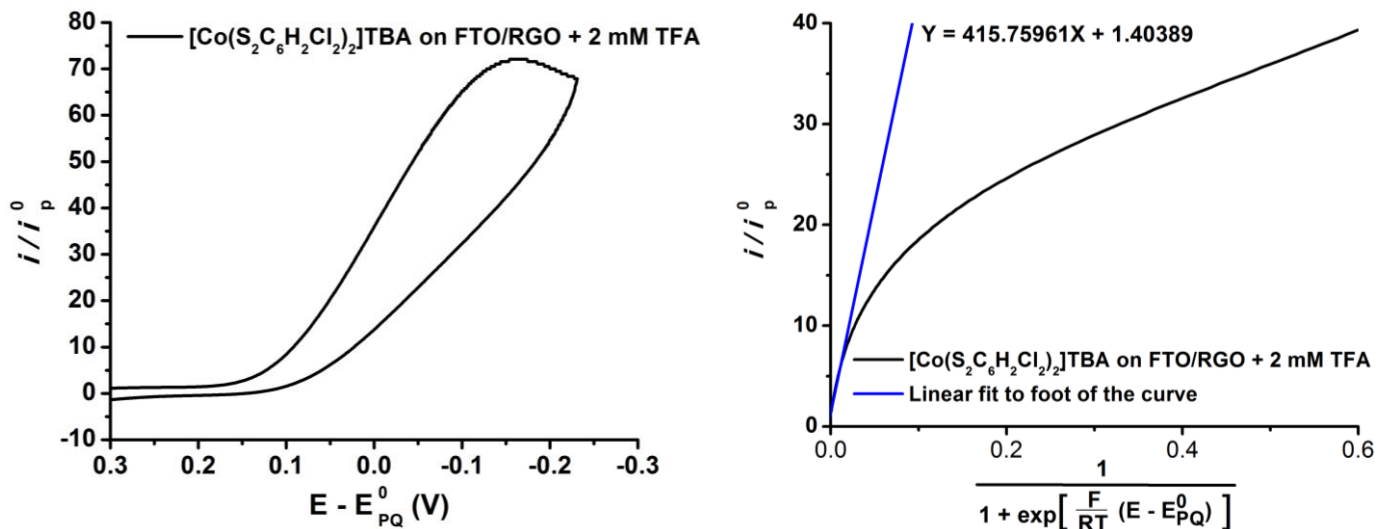


Figure 3.11. Foot-of-the-wave analysis of (TBA)[Co(S₂C₆H₂Cl₂)₂] (**1**) on FTO/graphene in the presence of 2 mM TFA. For **1** adsorbed on FTO/graphene with 2 mM TFA, foot-of-the-wave analysis gives a slope of 415.76, resulting in a rate constant of $3.35 \times 10^7 \text{ M}^{-1} \text{ s}^{-1}$ (from **equation 3**).

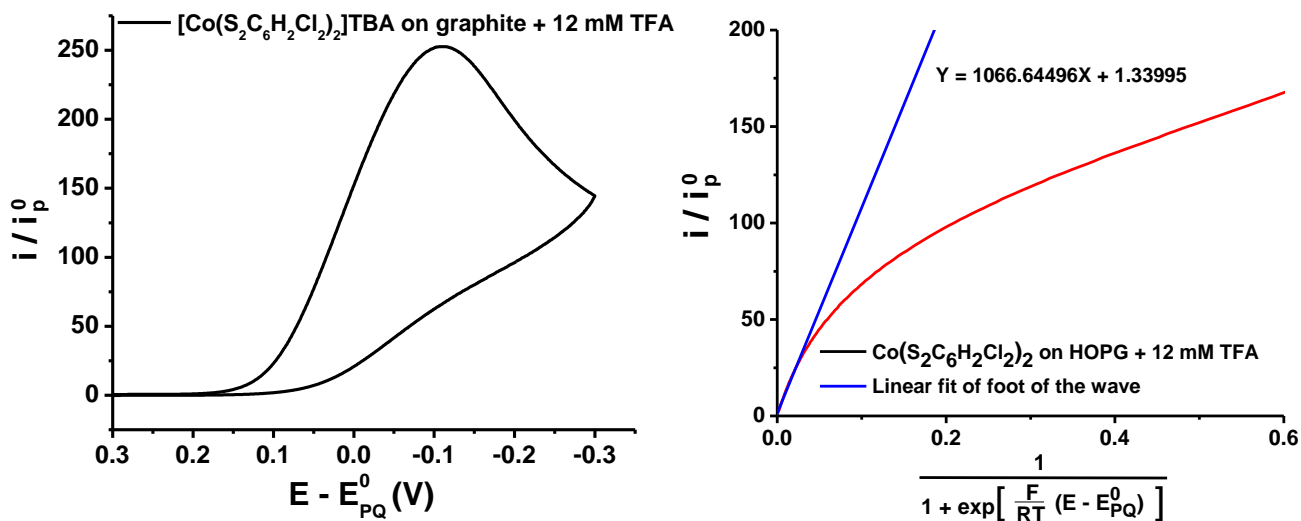


Figure 3.12. Foot-of-the-wave analysis of. (TBA)[Co(S₂C₆Cl₂H₂)₂] (**1**) on graphite in the presence of 12 mM TFA. For **1** adsorbed on graphite with 12 mM TFA, foot-of-the-wave analysis gives a slope of 1066.65, resulting in a rate constant of $3.68 \times 10^7 \text{ M}^{-1} \text{ s}^{-1}$ (from equation 3).

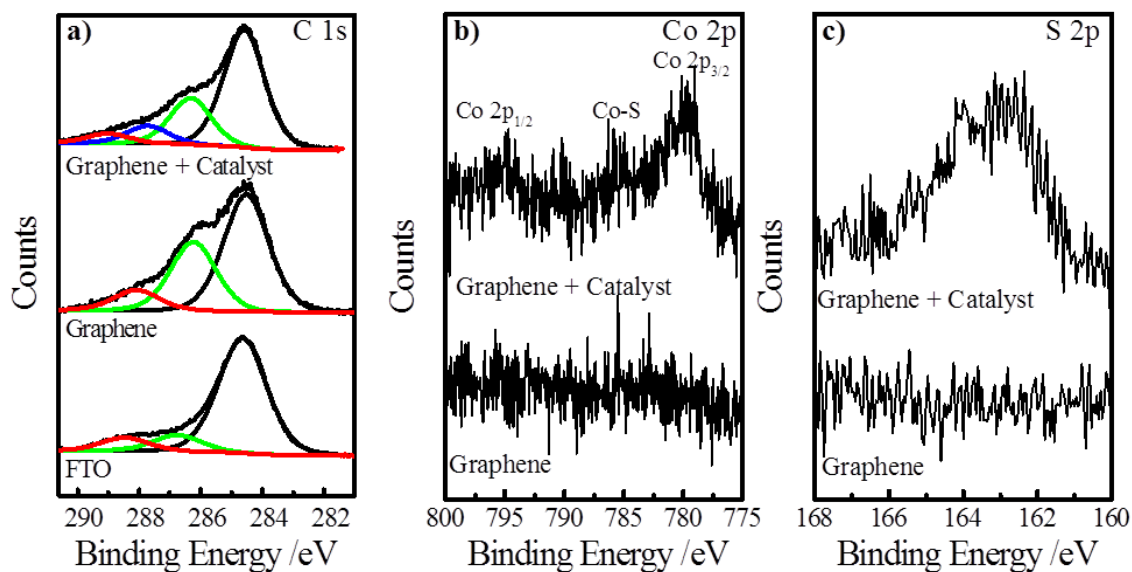


Figure 3.13. (a) High-resolution C 1s XPS data collected at a pass energy of 23.3 eV of (bottom) bare FTO, (middle) FTO/RGO, and (top) FTO/RGO surfaces after soaking in a 5 mM solution of **1** in acetonitrile for 12 hours. Co 2p (b) and S 2p (c) XPS data of (bottom) RGO-deposited FTO glass and (top) the RGO surfaces after deposition of (TBA)[Co(S₂C₆Cl₂H₂)₂] (**1**) (using similar conditions).

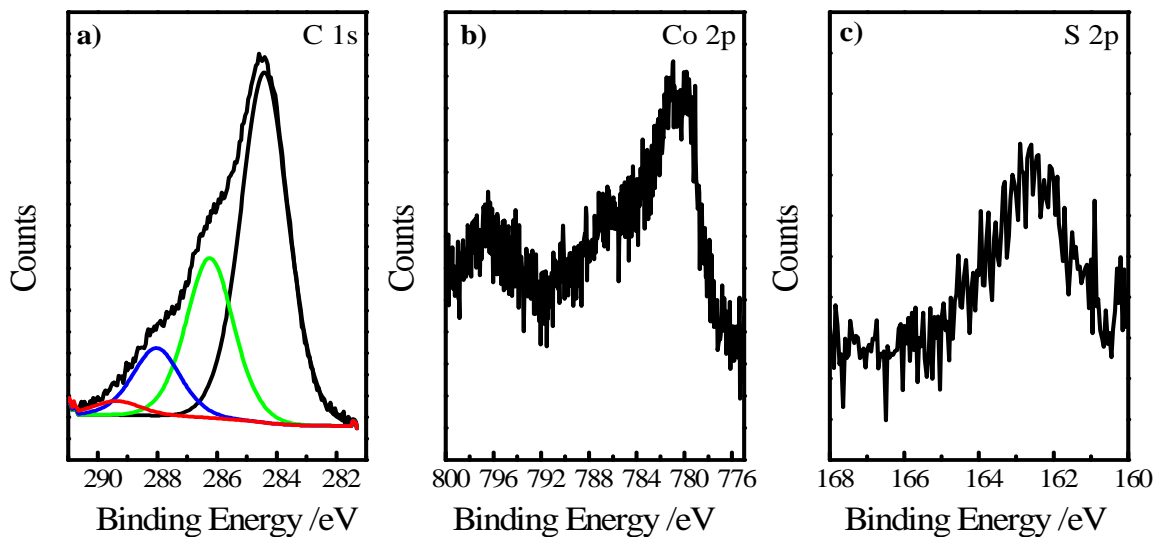


Figure 3.14. High-resolution (a) C 1s, (b) Co 2p and (c) S 2p XPS data of (TBA)[Co(S₂C₆Cl₂H₂)₂] (**1**) adsorbed on a FTO/RGO electrode **after** analysis by acid titration cyclic voltammetry study.

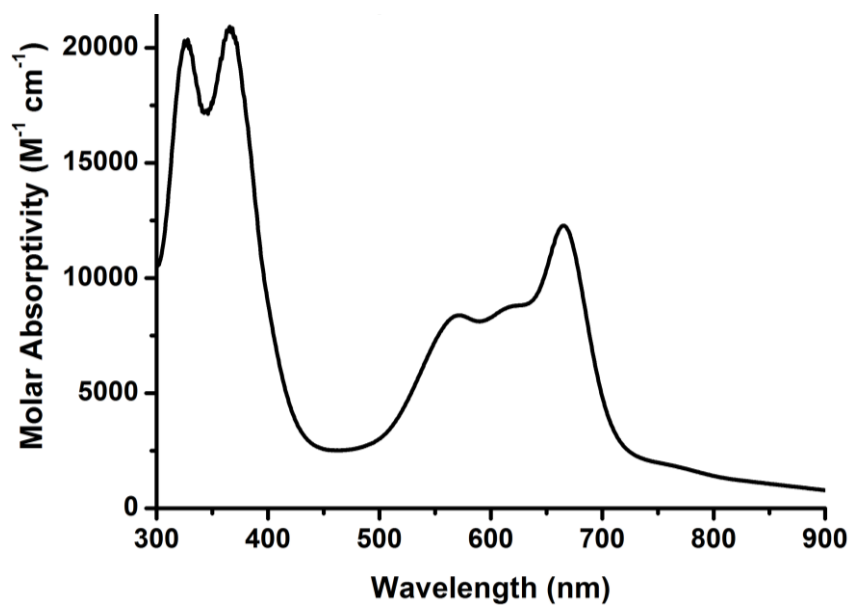


Figure 3.15. UV-Visible spectrum of (TBA)[Co(S₂C₆Cl₂H₂)₂] (**1**) in dichloromethane solution.

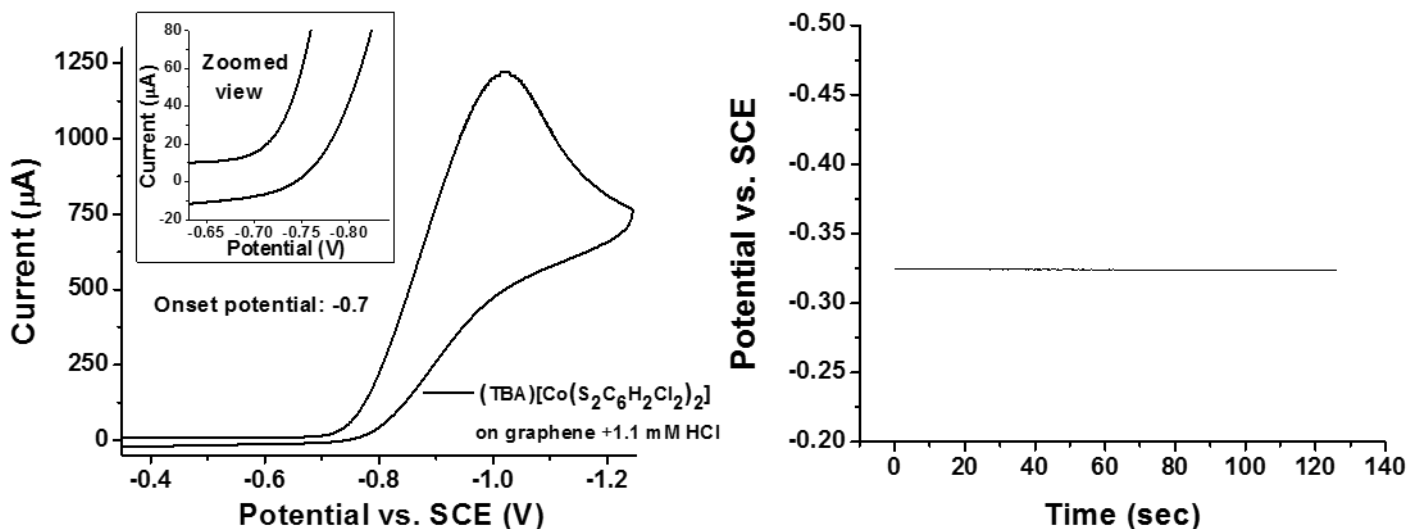


Figure 3.16. *Left:* Cyclic voltammetry of (TBA)[Co(S₂C₆Cl₂H₂)₂] (**1**) adsorbed on a FTO/graphene working electrode in a 1.1 mM HCl solution with a 100 mV/s scan rate. *Right:* Open circuit potential over time of a platinum mesh working electrode in the same acid solution under 1 atm H₂ atmosphere to indicate overpotential. The solution was 0.1 M aqueous potassium hexafluorophosphate, the counter electrode was a platinum wire, and the reference electrode was Ag/AgCl (saturated KCl solution). An equimolar solution of potassium ferricyanide/ferrocyanide (0.5 mM total) was used as an internal reference. Potentials are reported versus the saturated calomel electrode.

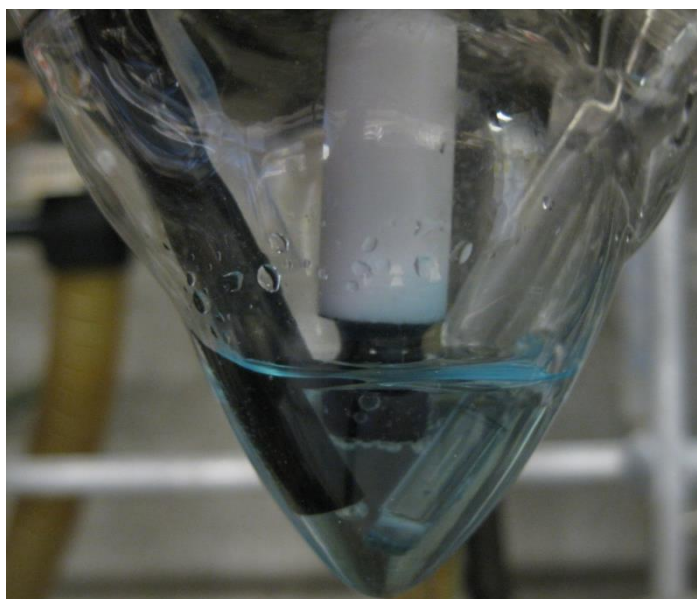
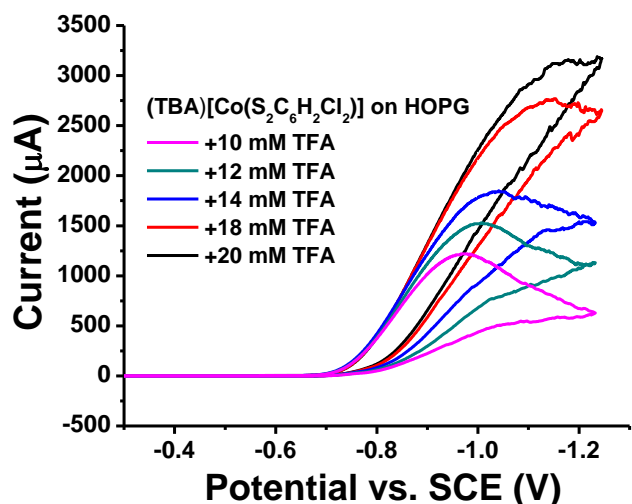


Figure 3.17. *Left:* Cyclic voltammetry of (TBA)[Co(S₂C₆Cl₂H₂)₂] (**1**) adsorbed on a HOPG working electrode in the presence of high concentrations of TFA. The solution was 0.1 M aqueous potassium hexafluorophosphate, the counter electrode was a platinum wire, and the reference electrode was Ag/AgCl (saturated KCl solution). An equimolar solution of potassium ferricyanide/ferrocyanide (0.5 mM total) was used as an internal reference. Potentials are reported versus the saturated calomel electrode. *Right:* Image of the HOPG working electrode (center) showing formation of H₂ gas during cathodic scan.

3.2. Electrocatalytic Analysis of Cobalt Bis(dithiolene) Derivatives: Effect of Ring Size and Substitution on Catalyst Loading, Activity and Overpotential

Due to the outstanding activity observed for a cobalt bis(dithiolene) catalyst on FTO/RGO and HOPG electrodes in our previous work⁶⁹, investigation into the effect of ligand modification on catalyst heterogenization is of great interest for optimization of these systems

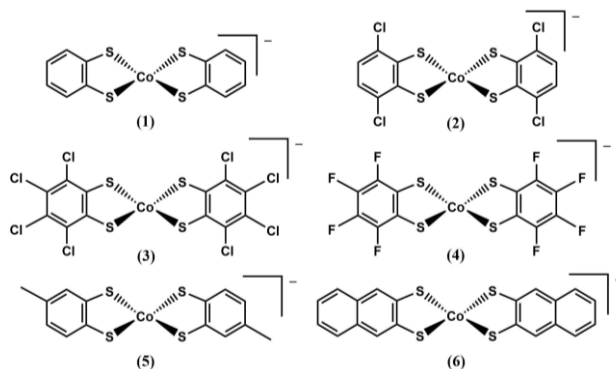


Chart 3.2. Cobalt bis(benzenedithiolene) derivatives

prior to application in photocathode manifolds. In particular, the effect of ligand ring size and halide substitution as well as the electron withdrawing nature of the substituted halide on catalyst loading, TOF and stability are important details for directed catalyst design. Herein, we report a series of cobalt bis(benzenedithiolene) derivatives (**Chart 1**) adsorbed to graphitic surfaces and investigations of their dihydrogen production activity in acidic aqueous solutions. Due to the ease of preparation and the potential future applications of this system, initial studies were conducted on reduced graphene oxide (RGO) electrodeposited on fluorine doped tin oxide (FTO), which allow for the analysis of current response as a function of acid concentration. These studies provide a fast means of screening different catalyst systems for RGO adsorption and proton reduction activity. However, quantitative comparisons are more difficult due to the fact that consistency in RGO coverage and topography are generally low. To complement these tests, the catalysts were also adsorbed on highly-ordered pyrolytic graphite (HOPG) electrodes.

HOPG electrodes provide a more consistent surface area and topography, therefore allowing for a quantitative comparison between different catalyst derivatives in the surface-immobilized state. The resulting series of heterogeneous electrocatalysts provides insight into the effect of benzenedithiolate ligand substitution on surface adsorption and coverage, electrocatalytic activity, and lifetime of the catalysts. Due to the large amount of data for analysis of all catalyst derivatives on both FTO/RGO and HOPG electrodes, the data in this section has been limited to discussion-relevant figures.

Results

Characterization

The cobalt bis(benzenedithiolene) complexes **1-6** (general formula: $[\text{Co}^{\text{III}}(\text{bdt})_2]^-$) were all synthesized using the same general procedure originally reported by Gray and coworkers⁵⁰, combining a cobalt(II) source with the dithiolate reagent in the presence of a base (sodium methoxide) and a counterion source to give the anionic cobalt(III) species as the tetrabutylammonium salt. The micro-crystalline products were then characterized by mass spectrometry, elemental analysis, and UV-visible spectroscopy, in addition to the crystallographic characterization for **6**.

The complexes all have strong absorption features in the near UV (~400 nm) and from ~500-700 nm, with respective extinction coefficients as high as 20,000 and 14,000 $\text{M}^{-1} \text{s}^{-1}$ as seen in the experimental section. The crystal structure of **6** (**Figure 3.18**) confirms the expected square planar structure observed in other examples of cobalt bis(benzenedithiolene) complexes, with a perfectly planar structure essentially giving the molecule the ‘thickness’ of the cobalt diameter. The packing of the molecules in the crystal shows layers of the flat molecules with

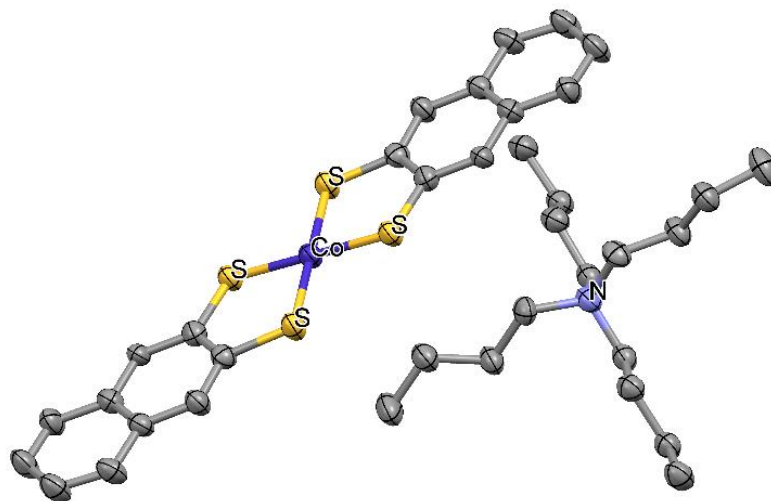


Figure 3.18. Crystal structure of TBA[Co(S₂C₁₀H₇)₂] (**6**) with ellipsoids shown at 50% probability. Hydrogen atoms are omitted for clarity. Selected bond distances [Å] and angles [degrees]: Co-S (all equivalent) 2.171(9), average S-C 1.764(5), S-Co-S 91.68(4), Co---N 6.456.

completely eclipsed rings, separated by slightly offset cations, with a distance of 8.3 Å between the sandwiched cobalt bis(benzenedithiolene) molecules.

X-ray Photoelectron Spectroscopy

XPS analysis of FTO surfaces before and after RGO electrodeposition were reported in our previous work,⁶⁹ and reflect the change in carbon signal in the C 1s core spectrum from only adventitious carbon on FTO to containing a variety of C-C and CO_x species upon RGO deposition. After soaking the FTO/RGO in catalyst solutions, XPS data of **3** and **6** adsorbed to FTO/RGO surfaces were collected at a pass energy of 20 eV to yield high resolution spectra. However, the substantially lower loading of these adsorbed catalyst systems ($\sim 10^{-10}$ mol_{Co}/cm²) compared to those in the polymeric systems (10^{-7} to 10^{-6} mol_{Co}/cm²) made high resolution XPS less effective, as signals were generally too low to distinguish energy differences provided at the higher resolution, and often showed trace signal if any at all.^{52,53} To better visualize the features present in the spectra, data were collected at a pass energy of 160 eV. The data

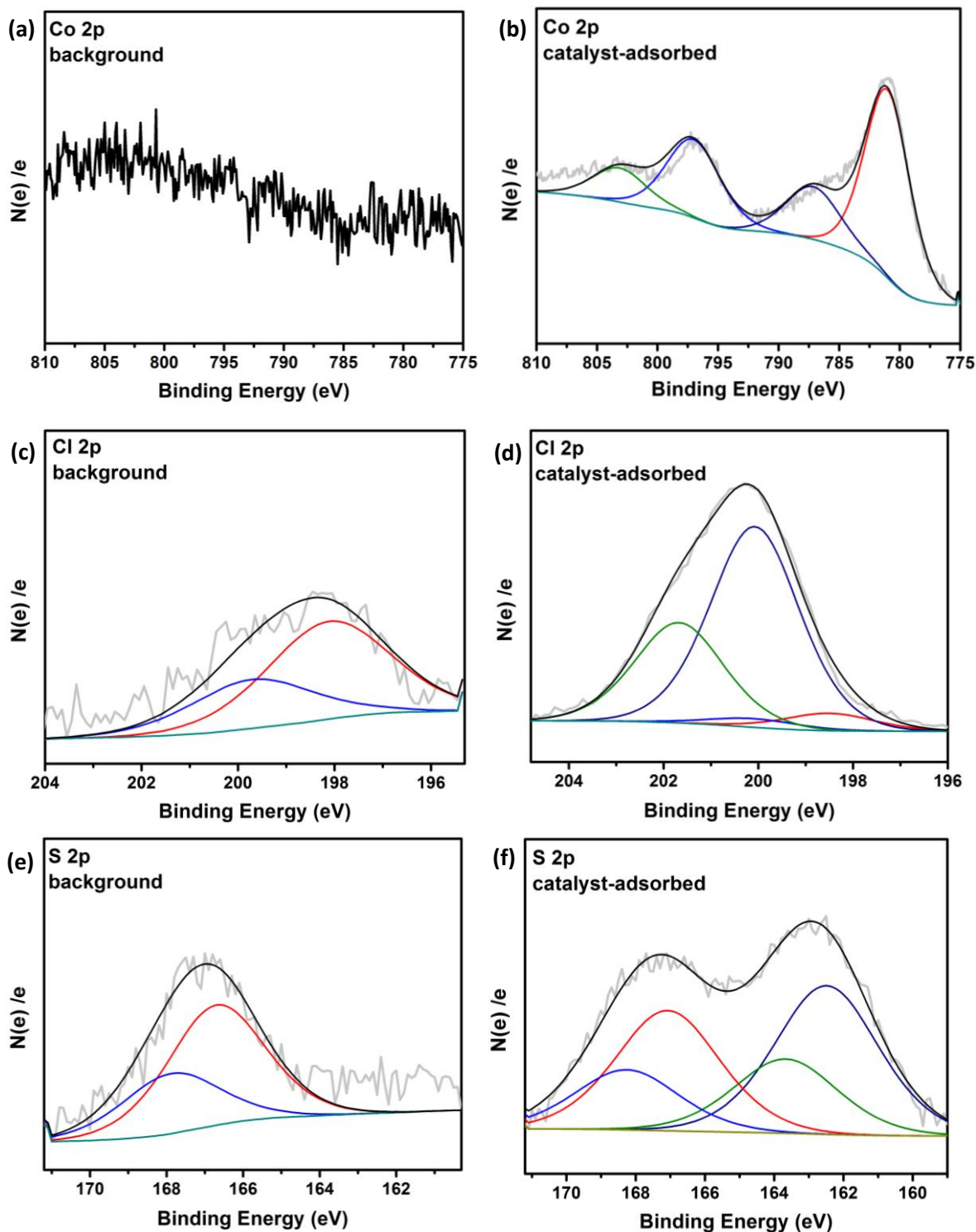


Figure 3.19. X-ray photoelectron spectroscopy (XPS) analysis of TBA[Co(S₂C₆Cl₄)₂] (3) on a FTO/RGO electrode. (a) background Co 2p core level XPS spectrum; (b) Co 2p core level XPS spectrum of catalyst-adsorbed bulk graphite; (c) background Cl 2p core level XPS spectrum of bare bulk graphite; (d) Cl 2p core level XPS spectrum of catalyst-adsorbed bulk graphite; (e) background S 2p core level XPS spectrum of bare bulk graphite; (f) S 2p core level XPS spectrum of catalyst-adsorbed bulk graphite. The envelope is included as a solid black trace.

generally show two new signals present in the Co 2p core spectrum, comprising two sets of Co 2p_{1/2} and 2p_{3/2} signals (**3.19b**). These signals have been attributed to the [Co^{III}(bdt)₂]⁻ (778 and 794.1 eV) and [Co^{II}(bdt•)(bdt)]⁻ (781 and 795 eV) resonance structures reported for cobalt bis(benzenedithiolene) complexes.⁵¹ These results are consistent with those reported for both linear and extended polymer systems of [Co(bdt)₂]⁻.^{52,53} The S 2p core spectrum also shows a new signal at 163 eV (**Figure 3.19f**), which is approximately at a 1.5 eV higher binding energy compared to cobalt sulfide materials and consistent with XPS data of phenyl-thiols previously reported in the literature.^{70,71} Analysis of **3** on FTO/RGO shows similar results for the Co 2p and S 2p spectra, in addition to showing a new signal for Cl 2p at 201 eV (**Figure 3.19d**), which is in agreement with previous literature reports for chloro-substituted ring systems.⁷²

Cyclic Voltammetry (CV) Characterization

Analysis of our cobalt bis(dithiolene) complexes on FTO/RGO surfaces by CV shows redox features in the range of -0.22 to -0.42 V vs. SHE, as can be seen below in **Table 3.1**. The features persist upon extended cycling, indicating the stability of the adsorbed species on the electrode surface. The redox events generally appear quasi-reversible in nature, with a higher cathodic current response than anodic (*i*_{pc}/*i*_{pa} values generally below 0.9) and further decreasing with increasing scan rate for most complexes as evidenced in **Figure 3.20**. Peak separation varies widely between species, ranging from just over 0.12 V for **4** to nearly 0.25 V for **6**. Most of the complexes on the FTO/RGO surfaces have E_{pc} and E_{pa} values that shift slightly with varying scan rate; however, both this phenomenon and the deviation in peak separation from the expected reversible value (0.057 V) are also observed for the ferricyanide internal standard (**Figure 3.20**, left), suggesting this is inherent to diffusion conditions in the

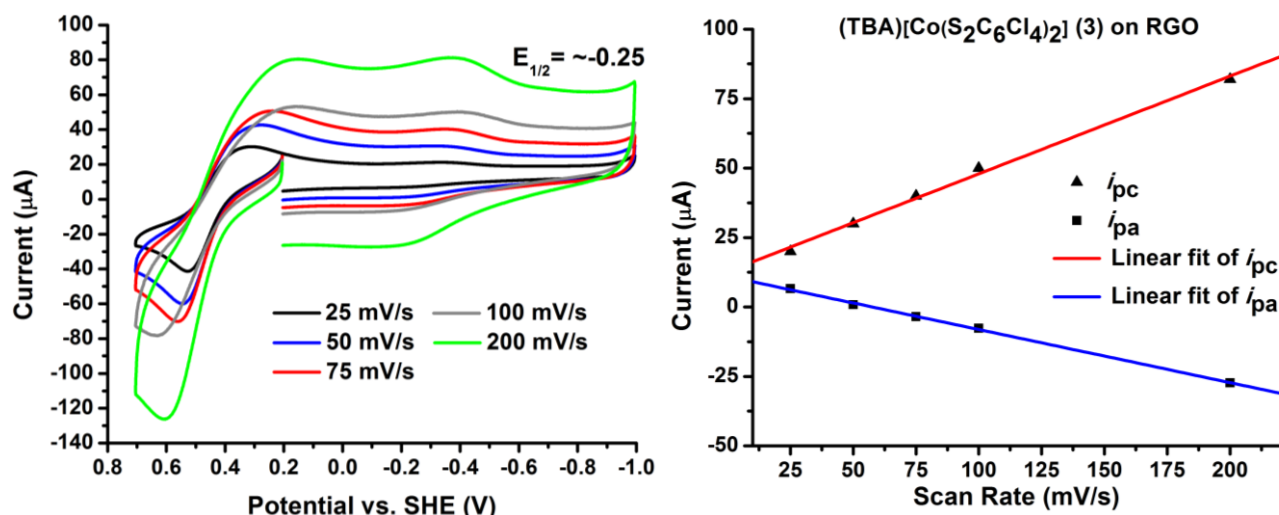


Figure 3.20. *Left:* Cyclic voltammetry of (TBA)[Co(S₂C₆Cl₄)₂] (**3**) adsorbed on a FTO/RGO working electrode at various scan rates. The solution contained 0.1 M aqueous potassium hexafluorophosphate. The counter electrode was a platinum disc, and the reference was an Ag/AgCl (saturated KCl solution) electrode. An equimolar solution of potassium ferricyanide/ferrocyanide (0.5 mM total) was used as an external standard. Potentials are reported versus the standard hydrogen electrode. *Right:* Linear fit of the peak cathodic and anodic current versus the scan rate.

cell and electron transfer for the variable FTO/RGO electrodes, and therefore cannot be entirely attributed to the adsorbed catalysts.

Cyclic voltammetry analysis of the complexes on the HOPG electrode shows redox features ranging from -0.33 to -0.57 V, consistently giving more negative $E_{1/2}$ values compared to the corresponding species on FTO/RGO surfaces. Peak anodic/cathodic current ratios are close to 1 (± 0.1) for complexes on HOPG, while a disproportionate increase of cathodic current compared to anodic current with increasing scan rate is still evident for all complexes with the exception of **4**. As seen for complex **2** in **Figure 3.21**, anodic and cathodic peak separations range from 0.2 to 0.4 V, which is generally consistent with the peak separation of the ferricyanide internal standard at the HOPG surface.

Table 3.1. Redox potentials (vs. SHE) and select catalytic properties of cobalt complexes.

Complex	$E_{1/2}^{RGO,HOPG}$ (V)	$E_{cat}^{RGO,HOPG}$ (V)	$[cat]_{HOPG}^0$ mol _{Co} /cm ²	$\eta_{RGO,HOPG}$ (V) [†]	$\frac{i_{cat}}{i_p}$ [‡]	TOF (s ⁻¹) [‡]	TON (time)
Co(bdt) ₂ (1)	-0.28, -0.57	-0.65, -0.71	-	0.55, 0.6	100.9	986	-
Co(dcbdt) ₂ (2)	-0.25, -0.52	-0.61, -0.67	$1.85 \cdot 10^{-10}$	0.52, 0.54	176.5	3,016	$1.27 \cdot 10^7$ (8 hrs)
Co(tcdbdt) ₂ (3)	-0.25, -0.35	-0.59, -0.52	$3.76 \cdot 10^{-10}$	0.5, 0.44	419.3	17,377	7×10^6 (8 hrs)
Co(tfbdtd) ₂ (4)	-0.22, -0.33	-0.57, -0.54	$9 \cdot 10^{-10}$	0.48, 0.51	171.5	2,848	-
Co(tdt) ₂ (5)	-0.28, -0.45	n/a	$1.3 \cdot 10^{-9}$	n/a	n/a	n/a	n/a
Co(ndt) ₂ (6)	-0.24, -0.46	n/a, -0.59	$9.85 \cdot 10^{-10}$	n/a, 0.36	125.7	1,530	2.5×10^4 (1 hour)

[‡]Determined by integration of cathodic current response in cyclic voltammograms of HOPG electrodes at 50 mV/s scan rate. Concentration densities are based on a HOPG electrode area of 0.2 cm².

[†]Overpotential determined by comparison of half-wave potential (E_{cat} or $E_{p/2}$) with open circuit potential of platinum in the same 1 mM TFA solution under 1 atm H₂ atmosphere (**Figure 3.35**)

[‡]Based on i_{cat} observed at pH 1.5 (or at activity saturation pH if lower) with HOPG electrode

[‡]Determined by use of equation 1 with i_{cat}/i_p determined at a scan rate of 50 mV/s at 298°K at pH 1.5

Quantification of complex loading was performed via integration of the cathodic current response at 50 mV/s in pH 7 0.1 M KPF₆ solution by directly attributing all passed charge to the 1 electron reduction of the Co^{III} species. This method gives a range of catalyst concentrations from $1.8 \cdot 10^{-10}$ mol/cm² for **2** to $1.3 \cdot 10^{-9}$ for **5**. Unfortunately, quantification

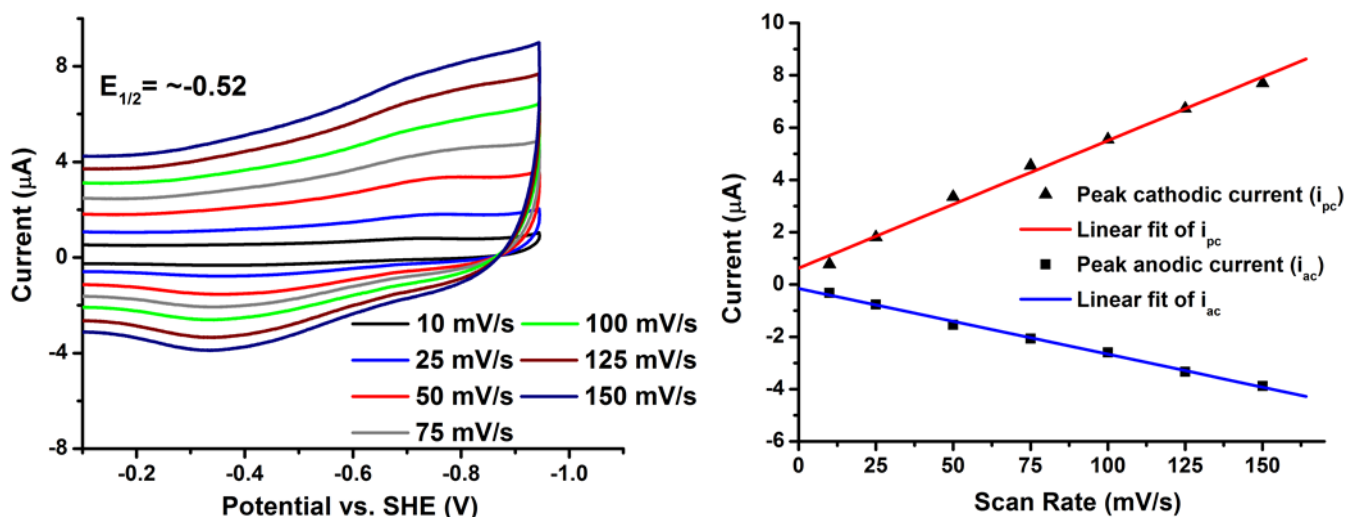


Figure 3.21. Left: Cyclic voltammetry of (TBA)[Co(S₂C₆Cl₂H₂)₂] (**2**) adsorbed on a HOPG working electrode at various scan rates. The solution contained 0.1 M aqueous potassium hexafluorophosphate. The counter electrode was a platinum disc, and the reference was an Ag/AgCl (saturated KCl solution) electrode. An equimolar solution of potassium ferricyanide/ferrocyanide (0.5 mM total) was used as an external standard. Potentials are reported versus the standard hydrogen electrode. Right: Linear fit of the peak cathodic and anodic current versus the scan rate.

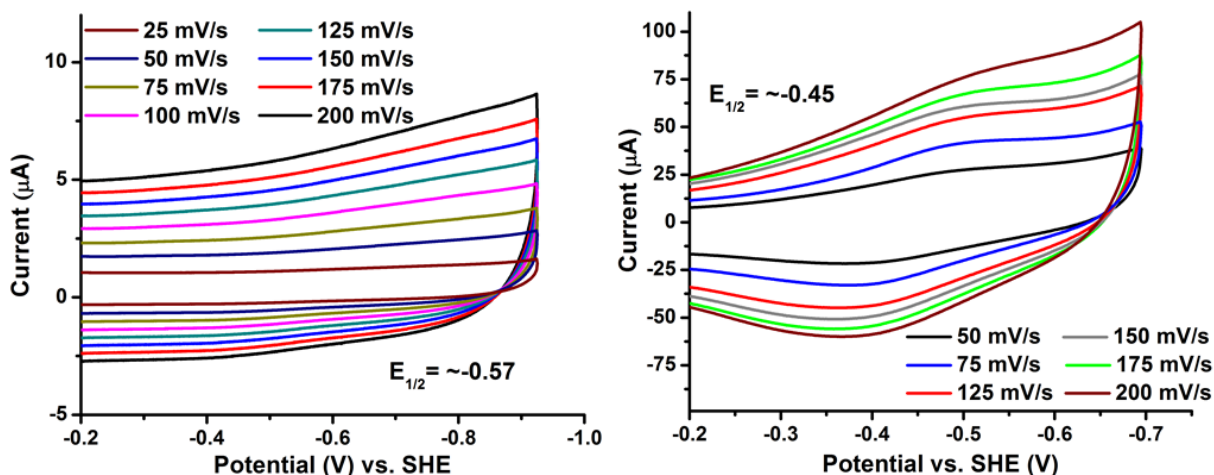


Figure 3.22. Cyclic voltammetry of (TBA)[Co(S₂C₆Cl₂H₂)₂] (**1**) (left) and (TBA)[Co(S₂C₁₀H₆)₂] (**6**) (right) adsorbed on a HOPG working electrode in an aqueous 0.1 M KPF₆ solution at varying scan rates. Platinum counter and Ag/AgCl reference electrodes were used, and potentials are reported *vs.* the standard hydrogen electrode.

of **1** was not possible, as the catalyst's cathodic peak was not discernable above the non-Faradaic current response. However, an upper limit can be estimated based on the measured value for **2**, which is substantially larger than that for **1** (Figures 3.21, left *vs.* 3.22, left, respectively). While quantitatively crude, these estimates taken on the same HOPG electrode allow for precise internal comparisons between catalyst derivatives, and thus can inform on the effect of the ligand system on catalyst adsorption. Particularly interesting are the effects of increasing halide substitution of the benzenedithiolate ligand. Our data in Table 3.1 show a clear increase from **1** to **2** and then again to **3**. The tetrafluoro-substituted complex **4** is observed to effect more than twice the loading of the tetrachloro-substituted species. Comparison of benzene and naphthalene ring systems for complex **1** and **6** show a substantial increase in catalyst loading. While this exact difference cannot be quantified, using the loading for **2** as an upper limit for that of **1** suggests more than a 5-fold increase with the larger ring system (Figure 3.22). Based on these results, compound **5** with a toluenedithiolate ligand is the best catalyst for adsorption on graphitic surfaces, resulting in the best surface coverage.

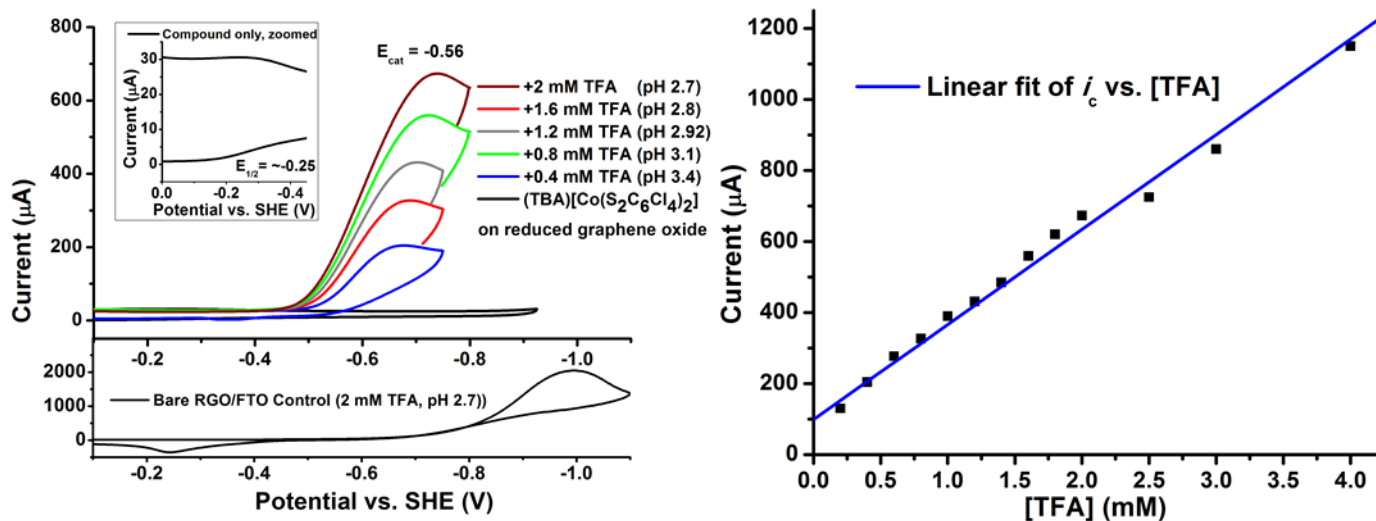


Figure 3.23. *Left:* Cyclic voltammetry of (TBA)[Co(S₂C₆Cl₄)₂] (**3**) adsorbed on a FTO/RGO working electrode with addition of TFA at a scan rate of 50 mV/s. The control surface (using an FTO/RGO electrode without adsorbed catalyst) under the same conditions is displayed on the bottom of the graph, and the inset provides a zoomed view of the CV of the Co catalyst functionalized surface in the absence of acid. The solution contained 0.1 M aqueous potassium hexafluorophosphate. The counter electrode was a platinum disc, and the reference was an Ag/AgCl (saturated KCl solution) electrode. Potentials are reported *vs.* the standard hydrogen electrode. *Right:* Linear fit of the peak catalytic current versus increasing TFA concentrations, indicating an acid-diffusion controlled process under these conditions.

Electrocatalytic Studies

For all complexes adsorbed on FTO/RGO electrodes, addition of trifluoroacetic acid to the aqueous solutions resulted in an increase in the cathodic current coinciding with disappearance of the anodic wave, indicative of proton reduction at the electrode surface (e.g., **Figure 3.23**). The complexes consistently required a pH lower than 4 to show an increase in current response (the exact pH at which the current increases varies between 3 and 4 depending on the applied complex). The current response increased linearly with further addition of acid except in the cases of **5** and **6**, which stopped increasing and subsequently decreased to background current upon further acid addition (**Figure 3.24**). In some of the repeated trials, even the initial current increase was absent for **5** and **6** upon acid addition, and the original redox feature was no longer observed, suggesting catalyst desorption or decomposition. For complexes **1-4**, activity saturation was not observed up to a TFA concentration of 2 mM (pH

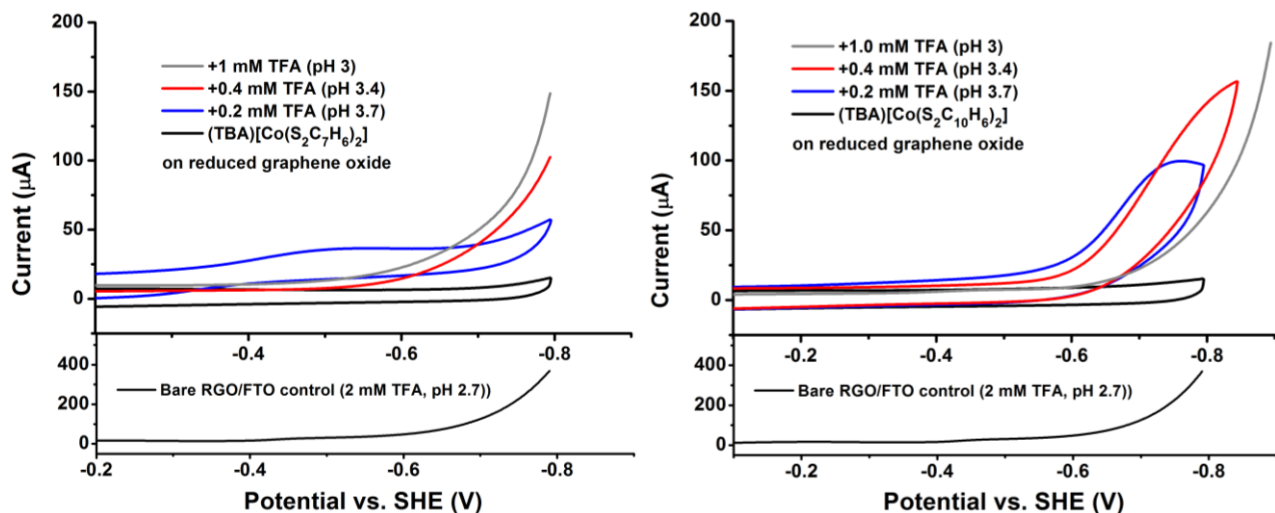


Figure 3.24. Cyclic voltammetry of (TBA)[Co(S₂C₇H₆)₂] (**5**) (*Left*) and (TBA)[Co(S₂C₁₀H₆)₂] (**6**) (*right*) adsorbed FTO/RGO working electrodes with addition of TFA at a scan rate of 50 mV/s. The control surface (using an FTO/RGO electrode without adsorbed catalyst) under the same conditions is displayed on the bottom of the graph. Return (anodic) scans are omitted for clarity in some plots. The solution contained 0.1 M aqueous potassium hexafluorophosphate. The counter electrode was a platinum disc, and the reference was an Ag/AgCl (saturated KCl solution) electrode. Potentials are reported vs. the standard hydrogen electrode. The electrode exhibit some increase in cathodic current with initial acid addition, but subsequent additions are only seen to produce background current.

2.7), below which pH the FTO surface is not cathodically durable for testing. E_{cat} values at this pH ranged from -0.57 to -0.65, with compounds **4** and **1** observed to have the most positive and negative potentials, respectively. In our previous work, overpotential was measured as the difference between the onset potential of the catalytic wave in a 1 mM (pH 3) aqueous solution and the open circuit potential of a platinum working electrode in the same solution under 1 atm H₂ pressure. However, recent literature has reviewed the E_{cat} (or $E_{\text{p}/2}$) to be a more systematic and accurate measure of the a catalyst's performance, therefore in this work the E_{cat} value in the same pH 3 aqueous solution is used in place of the catalytic wave onset potential (see experimental section). This method has provided an overpotential range of 0.5 to 0.63 V vs. platinum for the series on FTO/RGO electrodes. All E_{cat} values were at least 0.2 V more negative than the $E_{1/2}$ value observed in the absence of acid for all complexes adsorbed on FTO/RGO electrodes.

Trifluoroacetic acid titration CV studies for HOPG-adsorbed complexes in aqueous solutions yield similar results to that of the FTO/RGO electrodes, in all cases eliciting an increasing cathodic current response. Increase in current response is linear with acid concentration for all complexes with the exception of **5**, which undergoes a change in response similar to this compound on FTO/RGO. The resulting current response for **5** at higher acid concentrations is close to HOPG background in potential and intensity, suggesting desorption or decomposition of the complex. Interestingly, complex **6** exhibits catalytic behavior consistent with complexes **1-4**, which conflicts with the inactivity observed for the complex on FTO/RGO electrodes.

For complexes **2-4** and **6**, activity saturation is not observed even at and below pH values of 1.5, whereas **1** reaches an activity plateau at approximately 8 mM TFA (pH 2.1). Catalytic rate estimates from cyclic voltammetry data were determined using the ratio of peak

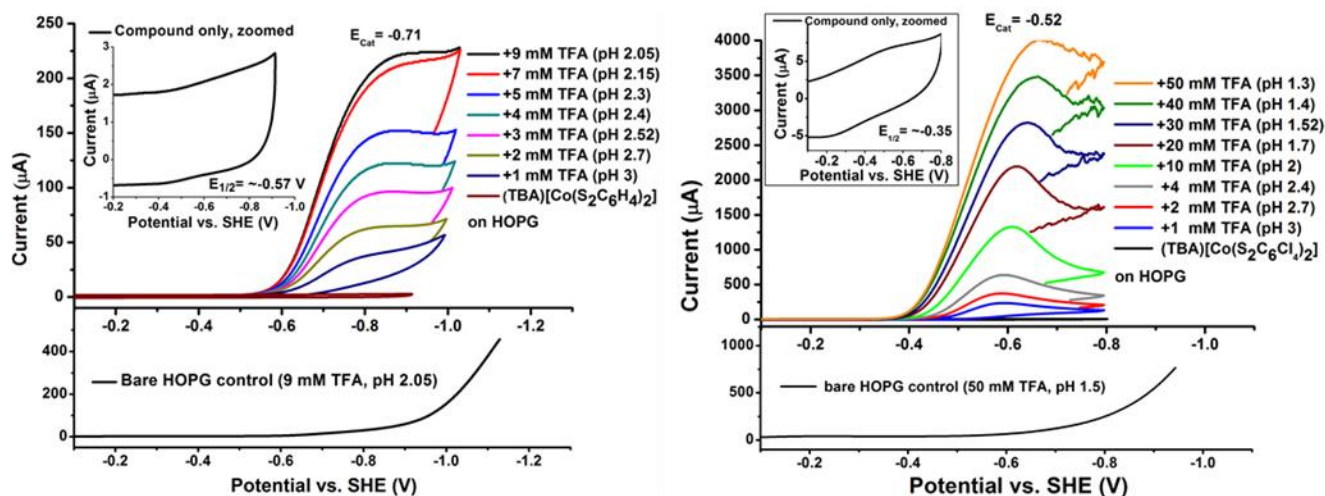


Figure 3.25 Cyclic voltammetry of **1** (left) and **3** (right) adsorbed on a HOPG working electrode in an aqueous 0.1 M KPF_6 solution with the addition of trifluoroacetic acid at a scan rate of 50 mV/s. The current response of the bare HOPG electrode in TFA solution is displayed in the lower plots, and the inset provides a zoomed view of the catalyst-adsorbed electrode in the absence of acid. Platinum counter and Ag/AgCl reference electrodes were used, and potentials are reported vs. the standard hydrogen electrode.

cathodic current in the presence and absence of acid (i_{cat}/i_p) in **equation 1**, with the i_{cat} value at pH 1.5 used as a lower limit for activity for **2-4** and **6**.

$$(1) \frac{i_{cat}}{i_p} = \frac{2}{0.446} \sqrt{\frac{RTk_{obs}}{Fv}}$$

This method provides a range of TOF estimates from $1,006 \text{ s}^{-1}$ for **1** to a mighty $17,377 \text{ s}^{-1}$ for **3** (see **Table 3.1**), demonstrating that a vast difference in activity is achievable by slight changes in ligand substitution (**Figure 3.25**). Based on these estimates, the most active complexes for surface attachment are those with maximum halide substitution on in the ligand system.

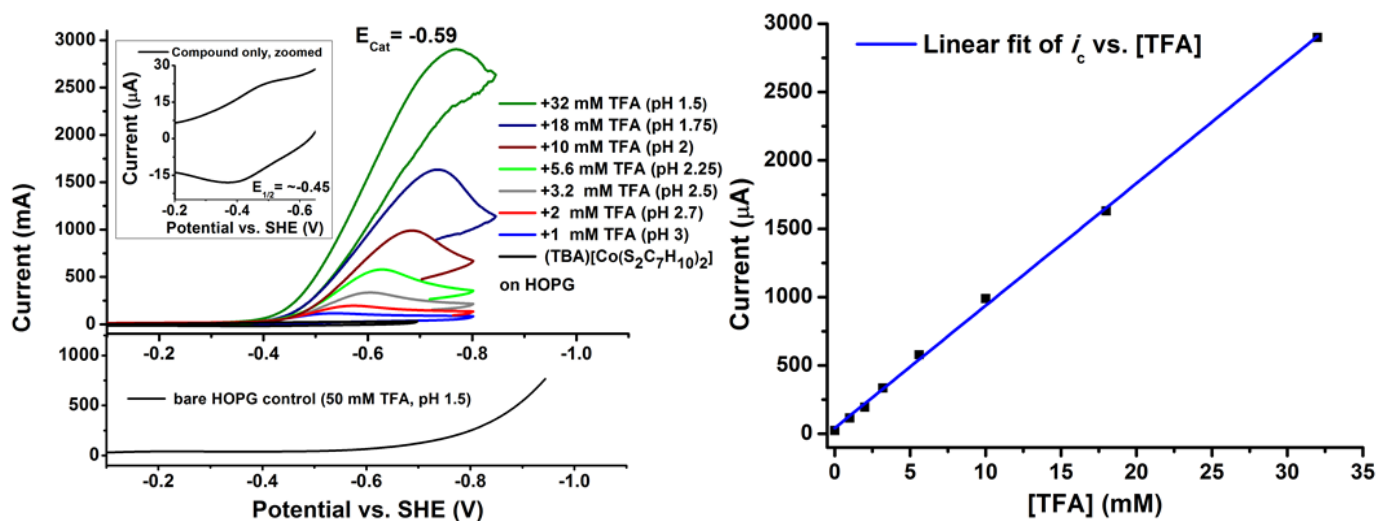


Figure 3.26. *Left:* Cyclic voltammetry of (TBA)[Co(S₂C₁₀H₆)₂] (**6**) adsorbed on a HOPG working electrode with addition of TFA at a scan rate of 50 mV/s. The control surface (using the same electrode before catalyst soaking) under the same conditions is displayed on the bottom of the graph, and the inset provides a zoomed view of the CV of the Co catalyst functionalized surface in the absence of acid. The solution contained 0.1 M aqueous potassium hexafluorophosphate. The counter electrode was a platinum disc, and the reference was an Ag/AgCl (saturated KCl solution) electrode. Potentials are reported vs. the standard hydrogen electrode. *Right:* Linear fit of the peak catalytic current versus increasing TFA concentrations, indicating an acid-diffusion controlled process under these conditions.

However, while the number of halide groups shows a clear increase in TOF from **1** to **2** and **3** with TOF estimates of 986, 3,016, and 17,377 s⁻¹, respectively, an increased electron withdrawing nature of the halide substituent does not increase activity as seen for comparison of **3** (17,377 s⁻¹) and **4** (2,848 s⁻¹). The size of the ligand ring system was also seen to effect an increase in TOF from 986 s⁻¹ for **1** to 1530 s⁻¹ for **6**, however this increase is comparatively small, and thus the overall increase in current density observed in cyclic voltammetry experiments (see **Figures 3.25**, left vs. **3.26**, left) is largely due to the drastic increase in catalyst loading from **1** to **6**. Alternative second order rate estimates of 3.23 * 10⁸ M⁻¹ s⁻¹ for **3** and 1.22 * 10¹⁰ M⁻¹ s⁻¹ for **6** were afforded by use of the foot of the wave analysis method (see experimental section).⁶⁸ While substantially higher than the estimates provided by **equation 1**, these rate constants compare fairly well with previous estimates provided for **2** on FTO/RGO and HOPG electrodes.⁶⁹ A comparison of the active catalyst derivatives on the same HOPG electrode under the same conditions (pH 2.4 TFA solution) is shown in **Figure 3.27**.

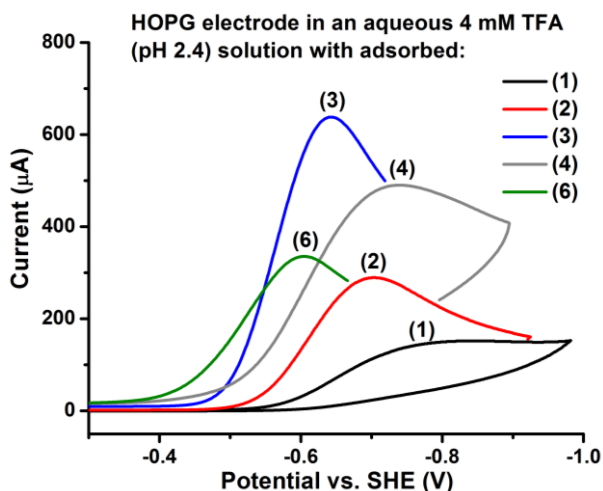


Figure 3.27. Cyclic voltammograms of active cobalt bis(dithiolene) catalyst derivatives adsorbed on the same HOPG working electrode in an aqueous 0.1 M KPF₆ solution with 4 mM TFA (pH 2.4).

E_{cat} values at pH 1.5 (or 2.1 in the case of **1**) range from -0.52 to -0.71, with the most negative and positive potential values obtained for compounds **1** and **3**, respectively. The overpotential range calculated for the series on HOPG was 0.36 to 0.6 V vs. platinum, with generally good agreement (within 50 mV) with the overpotential values on FTO/RGO (**Table 3.1**). The compounds exhibiting the lowest overpotentials were those with a high level of halide substitution as in the case of **3** ($\eta = 0.44$ V) and especially those with a larger ligand ring system as in the case of **6** ($\eta = 0.36$ V). On average, E_{cat} values are approximately 0.15 V more negative than their corresponding $E_{1/2}$ value. As in the case of the FTO/RGO electrodes, onset potentials occurred after the $E_{1/2}$, indicating reduction proceeds prior to protonation in the initial mechanism.

In summary, trends in E_{cat} are consistent across the complex series for both FTO/RGO and HOPG surfaces. Most significantly, a decreasing overpotential is observed with increasing halide substitution on the ligand ring. A shift from an E_{cat} value of -0.65 V to -0.61 and -0.59 is observed from **1** to **2** and then **3** respectively on FTO/RGO electrodes, corresponding to 0, 2 and 4 chloro-substitutions on each ligand. Similarly, on HOPG, a shift from -0.71 to -0.61 and then -0.59 is observed from **1-3**. Neither surface shows a significant difference in E_{cat} between the tetrachloro- and tetrafluoro- substituted ligand systems (**3** and **4** respectively), with a 20 mV lower overpotential for **4** on FTO/RGO, and the exact opposite observed on HOPG. Extension of the ligand ring system from benzene to naphthalene induced a shift in E_{cat} from -0.71 to -0.59 V, which is notably similar to the shift observed with halide substitution on the ring from **1** to **3** or **4**.

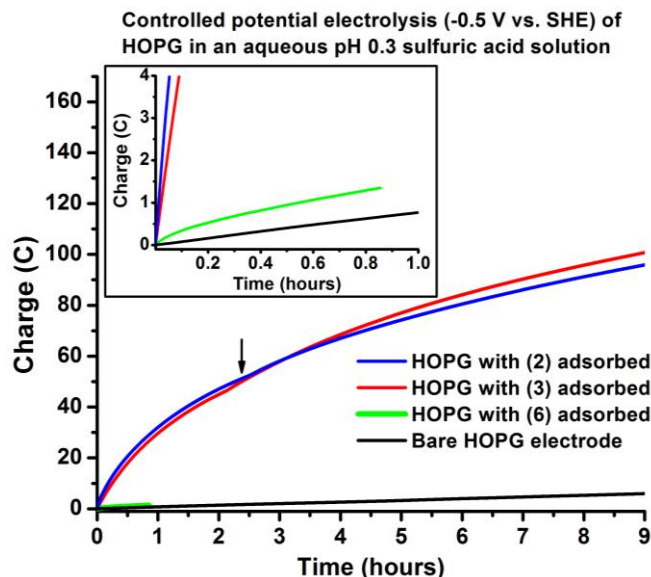


Figure 3.28. Controlled Potential Electrolysis at -0.5 V vs. SHE of several cobalt bis(dithiolene) catalyst derivatives adsorbed to the same HOPG electrode in an aqueous 0.1 M KPF_6 solution with 0.5 M H_2SO_4 (pH 0.3). A two-compartment cell is used with platinum counter and Ag/AgCl reference electrodes. The arrow indicates when the pH was adjusted back to 0.3. The inset provides a zoomed view to observe the limited stability of **6**.

Long-Term Bulk Electrolysis

Controlled potential electrolysis (CPE) studies were performed on a HOPG electrode after adsorbing the catalyst in the same manner used for cyclic voltammetry studies. For this purpose, the most active compounds from the CV studies described above were selected. These correspond to complexes **2**, **3** and **6**, representing the highest activity and highest catalyst loading on the graphitic surfaces (**Figure 3.28**). Under an applied potential of -0.5 V in a 0.5 M (pH 0.3) sulfuric acid solution, complex **3** drew an initial current density of approximately 65 mA/cm^2 , where the background is notably only 1 mA/cm^2 . Current density diminishes over the course of many hours, reaching a plateau current of approximately 7 mA/cm^2 (~11% original) after approximately 8 hours. This current density is maintained for the duration of the experiment spanning over 14 hours, never returning to the background current level observed for bare HOPG (**Figure 3.29**). In addition, in-situ cyclic voltammetry of the electrode directly

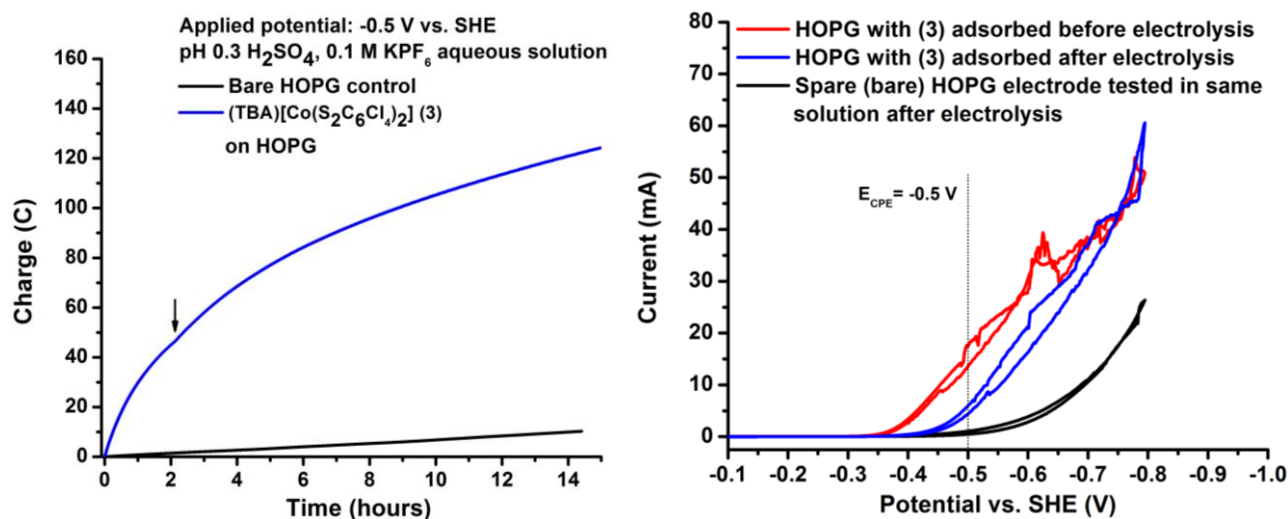


Figure 3.29. Left: Controlled Potential Electrolysis at -0.5 V vs. SHE of (TBA)[Co(S₂C₆Cl₄)₂] (**3**) adsorbed to a HOPG electrode in an aqueous 0.1 M KPF₆ solution with 0.5 M H₂SO₄ (pH 0.3). A two-compartment cell is used with platinum counter and Ag/AgCl reference electrodes. The arrow indicates when the pH was adjusted back to 0.3. Right: Cyclic voltammograms of the electrolysis setup in situ before (red trace) and after (blue trace) the CPE experiment. A separate bare HOPG working electrode was tested in the solution after electrolysis (black trace) to confirm residual catalytic current was present after electrolysis. The abnormal shapes of the cathodic waves are both due to the diffusion conditions (stirring) in the cell and due to the hydrogen bubbles generated at the working electrode.

after electrolysis, while showing substantially less current than before electrolysis, still exhibits notably more current drawn than a bare HOPG electrode (**Figure 3.29**).

Over the first 8 hours of turnover for **3**, a total of 96 C is passed by the catalyst-adsorbed HOPG electrode, while the same electrode without catalyst only passes 5 C in this time. To provide a TON for comparison, the initial active species is considered inactive after the plateau current is reached (~8 hours). This corresponds to 9.95×10^{-4} moles of electrons passed and approximately 5×10^{-4} moles of hydrogen formed based on a quantitative Faradaic efficiency previously reported for the HOPG/cobalt bis(dithiolene) systems.⁶⁹ From this value and an HOPG catalyst concentration of 7.14×10^{-11} moles determined by CV quantification for **3**, we can calculate a TON of 7×10^6 over the 8-hour period, as well as an average TOF of 243 s^{-1} . In contrast, the initial rate of the system is significantly higher, producing 18 C (9.3×10^{-5} moles H₂) over the first 30 minutes to give a rate of 723 s^{-1} .

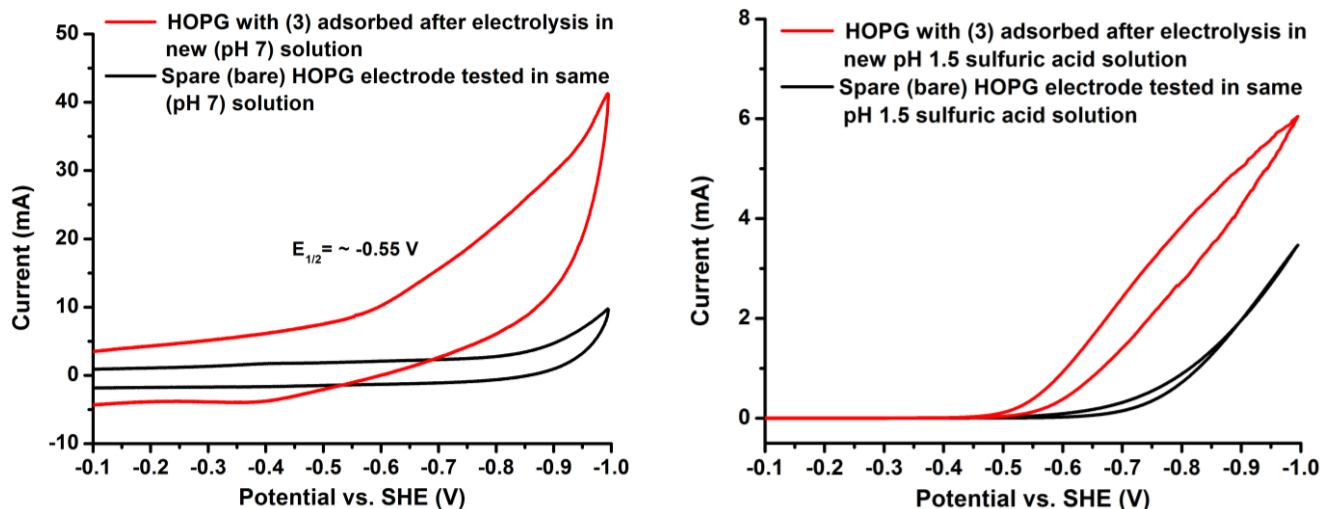


Figure 3.30. *Left:* Cyclic voltammogram of (TBA)[Co(S₂C₆Cl₄)₂] (**3**) adsorbed to a HOPG electrode (red trace) after CPE experiment in a new (pH 7) aqueous 0.1 M KPF₆ solution. A separate (bare) HOPG electrode tested in the same solution (black trace) is provided for comparison. *Right:* Cyclic voltammogram of (TBA)[Co(S₂C₆Cl₄)₂] (**3**) adsorbed to a HOPG electrode (red trace) after CPE experiment in a new solution with sulfuric acid added to pH 1.5, showing residual catalytic activity in the new solution. A separate (bare) HOPG electrode tested in the same solution (black trace) is provided for comparison.

Further analysis of the HOPG/**3** system after CPE was conducted to assure the residual activity was not related to an uncontrolled cell variable or inaccuracy in pH measurement. A separate HOPG electrode (never exposed to catalyst) was tested in the same solution and confirmed a definite difference in activity (**Figure 3.29**) by CV. Further analysis of the HOPG/**3** system after electrolysis in a fresh, pH neutral electrolyte solution shows a residual redox signal, albeit at a more negative potential ($E_{1/2} = -0.55$ vs. -0.35 V initially) and with a much larger peak separation, indicative of a new species or altered electronic environment of the remaining surface-bound catalyst. Upon addition of sulfuric acid to a pH of 1.5, comparison of the HOPG/**3** system with the control HOPG electrode by cyclic voltammetry again showed substantially higher current levels, with an onset potential of approximately -0.45 V for the catalytic wave. These results shown in **Figure 3.30** confirm an active species remains after

electrolysis, although exhibiting nearly ten times lower current densities with the previously applied potential.

Complex **2** was observed to have very similar behavior to **3** under CPE conditions, with an initial current density of approximately 65 mA/cm². Current density is again seen to diminish over the course of many hours, reaching a plateau current of approximately 6 mA/cm² (~9% original) after approximately 8 hours. Over this time 91 coulombs of charge is passed, corresponding to 9.43×10^{-4} moles of electrons passed and 4.7×10^{-4} moles of hydrogen formed. From these data and an HOPG catalyst concentration of 3.7×10^{-11} moles for **3**, a TON of 1.27×10^7 can be calculated for the 8 hour period, with an average TOF of 441 s⁻¹.

Analysis of complex **6** under electrolysis conditions shows an initial current density of 15 mA/cm². Unlike in the case of complex **3**, current density decreases exponentially over the course of the first 10 minutes, reaching a plateau current consistent with background HOPG within less than an hour of electrolysis, indicating complete loss of catalyst activity via desorption or catalyst degradation, in agreement with the CV results. After the plateau current was reached at $t \approx 30$ minutes, a total of 0.95 C had passed, corresponding to 4.92×10^{-6} moles of hydrogen produced and a TON of 2.5×10^4 based on a catalyst loading of 1.97×10^{-10} moles. An average TOF of 13.8 s⁻¹ is determined for the 30 minutes, although it is important to note the relatively low rate combined with the short lifetime of the catalyst produced a significantly smaller amount of current compared to **3**, so both TON and TOF estimates are convoluted due to comparatively higher background current. Post-electrolysis analysis, performed analogously to complex **3**, showed no substantial redox signal above background in fresh pH-neutral electrolyte solution, indicating no trace of **6** or a redox-active decomposition product present on the surface after electrolysis.

Discussion

To design photoelectrode and fuel cell systems capable of efficiently interconverting feedstock materials into products that are useful as energy carriers or industrial precursors (especially H₂ from water, methanol from CO₂, etc.), it is a key challenge to design electrode surfaces with catalytic properties that can then act as heterogeneous catalysts in large scale flow reactors. This can be accomplished by either developing solid state electrode materials with catalytically active surfaces, or by immobilizing a catalyst on the electrode surface. With respect to the latter, commonly applied strategies in the literature include covalent attachment of molecular catalysts, or development of polymeric or solid state catalysts that are deposited on an electrode (for example, by spin coating).^{36,39-41,52,53} Here, we describe a new approach where catalyst binding is only based on electrostatic interactions using a thin coating of RGO as the interface between the catalyst and a metal oxide electrode. This strategy provides substantial merits over other approaches in terms of simplicity and flexibility in application, as RGO can be electrodeposited on almost any conductive material, and alternatively, can be produced by chemical reduction of graphene oxide (GO) and then deposited on other substrates if necessary. Further, the variety of molecular catalysts that can be incorporated using this method is essentially unlimited, as catalysts that do not contain an aromatic ring system in their ligand periphery (as in the case of the Co-bis(dithiolene) complexes studied here) can be modified by attachment of an aromatic “foot” as described in the literature.^{38,73-75} The combination of versatility in substrate selection and the ability to easily tune molecular catalysts provides an opportunity to design nearly limitless systems in terms of activity and overpotential. This manuscript provides an example of such a system in which catalysts were

easily prepared and functionalized to afford chemically tuned, highly active yet inexpensive, oxygen stable heterogeneous catalyst systems functional in acidic aqueous media for proton reduction. In this way, this work highlights the advantage of using immobilized, molecular catalysts for heterogeneous H₂ production systems over solid state approaches, since the overpotential, catalyst loading and activity can all be directly controlled by simple ligand modifications in molecular systems. This is in contrast to solid state catalysts, where catalytic sites often correspond to defect sites on the surface that are hard to identify, characterize, and systematically improve.

Characterization of the catalyst-adsorbed FTO/RGO surfaces by XPS confirms the presence of a cobalt species with two distinct resonance states, which is a hallmark of the cobalt bis(dithiolene) complexes.^{51,60} In addition, XPS confirms the presence of thiol and chloride components. The Co and S 2p spectra are also consistent with the S 2p signal observed for the polymer systems.^{52,53} Importantly, the new signals observed for **3** and **6** in the S 2p core spectra and for **3** in the Cl 2p core spectra at binding energies of ~163 and ~201 eV respectively, correlate well with other thiophenyl and chlorophenyl-containing compounds in the literature.^{70,72} These results support the hypothesis that the species adsorbed to the surface are not cobalt nanoparticles or solid state materials such as cobalt sulfide, but rather molecular species that contain an organic phenyl moiety. As these results are consistent with reports of polymeric Co(S₂R) systems, it is very likely that they maintain their molecular structure on the surface. Further, the catalytic activity profiles observed (see below) match closely to those of the homogeneous and heterogeneous (polymeric) catalyst systems, supporting an electrostatically adsorbed molecular species.^{18,52,53}

Cyclic voltammetry of the cobalt bis(benzenedithiolene) complexes on FTO/RGO and HOPG electrodes give very interesting responses, particularly in comparison to the $\text{Co}^{\text{III/II}}$ couple observed for the corresponding complexes in solution. The consistently more negative $E_{1/2}$ values observed for **1-6** on the HOPG electrode vs. the FTO/RGO electrode suggest that the electronic interaction of the species with the surface is different for the two materials, which is reasonable considering the relative topography and surface moieties present for edge-plane graphite and reduced graphene oxide. More specifically, intensive electron microscopy studies reveal a regular sp^2 -hybridized honeycomb lattice, albeit with notable corrugations and site asymmetry for HOPG, whereas investigation of RGO has revealed not only the presence of many CO_x moieties and substantially less sp^2 -hybridized bonding character (~70% area), but also significantly more disorder and the presence of substantially more holes (~5% area).⁷⁶⁻⁷⁹ It is also important to note that this comparison is complicated by the trace background signal observed in the FTO/RGO system in the 0 to -0.2 V region (See experimental section), which, when coupled with the low signals from adsorbed catalysts, decreases the accuracy at which exact $E_{1/2}$ values can be determined. In addition, as previously reported for **2**, variances in peak separation and broadness of current signals are commonly observed for $E_{1/2}$ values of FTO/RGO/catalyst systems, and can likely be attributed to the fact that each FTO/RGO-deposited surface varies substantially in topography and in surface CO_x speciation.^{78,79} It is therefore advantageous to use the more homogeneous HOPG electrodes to quantitatively compare catalysts **1-6**. However, in terms of future applications, the FTO/RGO system provides a design blueprint along with catalyst activity profiles of how other types of semiconductors could be surface-functionalized using an RGO interface.

Comparison of catalyst loading on the same HOPG electrode for the various cobalt bis(dithiolene) complexes provides an effective internal standard to determine the effect of ligand substitution on surface adsorption and catalyst activity. A substantial increase in catalyst loading is observed with the addition of two halide substituents to the benzenedithiolate rings. In fact, whereas an unmeasurably low amount of catalyst (within CV background) is present on the graphitic surfaces for **1**, **2** shows a much larger CV signal. Further increasing halide substitution results in still higher loadings, with approximately twice the loading observed for **3** compared to **2**. A change in the halide substituent also affects loading, as the tetrafluoro-substituted benzenedithiolate ring in **4** leads to more than twice the catalyst concentration on the surface compared to the analogous tetrachloro-substituted derivative **3**. Comparison of the naphthalene ligand system with the benzene derivative shows the largest increase in loading across the different ligand systems, effecting a change from the lowest observed loading to the highest in the series. Overall, the loading for **6** is several times higher than that of **3** and still slightly higher than that of **4**, suggesting the effect of the larger ring in adsorption outweighs that of the halides for this ligand system. Notably, these estimates are comparable to those reported by Dey and coworkers ($\sim 10^{-10}$ moles/cm²) for adsorption of hydrogenase model catalyst systems on nearly identical EPG electrodes.

The electrocatalytic responses of complexes **1-4** adsorbed on FTO/RGO are generally impressive in magnitude, given that the electrodes were constructed to be approximately 1 cm² and most of the active complexes display nearly 1 mA at only mildly acidic pH values of 2.7. This activity level demonstrates the potential which RGO-deposited electrodes systems have for use in a variety of applications interfacing catalysts with substrates given the appropriate catalyst design. The current responses of the catalyst-adsorbed electrodes are generally very

similar in shape, and linear behavior with increasing acid concentration is observed. With the exception of complexes **5** and **6**, none of the catalysts were observed to have activity saturation behavior at the maximum acid concentration of 2 mM TFA (pH 2.7) on FTO/RGO, indicating the rate of catalytic hydrogen production under these conditions is only limited by diffusion of substrate to the catalyst (total catalysis). E_{cat} values are typically at least 0.25 V more negative than the $E_{1/2}$ values, and as much as 0.36 V more negative in the case of **3**. The onset of the current wave under low acid concentrations also occurs over 0.05 V more negative than the $E_{1/2}$, suggesting that reduction precedes protonation in the initial mechanism for these RGO-supported catalyst systems.

The unique catalytic response observed for **5** and **6** on FTO/RGO electrodes is interesting considering the general stability of adsorbed cobalt bis(dithiolene) complexes seen in these and previously reported results. All complexes were tested repeatedly to assure relative consistency across FTO/RGO surfaces, indicating this result is independent of exact RGO topography and likely inherent to specific electronic or steric characteristics of the catalyst species. Considering the complexes were adsorbed to the FTO/RGO surface (as evidenced by cyclic voltammetry in the absence of acid) and remained adsorbed until the addition of higher acid equivalents (as evidenced by the initial current increase), the most likely explanation for this finding is desorption or decomposition of these complexes (in the surface-bound state) in the presence of acid.

Analysis of complexes **1-6** adsorbed on HOPG allows for observation of the catalysts under low pH conditions, revealing a truly impressive activity level for hydrogen production. The catalyst-adsorbed electrodes typically reach current densities of 10 mA/cm² at pH 1.5 with potentials lower than -0.5 V vs. RHE, and **2** and **3** can attain current densities higher than 60

mA/cm² at pH 0.3 with an applied potential of only -0.48 V vs. RHE. Electrocatalytic behavior of the series is overall very similar to results on the FTO/RGO electrodes, despite the fact that generally more negative $E_{1/2}$ values are observed for HOPG, leading to a slight deviation in E_{cat} values between the two materials. Nonetheless, the key features remain constant, including linear response of current with acid concentration, lack of activity saturation even at higher acid concentrations, and catalytic current onset potentials that typically occur at a more negative potential than the observed $E_{1/2}$. As in the case of the FTO/RGO electrodes, while **5** was seen to adsorb to the electrode, no sustained current increase was seen upon acid addition, indicating instability on the surface under acidic conditions. Interestingly, while **6** behaved similarly to **5** on the FTO/RGO electrodes, it behaved normally (i.e., as in the cases of **1-4**) on the HOPG electrode, suggesting the ring system interacts more favorably with the HOPG under acidic and turnover conditions than with the FTO/RGO surface.

Comparison of catalytic behavior across the ligand series on a HOPG electrode provides insight into the effect of ligand substitution on activity and overpotential. Most apparent is the trend for lower overpotential with higher halide substitution seen across complexes **1**, **2**, and **3**. Surprisingly, while the halide substitution from **1** to **3** effects a decrease of more than 100 mV in overpotential ($\eta = 0.6$ vs. 0.44), the overpotential effect of the tetrafluoro-substituted ligand in **4** compared to the tetrachloro-substitution in **3** is much less substantial, seemingly unbeneficial ($\eta = 0.51$ vs. 0.44). Considering the difference in $E_{1/2}$ value is similarly small, these results suggest the more electron withdrawing fluoride substituents are not actually effecting a more positive reduction potential for the Co^{III} metal center. Overpotential also decreases significantly from **1** to **6** ($\eta = 0.6$ vs. 0.36), likely due to the enhanced electron withdrawing effect of a larger ring system.

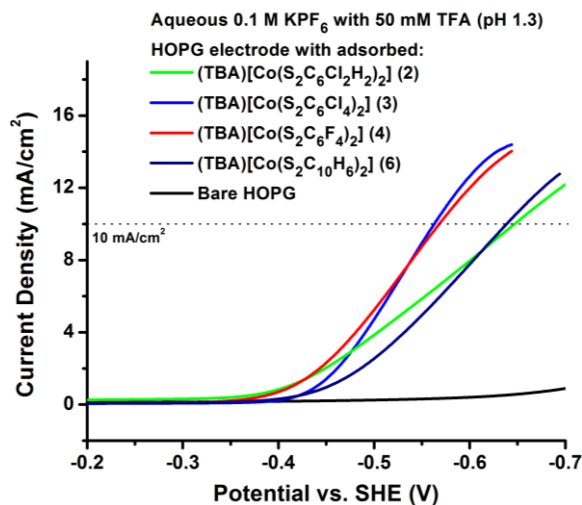


Figure 3.31. Polarization curves of active cobalt bis(dithiolene) catalyst derivatives adsorbed on the same HOPG working electrode in an aqueous 0.1 M KPF_6 solution with 50 mM TFA (pH 1.3). Platinum counter and Ag/AgCl reference electrodes are used, and potentials are reported vs. the standard hydrogen electrode.

Trends in activity are seen to follow a similar patterns, with an impressive increase in estimated TOF (**equation 1**) from **1** to **3** of over $16,000 \text{ s}^{-1}$ as an apparent effect of increasing halide substitution on the ligand. Rates are only minimally affected by increased ring system size by this estimate; however, with an increase of $\sim 500 \text{ s}^{-1}$ from **1** to **6**, suggesting the comparable current densities for **2** and **6** at pH 1.3 (**Figure 3.31**) are mostly due to the impressive increase in catalyst loading for **6** mentioned previously. It is interesting to note that, despite the lower overpotential observed for **6** compared to **3** and **4** (0.36 vs. 0.44 and 0.51, respectively), **3** and **4** are able to attain a current density of 10 mA/cm^2 at a lower overpotential (-0.48 vs. RHE for **3** and **4** compared to -0.56 vs. RHE for **6**) due to their higher catalytic activity. These data demonstrate that the superior activity provided by halide substitution in our Co catalysts trumps the improved loading and overpotential obtained with larger ligand ring systems. Based on all of these considerations, catalyst 3 is clearly the overall champion

in terms of TOF, overpotential under application conditions, and stability on graphitic surfaces.

In a **Section 3.1**, complex **2** adsorbed on HOPG was observed under controlled potential electrolysis conditions with an applied potential of -0.95 V vs. SCE (-0.7 V vs SHE) in 40 mM TFA aqueous solution, and the catalyst was found to have high activity and a quantitative faradaic efficiency.⁶⁹ While the exact catalytic lifetime was not determined, the data suggested residual catalyst activity after 12 hours of electrolysis. In order to further reduce the amount of background current drawn (by the blank HOPG electrode) in the bulk electrolysis experiments, we decided to use a more positive applied potential of -0.5 V vs. SHE (-0.48 V vs. RHE) and a lower pH of 0.3 for the long-term bulk electrolysis experiments performed here, with the addition of real-time monitoring of electrolysis solution pH. In addition, sulfuric acid was substituted for TFA in these electrolysis studies to provide more comparable conditions to similar catalytic systems reported in the literature.^{15,52,53}

Controlled potential electrolysis of complex **3** under these conditions shows impressive initial current density of 65 mA/cm²; however, a gradual decrease in activity is observed over the course of 8 hours. Importantly, the TOF values observed during long-term electrolysis are much lower than the CV estimates determined by **equation 1**. This suggests that either the CV quantification method overestimates catalyst loading on HOPG, or, more likely, this estimation method is not accurate for real application conditions. It is therefore particularly important that new proton reduction catalysts are tested under bulk electrolysis conditions to obtain a realistic measure of their true electrocatalytic activity.

The disparity in lifetime observed between **3** and **6** is substantial, with complete loss of activity for **6** in less than an hour, while current density slowly decreases for **3** over

approximately 8 hours. On the other hand, **6** shows a much larger amount of surface adsorption compared to the halide-substituted catalyst derivatives. *These results indicate an inherent difference in ligand properties that promote initial adsorption vs those that promote catalyst retention under turnover conditions.* This suggests that larger aromatic systems, such as those in **6**, are beneficial for adsorption onto graphitic surfaces, while the more electron-poor ring systems such as that used for **3** are less prone to desorption under turnover conditions.

Sustained activity above background current for **2** and **3** after the initial 8 hours suggests that either a small percentage of the catalyst remains active indefinitely, or that a stable species is formed under turnover conditions after the first 6-8 hours. Given the wealth of literature regarding cobalt sulfide and cobalt nanoparticles active for dihydrogen production, it is probably that an active species analogous to these reported catalysts is created upon decomposition of the Co complexes. However, it is interesting that in the case of **6**, CPE experiments show nearly immediate loss of activity, and residual activity above baseline (bare HOPG) current is not observed. With the overall similarity in elemental components (particularly cobalt and sulfur) between **6** and complexes **2** and **3**, observed to have residual catalytic behavior, formation of the aforementioned catalytic species upon decomposition is not consistent with our results and seems unlikely. Rather, our results seem to suggest long-term modification of the graphitic supports with the more rugged halide-substituted catalyst derivatives.

The rates observed here for **3** are comparable to those reported for the surface-immobilized diiron hydrogenase models by Dey and coworkers (adsorbed on similar EPG electrodes and tested under identical conditions). Dey's system is reported to have an overpotential of 0.18 V vs. the thermodynamic limit of proton reduction for a pH 3 H₂SO₄

solution. Under identical CPE conditions, the catalyst-adsorbed EPG discs produced $\sim 5.5 \cdot 10^{-4}$ moles hydrogen (vs. $\sim 5 \times 10^{-4}$ moles obtained here for **3**) in the same timeframe with nearly identical catalyst loading ($\sim 10^{-10}$ mol/cm²). This ranks our heterogeneous catalyst systems among those with the highest molecular TOFs reported so far in the literature.^{15,27,80,81}

The ability of halide substituents to effect increased stability in our system (i.e. **6** vs. **2** and **3**) also draws comparison to the systems reported by Dey and coworkers, as their catalysts contain a single phenyl ring with a *p*-substituted bromide for adsorption to HOPG. If the adsorption of these systems is assumed to be predominantly through the ring moiety as proposed, then this implies that long term stability of catalyst surface attachment to EPG does not require a large ring system, but may benefit from halide substitution as observed here. In addition, as seen by comparison of **2** and **3** under turnover conditions, the effect of the extra halide groups in **3** does not provide a significant difference in either initial rate or the lifetime of the catalyst (TON of 1.27×10^7 for **2** vs. 7×10^6 for **3**). These data shows that while the extra halide substitutions in the ligand system of **3** provide a lower overpotential at higher pH values and higher rates are estimate by CV analysis, under turnover conditions at low pH the catalysts behave very similarly.

In addition to closely matching the XPS spectra, the graphite-adsorbed cobalt bis(benzenedithiolene) systems prepared here show very similar electrocatalytic characteristics compared to the polymeric forms of these molecules reported by Marinescu and coworkers.^{52,53} Onset potentials of approximately -0.33 V and -0.4 V for **3** and **6** on HOPG at pH 1.3 are also similar to those seen for the two-dimensional (-0.28) and one-dimensional (~ -0.45 V) polymer materials. A current density of 10 mA/cm² is reached by **3** at a potential of -0.56 V vs. SHE (-0.48 V vs. RHE) at pH 1.3 (**Figure 3.29**), compared to -0.34 V vs. RHE reported for the two

dimensional MOS1 on glassy carbon and -0.56 V vs. RHE reported for the one-dimensional polymer on glassy carbon. The current density of **3** is particularly impressive given the catalyst loading is approximately 3 orders of magnitude lower than that reported in the case of the polymer system, while still reaching the 10 mA/cm² threshold at similar potentials. This implies that the molecular catalyst **3** is either ~3 orders of magnitude more active than the polymeric catalysts, or that the polymeric materials stack on the surface, but only the top layer(s) is/are active for proton.

Nickel bis(diphosphine) dihydrogen production catalysts with pendant amines covalently bound to indium tin oxide-supported multi-walled carbon nanotubes (ITO/MWCNT) reported by Le Goff and coworkers are seen to have very similar catalyst loadings to **6** (~1.5 x 10⁻⁹ vs. 1.3 x 10⁻⁹ mol/cm²). The covalently bound catalysts require a relatively lower overpotential of only 200 mV for activation in non-aqueous media, and an exceptionally low overpotential of 20 mV in aqueous media. CPE of the catalyst-bound (ITO/MWCNT) systems in an aqueous pH 0.3 solution at a potential of -0.3 V vs. NHE showed impressive stability with no decrease in current density over a ten hour period and quantitative Faradaic efficiency. However, the TOF determined in these experiments was relatively low compared to similar catalysts in solutions with a rate of ~2.8 s⁻¹ for the entire electrode (100,000 turnovers in 10 hours). This is in line with the lower i_{cat}/i_p value observed for the system vs. the catalyst in solution (5 vs. 50) and a current density of only 4 mA/cm² observed at -0.4 V vs. NHE.³⁹ A similar system reported by Tran and coworkers features nearly identical nickel bis(diphosphine) dihydrogen production catalysts non-covalently bound to multi-walled carbon nanotubes supported on commercial gas diffusion layers (MWCNT/GDL) via a ligand-appended pyrene moiety. A substantially higher loading of up to 1.1 x 10⁻⁸ mol/cm² can be

attained by adjusting MWCNT loading, highlighting the benefit of the increased surface area for MWCNT on catalyst adsorption. Overpotentials for these catalyst systems were reported to be incredibly low with onset potentials essentially at the equilibrium potential for hydrogen production, and CPE in an aqueous pH 0.3 solution at -0.3 V vs. NHE showed negligible decrease in current density over 6 hours, with an average TOF of 8.2 s^{-1} (8.5×10^4 turnovers in 6 hours with $\sim 2 \times 10^{-9} \text{ mol}_{\text{cat}}/\text{cm}^2$). The MWCNT/GDL materials could also attain current densities of over $15 \text{ mA}/\text{cm}^2$ at maximum catalyst loading with potentials of only -0.3 V vs. NHE.³⁸

Comparison of the covalently and non-covalently bound nickel bis(diphosphine) catalyst systems with each other and the results reported here gives insight into the limitations of each attachment method. Non-covalent attachment appears to provide substantially higher catalytic rates considering both the TOF values reported here and the much higher TOF values seen for the non-covalently bound nickel bis(diphosphine) vs. the covalently attached system. Further, for some catalyst systems it appears non-covalent interfaces can provide much higher catalyst loadings with the use of high surface area materials such as MWCNT, which may be advantageous if applied to cobalt bis(dithiolene) systems. The similar overpotentials seen for the systems reported here and polymeric $\text{Co}(\text{S}_2\text{R})$ materials in addition to the exceptionally low overpotentials maintained for both the covalently and non-covalently bound nickel bis(diphosphine) systems seems to suggest that the attachment method does not as significantly affect the overpotential as much as the TOF under these conditions, and thus overpotential tuning may be more successful via catalyst selection and functionalization. Finally, as supported by the impressive stability of both Dey's and Tran's non-covalently modified catalyst systems over many hours, this interface method has the potential to provide relatively

long-term stability in application, although as seen by the somewhat limited stability of our system and those reported by Gray and coworkers this varies on a catalyst to catalyst basis.^{15,38,39,73}

In summary, a series of cobalt bis(dithiolene) derivatives has been prepared and adsorbed on graphitic surfaces to create heterogeneous electrocatalysts for efficient proton reduction. These systems exhibit incredible catalytic performance for hydrogen production in mildly acidic aqueous solutions. These catalysts are simple and inexpensive to prepare, and can be easily adsorbed onto graphitic surfaces using a small amount of catalyst material in as little as 12 hours. Catalyst loading increases as more electron withdrawing substituents are added to the ligand, though an even stronger effect is seen as the size of the ring system increases. Overpotential decreases with increasing halide substitution of the benzenedithiolate ligand, although differences observed between Cl- and F- substituents were minimal. The inductive effect of the extended ring system is also seen to decrease overpotential to a similar extent as the halide substituents. Activity trends are evident across the ligand series as turnover frequencies are over fourfold higher with halide substituted derivatives compared to the unsubstituted compound **1**. Under turnover conditions, halide-substituted derivatives slowly decrease in activity over the course of ~8 hours, while naphthalene derivatives rapidly deactivate within an hour, despite higher initial catalyst loading. Determination of the fate of these catalyst systems upon deactivation is of great interest to design more stable systems, and thus is under current active investigation.

With the insight obtained from electrocatalytic analysis of our Co complexes on HOPG, use of the most effective ligand systems with a variety of metals is now of great interest for further study. Heterogeneous catalyst screening for a number of metal bis(benzenedithiolene)

complexes using this method is currently underway. In addition, assessment of catalytic activity on FTO/RGO surfaces has shown comparable activity profiles to HOPG in cyclic voltammetry experiments. Given the ease with which RGO can be applied to a variety of materials, e.g. semiconductors, this graphitic support in particular is an exciting prospect for use as an inexpensive, versatile interface for catalyst attachment in photocathode systems. Design of such systems for hydrogen production is currently underway.

Experimental

General methods

Chemicals were of highest purity grade commercially available and used without further purification (unless mentioned). Methanol (anhydrous, ACS grade) was purchased from Fisher and distilled over calcium hydride, then degassed via extended nitrogen purges prior to use. Acetonitrile (ACS grade), sodium methoxide, trifluoroacetic acid, sulfuric acid, potassium ferricyanide, and potassium ferrocyanide were purchased from Fisher. 1,2-benzenedithiol, toluene-3,4-dithiol, and 3,6-dichloro-1,2-benzenedithiol were purchased from Sigma and used without further purification. Graphite powder was purchased from MTI Corp. All procedures were performed under a nitrogen atmosphere unless otherwise specified.

Preparation of Dithiol Ligand Derivatives

Tetrahalide dithiol ligands were prepared using a slightly modified method from that reported by Gray and coworkers.⁵⁰ Naphthalene dithiol was prepared by first following procedures reported by Hart et al. to give *o*-dibromonaphthalene, followed by alkyl thiol formation and alkyl cleavage as outlined by Montanucci and coworkers.^{82,83}

3,4,5,6-tetrachlorobenzenedithiolate

A mixture of hexachlorobenzene (1 g, 3.5 mmol), sodium hydrosulfide (0.75 g, 13 mmol), sulfur (0.08 g, 2.5 mmol), and iron powder (0.18 g, 3.2 mmol) was heated in 50 mL N,N-dimethylformamide at 140°C for 8 hours. After cooling, 100 mL distilled water was added, and the mixture was allowed to briefly stir at room temperature, during which time a black precipitate formed. The precipitate was filtered and washed with water, then dried en vacuo. The dried solid was added to a suspension of zinc oxide in a 1:1 methanol:1 M aqueous sodium hydroxide solution, which was refluxed for 1 hour. After cooling, the mixture was filtered and the yellow filtrate was acidified with a 1 M HCl solution to precipitate the dithiol product. The solid was dried and recrystallized from benzene to afford 3,4,5,6-tetrachlorobenzenedithiol 0.44 g (45%) as pale yellow powder. ¹H-NMR (400 MHz, CD₂Cl₂): δ_H = 4.79 (s, 2H) ppm.

3,4,5,6-tetrafluorobenzenedithiolate

A mixture of 1,2-dibromo-3,4,5,6-tetrafluorobenzene (1 g, 3.2 mmol), sodium hydrosulfide (0.75 g, 13 mmol), sulfur (0.08 g, 2.5 mmol), and iron powder (0.18 g, 3.2 mmol) was heated in 50 mL N,N-dimethylformamide at 120°C for 8 hours. After cooling, 100 mL distilled water was added, and the mixture was allowed to briefly stir at room temperature, during which time a black precipitate formed. The precipitate was filtered and washed with water, then dried en vacuo. The dried solid was added to a suspension of zinc oxide in a 1:1 methanol:1 M aqueous sodium hydroxide solution, which was refluxed for 1 hour. After cooling, the mixture was filtered and the yellow filtrate was acidified with a 1 M HCl solution to precipitate the dithiol product. The solid was dried and recrystallized from benzene to afford 0.12 g (17 %) 3,4,5,6-tetrafluorobenzenedithiol as a pale yellow powder. ¹H-NMR (400 MHz, CD₂Cl₂): δ_H = 4.03 (s, 2H) ppm.

6,7-Dibromo-1,4-dihydronaphthalene-1,4-epoxide

To a stirred solution of 1,2,4,5 tetrabromobenzene (8 g, 20mmol) and furan (10mL) in dry toluene (200 ml) at -23° under argon, n-butyl lithium (22 mmol in 200 ml hexane) was added drop wise over 3 hr. After the mixture slowly warmed to room temperature, methanol (1 ml) was added, and the mixture was washed with water, dried, and the solvent removed (rotovap). The resulting yellow oily solid was triturated with hexane to give an off-white solid. This crude product was chromatographed over silica gel using dichloromethane-hexane (1:1) as eluent to give 0.7 g (74%) of 6,7-Dibromo-1,4-dihydronaphthalene-1,4-epoxide as a white powder. ¹H-NMR (400 MHz, CD₂Cl₂): δ_H = 5.62 (s, 2H), 6.95 (S, 2H), 7.44 (s, 2H) ppm.

1,2-Dibromonaphthalene

A suspension of zinc powder (2 g) in 60 mM of dry THF under a nitrogen atmosphere was cooled to 0°C. Titanium tetrachloride (2 mL) was added dropwise, and the mixture was heated to reflux for 30 minutes. The reaction was then again cooled to 0°C and a solution of 6,7-Dibromo-1,4-dihydronaphthalene-1,4-epoxide (1.0 g, 3.3 mmol) in 20 mL THF was added dropwise. The mixture was refluxed overnight, cooled and poured into 100 ml of cold 10% HCl. The mixture was extracted with dichloromethane and then washed with water, dried with sodium sulfate, and reduced in vacuo to an off-white powder. The crude product was chromatographed over silica gel using dichloromethane-hexane (1:1) as eluent to afford 0.7 g (74%) of 1,2-Dibromonaphthalene as a white powder. ¹H-NMR (400 MHz, CD₂Cl₂): δ_H = 8.15 (s, 2H), 7.75 (m, 2H), 7.5 (m, 2H) ppm.

1,2-Naphthalenedithiolate

A solution of 1,2-dibromoapthalene (1 g, 3.5 mmol) and sodium propanethiolate (1.7 g, 17.5 mmol) in 50 mL of N,N-dimethylacetamide was stirred under a nitrogen atmosphere at 100°C for 12 hours. Sodium metal (0.6 g, 26 mmol) was cut into small pieces and added to the

solution, which was allowed to continue stirring at 100°C for 12 hours. The resulting mixture was poured into 100 mL of 0.1 M HCl solution and subsequently extracted three times with ether. The combined organic layer was washed with water, dried with sodium sulfate, and reduced down in vacuo to give 0.6 g (89%) of 1,2-Naphthalenedithiolate as a yellow solid. ¹H-NMR (400 MHz, CD₂Cl₂): δ_H = 7.9 (s, 2H), 7.42 (m, 2H), 6.64 (m, 2H), 3.95 (s, 2H) ppm.

Preparation of cobalt bis(dithiolene) derivatives

The general procedure for the synthesis of cobalt bis(dithiolene) complexes is based on the procedure reported by Gray and coworkers:⁵⁰

In a N₂ atmosphere glove box, a solution of dithiol ligand (2.05 mmol) and sodium methoxide (0.23 g, 4.10 mmol) was added dropwise to a suspension of cobalt(II) sulfate hexahydrate (1 mmol) in 30 mL of dry methanol, and the resulting solution was stirred for 2 hours. A solution of tetrabutylammonium bromide (1.05 mmol) in 5 mL methanol was added at this time, and the solution was stirred for an additional 2 hours. The solvent volume was reduced by vacuum to <10 mL, giving a precipitate which was filtered, washed with methanol and dried. Recrystallization of the solid from dichloromethane/ether yielded the cobalt bis(dithiolene) complexes as dark blue-black microcrystalline solids.

Tetrabutylammonium Cobalt bis(benzenedithiolate) (1)

Recrystallization of the solid from dichloromethane/ether yielded (TBA)[Co(S₂C₆H₂Cl₂)₂] as a dark blue crystalline solid in 79% yield (0.460 g). ESI MS: m/z 339.9 (expected), 338.9 (found) amu. Spectroscopic data of the product (see **Figure 3.32**) match those available in the literature.⁵⁰

Tetrabutylammonium Co bis(3,6-dichlorobenzenedithiolate) (2)

Recrystallization of the solid from dichloromethane/ether yielded (TBA)[Co(S₂C₆H₂Cl₂)₂] as a dark blue crystalline solid in 64% yield (0.462 g). ESI MS: m/z 477.7 (expected), 476.7 (found) amu. Spectroscopic data of the product (see **Figure 3.32**) match those available in the literature.¹⁸

Tetrabutylammonium Co bis(3,4,5,6-tetrachlorobenzenedithiolate) (3)

Recrystallization of the solid from dichloromethane/ether yielded (TBA)[Co(S₂C₆H₂Cl₂)₂] as a dark blue-black solid in 28% yield (0.06 g ESI MS: m/z 615.5 (expected), 614.5 (found) amu. Spectroscopic data of the product (see **Figure 3.32**) match those available in the literature.⁵⁰

Tetrabutylammonium Co bis(3,4,5,6-tetrafluorobenzenedithiolate) (4)

Recrystallization of the solid from dichloromethane/ether yielded (TBA)[Co(S₂C₆H₂Cl₂)₂] as a dark blue-black solid in 22% yield. ESI MS: m/z 483.9 (expected), 483.1 (found) amu.

Tetrabutylammonium Cobalt bis(toluenedithiolate) (5)

Recrystallization of the solid from dichloromethane/ether yielded (TBA)[Co(S₂C₇H₇)₂] as a dark blue crystalline solid in 69% yield (0.420 g). ESI MS: m/z 366.92 (expected), 366.9 (found) amu. Spectroscopic data of the product (see **Figure 3.32**) match those available in the literature.¹⁸

Tetrabutylammonium Cobalt bis(naphthalenedithiolate) (6)

Recrystallization of the solid from dichloromethane/ether yielded (TBA)[Co(S₂C₁₀H₆)₂] as a dark blue-black crystalline solid in 29% yield (0.1 g). ESI MS: m/z 440 (expected), 439 (found) amu. Crystals suitable for X-ray analysis were obtained by layering of ether on a dilute solution of **6** in dichloromethane.

Graphene Oxide

Graphene oxide for graphene depositions was prepared as in previous studies outlined in the experimental details for chapter 2.

Reduced Graphene Oxide Depositions

RGO depositions were performed in an identical manner to the procedure outlined in the experimental details for chapter 2.

Catalyst-Adsorbed Electrode Preparation

All catalyst-adsorbed electrode surfaces reported in this section were prepared by soaking the graphitic electrode surfaces (FTO/RGO and HOPG) in saturated acetonitrile solutions of the cobalt bis(benzenedithiolene) complexes for 24 hours. After this period, surfaces were extensively rinsed with fresh acetonitrile, acetone and water. In addition, the surfaces were electrochemically polished by cycling from 0 to -1 V to assure any loosely bound catalyst was sufficiently removed prior to electrochemical and XPS analysis.

UV-Visible Spectroscopy

Electronic absorption spectra were collected at room temperature using an Analytic Jena Specord S600 spectrometer with a WinASPECT (V2.2) interface.

Electrochemical Measurements

All electrochemical measurements were conducted in 18.2 Millipore water. Cyclic voltammetry and controlled potential coulometry were carried out using an CHI600 electrochemical analyzer. A platinum disc (BASi, **MF-2013**) was used as the counter electrode in all voltammetry experiments, and the reference was an aqueous Ag/AgCl electrode (CH Instruments, with saturated AgCl and KCl fill solutions). All potentials are reported vs. SHE by adding 0.205 V to the measured potential vs. Ag/AgCl/saturated KCl. Bulk electrolysis experiments were conducted in a 2-compartment cell separated by a frit with the same working

and reference electrodes previously mentioned and a carbon felt counter electrode (purchased from Alfa Aesar). To maintain a steady pH and provide a consistent activity profile during electrolysis, the solution pH was monitored and adjusted back to the starting pH after increasing by more than 0.05 units. All solutions were prepared with 0.1 M potassium hexafluorophosphate supporting electrolyte, which was purchased from Fisher and subsequently recrystallized from an aqueous 0.1 M NaOH solution. Argon gas was used to deoxygenate all solutions for a minimum of 30 minutes prior to data collection.

Determination of Catalytic TOF

The two primary methods for calculating turnover frequency outline in section 3.1, that reported by Bard and Faulkner (using **equation 1**) and that reported by Saveant and coworkers (using **equations 2** and **3** with the foot-of-the-wave analysis), were also used in this study.^{67,68} The methods were applied in the same manner as reported in the experimental details of section 3.1.

X-ray photoelectron Spectroscopy

All X-ray photoelectron spectra were acquired with a Kratos Axis Ultra analyzer using an Al K α (1486.6 eV) source with a monochromator. Spectra were recorded without charge neutralization at a base pressure of $<2.5 \times 10^{-9}$ Torr. A 8 mA emission current and 14 kV anode HT were used. Survey scans were acquired at a pass energy of 160 eV. Due to the low level of catalyst loading, high-resolution XP spectra of C 1s, Co 2p, Cl 2p and S 2p recorded at a pass energy of 20 eV provided very low signals difficult to visualize. For this reason, lower resolution data recorded at a pass energy of 160 eV are shown here. The binding energies of all spectra were corrected by using the difference between the observed C 1s peak energy and the peak energy of adventitious carbon (284.6 eV).⁶⁶ Spectra were fit with a Shirley type

background using the CASAXPS software version 2.313. Co 2p, Cl 2p and S 2p spectra were fit using 45% Gaussian and 55% Lorentzian line shapes. The full width at half maximum (fwhm) was constrained between 0.6 and 3.0 for Cl 2p and S 2p spectra, and between 0.6 and 5 for Co 2p spectra. Additional peaks used for fitting all spectra applied the same fitting parameters.

X-ray Crystallography

*Structural Determination of $[(C_4H_9)_4N][Co(S_2C_{10}H_6)_2]$ (**6**)*

Blue plates of **6** were grown from a dichloromethane solution of the compound layered with diethyl ether at 22 deg. C. A crystal of dimensions 0.09 x 0.03 x 0.01 mm was mounted on a Rigaku AFC10K Saturn 944+ CCD-based X-ray diffractometer equipped with a low temperature device and a Micromax-007HF Cu-target micro-focus rotating anode ($\lambda = 1.54187$ Å) operated at 1.2 kW power (40 kV, 30 mA). The X-ray intensities were measured at 85(1) K with the detector placed at a distance of 42.00 mm from the crystal. A total of 2028 images were collected with an oscillation width of 1.0° in ω . The exposure times were 15 sec. for the low angle images, 120 sec. for high angle. Rigaku d*trek images were exported to CrysAlisPro for processing, and corrected for absorption. The integration of the data yielded a total of 25589 reflections to a maximum 2θ value of 139.28° of which 3213 were independent and 2640 were greater than $2\sigma(I)$. The final cell constants (Table 1) were based on the xyz centroids of 5786 reflections above $10\sigma(I)$. Analysis of the data showed negligible decay during data collection. The structure was solved and refined with the Bruker SHELXTL (version 2014/6) software package, using the space group C2/c with $Z = 4$ for the formula $C_{36}H_{48}NS_4Co$. The cobalt dithiolene complex lies on an inversion center of the crystal lattice. The tetrabutyl

ammonium cation lies on a two-fold axis. All non-hydrogen atoms were refined anisotropically with the hydrogen atoms placed in idealized positions. Full matrix least-squares refinement based on F^2 converged at $R1 = 0.0806$ and $wR2 = 0.2126$ [based on $I > 2\sigma(I)$], $R1 = 0.0949$ and $wR2 = 0.2567$ for all data.

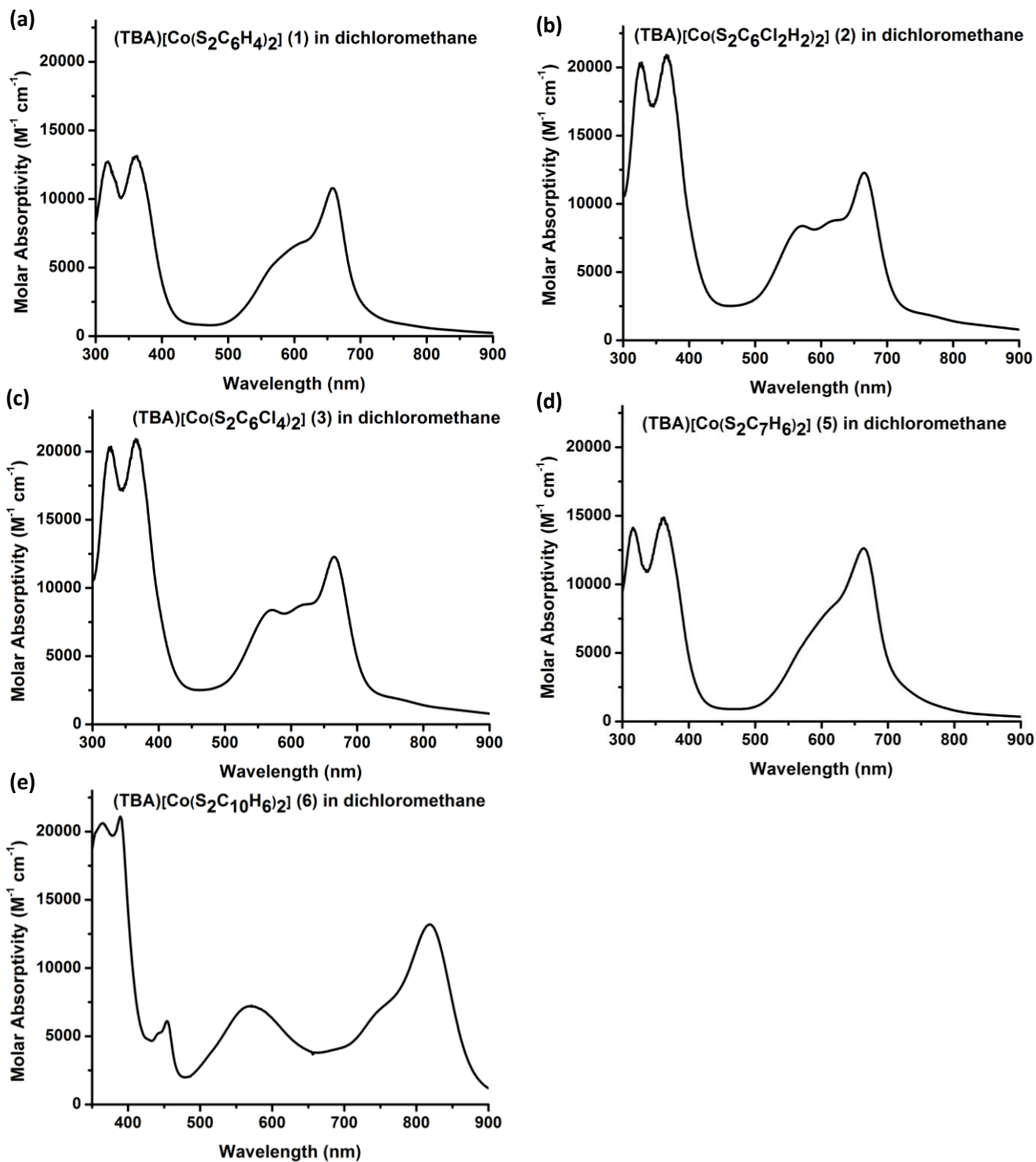


Figure 3.32. UV-Visible spectra in dichloromethane solution of (a) (TBA)[Co(S₂C₆H₄)₂] (1); (b) (TBA)[Co(S₂C₆Cl₂H₂)₂] (2); (c) (TBA)[Co(S₂C₆Cl₄)₂] (3); (d) (TBA)[Co(S₂C₇H₆)₂] (5); and (e) (TBA)[Co(S₂C₁₀H₆)₂] (6);

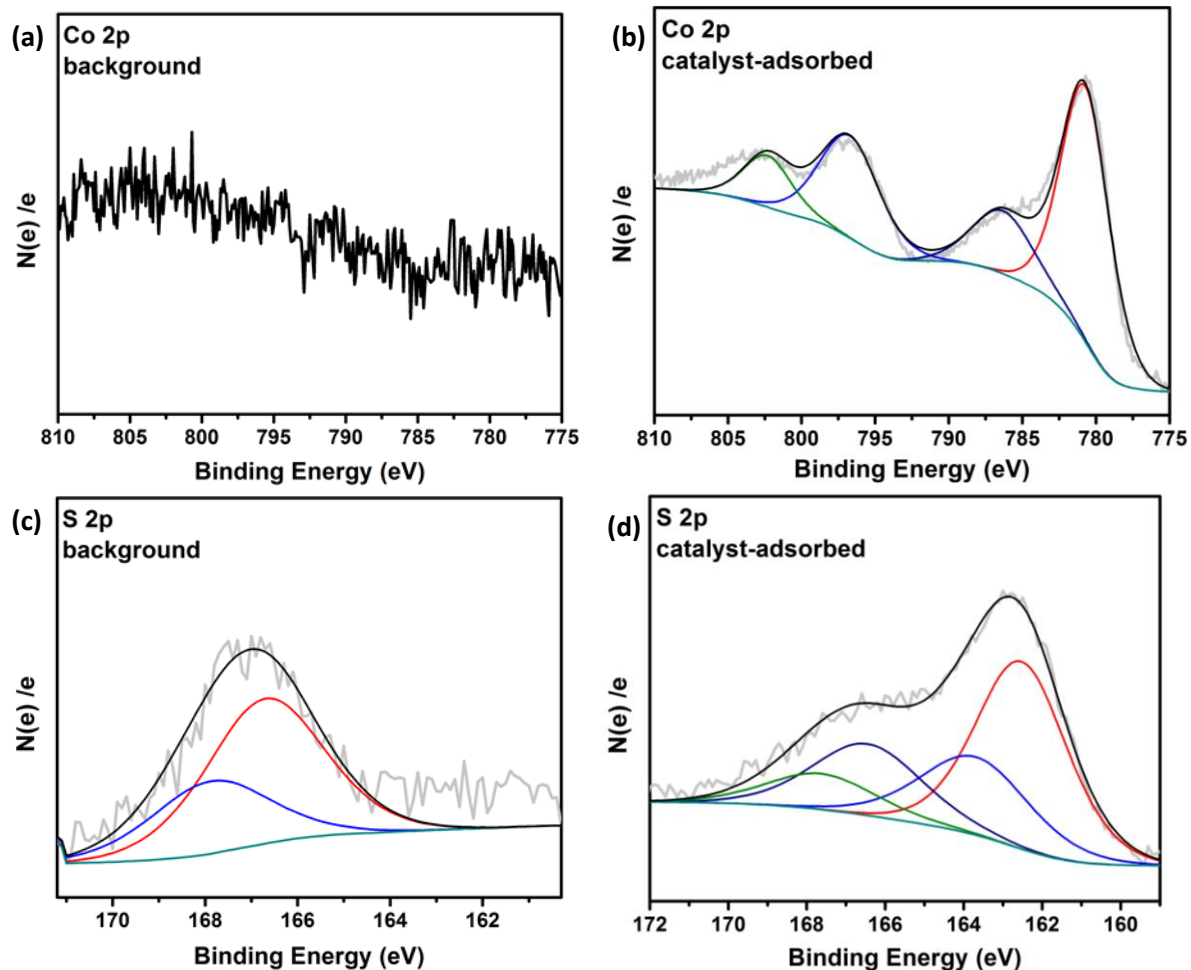


Figure 3.33. X-ray photoelectron spectroscopy (XPS) analysis of TBA[Co(S₂C₁₀H₆)₂] (**6**) on a FTO/RGO electrode. (a) background Co 2p core level XPS spectrum; (b) Co 2p core level XPS spectrum of catalyst-adsorbed bulk graphite; (c) background S 2p core level XPS spectrum of bare bulk graphite; (d) S 2p core level XPS spectrum of catalyst-adsorbed bulk graphite. The envelope is included as a solid black trace.

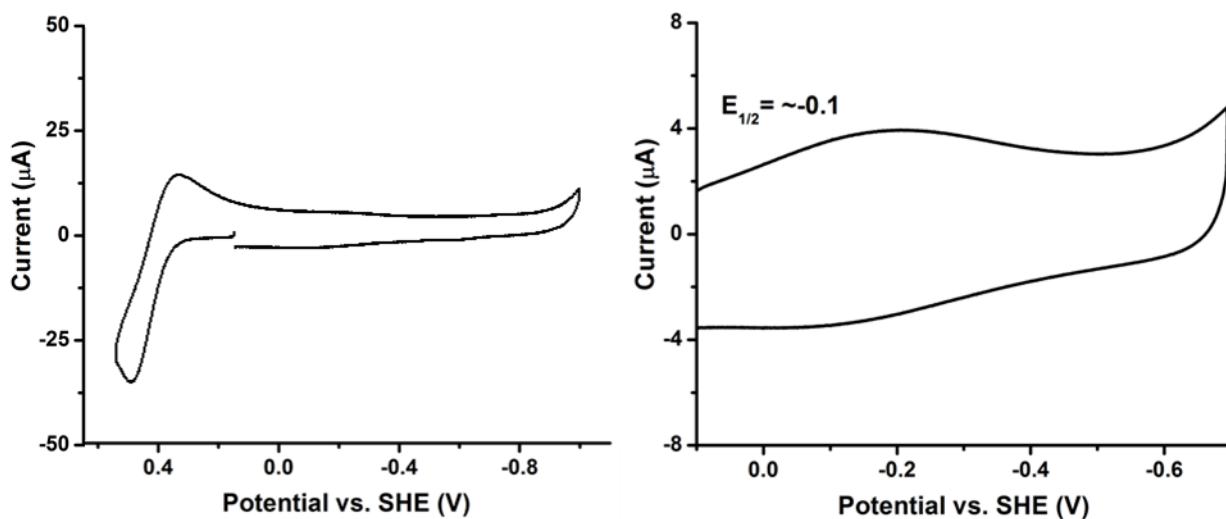


Figure 3.34. *Left:* Electrochemical window of RGO-coated FTO in aqueous 0.1 M potassium hexafluorophosphate with potassium ferricyanide/ferrocyanide (0.5 mM total) as the internal reference. *Right:* Zoomed view of cathodic window to show background signal for FTO/RGO electrodes. The scan rate was 50 mV/s. Potentials reported are versus the standard hydrogen electrode (SHE).

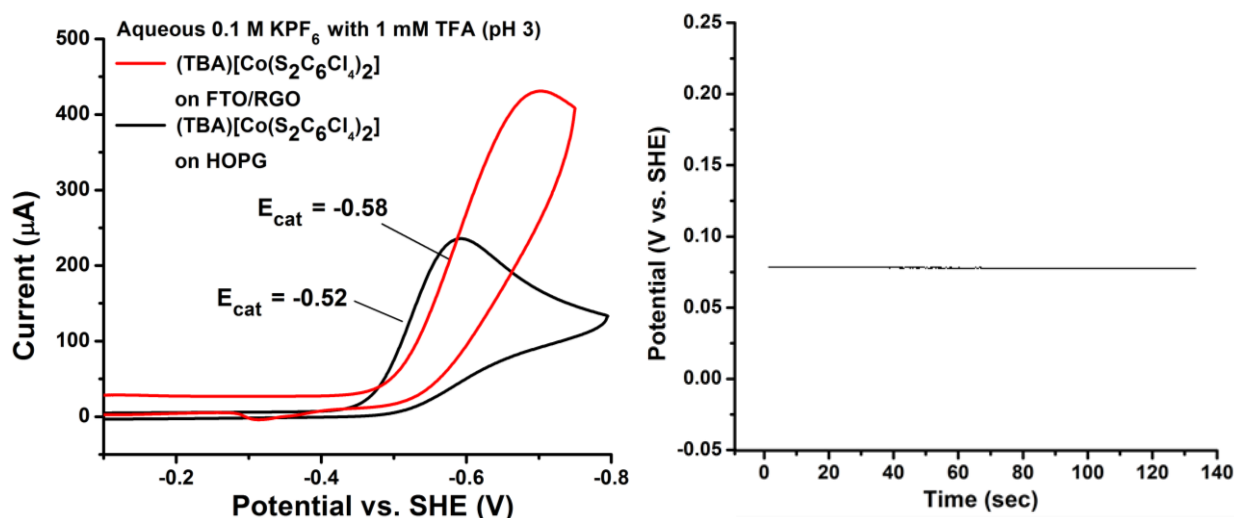


Figure 3.35. *Left:* Cyclic voltammetry of (TBA)[Co(S₂C₆Cl₄)₂] (**3**) adsorbed on FTO/RGO and HOPG working electrodes in a 1 mM TFA solution with a 50 mV/s scan rate as a representation of how overpotentials were determined for catalyst-adsorbed electrode systems, i.e. $\eta = E_{\text{cat}} - E_{\text{oc}}$. *Right:* Open circuit potential over time of a platinum mesh working electrode in the same acid solution under 1 atm H₂ atmosphere to indicate overpotential. The solution contained 0.1 M aqueous potassium hexafluorophosphate. The counter electrode was a platinum wire, and the reference was an Ag/AgCl (saturated KCl solution) electrode.

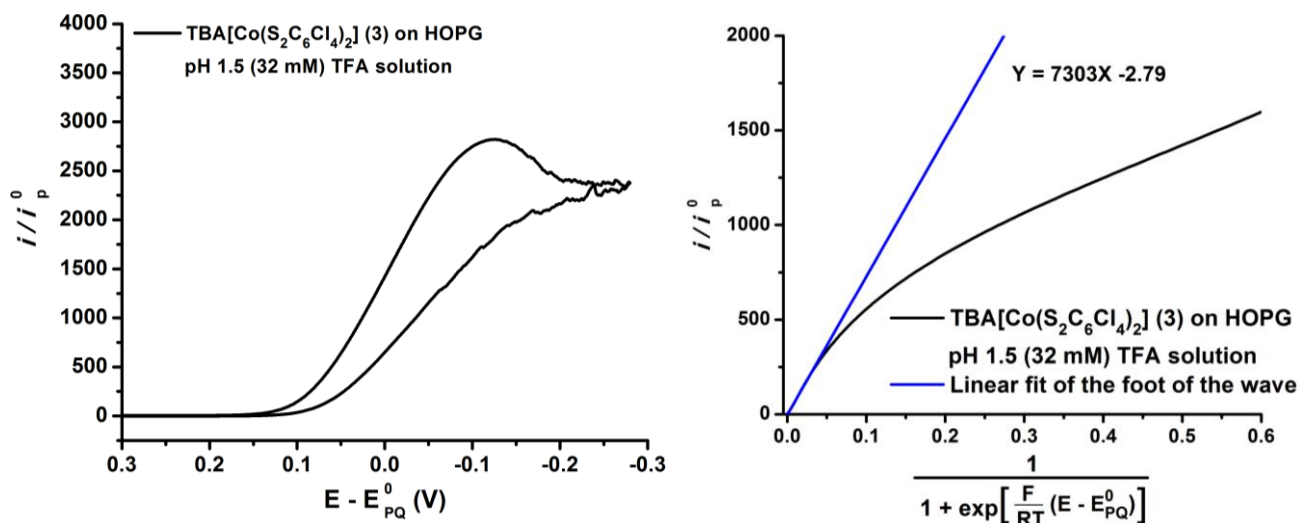


Figure 3.36. Foot-of-the-wave analysis of (TBA)[Co(S₂C₆Cl₄)₂] (3) on HOPG in the presence of 32 mM TFA (pH 1.5).

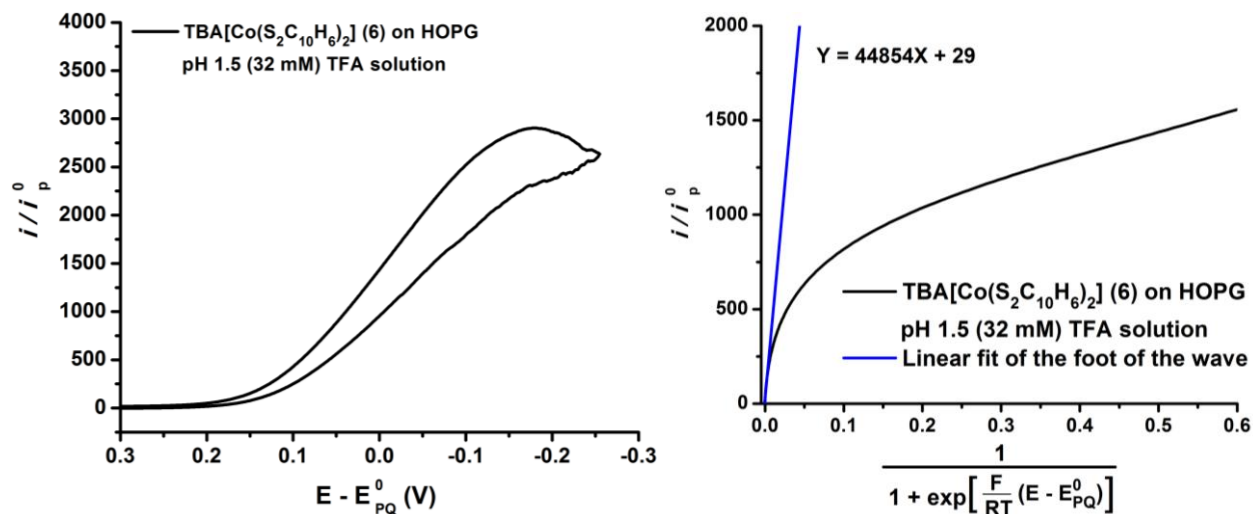


Figure 3.37. Foot-of-the-wave analysis of (TBA)[Co(S₂C₁₀H₆)₂] (6) on HOPG in the presence of 32 mM TFA (pH 1.5).

3.3. A Smorgasbord of Carbon: Comparison of Catalyst Loading and Performance Across a Variety of Graphitic Supports

As noted earlier in this chapter, while the development of both solid state and surface-immobilized catalyst manifolds has been prolific even in the last few years, a general difficulty has been the expense or complexity of such designs, or the limited lifetime of the materials/catalysts for practical use. One practical solution to designing heterogeneous catalyst manifolds is to exploit the electrostatic adsorption of catalyst systems with aromatic moieties on graphitic surfaces, as has shown effective in several literature examples.^{15,38,69,73,74,84} Specifically, the use of inexpensive catalyst supports such as bulk graphite could drastically reduce the cost of the functionalized electrode materials. Further, the simple and highly cost-effective process of simply soaking the graphitic supports in the catalyst solution would be ideal for scaling and industrial use. The ease of catalyst application in this case would also provide an alternative solution to limited catalyst lifetimes, allowing for facile reapplication of the catalyst to the graphitic supports, or simply replacement of the inexpensive support itself, after use.

In **section 3.1**, we reported reduced graphene oxide (RGO) coated fluorine-doped tin oxide (FTO) and HOPG supports soaked in a solution of the proton reduction catalyst (TBA)[Co(S₂C₆Cl₂H₂)₂] (**Chart 3.3**).⁶⁹ These heterogeneous catalyst manifolds are capable of

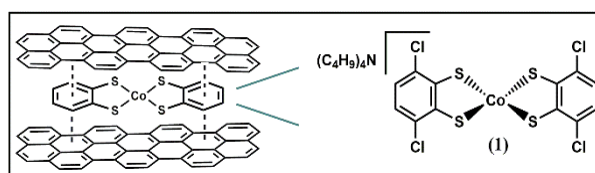


Chart 3.3 Cobalt bis(dithiolate) complex **1** used for graphite adsorption (right), schematic representation of the catalyst in graphitic materials (left)

dihydrogen production in mildly acidic ($\text{pH} < 4$) aqueous solutions of trifluoroacetic or hydrochloric acids at an overpotential (η) of 0.37 V. In this study, we report the preparation of heterogeneous dihydrogen production manifolds designed by soaking various alternative graphitic supports in catalyst solutions to provide further insight into the effect of the support on catalysis, and to test alternative, cheap forms of graphite for their abilities to bind the catalyst and support proton reduction. To assure a direct comparison between the different catalyst supports, the same proton reduction catalyst, $\text{TBA}[\text{Co}(\text{S}_2\text{C}_6\text{Cl}_2\text{H}_2)_2]$ (**1**), was used on all supports.

For analysis of the catalyst on a bulk graphite surface, graphite rods purchased from NAC carbon products, Inc. (\$4 per rod) were halved, polished and epoxy coated to give a disc electrode with a surface area of 0.32 cm^2 . CV analysis of the graphite electrodes after 12 hours of soaking in a 1 mM solution of **1** (after extensive rinsing and electrochemical polishing regiments) in aqueous solutions shows a quasi-reversible redox couple at an average potential

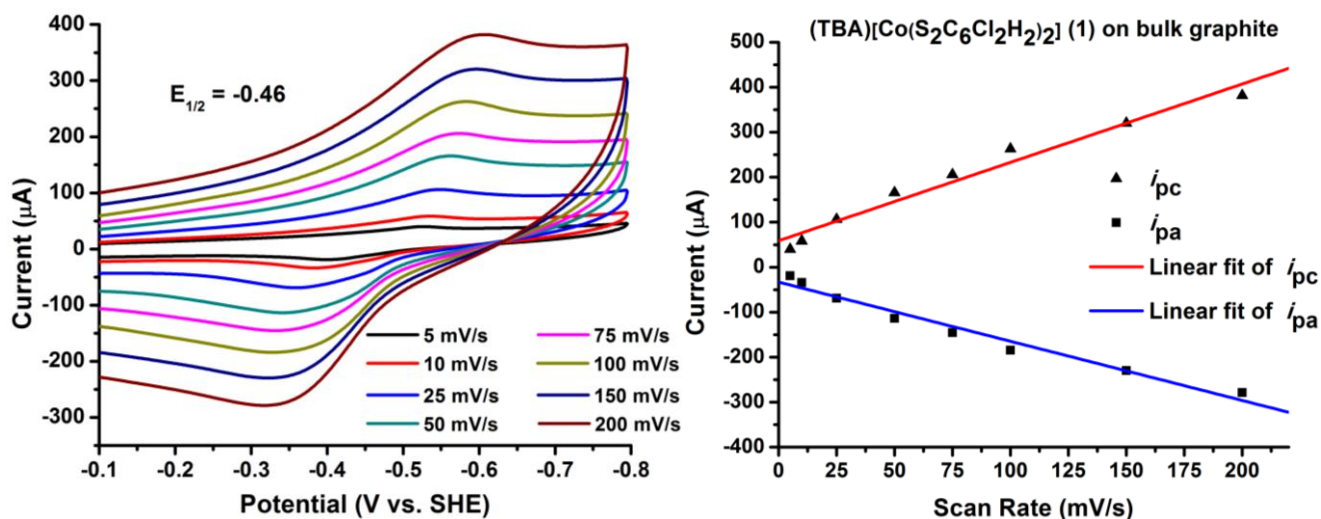


Figure 3.38. *Left:* Cyclic voltammetry of $(\text{TBA})[\text{Co}(\text{S}_2\text{C}_6\text{Cl}_2\text{H}_2)_2]$ (**1**) adsorbed on a bulk graphite working electrode at various scan rates. The solution contained 0.1 M aqueous potassium hexafluorophosphate. The counter electrode was a platinum disc, and the reference was an Ag/AgCl (saturated KCl solution) electrode. Potentials are reported vs. the standard hydrogen electrode. *Right:* Linear fit of the peak cathodic and anodic current versus the scan rate.

of -0.46 V vs. SHE (**Figure 3.38**, left). This potential is slightly lower than that previously seen for **1** on a HOPG electrode (-0.52 V), while it is over 0.2 V higher than both with the species seen on FTO/RGO and **1** in acetonitrile solution, which both exhibit an $E_{1/2}$ of about -0.25 to -0.3 V.^{18,69} As previously reported, this difference on graphitic surfaces is consistent across a series of cobalt bis(benzenedithiolene) derivatives, and is likely due to the electronic interaction of the catalyst with the graphite surface.⁶⁹ The ratio of peak anodic to cathodic current (i_{pa}/i_{pc}) is approximately 1 (± 0.1) and the peak current values are seen to increase linearly with scan rate (**Figure 3.38**, right). Integration of the CV wave at 50 mV gives a total of 1.13×10^{-9} mol electrons passed, which, if directly attributed to the $\text{Co}^{\text{III/II}}$ couple, corresponds to a catalyst loading of 1.13×10^{-9} mol or 3.53×10^{-9} mol/cm². This value is over an order of magnitude higher than the loading reported in **Section 3.2** on a HOPG electrode (1.85×10^{-10} mol/cm²), suggesting

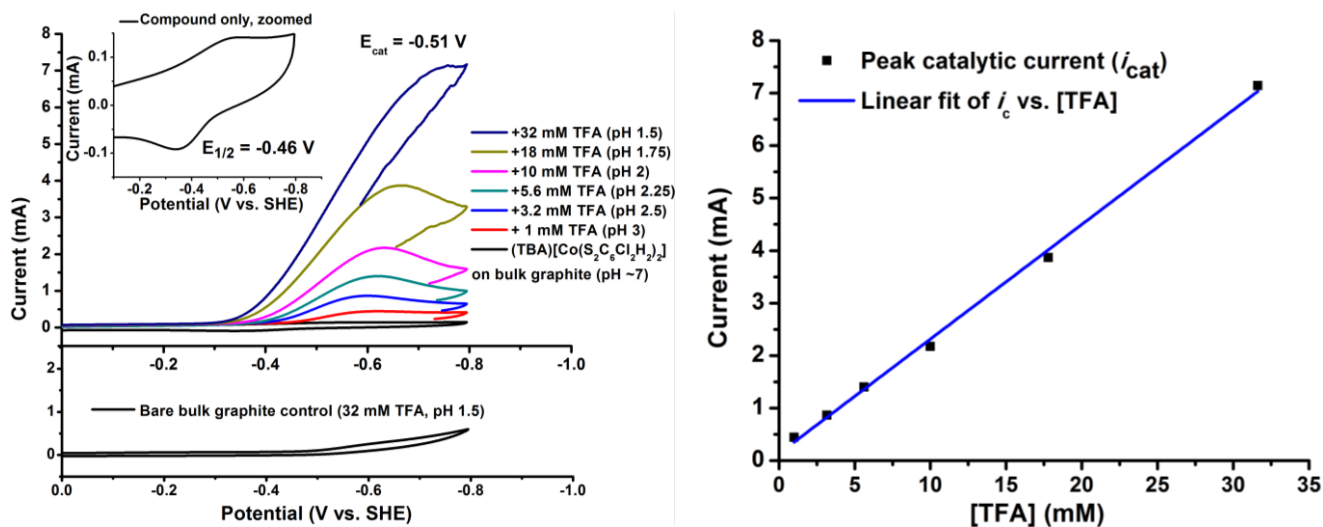


Figure 3.39. Left: Cyclic voltammetry of (TBA)[Co(S₂C₆Cl₂H₂)₂] (**1**) adsorbed on a bulk graphite working electrode with addition of TFA at a scan rate of 50 mV/s. The control surface (using the same electrode before catalyst soaking) under the same conditions is displayed on the bottom of the graph, and the inset provides a zoomed view of the CV of the Co catalyst functionalized surface in the absence of acid. The solution contained 0.1 M aqueous potassium hexafluorophosphate. The counter electrode was a platinum disc, and the reference was an Ag/AgCl (saturated KCl solution) electrode. Potentials are reported vs. the standard hydrogen electrode. Right: Linear fit of the peak catalytic current versus increasing TFA concentrations, indicating an acid-diffusion controlled process under these conditions.

the less-ordered nature and higher surface area of the bulk graphite is actually beneficial for catalyst uptake.

Addition of trifluoroacetic acid (TFA, $pK_a = 0.23$) induces a significant increase in cathodic current at the $E_{1/2}$ along with a corresponding disappearance of the anodic peak, a behaviour indicative of electrocatalytic reduction of protons from TFA (**Figure 3.39**, left). Testing of the same bulk graphite electrode in identical conditions prior to catalyst adsorption shows substantially lower background current as seen on the bottom of Figure 1, confirming this activity as being directly a result of the catalyst's presence. The cathodic current continues to increase linearly with sequential acid additions, with no activity saturation seen (i.e. total catalysis conditions) down to and below a pH of 1.5 (**Figure 3.39**, right). An i_{cat}/i_p ratio of 50 can be calculated at this pH with i_{cat} measured at the peak cathodic potential (E_p , -0.76 V). This value is significantly lower than the i_{cat}/i_p ratio observed for the HOPG/**1** system (176). **Equation 1** provides a TOF estimate of 115 s^{-1} from the i_{cat}/i_p ratio at this pH, although it should be noted that these conditions are not ideal for use of this equation due to the fact catalyst activity saturation is not observed.⁶⁷ The bimolecular rate constant $2.85 * 10^{11} \text{ M}^{-1} \text{ s}^{-1}$ is determined by the foot of the wave analysis (see experimental section), several orders of magnitude higher than determined for HOPG/**1** by the same method.⁶⁸ The E_{cat} of -0.51 V observed at pH 1.5 also differs from that of the HOPG/**1** system (-0.67 V). The electrocatalytic response of **1** on bulk graphite has an onset overpotential of 0.36 V as compared to the reduction of TFA at a platinum electrode under the same conditions (See experimental section), which is notably similar to that of **1** in MeCN solution and **1** on both FTO/RGO and HOPG electrodes.^{18,69} This indicates that the surface-bound catalysts maintain their environment around the cobalt center and thus, the thermodynamic properties of the molecular system. The

disparity seen in half-wave potential and for the $i_{\text{cat}}/i_{\text{p}}$ ratio of the bulk graphite/**1** system vs. that of HOPG/**1** (-0.51 V and -0.67 V, respectively) suggests that the ordering of the graphite is in fact relevant for the catalyst's activity, but not for the thermodynamic driving force for electrocatalysis as evidenced by the identical onset overpotentials. At a pH of 1.3, a current density of 10 mA/cm² is achieved by the bulk graphite/**1** electrode at a potential of only -0.48 V vs. SHE (-0.4 V vs. RHE) (**Figure 3.40**). Compared to the one- and two-dimensional [Co(S₂R)₂]⁻ polymer systems studied by Marinescu and coworkers, the overpotential of our system is more positive by 80 mV and more negative by 60 mV, respectively.^{52,53} However, it is worth noting that the bulk graphite/**1** system achieves this current density with a catalyst loading 2-3 orders of magnitude lower than in the polymer systems, indicating a substantially faster molecular TOF for our system or partial catalyst inactivity for the polymer Co(S₂R)₂ systems.

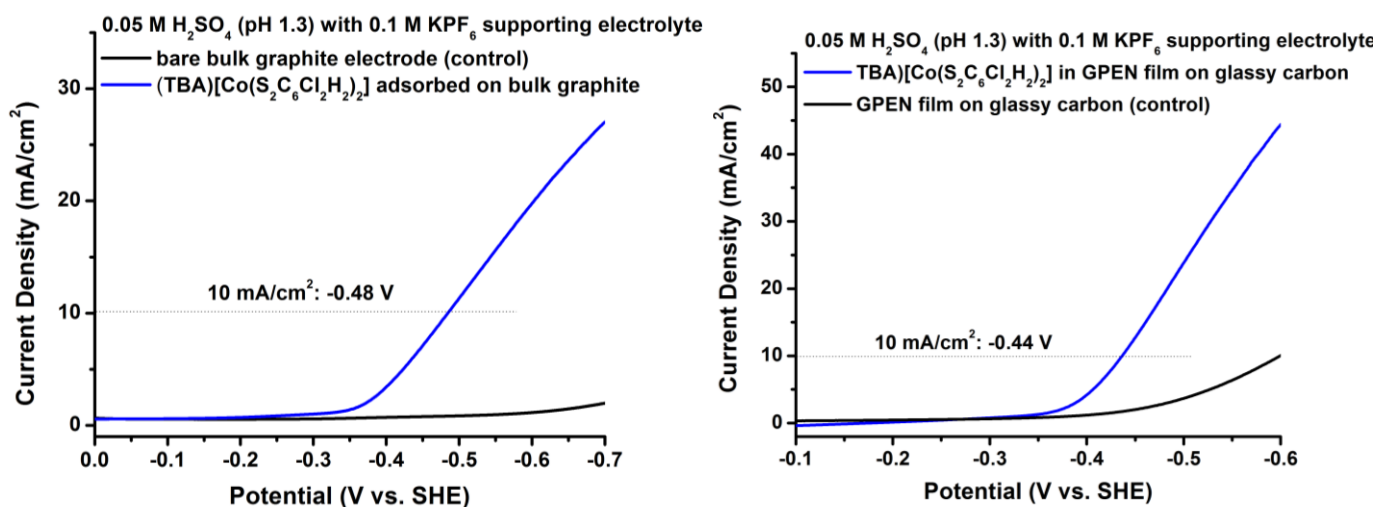


Figure 3.40. Polarization curves of (TBA)[Co(S₂C₆Cl₂H₂)₂] (**1**) adsorbed on a bulk graphite working electrode (*left*) and adsorbed in a GPEN film on a glassy carbon working electrode (*Right*) with 0.05 M TFA (pH 1.3) at a scan rate of 50 mV/s (blue). The control surface (using the same electrode without adsorbed catalyst) under the same conditions is displayed in black. The solution contained 0.1 M aqueous potassium hexafluorophosphate. The counter electrode was a platinum disc, and the reference was an Ag/AgCl (saturated KCl solution) electrode. Potentials are reported vs. the standard hydrogen electrode.

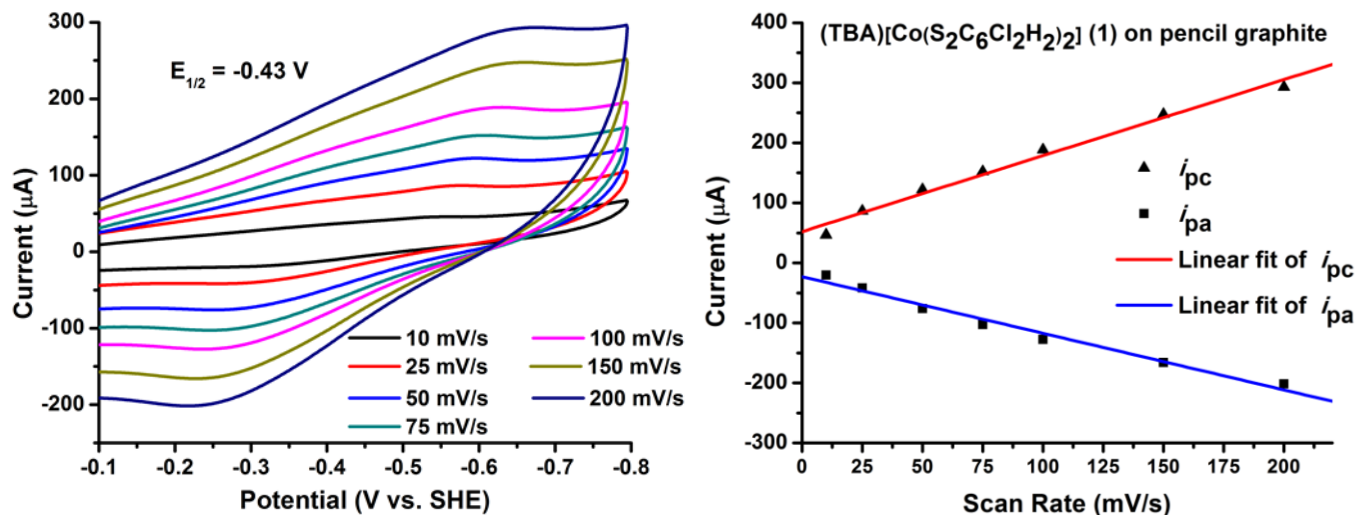


Figure 3.41. *Left:* Cyclic voltammetry of (TBA)[Co(S₂C₆Cl₂H₂)₂] (**1**) adsorbed on a pencil graphite working electrode at various scan rates. The solution contained 0.1 M aqueous potassium hexafluorophosphate. The counter electrode was a platinum disc, and the reference was an Ag/AgCl (saturated KCl solution) electrode. Potentials are reported vs. the standard hydrogen electrode. *Right:* The peak cathodic and anodic current versus the scan rate.

To assure these results can be extended to a variety of common graphite materials, further testing was conducted on a pencil graphite electrode (PGE), which was electrochemically pretreated as previously reported in the literature (see experimental section), and then soaked in a solution of **1**.⁸⁵ Cyclic voltammetry analysis of PGE/**1** systems shows similar results to that of bulk graphite/**1**, with a quasi-reversible feature at an $E_{1/2}$ of approximately -0.43 V. Slight differences from bulk graphite/**1** are observed in i_{pa}/i_{pc} trends as well as peak separation (**Figure 3.41**), likely due to the inherent differences in diffusion or electron transfer rates at the different types of graphitic materials. However, addition of TFA to the solution induces an analogous increase in current density observed with an onset potential approximately equivalent to the $E_{1/2}$ (-0.46 V, $\eta = 0.38$ V), confirming catalytic performance and preservation of the established EC mechanism for these systems, despite differences in exact graphitic structure of the support (**Figure 3.42**).

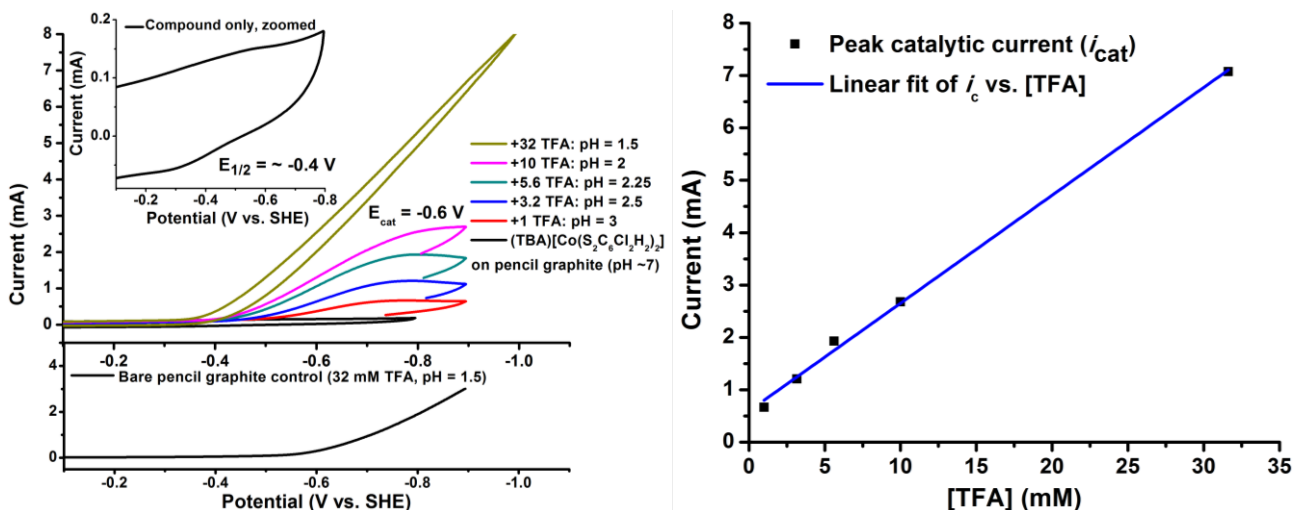


Figure 3.42. *Left:* Cyclic voltammetry of (TBA)[Co(S₂C₆Cl₂H₂)₂] (**1**) adsorbed on a pencil graphite working electrode with addition of TFA at a scan rate of 50 mV/s. The control surface (using the same electrode before catalyst soaking) under the same conditions is displayed on the bottom of the graph, and the inset provides a zoomed view of the CV of the Co catalyst functionalized surface in the absence of acid. The solution contained 0.1 M aqueous potassium hexafluorophosphate. The counter electrode was a platinum disc, and the reference was an Ag/AgCl (saturated KCl solution) electrode. Potentials are reported vs. the standard hydrogen electrode. *Right:* Linear fit of the peak catalytic current versus increasing TFA concentrations, indicating an acid-diffusion controlled process under these conditions.

Electrochemical behaviour of **1** on a glassy carbon surface (BASi, MF-2012) was assessed by soaking the electrode as purchased in a solution of **1**. Analysis of the resulting electrode by cyclic voltammetry showed a very low current response, nearly within background, with an approximate E_{1/2} of -0.4 V. Addition of TFA to the solution was observed to induce an increase in cathodic current; however, closer analysis reveals the response to be the same as for the bare electrode control at the same pH prior to catalyst soaking (**Figure 3.43**), suggesting the material is inherently unable to retain catalyst under turnover conditions.

Graphene (ACS materials) was transferred to glassy carbon and FTO electrodes for electrochemical analysis (detailed in the experimental section; both of these support materials do not retain our catalysts directly), followed by soaking of these electrodes in a solution of catalyst **1**. Cyclic voltammetry of the glassy carbon/graphene system shows only a slightly higher redox response compared to the glassy carbon/**1** system, but with a more definite shape

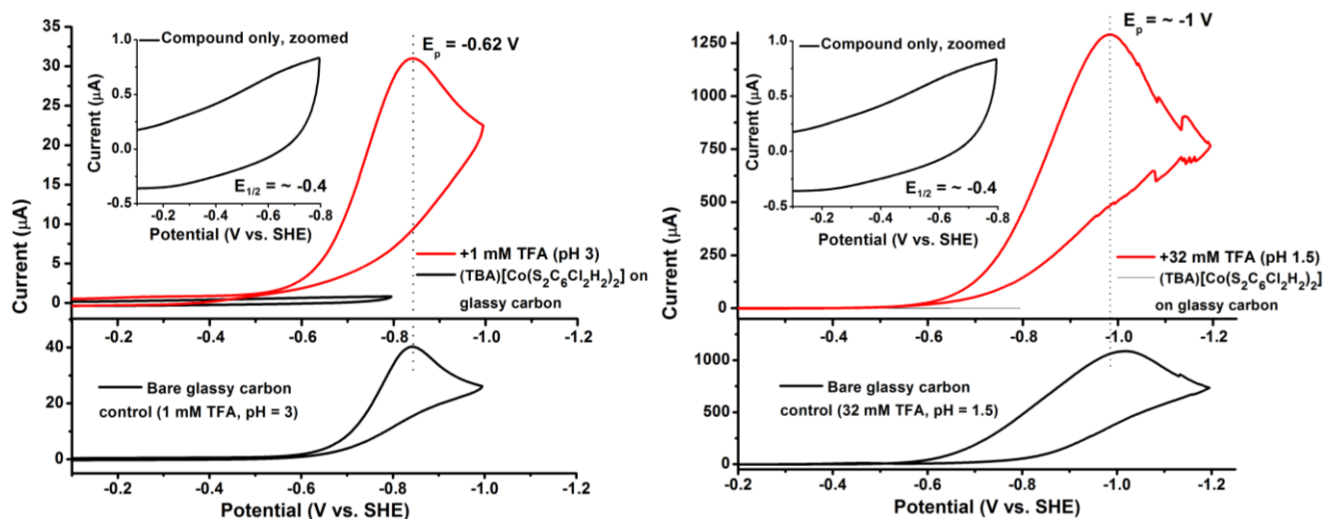


Figure 3.43. Cyclic voltammetry of (TBA)[Co(S₂C₆Cl₂H₂)₂] (**1**) adsorbed on a glassy carbon working electrode with the addition of low (*Left*) and high (*Right*) TFA concentrations, with the background current response displayed in the lower section of the graph and a zoomed view of current response in the absence of acid displayed in the insets. In both cases, no current above background was observed. The solutions contained 0.1 M aqueous potassium hexafluorophosphate. The counter electrode was a platinum wire, and the reference was an Ag/AgCl (saturated KCl solution) electrode. Potentials are reported vs. the standard hydrogen electrode.

and an $E_{1/2}$ of approximately 0.45 V (**Figure 3.44**, left). Addition of TFA to the solution was observed to induce an increase in cathodic current to a pH of 3, with an E_{cat} of -0.62 V and an onset potential approximately equal to the $E_{1/2}$ (**Figure 3.44**, right). However, upon repeated scanning at this pH a decrease in the cathodic wave is observed, indicating loss of catalyst from the surface. Upon further acid addition the current increase is seen to disappear, leaving only the background response of proton reduction at glassy carbon. Given that the same catalyst is seen to display persisting activity on the CV timescale at these acid concentrations on HOPG, FTO/RGO, and bulk graphite electrodes, these results suggest that pristine, single-layer graphene does actually not bind catalyst **1** well, which is easily desorbed and lost from the corresponding electrode surfaces.

This lack of sustained activity for **1** adsorbed on glassy carbon and single-layer graphene surfaces has very interesting implications for the interaction of the catalyst with

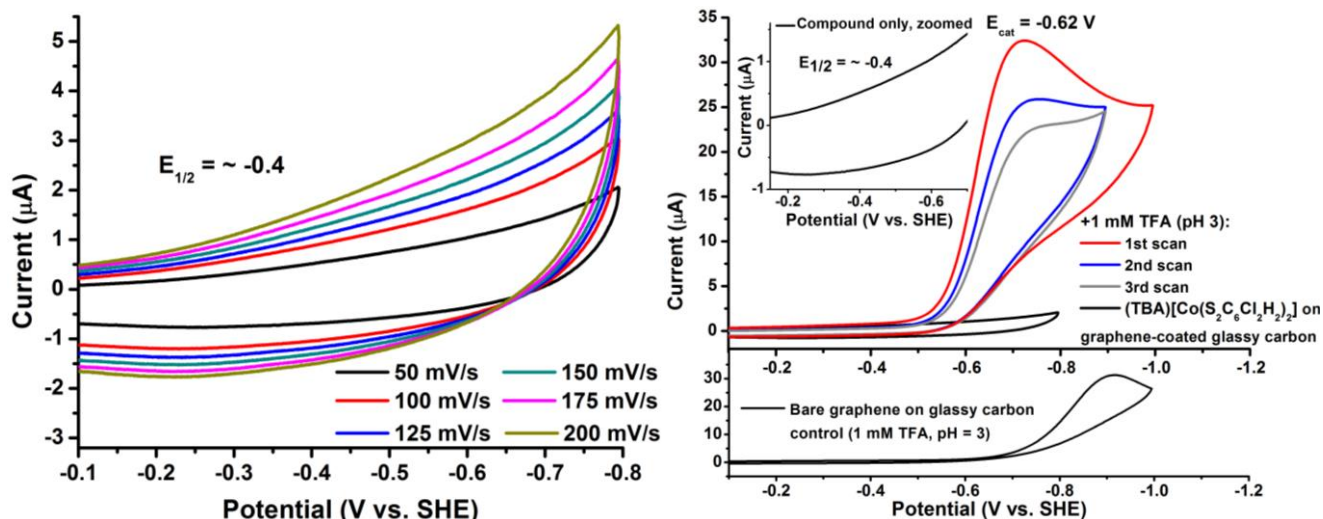


Figure 3.44. *Left:* Cyclic voltammetry of (TBA)[Co(S₂C₆Cl₂H₂)₂] (**1**) adsorbed on a graphene-coated glassy carbon working electrode at various scan rates. *Right:* Cyclic voltammetry of **1** adsorbed on a graphene-coated glassy carbon working electrode with 1 mM TFA at a scan rate of 50 mV/s. The control surface (using the same electrode before catalyst soaking) under the same conditions is displayed on the bottom of the graph, and the inset provides a zoomed view of the CV of the Co catalyst functionalized surface in the absence of acid. The counter electrode was a platinum disc, and the reference was an Ag/AgCl (saturated KCl solution) electrode. Potentials are reported vs. the standard hydrogen electrode

graphitic electrode surfaces. As glassy carbon has been reported to contain largely sp²-hybridized networks with a dense layered fullerene structure, it can be assumed that the difficulty in adsorption is not likely due to an electronic difference in the material, but rather structural.⁸⁶ This is further supported by the weak adsorption and minimal retention seen for single-layer graphene, indicating the electronic interaction of the graphitic surface with catalyst is not sufficient for catalyst retention. This implies that stable catalyst binding to graphitic surfaces requires multi-layered structures, allowing for (partial) catalyst intercalation as indicated in Scheme 1.

Inspired by the strong binding of catalyst **1** to bulk graphite electrodes, we further investigated whether **1** could also be adsorbed onto graphite powder. In order to make an electrode from this material, the graphite powder with adsorbed catalyst was embedded in nafion films (details in the experimental section) and dried on a glassy carbon electrode surface

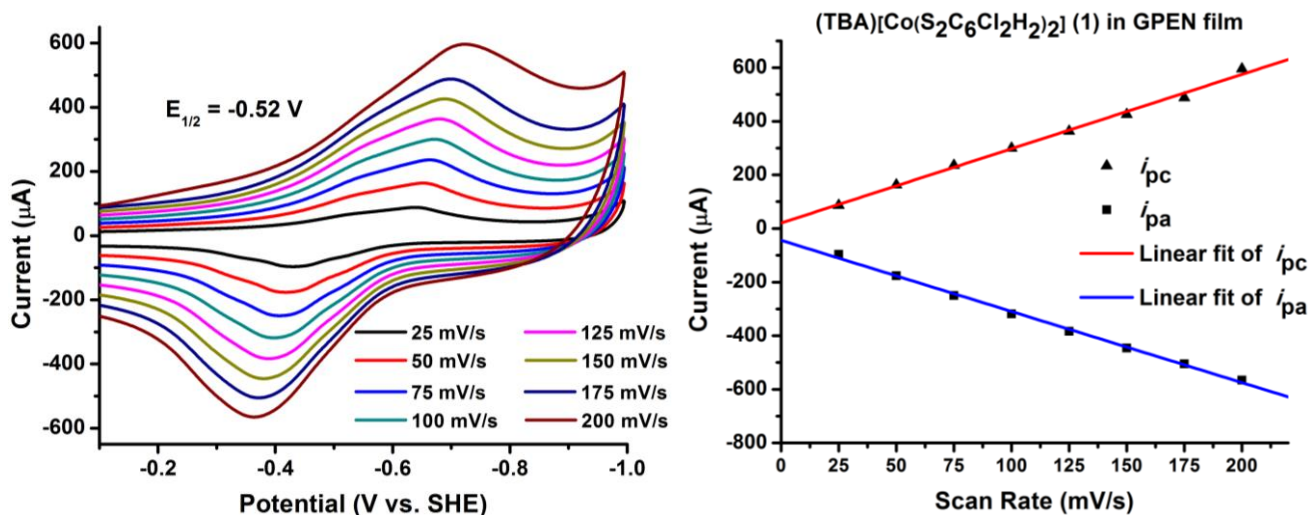


Figure 3.45. *Left:* Cyclic voltammetry of (TBA)[Co(S₂C₆Cl₂H₂)₂] (1) adsorbed in a GPEN film on a glassy carbon working electrode at various scan rates. The solution contained 0.1 M aqueous potassium hexafluorophosphate. The counter electrode was a platinum wire, and the reference was an Ag/AgCl (saturated KCl solution) electrode. Potentials are reported vs. the standard hydrogen electrode. *Right:* Linear fit of the peak cathodic and anodic currents versus the scan rate.

prior to electrochemical analysis. These graphite powder-embedded nafion (GPEN) films were observed to have a redox response containing multiple features with approximately the same $E_{1/2}$ of -0.52 V (**Figure 3.45**), possibly due to the presence of catalyst in a multitude of microenvironments in the film (i.e. at the film surface vs. internal, and closer to the glassy carbon surface). Integration of the CV wave provides a catalyst loading estimate of 7.03×10^{-9} mol Co in the GPEN film (2.11×10^{-9} mol/cm²). An increase in cathodic current response is seen upon addition of TFA with two discernible peaks in agreement with the CV results prior to acid addition. Linear increase in current response analogous to that for the bulk graphite electrodes is observed with successive acid addition, with an E_{cat} of -0.47 V at pH 1.5 (**Figure 3.46**). At this pH, an i_{cat}/i_p ratio of 24.4 is observed, corresponding to a TOF of 57 s^{-1} from **equation 1**.

The graphite and graphene surfaces as well as the GPEN films were analysed by X-ray photoelectron spectroscopy (XPS) at a pass energy of 160 eV before and after soaking in a

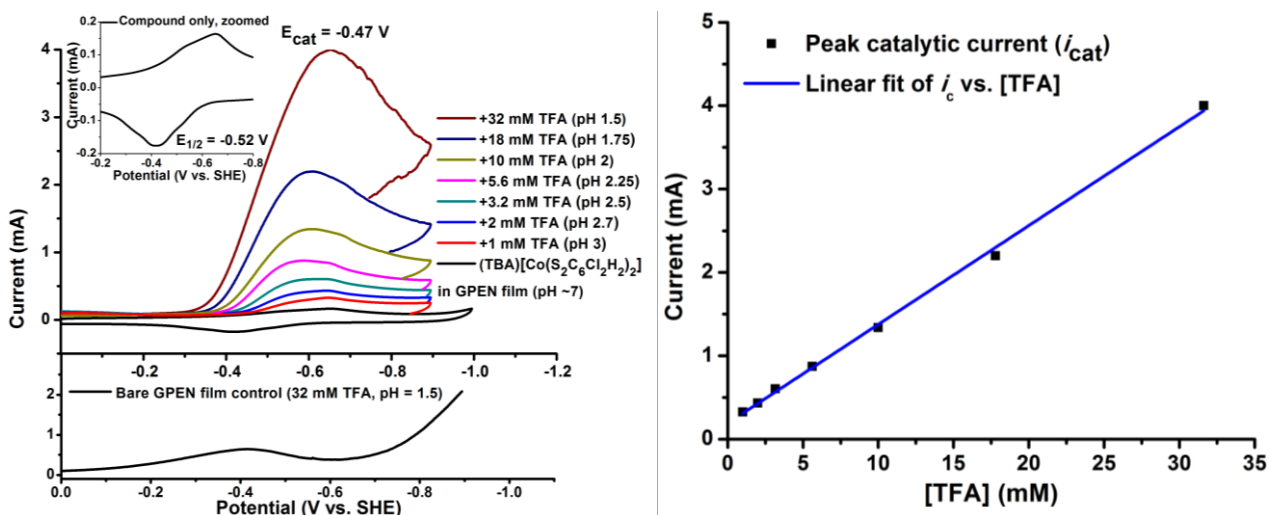


Figure 3.46. *Left:* Cyclic voltammetry of (TBA)[Co(S₂C₆H₂Cl₂)₂] (**1**) adsorbed in a GPEN film on a glassy carbon working electrode with addition of TFA at a scan rate of 50 mV/s. The control surface (using the same electrode before catalyst soaking) under the same conditions is displayed on the bottom of the graph, and the inset provides a zoomed view of the CV of the Co catalyst functionalized surface in the absence of acid. The solution contained 0.1 M aqueous potassium hexafluorophosphate. The counter electrode was a platinum disc, and the reference was an Ag/AgCl (saturated KCl solution) electrode. Potentials are reported vs. the standard hydrogen electrode. *Right:* Linear fit of the peak catalytic current versus increasing TFA concentrations, indicating an acid-diffusion controlled process under these conditions.

solution of **1**. The Co 2p core spectrum of bulk graphite after soaking in catalyst solution is observed to contain two new broad signals at binding energies of 780.3 and 795.9 eV. Deconvolution of the data reveals two sets of signals corresponding to the 2p_{1/2} and 2p_{3/2} signals for [Co^{III}(bdt)₂]⁻¹ (780.2 and 795.3 eV) and [Co^{II}(bdt•)(bdt)]⁻¹ (783.6 and 798.5 eV) resonance structures, which is in agreement with previous results on FTO/RGO electrodes as well as in polymeric Co(S₂R) species (**Figure 3.47**).^{52,53} The presence of complex **1** on the surface is further corroborated by new signals observed in the S 2p and Cl 2p core spectra with binding energies of ~163 and ~201 eV respectively, which are also consistent with previous accounts in the literature.^{52,53} Spectra for graphite powder and graphene surfaces were observed to have nearly identical spectra (see experimental section), albeit with much lower intensity on graphene, suggesting the same species is adsorbed to the surface of each support.

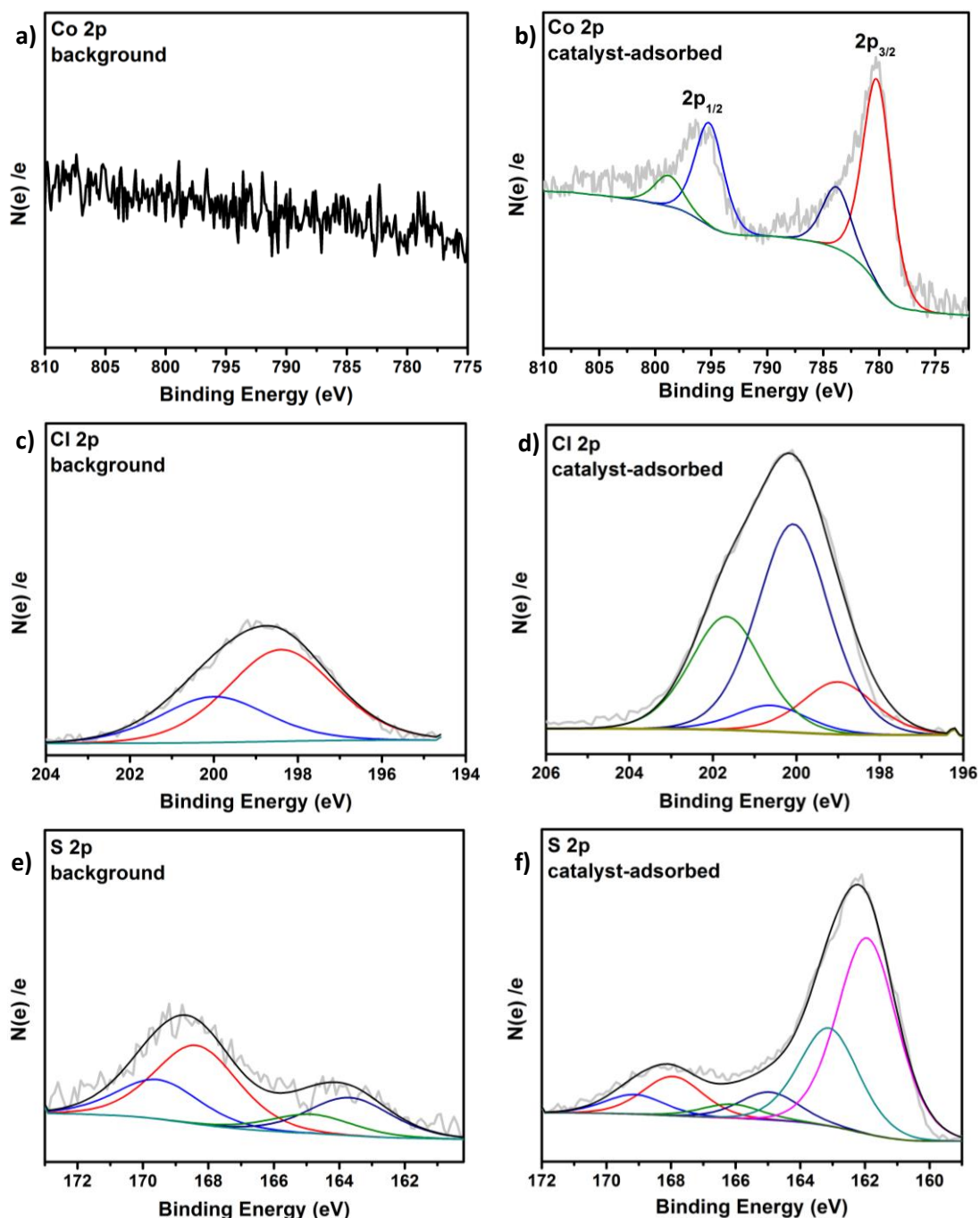


Figure 3.47. X-ray photoelectron spectroscopy (XPS) analysis of TBA[Co(S₂C₆Cl₂H₂)₂] (**1**) on bulk graphite. (a) background Co 2p core level XPS spectrum; (b) Co 2p core level XPS spectrum of catalyst-adsorbed bulk graphite; (c) background Cl 2p core level XPS spectrum of bare bulk graphite; (d) Cl 2p core level XPS spectrum of catalyst-adsorbed bulk graphite; (e) background S 2p core level XPS spectrum of bare bulk graphite; (f) S 2p core level XPS spectrum of catalyst-adsorbed bulk graphite. Envelope (black) omitted in some spectra for clarity.

Throughout our analysis of cobalt bis(dithiolene) catalyst derivatives on HOPG electrodes (outlined in **Sections 3.1** and **3.2**), catalyst removal from the electrode was found to be non-trivial, as a residual catalytic response in acid was still observed even after fairly extensive polishing regimens. These findings coupled to the extremely flat, square planar structures previously reported for the Co complexes prompted us to investigate potential catalyst intercalation into graphite via XPS coupled argon ion sputtering experiments.¹⁸ Bulk graphite with **1** adsorbed was used as representative material for the study, and the Co 2p core spectrum was monitored over the course of the experiment. After 20 minutes of sputtering at 4 kV, a significant portion of the Co 2p signal remained with no observed changes in the binding energies of the $2p_{1/2}$ and $2p_{3/2}$ signals, suggesting that the catalyst may be present below the surface layer of graphite (**Figure 3.48**). Analysis of the S and Cl 2p core spectra after sputtering also confirmed that the original species is still present with unaltered binding energies, again suggesting the molecular structure of the catalyst is preserved on the surface. Analysis of bulk

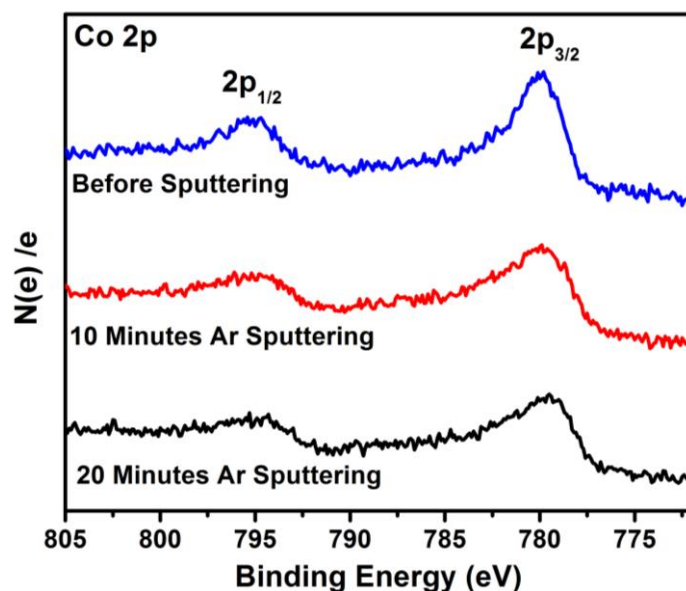


Figure 3.48. X-ray photoelectron spectroscopy analysis of TBA[Co(S₂C₆Cl₂H₂)₂] (**1**) on bulk graphite. Co 2p core spectra are monitored at intervals between argon ion sputtering performed with a 2 mm raster at a beam energy of 4 kV.

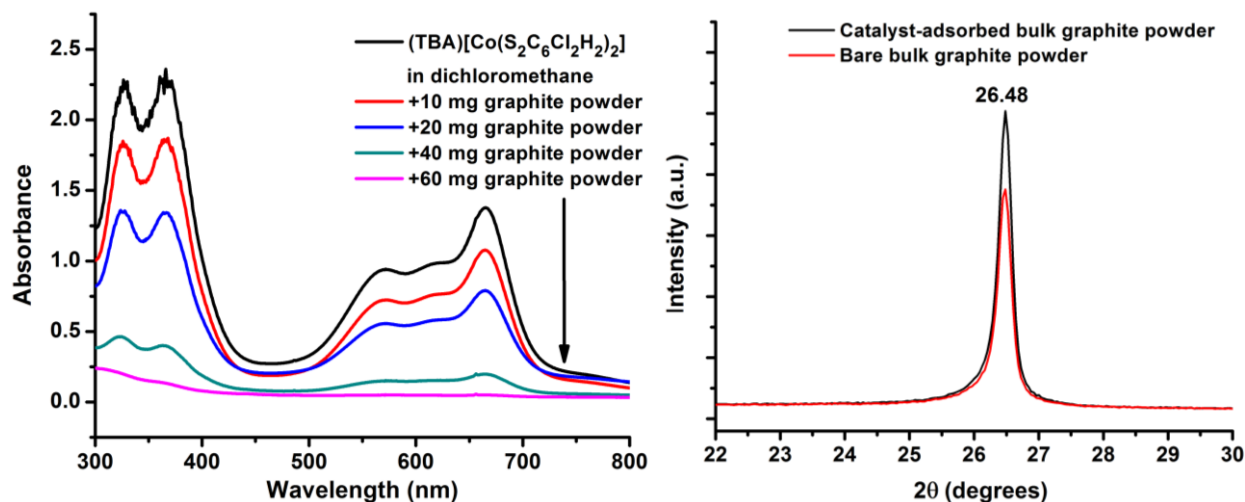


Figure 3.49. *Right:* UV-Visible spectra of TBA[Co(S₂C₆Cl₂H₂)₂] (**1**) in a 0.2 mM dichloromethane solution with the titration of bulk graphite powder. *Left:* X-ray diffraction of bulk graphite powder before (red trace) and after (black trace) adsorption of TBA[Co(S₂C₆Cl₂H₂)₂] (**1**).

graphite powder before and after catalyst adsorption by X-ray diffraction (XRD) shows no change in the graphite G peak with a 2θ value of 26.48 degrees, suggesting that the bulk of the powder is not intercalated by the catalyst molecules (**Figure 3.49**, right). However, it is worth noting that the catalyst loading in the graphite powder samples is approximately $4 \cdot 10^{-9}$ moles/mg according to the decrease in signal intensity in the UV-Visible spectra obtained from graphite titration into catalyst solutions (**Figure 3.49**, left). This catalyst loading corresponds to a mass percent of only 0.003% in the powder, which may not be high enough to observe a significant change via XRD. While these results may suggest only insertion into the edge of the graphite via defects or pores of the material, further analysis of the bulk material (ideally at higher catalyst loadings) is required to determine if catalyst is able to insert deeper into the bulk of the material.

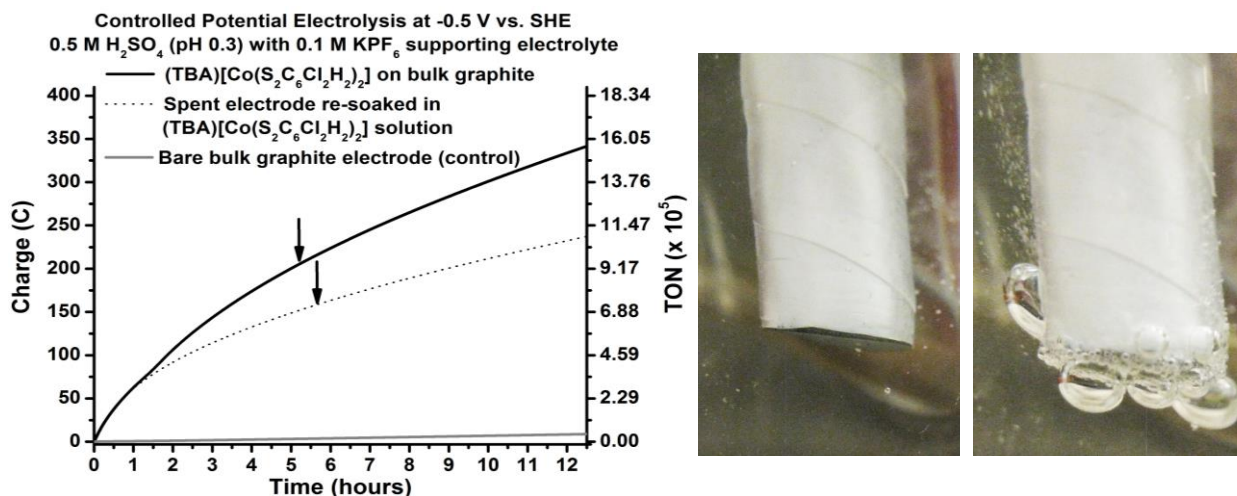


Figure 3.50. *Left:* Controlled Potential Electrolysis of (TBA)[Co(S₂C₆Cl₂H₂)₂] (**1**) adsorbed on a bulk graphite working electrode at -0.5 V in an aqueous pH 0.3 sulfuric acid solution with 0.1 M KPF₆ supporting electrolyte. Carbon felt is used as counter electrode and Ag/AgCl (sat. KCl) was used as a reference. *Right:* Bulk graphite electrode with **1** adsorbed before (left) and after (right) applying a potential of -0.5 V vs. SHE.

As reported in **Section 3.1**, the long-term activity of HOPG/**1** was assessed by gas chromatography-coupled controlled potential electrolysis (CPE) and it was determined that HOPG/**1** has quantitative Faradaic efficiency for H₂ production and residual activity after a 12 hour period.⁶⁹ Further CPE analysis of the HOPG/**1** system under more controlled pH conditions (-0.5 V, pH 0.3 H₂SO₄ solution) was reported in **Section 3.2**, and showed a turnover number (TON) of 1.27 10⁷ with 90% of catalytic activity ceasing after approximately 8 hours with an average molecular TOF of 441 s⁻¹. To determine if stability of **1** was comparable on bulk graphite and GPEN films, the alternative graphitic support systems were also studied under these conditions. CPE analysis of bulk graphite/**1** systems in a 0.5 M (pH 0.3) sulfuric acid solution with 0.1 M KPF₆ supporting electrolyte was observed to give an initial current density of 78.1 mA/cm², with an initial molecular TOF of 96 s⁻¹ over the first 30 minutes determined from the charge passed (37.7 C) and the catalyst loading from CV integration (**Figure 3.50**). This rate is significantly lower compared to the initial rate previously seen for HOPG/**1**. The overall increase in current density can therefore be attributed to the substantially

higher catalyst loading observed on bulk graphite electrodes compared to HOPG, as opposed to increased catalytic performance. With the use of inexpensive graphite electrodes, this current density translates to a cost of less than \$0.03 per mA (~\$2/electrode). As observed for the HOPG/1 systems, a gradual decrease in current density is observed, reaching a plateau current of 12% of the initial current density after approximately 8 hours. During this period, 190 C of charge is passed at the bulk graphite/1 electrode, providing a TON estimate of 8.71×10^5 and an average TOF of 30 s^{-1} . Upon soaking the spent electrode in the same catalyst solution, a second electrolysis experiment with the electrode shows an initial current density of 80 mA/cm^2 , approximately the same as the original value (Figure 2). Activity duration was seen to be ~2 hours lower than in the first experiment, indicating the graphitic supports can be reloaded with catalyst and reused, albeit with a slight decrease in performance.

Analysis of GPEN films on glassy carbon by CPE at -0.5 V vs. SHE in $\text{pH } 1.5 \text{ H}_2\text{SO}_4$ (Figure 3.51) shows an initial current density of 35 mA/cm^2 , with a total charge of 17.5 C

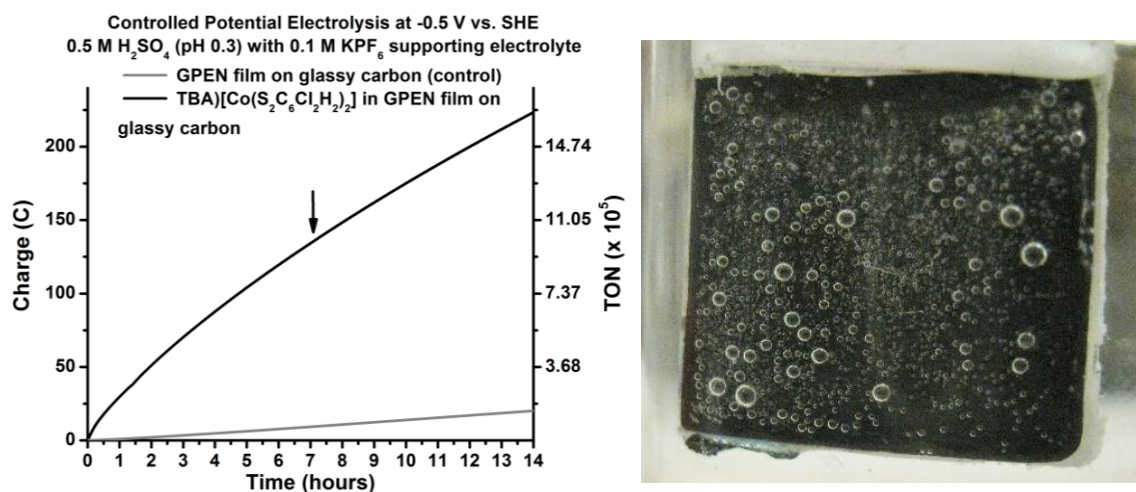


Figure 3.51. *Left:* Charge accumulation over time for the controlled potential electrolysis of a GPEN film on glassy carbon at -0.5 V vs. SHE in a $\text{pH } 0.3$ sulfuric acid solution before (grey) and after (black) soaking the graphite powder in a 5 mM solution of $\text{TBA}[\text{Co}(\text{S}_2\text{C}_6\text{H}_2\text{Cl}_2)_2]$ (**1**). *Right:* Formation of hydrogen gas at the surface of a GPEN film upon applying a potential of -0.5 V vs. SHE .

accumulated in the first 30 minutes. This corresponds to a molecular TOF of 47 s^{-1} , which is similar to the initial rate previously seen for HOPG/1. The activity profile over time seen for bulk graphite/1 is maintained in the films, with a gradual decrease in current density reaching a plateau current after approximately 7 hours and 134 C, with a TON estimate of 9.87×10^5 and an average TOF of 39 s^{-1} over this period. The plateau current for the films is notably higher than that of the bulk graphite/1 system, with approximately 37% (13 mA/cm^2) of the initial current density persisting for the remainder of the 14 hour experiment.

In summary, in this study we compare adsorption and electrocatalytic activity of cobalt bis(benzenedithiolene) dihydrogen production catalysts across a variety of graphitic surfaces. Inexpensive graphite in the form of bulk graphite and pencil graphite electrodes were found to be an effective support for catalyst loading, and exhibited similar electrochemical characteristics as previously observed on HOPG, but at a fraction of the cost. Further, these graphite/catalyst systems improve on the HOPG system in a number of aspects, including catalyst loading and overpotential to achieve a 10 mA/cm^2 current density, making graphite-supported catalyst systems an exciting prospect for use in devices for dihydrogen production. Initial evidence of catalyst intercalation into graphite was also obtained via XPS sputtering experiments, which explain the low retention of catalyst observed for single-layer graphene. Finally, catalyst-adsorbed graphite powder embedded in nafion films have been shown to conserve electrocatalytic behaviour while improving catalyst loading. This comprises one of the most versatile support platforms for these catalyst systems to date. Investigation of these materials especially when embedded in conductive films for use in fuel cells and for a variety of other applications is currently underway.

Experimental Section

General Methods

Chemicals were of highest purity grade commercially available and used without further purification (unless mentioned in the following). Methanol (anhydrous, ACS grade) was purchased from Fisher and distilled over calcium hydride, then degassed via extended dinitrogen purges prior to use. Acetonitrile (ACS grade), sodium methoxide, trifluoroacetic acid, sulfuric acid, potassium ferricyanide, and potassium ferrocyanide were purchased from Fisher. 3,6-dichloro-1,2-benzenedithiol was purchased from Sigma and used without further purification. Graphite powder was purchased from MTI Corp. All procedures were performed under a dinitrogen atmosphere unless otherwise specified.

Synthesis

Cobalt bis(dithiolate) complexes were prepared as previously reported.^{18,69}

Tetrabutylammonium Co-bis(3,6-dichlorobenzenedithiolate) (1)

In a N₂ atmosphere glove box a solution of 3,6-dichloro-1,2-benzenedithiol (0.21 g, 2.05 mmol) and sodium methoxide (0.23 g, 4.10 mmol) in methanol was added dropwise to a suspension of cobalt(II) sulfate hexahydrate (0.283 g, 1 mmol) in 30 mL of dry methanol, and the resulting solution was stirred for 2 hours. A solution of tetrabutylammonium bromide (1.05 mmol) in 5 mL methanol was added at this time, and the solution was stirred for an additional 2 hours. The solvent volume was reduced by vacuum to <10 mL, giving a precipitate which was filtered, washed with methanol and dried. Recrystallization of the solid from dichloromethane/ether afforded 0.46 g (64%) of the complex as a dark blue microcrystalline solid. For characterization, see experimental sections in **3.1** and **3.2**.

Electrochemical Measurements

All electrochemical measurements were conducted in the same manner and with the same materials and equipment as detailed in the experimental section **3.2**.

Determination of Catalytic TOF

The two primary methods for calculating turnover frequency outline in **Section 3.1**, the method in the text by Bard and Faulkner (using **equation 1**) and the foot-of-the-wave analysis reported by Saveant and coworkers (using **equations 2 and 3**), were also used in this study.^{67,68} The methods were applied as reported in the experimental details of **Section 3.1**.

Electrode Preparation

Bulk graphite electrodes

Graphite rods of ¼ inch diameter were purchased from NAC carbon products, Inc. (ash level <5 ppm) and then coated along the rod length with Loctite insulating epoxy (McMaster Carr, E-30CL) to construct disk electrodes which were polished with sandpaper (McMaster Carr, 4673A73), alumina (BASi, CF-1050), and finally with 15 µm diamond polish (BASi, MF-2051).

Graphite powder/nafion electrodes

Graphite powder was prepared by taking a graphite rod and filing it using a metal file to provide a fine powder. The powder was then soaked in an acetonitrile catalyst solution, after which it was filtered, rinsed extensively with fresh acetonitrile, and dried. The powder was then suspended in a Nafion perfluorinated resin solution (Sigma, 274704) at a concentration of 50 mg/mL. A small volume of the suspension (~0.5 mL) was subsequently dropped on a freshly purchased and polished glassy carbon electrode to form a Nafion film with embedded graphite particles.

Pencil graphite electrodes

Pencils were purchased from a local stationary (HB, Abbott) and were electrochemically pretreated using the methods described by Keskin and coworkers.⁸⁵ The pencil electrode was electrolyzed at 1.4 V vs. Ag/AgCl in a 0.1 M KPF₆ solution for 1 minute without stirring, after which time the surface was rinsed and soaked in catalyst solution for analysis.

Glassy carbon/graphene and FTO/graphene electrodes

Predominantly single-layer graphene was purchased from ACS materials and treated in a 0.05 g/mL aqueous solution of iron nitrate (Sigma, 96%) to dissolve the copper layer, after which the graphene piece was floated on to the FTO or glassy carbon electrode. After drying, the graphene-coated electrodes were soaked in solutions of isopropanol, acetone, and dichloromethane to remove the protective PMMA layer from the graphene surface. Finally, the electrodes prepared in this way were then soaked in catalyst solution for further analysis.

X-Ray Diffraction

X-ray diffraction patterns were recorded on a Bruker D8 Advance diffractometer equipped with a graphite monochromator, a Lynx-Eye detector, and parallel beam optics using Cu-K α radiation ($\lambda = 1.54184 \text{ \AA}$). Patterns were collected using a 0.6 mm incidence slit, with a step size and scan rate of 0.048/step and 0.5 s/step, respectively.

X-ray photoelectron Spectroscopy

All XPS data was collected using the same equipment and methods described in the experimental details of **Section 3.2**. Data analysis was also performed using the same software and fitting parameters as previously described.

UV-Visible Spectroscopy

All spectra were collected on the same instrument defined in the experimental details of **Section 3.1**.

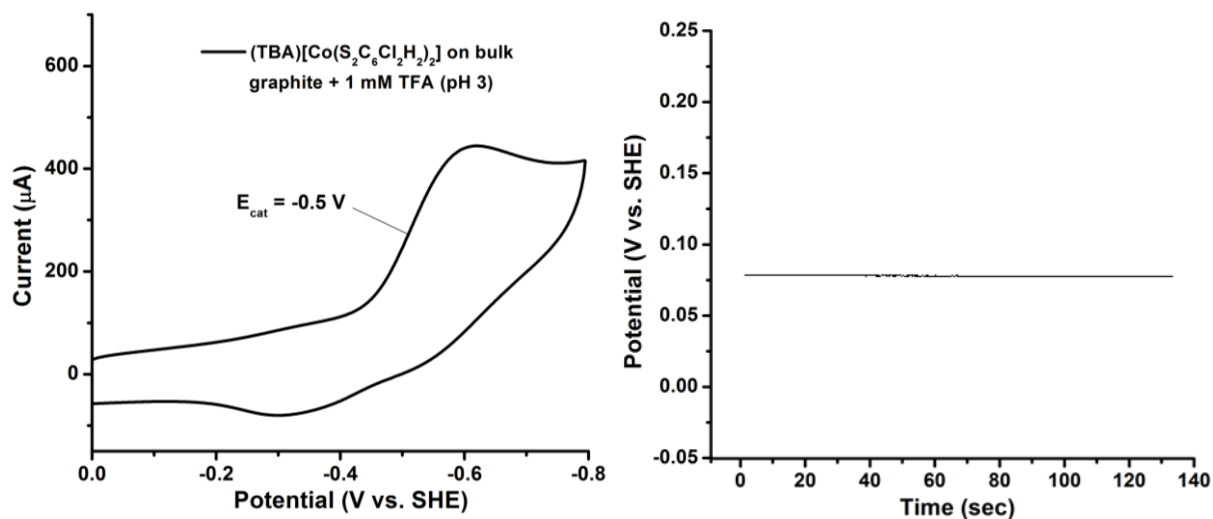


Figure 3.52. *Left:* Cyclic voltammety of (TBA)[Co(S₂C₆Cl₂H₂)₂] (**1**) adsorbed on a bulk graphite working electrode in a 1 mM TFA solution with a 50 mV/s scan rate as an example of how overpotential was calculated ($\eta = E_{\text{cat}} - Pt(E_{\text{OC}})$). *Right:* Open circuit potential over time of a platinum mesh working electrode in the same acid solution under 1 atm H₂ atmosphere to indicate overpotential. The solution contained 0.1 M aqueous potassium hexafluorophosphate. The counter electrode was a platinum wire, and the reference was an Ag/AgCl (saturated KCl solution) electrode. Potentials are reported vs. the standard hydrogen electrode.

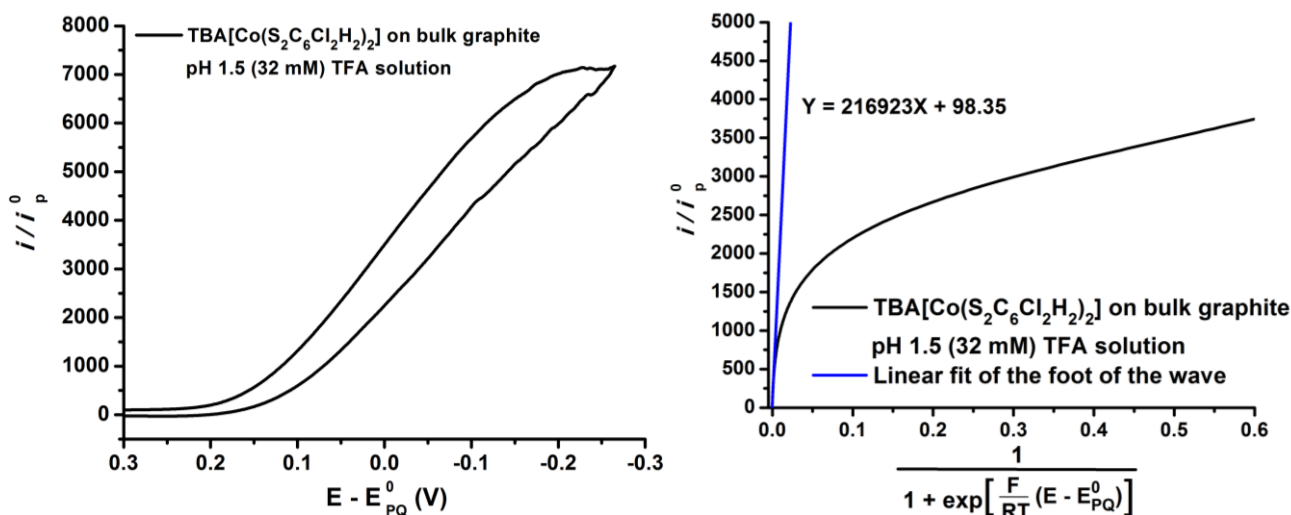


Figure 3.53. Foot-of-the-wave analysis of (TBA)[Co(S₂C₆Cl₂H₂)₂] (**1**) on bulk graphite in the presence of 32 mM TFA. For **1** adsorbed on bulk graphite with 32 mM TFA, foot-of-the-wave analysis gives a slope of 2.17×10^5 , resulting in a bimolecular rate constant of $2.85 \times 10^{11} \text{ M}^{-1} \text{ s}^{-1}$ (from **equation 3**).

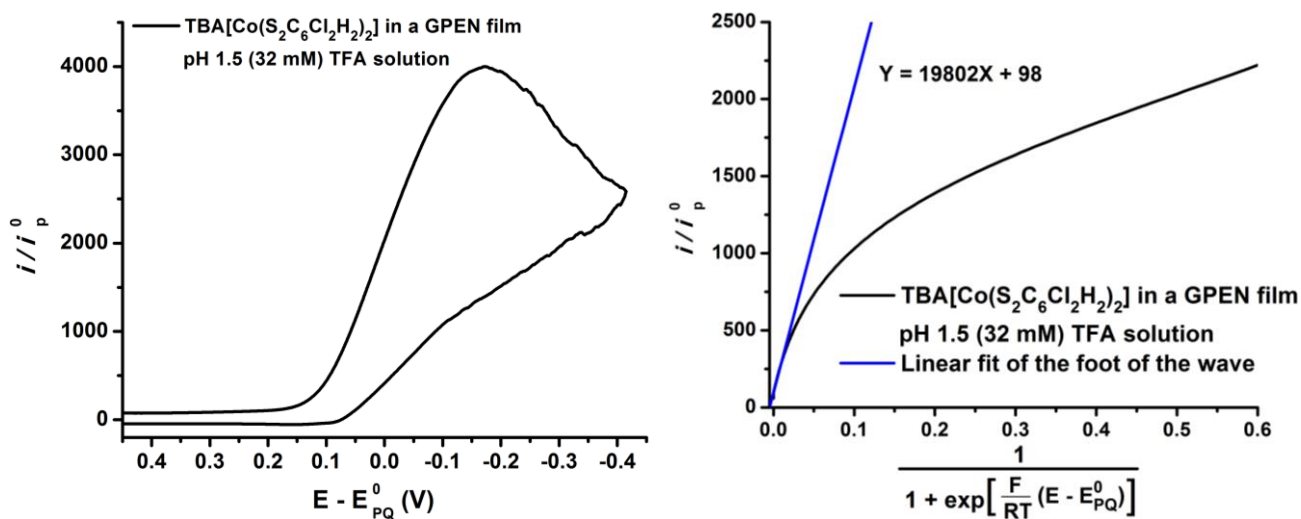


Figure 3.54. Foot-of-the-wave analysis of (TBA)[Co(S₂C₆H₂Cl₂)₂] (**1**) adsorbed on bulk graphite powder embedded in nafion (50 mg/mL) in the presence of 32 mM TFA. For **1** in a GPEN film with 32 mM TFA, foot-of-the-wave analysis gives a slope of 1.98×10^4 , resulting in a bimolecular rate constant of $2.38 \times 10^9 \text{ M}^{-1} \text{ s}^{-1}$ (from **equation 3**).

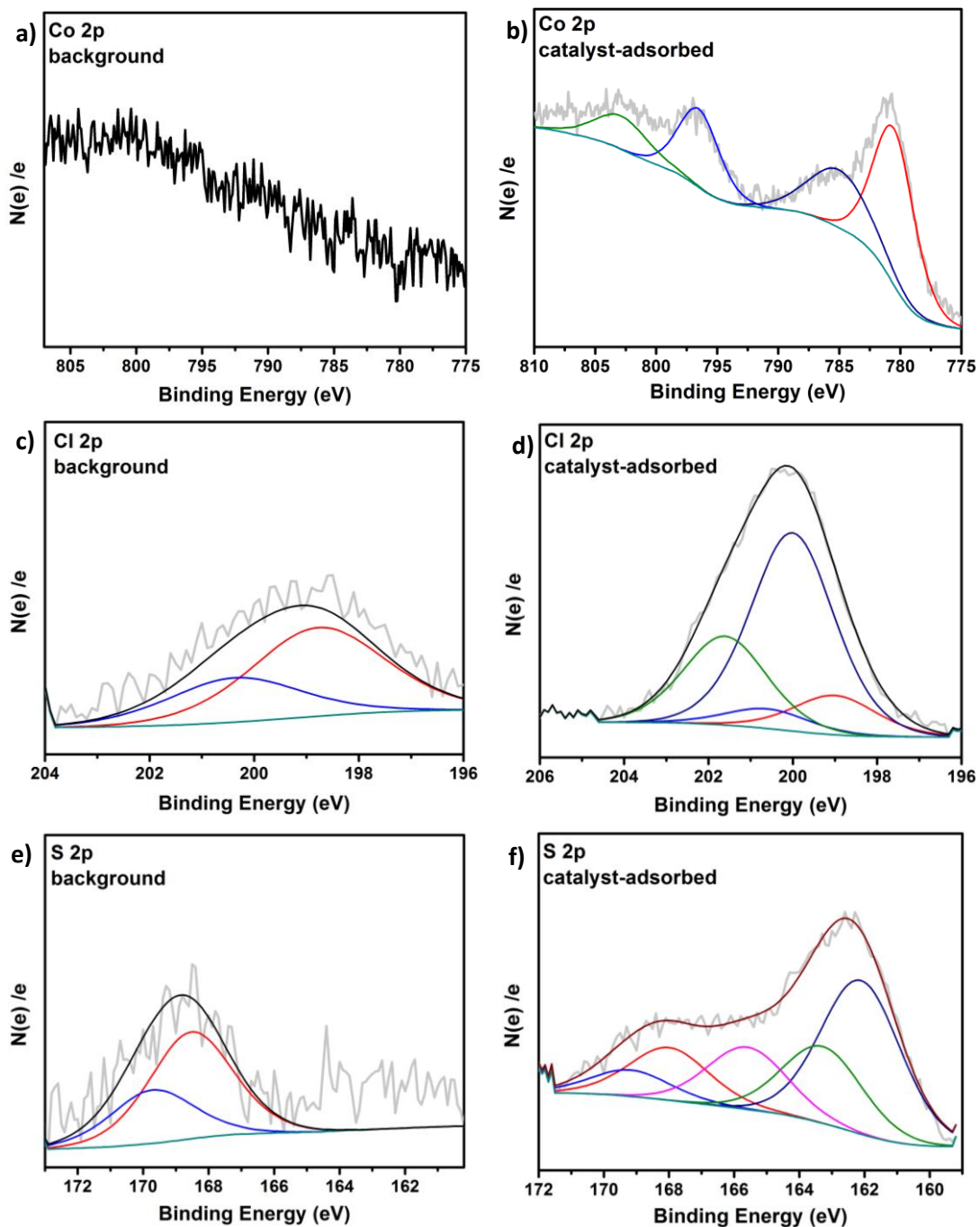


Figure 3.55. X-ray photoelectron spectroscopy (XPS) analysis of TBA[Co(S₂C₆Cl₂H₂)₂] (**1**) on a FTO/graphene electrode. (a) background Co 2p core level XPS spectrum; (b) Co 2p core level XPS spectrum of catalyst-adsorbed FTO/graphene; (c) background Cl 2p core level XPS spectrum of bare FTO/graphene; (d) Cl 2p core level XPS spectrum of catalyst-adsorbed FTO/graphene; (e) background S 2p core level XPS spectrum of bare FTO/graphene; (f) S 2p core level XPS spectrum of catalyst-adsorbed FTO/graphene. Envelope (black) omitted in some spectra for clarity.

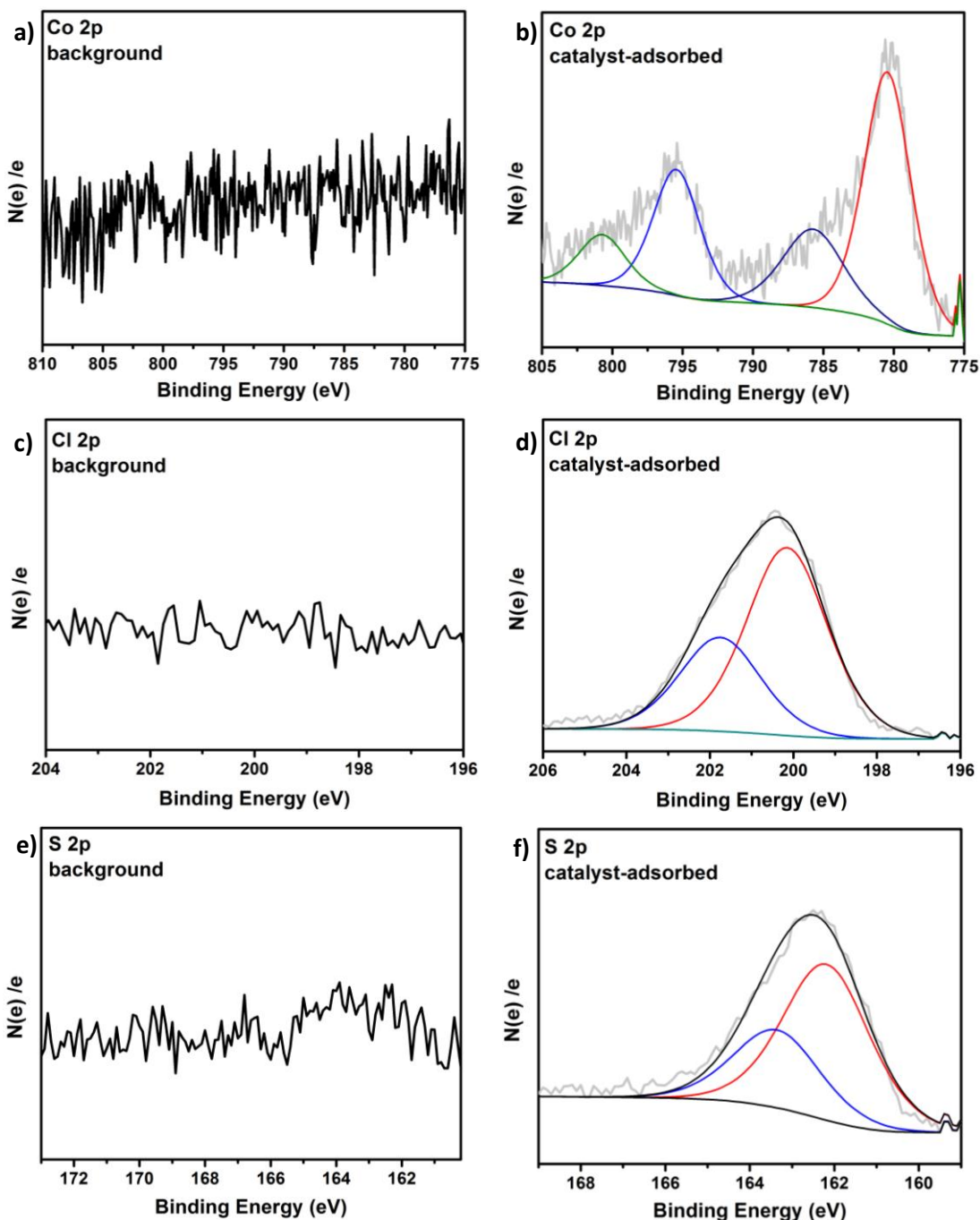


Figure 3.56. X-ray photoelectron spectroscopy (XPS) analysis of TBA[Co(S₂C₆Cl₂H₂)₂] (**1**) on bulk graphite powder used in GPEN films. (a) background Co 2p core level XPS spectrum; (b) Co 2p core level XPS spectrum of catalyst-adsorbed GPEN film; (c) background Cl 2p core level XPS spectrum of bare GPEN film; (d) Cl 2p core level XPS spectrum of catalyst-adsorbed GPEN film; (e) background S 2p core level XPS spectrum of bare GPEN film; (f) S 2p core level XPS spectrum of catalyst-adsorbed GPEN film. Envelope (black) omitted in some spectra for clarity.

References

- (1) Beyler, M.; Ezzaher, S.; Karnahl, M.; Santoni, M.-P.; Lomoth, R.; Ott, S. *Chem. Commun.* **2011**, *47*, 11662.
- (2) Canaguier, S.; Artero, V.; Fontecave, M. *J. Chem. Soc. Dalton Trans.* **2008**, 315.
- (3) Capon, J.-F.; Ezzaher, S.; Gloaguen, F.; Pétillon, F. Y.; Schollhammer, P.; Talarmin, J. *Chem. Eur. J.* **2008**, *14*, 1954.
- (4) Baffert, C.; Artero, V.; Fontecave, M. *Inorg. Chem.* **2007**, *46*, 1817.
- (5) Yu, Z.; Wang, M.; Li, P.; Dong, W.; Wang, F.; Sun, L. *J. Chem. Soc. Dalton Trans.* **2008**, 2400.
- (6) Roy, S.; Mazinani, S. K. S.; Groy, T. L.; Gan, L.; Tarakeshwar, P.; Mujica, V.; Jones, A. K. *Inorg. Chem.* **2014**, *53*, 8919.
- (7) Dempsey, J. L.; Brunschwig, B. S.; Winkler, J. R.; Gray, H. B. *Acc. Chem. Res.* **2009**, *42*, 1995.
- (8) McKone, J. R.; Marinescu, S. C.; Brunschwig, B. S.; Winkler, J. R.; Gray, H. B. *Chem. Sci.* **2014**, *5*, 865.
- (9) Wang, M.; Chen, L.; Sun, L. *Energy & Environmental Science* **2012**, *5*, 6763.
- (10) Helm, M. L.; Stewart, M. P.; Bullock, R. M.; DuBois, M. R.; DuBois, D. L. *Science* **2011**, *333*, 863.
- (11) Losse, S.; Vos, J. G.; Rau, S. *Coord. Chem. Rev.* **2010**, *254*, 2492.
- (12) Tard, C.; Pickett, C. J. *Chem. Rev.* **2009**, *109*, 2245.
- (13) Stewart, M. P.; Ho, M.-H.; Wiese, S.; Lindstrom, M. L.; Thogerson, C. E.; Raugei, S.; Bullock, R. M.; Helm, M. L. *J. Am. Chem. Soc.* **2013**, *135*, 6033.
- (14) Eckenhoff, W. T.; Eisenberg, R. *Dalton Trans.* **2012**, *2012*, 13004.
- (15) Dey, S.; Rana, A.; Dey, S. G.; Dey, A. *ACS Catalysis* **2013**, *3*, 429.
- (16) Eckenhoff, W. T.; McNamara, W. R.; Du, P.; Eisenberg, R. *Biochimica et Biophysica Acta (BBA) - Bioenergetics* **2013**, *1827*, 958.

- (17) McNamara, W. R.; Han, Z.; Alperin, P. J.; Brennessel, W. W.; Holland, P. L.; Eisenberg, R. *J. Am. Chem. Soc.* **2011**, *133*, 15368.
- (18) McNamara, W. R.; Han, Z.; Yin, C.-J.; Brennessel, W. W.; Holland, P. L.; Eisenberg, R. *Proc. Natl. Acad. Sci. USA* **2012**, *109*, 15594.
- (19) Lakadamyali, F.; Kato, M.; Muresan, N. M.; Reisner, E. *Angew. Chem. Int. Ed.* **2012**, *51*, 9381.
- (20) Gao, W.; Ekström, J.; Liu, J.; Chen, C.; Eriksson, L.; Weng, L.; Åkermark, B.; Sun, L. *Inorg. Chem.* **2007**, *46*, 1981.
- (21) Duan, L.; Wang, M.; Li, P.; Na, Y.; Wang, N.; Sun, L. *J. Chem. Soc. Dalton Trans.* **2007**, 1277.
- (22) Cheah, M. H.; Tard, C.; Borg, S. J.; Liu, X.; Ibrahim, S. K.; Pickett, C. J.; Best, S. P. *J. Am. Chem. Soc.* **2007**, *129*, 11085.
- (23) Bigi, J. P.; Hanna, T. E.; Harman, W. H.; Chang, A.; Chang, C. J. *Chem. Commun.* **2010**, *46*, 958.
- (24) Pantani, O.; Naskar, S.; Guillot, R.; Millet, P.; Anxolabéhère-Mallart, E.; Aukauloo, A. *Angew. Chem. Int. Ed. Engl.* **2008**, *47*, 9948.
- (25) McCrory, C. C. L.; Uyeda, C.; Peters, J. C. *J. Am. Chem. Soc.* **2012**, *134*, 3164.
- (26) Hu, X.; Brunschwig, B. S.; Peters, J. C. *J. Am. Chem. Soc.* **2007**, *129*, 8988.
- (27) Berben, L. A.; Peters, J. C. *Chem. Commun.* **2010**, *46*, 398.
- (28) Andreiadis, E. S.; Jacques, P.-A.; Tran, P. D.; Leyris, A.; Chavarot-Kerlidou, M.; Jousseme, B.; Matheron, M.; Pecaut, J.; Palacin, S.; Fontecave, M.; Artero, V. *Nat. Chem.* **2013**, *5*, 48.
- (29) Carroll, M. E.; Barton, B. E.; Gray, D. L.; Mack, A. E.; Rauchfuss, T. B. *Inorg. Chem.* **2011**, *50*, 9554.
- (30) Gärtner, F.; Boddien, A.; Barsch, E.; Fumino, K.; Losse, S.; Junge, H.; Hollmann, D.; Brückner, A.; Ludwig, R.; Beller, M. *Chemistry – A European Journal* **2011**, *17*, 6425.
- (31) Rakowski DuBois, M.; DuBois, D. L. *Acc. Chem. Res.* **2009**, *42*, 1974.

- (32) Ott, S.; Kritikos, M.; Åkermark, B.; Sun, L. *Angew. Chem. Int. Ed. Engl.* **2003**, *42*, 3285.
- (33) Wiedner, E. S.; Yang, J. Y.; Dougherty, W. G.; Kassel, W. S.; Bullock, R. M.; DuBois, M. R.; DuBois, D. L. *Organometallics* **2010**, *29*, 5390.
- (34) Orthaber, A.; Karnahl, M.; Tschierlei, S.; Streich, D.; Stein, M.; Ott, S. *Dalton Transactions* **2014**, *43*, 4537.
- (35) Eady, S. C.; Breault, T.; Thompson, L.; Lehnert, N. *Dalton Transactions* **2016**.
- (36) Ibrahim, S. K.; Liu, X.; Tard, C.; Pickett, C. J. *Chem. Commun.* **2007**, 1535.
- (37) Chiou, T.-W.; Lu, T.-T.; Wu, Y.-H.; Yu, Y.-J.; Chu, L.-K.; Liaw, W.-F. *Angew. Chem. Int. Ed.* **2015**, *54*, 14824.
- (38) Tran, P. D.; Le Goff, A.; Heidkamp, J.; Joussetme, B.; Guillet, N.; Palacin, S.; Dau, H.; Fontecave, M.; Artero, V. *Angew. Chem. Int. Ed.* **2011**, *50*, 1371.
- (39) Le Goff, A.; Artero, V.; Joussetme, B.; Tran, P. D.; Guillet, N.; Métayé, R.; Fihri, A.; Palacin, S.; Fontecave, M. *Science* **2009**, *326*, 1384.
- (40) Krawicz, A.; Yang, J.; Anzenberg, E.; Yano, J.; Sharp, I. D.; Moore, G. F. *J. Am. Chem. Soc.* **2013**, *135*, 11861.
- (41) Seo, J.; Pekarek, R. T.; Rose, M. J. *Chem. Commun.* **2015**, *51*, 13264.
- (42) Rao, H.; Wang, Z.-Y.; Zheng, H.-Q.; Wang, X.-B.; Pan, C.-M.; Fan, Y.-T.; Hou, H.-W. *Catalysis Science & Technology* **2015**, *5*, 2332.
- (43) Fei, H.; Dong, J.; Arellano-Jimenez, M. J.; Ye, G.; Dong Kim, N.; Samuel, E. L. G.; Peng, Z.; Zhu, Z.; Qin, F.; Bao, J.; Yacaman, M. J.; Ajayan, P. M.; Chen, D.; Tour, J. M. *Nat Commun* **2015**, *6*.
- (44) Zou, X.; Huang, X.; Goswami, A.; Silva, R.; Sathe, B. R.; Mikmeková, E.; Asefa, T. *Angew. Chem.* **2014**, *126*, 4461.
- (45) Chen, W.-F.; Muckerman, J. T.; Fujita, E. *Chem. Commun.* **2013**, *49*, 8896.
- (46) Hou, J.; Fang, M.; Cardenas, A. J. P.; Shaw, W. J.; Helm, M. L.; Bullock, R. M.; Roberts, J. A. S.; O'Hagan, M. *Energy & Environmental Science* **2014**, *7*, 4013.

- (47) Gao, M.-R.; Liang, J.-X.; Zheng, Y.-R.; Xu, Y.-F.; Jiang, J.; Gao, Q.; Li, J.; Yu, S.-H. *Nat Commun* **2015**, *6*.
- (48) Yang, Y.; Fei, H.; Ruan, G.; Tour, J. M. *Adv. Mater.* **2015**, *27*, 3175.
- (49) Nocera, D. G. *Acc. Chem. Res.* **2012**, *45*, 767.
- (50) Baker-Hawkes, M. J.; Billig, E.; Gray, H. B. *J. Am. Chem. Soc.* **1966**, *88*, 4870.
- (51) Sproules, S.; Wieghardt, K. *Coord. Chem. Rev.* **2011**, *255*, 837.
- (52) Downes, C. A.; Marinescu, S. C. *J. Am. Chem. Soc.* **2015**, *137*, 13740.
- (53) Clough, A. J.; Yoo, J. W.; Mecklenburg, M. H.; Marinescu, S. C. *J. Am. Chem. Soc.* **2015**, *137*, 118.
- (54) Letko, C. S.; Panetier, J. A.; Head-Gordon, M.; Tilley, T. D. *J. Am. Chem. Soc.* **2014**, *136*, 9364.
- (55) W. Seidel, W.; Ekkehardt Hahn, F. *J. Chem. Soc., Dalton Trans.* **1999**, 2237.
- (56) Nomura, M.; Fujita-Takayama, C.; Yagisawa, T.; Sugiyama, T.; Kajitani, M. *Dalton Transactions* **2013**, *42*, 4764.
- (57) Seidel, W. W.; Hahn, F. E. *Bioinorganic Chemistry and Applications* **2005**, *3*, 69.
- (58) Machata, P.; Herich, P.; Lušpai, K.; Bucinsky, L.; Šoralová, S.; Breza, M.; Kozisek, J.; Rapta, P. *Organometallics* **2014**, *33*, 4846.
- (59) Solis, B. H.; Hammes-Schiffer, S. *J. Am. Chem. Soc.* **2012**, *134*, 15253.
- (60) Eisenberg, R.; Gray, H. B. *Inorg. Chem.* **2011**, *50*, 9741.
- (61) Periyasamy, G.; Burton, N. A.; Hillier, I. H.; Vincent, M. A.; Disley, H.; McMaster, J.; Garner, C. D. *Faraday Discuss.* **2007**, *135*, 469.
- (62) Weingarten, A. S.; Kazantsev, R. V.; Palmer, L. C.; McClendon, M.; Koltonow, A. R.; SamuelAmanda, P. S.; Kiebala, D. J.; Wasielewski, M. R.; Stupp, S. I. *Nat Chem* **2014**, *6*, 964.
- (63) Hummers, W. S.; Offeman, R. E. *J. Am. Chem. Soc.* **1958**, *80*, 1339.

- (64) Zhao, X.; Georgakaki, I. P.; Miller, M. L.; Mejia-Rodriguez, R.; C.-Y., C.; Darensbourg, M. Y. *Inorg. Chem.* **2002**, *41*, 3917.
- (65) Sobon, G.; Sotor, J.; Jagiello, J.; Kozinski, R.; Zdrojek, M.; Holdynski, M.; Paletko, P.; Boguslawski, J.; Lipinska, L.; Abramski, K. M. *Opt. Express* **2012**, *20*, 19463.
- (66) Haber, J. A.; Lewis, N. S. *The Journal of Physical Chemistry B* **2002**, *106*, 3639.
- (67) Bard, A. J.; Faulkner, L. R. *Electrochemical Methods: Fundamentals and Applications*; 2nd edition ed., 2000.
- (68) Costentin, C.; Drouet, S.; Robert, M.; Savéant, J.-M. *J. Am. Chem. Soc.* **2012**, *134*, 11235.
- (69) Eady, S. C.; Peczonczyk, S. L.; Maldonado, S.; Lehnert, N. *Chem. Commun.* **2014**, *50*, 8065.
- (70) Lindberg, B. J.; Hamrin, K.; Johansson, G.; Gelius, U.; Fahlman, A.; Nordling, C.; Siegbahn, K. *Phys. Scr.* **1970**, *1*, 286.
- (71) Peng, S.; Li, L.; Han, X.; Sun, W.; Srinivasan, M.; Mhaisalkar, S. G.; Cheng, F.; Yan, Q.; Chen, J.; Ramakrishna, S. *Angew. Chem.* **2014**, *126*, 12802.
- (72) Clark, D. T.; Kilcast, D.; Musgrave, W. K. R. *Journal of the Chemical Society D: Chemical Communications* **1971**, 516b.
- (73) Blakemore, J. D.; Gupta, A.; Warren, J. J.; Brunschwig, B. S.; Gray, H. B. *J. Am. Chem. Soc.* **2013**, *135*, 18288.
- (74) Ding, S.-N.; Shan, D.; Cosnier, S.; Le Goff, A. *Chemistry – A European Journal* **2012**, *18*, 11564.
- (75) Jain, D.; Saha, A.; Marti, A. A. *Chem. Commun.* **2011**, *47*, 2246.
- (76) Park, S. I.; Quate, C. F. *Appl. Phys. Lett.* **1986**, *48*, 112.
- (77) Gwo, S.; Shih, C. K. *Physical Review B* **1993**, *47*, 13059.
- (78) Dreyer, D. R.; Park, S.; Bielawski, C. W.; Ruoff, R. S. *Chem. Soc. Rev.* **2010**, *39*, 228.
- (79) Erickson, K.; Erni, R.; Lee, Z.; Alem, N.; Gannett, W.; Zettl, A. *Adv. Mater.* **2010**, *22*, 4467.

- (80) Karunadasa, H. I.; Chang, C. J.; Long, J. R. *Nature* **2010**, *464*, 1329.
- (81) Quentel, F.; Passard, G.; Gloaguen, F. *Energy & Environmental Science* **2012**, *5*, 7757.
- (82) Hart, H.; Bashir-Hashemi, A.; Luo, J.; Meador, M. A. *Tetrahedron* **1986**, *42*, 1641.
- (83) Testaferri, L.; Tiecco, M.; Tingoli, M.; Chianelli, D.; Montanucci, M. *Synthesis* **1983**, *1983*, 751.
- (84) Liu, G.; Wu, B.; Zhang, J.; Wang, X.; Shao, M.; Wang, J. *Inorg. Chem.* **2009**, *48*, 2383.
- (85) Keskin, E.; Yardım, Y.; Şentürk, Z. *Electroanalysis* **2010**, *22*, 1191.
- (86) Harris, P. J. F. *Philosophical Magazine* **2004**, *84*, 3159.

Chapter 4

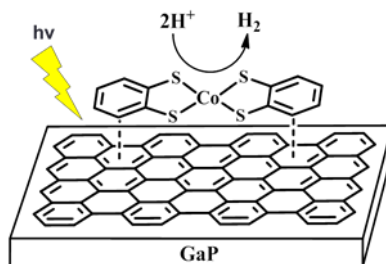
Application of Catalyst Interfaces on Semiconductor Surfaces

Introduction

As outlined in **Section 1.3**, the development of efficient interfaces coupling photosensitizers and catalysts is critical for the development of solar-to-fuel systems, and has been a substantial focus of electrocatalysis research in the last few decades.¹⁻⁴ Photocatalytic systems in which the catalyst and photosensitizer are directly coupled, such as by means of covalent attachment, have shown noticeably more promise in terms of stability and electron transfer rates.⁵⁻¹² However, many of these systems require a relatively large amount of synthetic preparation for this attachment, and often are effective in coupling only a very specific combination of catalyst and photosensitizer. The work outlined in this chapter aims to develop a system which minimizes the synthetic efforts required to provide a functional catalyst-semiconductor interface, and to increase the variance in catalyst-semiconductor pairings that can be facilitated with the same interface.

4.1. Construction and Characterization of Cobalt Bis(dithiolene) Catalyst-Adsorbed CH₃-GaP/Graphene Photoelectrodes

Graphene and reduced graphene oxide (RGO), both notably cheap and plentiful materials, have been researched for surface modification of a variety of semiconductor materials to enhance



Scheme 4.1. Schematic representation of photocatalytic hydrogen production at the surface of a graphene-covered gallium phosphide electrode with a cobalt bis(dithiolene) catalyst adsorbed.

electron transfer kinetics, decrease recombination, chemically passivate surfaces towards oxide formation, and even modify semiconductor electronic properties.¹³⁻¹⁹ In chapter 3, our detailed study of cobalt bis(dithiolene) hydrogen production catalyst derivatives adsorbed on a variety of graphitic supports including RGO evidences the ability of such graphitic supports to provide an effective catalyst-electrode interface. Given the ease with which these materials can be deposited on semiconductor surfaces either chemically or electrochemically and the benefits they inherently can provide to semiconductor function, use of graphene and RGO as catalyst interfaces has the potential to provide all the aforementioned benefits in addition to enabling more efficient solar-to-fuel conversion.

In this section the application of thin layers of RGO and predominantly single layer graphene on semiconductor surfaces to serve as a catalyst interface for cobalt bis(dithiolene) catalysts previously studied on graphitic supports (**Chapter 3**) is reported. Due to its strong driving force for proton reduction, the III-V semiconductor gallium phosphide (GaP), with an indirect band gap of 2.26 eV, was used in the form of p-type (zinc-doped) single crystals to facilitate a solar-driven cathodic process.²⁰ These photocatalytic manifolds for hydrogen production can be seen in **Scheme 4.1**. Preparation of methylated gallium phosphide surfaces and Grazing Angle

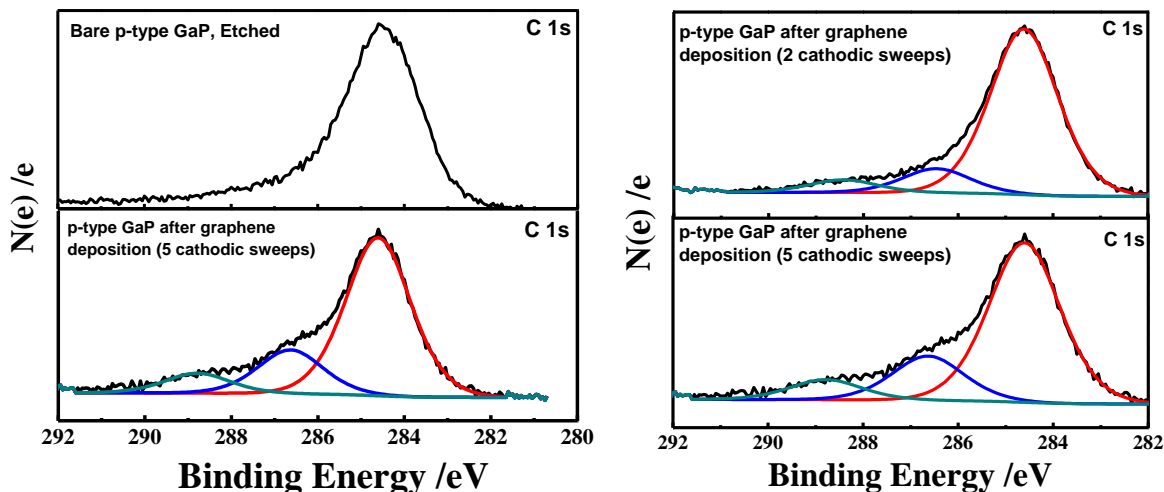


Figure 4.1. *Left:* XPS of a gallium phosphide surface before (top) and after (bottom) electrodeposition of RGO. *Right:* electrodeposition of RGO with two cathodic scans (top) and five cathodic scans (bottom).

Infrared Spectroscopy (GATR) measurements were performed by Betsy Brown and Sabrina Peczonczyk as part of a collaborative study between the Lehnert and Maldonado groups.

Construction of GaP/RGO Electrodes and Analysis as Catalyst Interfaces

Initial attempts at constructing these photocathode manifolds proceeded by electrodeposition of RGO on GaP surfaces using the same methods as for fluorine-doped tin oxide (FTO) substrates as described in **Chapters 2 and 3**. Cyclic voltammetry (CV) electrodeposition was performed with the GaP substrate used as a working electrode in the graphene oxide solution. Unlike in the case of the FTO surfaces, the opaque nature of the substrate did not allow for direct visual confirmation of RGO deposition. XPS of the RGO-deposited GaP surface confirmed an increase in signal in the C 1s spectrum indicative of C-O (hydroxyl, epoxy) groups at 286.7 eV and C=O (carbonyl groups) at 288.4 eV (**Figure 4.1**, left). This result mirrors those we observed previously on FTO electrodes and is consistent with previous reports of reduced graphene oxide on surfaces.²¹ Comparative analysis of the GaP surfaces after two and five cathodic scans during RGO deposition clearly shows an increase of the C-O and C=O signals relative to adventitious

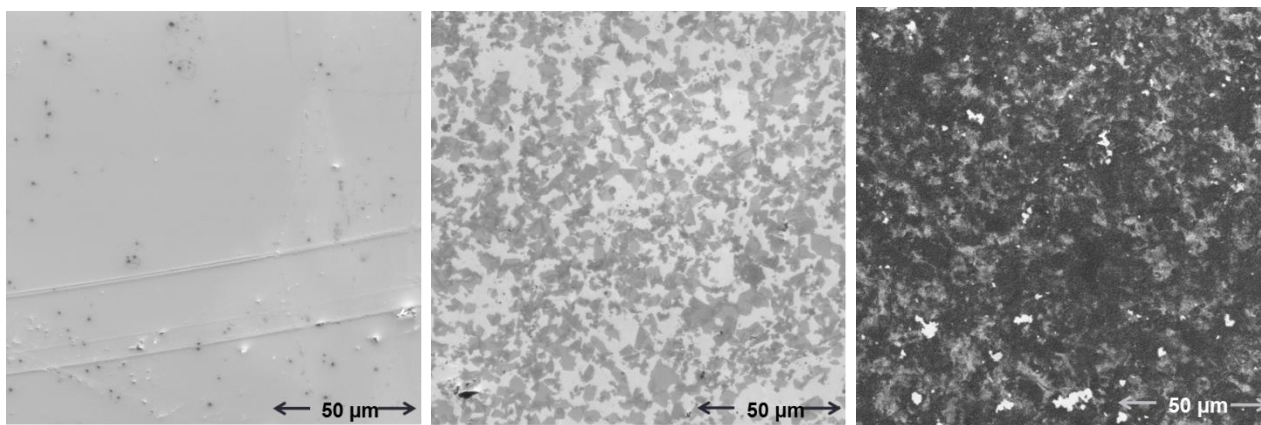


Figure 4.2. SEM image of a bare gallium phosphide surface (*left*), gallium phosphide with RGO electrodeposited on the surface (*middle*), and a FTO electrode with RGO electrodeposited on the surface (*right*).

carbon (**Figure 4.1**, right), indicating the relative amount of deposited RGO could be controlled by the number of cathodic scans.

Scanning electron microscopy (SEM) imaging of the GaP electrodes before and after RGO deposition also confirmed the presence of RGO on the semiconductor surface (**Figure 4.2**, left and middle); however, the loading was somewhat scarce with a large portion of uncovered GaP, notably much lower than that observed with the same number of CV deposition scans on FTO

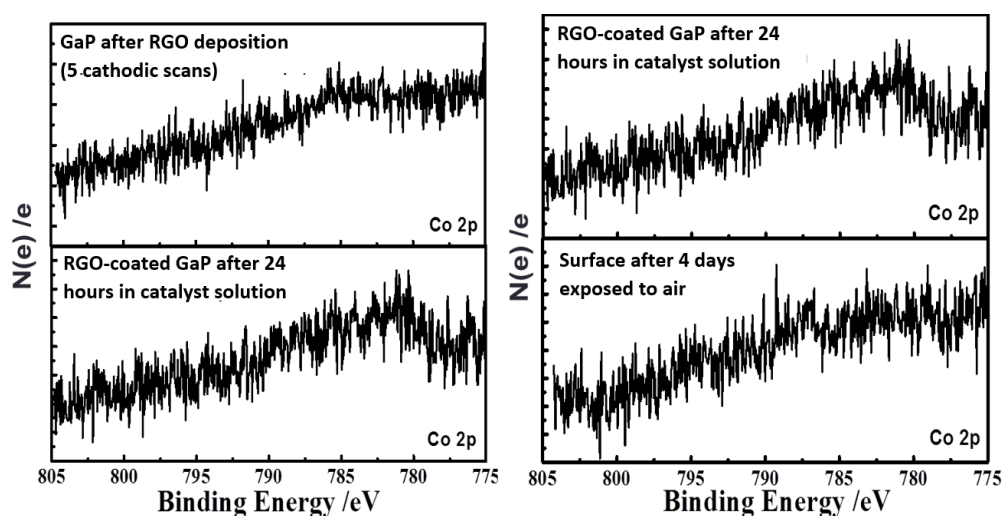


Figure 4.3. *Left:* XPS Co 2p core spectra of a GaP/RGO surface before (top) and after (bottom) adsorption of $(\text{TBA})[\text{Co}(\text{S}_2\text{C}_6\text{Cl}_2\text{H}_2)_2]$ (**1**). *Right:* GaP/RGO/**1** surface before (top) and after (bottom) exposure to air for 4 days. Data collected at a pass energy of 23.3 eV.

surfaces (**Figure 4.2**, middle and right). These differences were assumed to be due to the inherently lower free electron concentration and mobility in a p-type semiconductor material compared to the FTO metal oxide surface, and the results from XPS analysis suggest that coverage can be further increased if required by simply increasing the number of CV deposition scans.

Analysis of the RGO-deposited surfaces after soaking in an acetonitrile solution of (TBA)[Co(S₂C₆Cl₂H₂)₂] (**1**), however, showed very little signal above background in the Co 2p core spectra (**Figure 4.3**, left). In addition, analysis of the same surfaces after several days reveals a complete decrease of the observed Co 2p signal to background (**Figure 4.3**, right). This result indicates that very little catalyst is adsorbed to the GaP/RGO surface, and what little is adsorbed is not retained over time. These results are not in agreement with the typical stability of the cobalt bis(dithiolene) catalysts on RGO surfaces under ambient conditions (without applied potential), and were therefore attributed to the difference in RGO loading on the GaP surface.²² While an increase in the number of CV deposition scans or even controlled potential electrolysis at the GaP

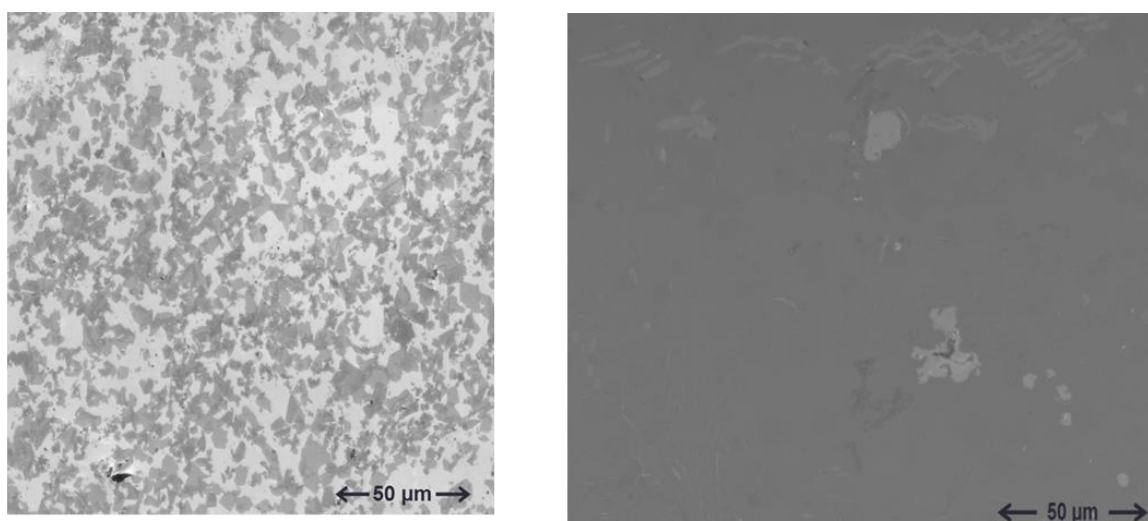


Figure 4.4. SEM image of a methylated gallium phosphide surface with RGO electrodeposited on the surface (*left*) and predominantly single layer graphene transferred on the surface (*right*).

surface could increase the RGO coverage, these options may also result in the partial reduction of GaP to gallium metal on the surface, disrupting the electronics of the semiconductor material.

Construction of CH₃-GaP/graphene Electrodes and Analysis as Catalyst Interfaces

To increase surface coverage with the graphitic support without degrading the gallium phosphide and to allow for more consistent surface properties from sample to sample, predominantly single layer graphene (ACS materials) was purchased and transferred to the GaP surface as outlined in the experimental section. While more expensive than RGO deposition (\$80 per cm²), this method was evidenced by SEM imaging to provide a more uniform topography and high coverage (**Figure 4.4**). As an additional modification, the p-type gallium phosphide surfaces were methylated prior to graphene coating, as recent work in the Maldonado group has highlighted the ability of short chain alkyl groups to chemically passivate GaP towards oxide formation while negligibly effecting the solar absorption properties.²³

XPS analysis of the graphene-coated CH₃-GaP surfaces after soaking overnight in a solution of **1** showed substantially higher signal above background in the Co 2p core spectra

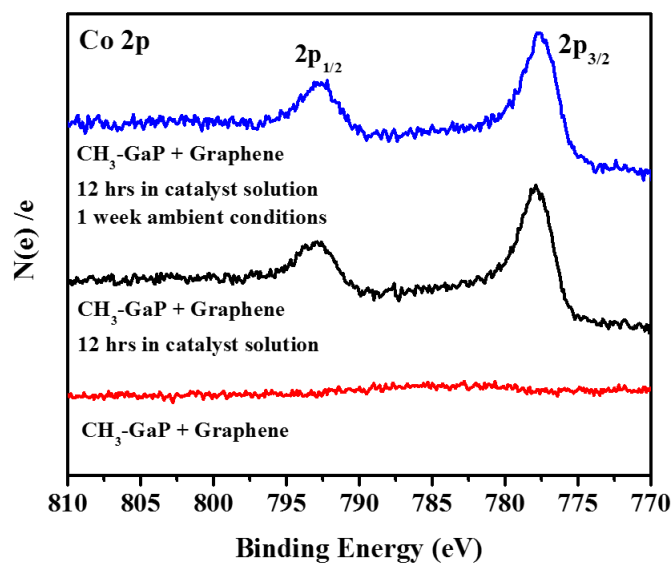


Figure 4.5. XPS Co 2p core spectra of (TBA)[Co(S₂C₆Cl₂H₂)₂] (**1**) adsorbed on CH₃-GaP/graphene collected at a pass energy of 160 eV.

(**Figure 4.5**, bottom and middle). In addition, analysis of the same surfaces after a week revealed an essentially unchanged Co 2p signal (**Figure 4.5**, top). These results confirm adsorption of the cobalt bis(dithiolene) catalysts to the graphene surface, and reflect the previously seen stability of the catalysts on graphitic surfaces even when open to air. This combined stability afforded by the methylation of GaP and observed for the adsorbed catalysts is impressive and ideal for use in device applications for photocatalytic H₂ production.

To further elucidate the nature of the adsorbed species on the CH₃-GaP/graphene surface, grazing angle attenuated total reflectance (GATR)-Fourier transform infrared (FTIR) spectroscopy was used to analyze the resulting surfaces. To compare to these data, an IR spectrum of the bulk solid material of **1** was also collected using an ATR accessory. An additional comparison was provided by a density functional theory (DFT) calculation of the IR spectrum, obtained from the optimized structure of [Co(S₂C₆Cl₂H₂)₂]⁻ with B3LYP/TZVP.²⁴ These spectra, which can be seen in **Figure 4.6**, show that the features observed for **1** in the bulk material and DFT calculation are largely conserved on the CH₃-GaP/graphene surface. A closer comparison of the peak energies across the spectra is provided in **Table 4.1**, showing that within approximately 10 wavenumbers

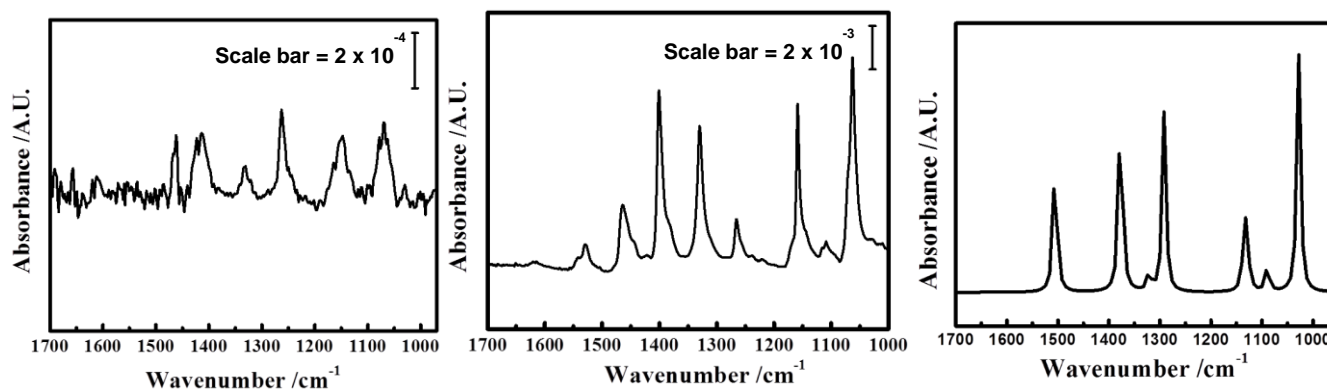


Figure 4.6. *Left:* GATR of (TBA)[Co(S₂C₆Cl₂H₂)₂]⁻ (**1**) adsorbed on CH₃-GaP/graphene; *Middle:* IR of solid bulk material of **1** by ATR; *Right:* calculated IR spectrum of (**1**) obtained from DFT calculations (B3LYP/TZVP).

Peak GATR	Peak Bulk	Peak Gaussian
1461	1464	1465
1413	1401	
1330	1330	1319
1263	1266	1260/1276
1147	1159	1142
1070	1063	1061

Table 4.1. IR spectra peak comparison of (TBA)[Co(S₂C₆Cl₂H₂)₂] (**1**) adsorbed on CH₃-GaP/graphene, solid bulk material of **1**, and the calculated IR spectrum of **1**.

the GATR spectrum closely matches the signals observed in the experimental and calculated spectra.

The CH₃-GaP/graphene/**1** surface was also analyzed by resonance Raman spectroscopy (rRaman) at an excitation wavelength of 647 nm, aligning with the broad absorption feature of **1** in the visible spectrum (see **Figure 3.15**).²⁵ For comparison, **1** was also analyzed by rRaman at the same excitation wavelength in a 1:1 propionitrile:butyronitrile solution (chosen due to the enhanced glassing ability of this solvent mixture). The spectra, which can be seen in **Figure 4.7**, show several features in solution that appear to be conserved on the GaP surface. Specifically, the features present in the solution spectrum at approximately 1150 and 1280 wavenumbers have corresponding signals in the surface spectrum at approximately the same energies. Further confirmation of the nature of these signals could be obtained by rRaman analysis of isotopically labeled compounds (e.g. ³⁴S or even Se substitution for S).

These data strongly suggest that the species adsorbed on the CH₃-GaP/graphene surfaces is in fact the molecular species [Co(S₂C₆Cl₂H₂)₂]. This is also in agreement with XPS analysis for FTO/graphene/**1** systems, which shows features both confirming the typical cobalt bis(dithiolene)

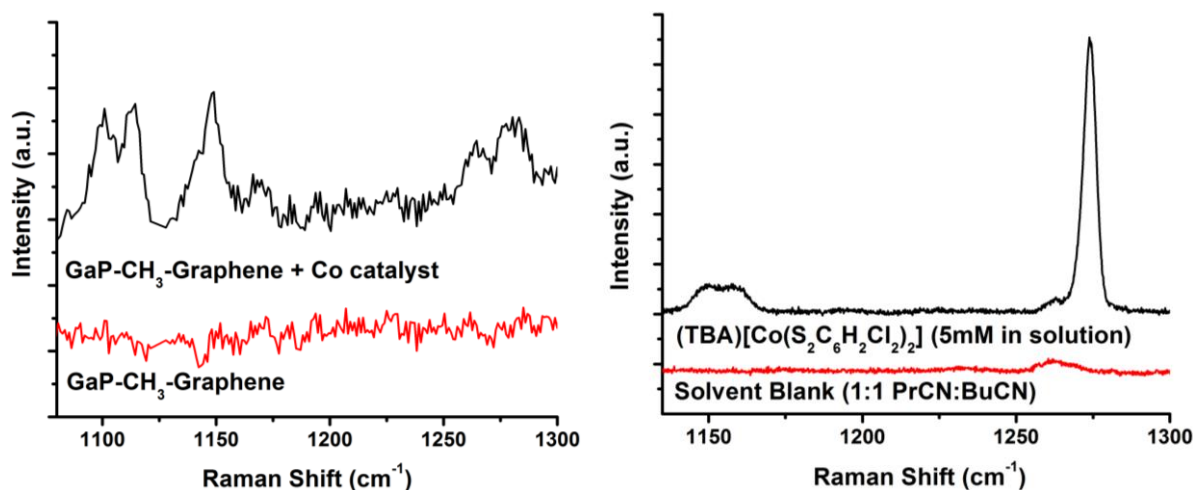


Figure 4.7. *Left:* Resonance Raman (647 nm) of (TBA)[Co(S₂C₆Cl₂H₂)₂] (**1**) adsorbed on CH₃-GaP/graphene; *Right* Resonance Raman of (TBA)[Co(S₂C₆Cl₂H₂)₂] (**1**) in a frozen 1:1 propionitrile:butyronitrile solution, measured at liquid nitrogen temperature.

electronic structure and the presence of ligand components (Cl) [see **Section 3.3**].^{8,26-28} These results also confirm that graphitic supports can effectively serve as an interface for the functionalization of semiconductor surfaces with cobalt bis(dithiolene) catalysts for hydrogen production. Unfortunately, as observed for the FTO/graphene/**1** heterogeneous catalyst systems detailed in **Section 3.3**, loss of the catalyst species occurs readily upon CV cycling at pH values below 3 (where the majority of catalyst activity is observed), and in some cases simply upon CV cycling of the CH₃-GaP/graphene/**1** electrodes. Based on the thorough analysis of these catalysts in chapter 3, catalyst loss from CH₃-GaP/graphene/**1** is likely caused by desorption of the catalyst from the single-layer graphene surfaces.

In summary, gallium phosphide surfaces have been modified with thin graphitic supports such as RGO and graphene, and the latter was determined to give a more full and consistent surface coverage without risk of damaging the semiconductor surface. These surfaces have been shown to successfully adsorb and retain cobalt bis(dithiolene) catalysts under ambient conditions as evidenced by GATR, rRaman and X-ray photoelectron spectroscopies, and were observed to have

similar spectroscopic features compared to the catalysts in the bulk solid and in solution. Preliminary studies for the CH₃-GaP/graphene/1 photocathode system have shown low catalyst stability under applied potentials, particularly in more acidic solutions, likely due to catalyst desorption under these conditions. To combat this desorption, results from previous analyses of the Co catalysts on graphitic supports suggests that introduction of a more porous and layered support with higher surface area than single-layer graphene may help to better retain adsorbed catalysts under turnover conditions (see **Section 3.3**).

Thus, future direction should focus on applying thicker layers of RGO or thin films of graphite to GaP surfaces. While thicker RGO coatings could be applied simply by performing controlled potential electrolysis for an extended period at the GaP working electrode, the resulting degradation of GaP via reduction to metallic gallium may compromise the efficiency of the resulting photocathode system. Alternatively, RGO may either be purchase or prepared from the bulk chemical reduction of graphene oxide, and subsequently be mechanically deposited on to the methylated GaP surface. Drop casting the RGO suspended in organic solvent (e.g., methanol) will allow for facile application. Alternatively, spin coating the RGO material can provide enhanced control over the RGO film thickness and distribution across the surface, allowing for more accurate assessment of catalyst retention for the resulting CH₃-GaP/RGO surfaces as a function of RGO film thickness. These electrodes can ideally be balanced to attain a thickness which best retains the catalyst under turnover conditions, while maintaining a thin enough coating to still allow facile light absorption. Alternatively, as other electrostatically adsorbed catalyst systems in the literature have shown higher stability under turnover conditions.^{29,30} Therefore, incorporation of alternative aromatic moieties in the catalyst's ligand system could be a more effective pathway to effectively retaining catalyst on graphene-coated GaP surfaces.

Experimental

Preparation of Catalyst

Tetrabutylammonium Co-bis(3,6-dichlorobenzenedithiolate) (1)

The cobalt bis(dithiolate) complex was prepared as described in our previous work²² and was characterized by UV-visible spectroscopy and mass spectrometry prior to use (see experimental section, **Sections 3.1** and **3.2**).

Preparation of RGO-deposited Gallium Phosphide Surfaces

Graphene Oxide

Graphene oxide for graphene depositions was prepared as outlined in previous studies, see experimental details for **Chapter 2**.

Reduced Graphene Oxide Depositions

RGO depositions were performed in an identical manner to the procedure outlined in the experimental details for **Chapter 2**, only using GaP as the working electrode in place of FTO.

Preparation of Functionalized Gallium Phosphide Surfaces (Maldonado Laboratory)

Chlorination of Gallium Phosphide Surface

GaP(111)A was diced into ~ 0.25 cm² pieces, degreased in water, methanol, water by 2 min sonication each, and etched in doubly distilled sulfuric acid for 30 s, rinsed with nanopure water, and dried in a stream of nitrogen gas. In a N₂-purged glovebox, the samples were reacted in a saturated solution of PCl₅ in chlorobenzene at 90°C for 50 minutes as previously described.³¹ The samples were thoroughly rinsed with chlorobenzene and dried in the glovebox.

Methylation via Grignard Reaction

The samples were alkylated with CH_3MgCl in a closed reaction vessel over 3 h at 150-160°C, thoroughly rinsed with THF and subsequently anhydrous methanol, and dried in the glovebox.

Graphene Immobilization

Predominantly single layer graphene sandwiched between copper metal and a protective polymethylmethacrylate layer was first floated on an aqueous solution of iron nitrate (50 mg/mL) overnight to dissolve the copper. The graphene was then floated on several portions of fresh water to rinse, then floated onto the methylated gallium phosphide substrate and allowed to dry under a nitrogen stream. The sample was then treated by rinsing in isopropanol and acetone consecutively for 10 minutes, after which the surface was allowed to sit in dichloromethane for 2 days to remove the majority of the polymethylmethacrylate layer. The graphene-modified surface was then thoroughly dried under a nitrogen stream.

Catalyst-Adsorbed Gallium Phosphide Electrode Preparation

Catalyst-adsorbed gallium phosphide surfaces were prepared by soaking in saturated acetonitrile solutions of the cobalt-bis(benzenedithiolate) complexes for 24 hours. After this period, surfaces were extensively rinsed with fresh acetonitrile and acetone before being dried under a nitrogen stream.

X-Ray Photoelectron Spectroscopy (XPS)

The elemental composition of functionalized GaP(111)A surfaces was investigated by XPS using a PHI 5400 analyzer equipped with Al K α (1486.6 eV) source, without a monochromator. Acquisition took place at a pressure of $< 2.5 \times 10^{-9}$ Torr, without charge neutralization. A 6 mA current emission and a 12 kV anode high tension were used. For each sample, survey scans were recorded between 0 and 1350 eV at pass energy of 117.40 eV and high resolution spectra were

collected at pass energy of 23.5 eV. All binding energies were referenced to the expected binding energy for adventitious carbon (284.6 eV).³² Data analysis was performed with CASA XPS 2.3.13 software.

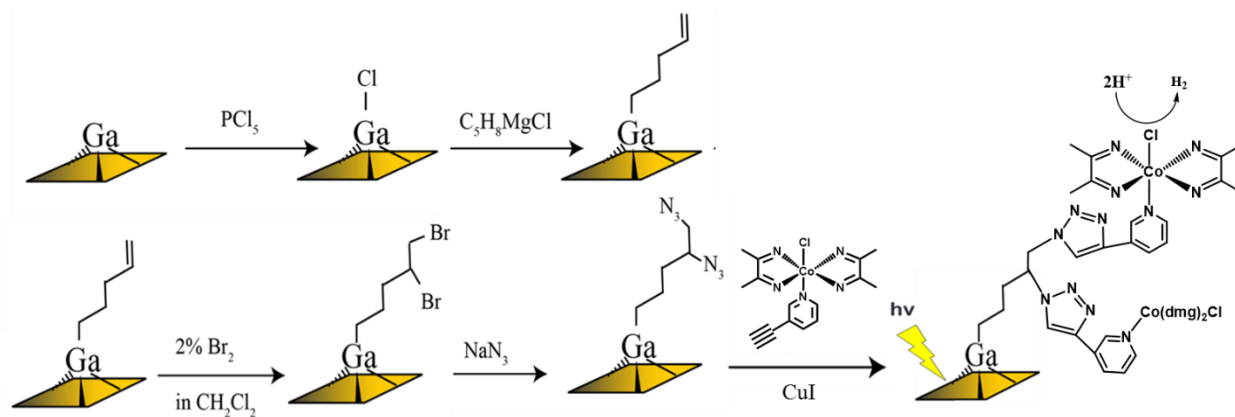
Computational Methods

All geometry optimizations and frequency calculations were performed with the Gaussian 09 program package²⁴ with the B3LYP functional and the TZVP basis set (as implemented in Gaussian 09).

Photoelectrochemical Measurements

Single crystals of p-type GaP(111)A were diced into 0.5 x 0.5 cm² pieces. The backside was gently scratched with a diamond scribe. In:Zn was soldered onto the back and annealed at 400°C for 10 min under flowing forming gas. Before the chemical reactions, the In:Zn back contact was etched off by 30 s treatment in concentrated H₂SO₄, using a razor blade to carefully remove excess In:Zn. After all reactions were completed, In:Zn was soldered on the back again but not annealed, keeping the soldering time to a minimum to mitigate damage to the organic layer from high heat. Samples were placed in a custom-made, Teflon o-ring cell, where back contact was made with a steel plate. A Pt counter and Ag/AgCl reference electrode were used. A Schlumberger SI 1286 Electrochemical Interface was used for potentiostatic control. Surfaces were illuminated using a tungsten white light lamp (ELH, Osram) with a quartz diffuser at an intensity of 100 mW cm⁻², measured by a thermopile (S302A, Thorlabs). Optical density filters (Newport) were used to achieve lower intensities.

4.2. Click Chemistry as a Versatile Interface for Catalyst Binding on GaP



Scheme 4.2. Functionalization of gallium phosphide surfaces with terminal azide groups and subsequent click reaction to covalently attach cobaloxime catalysts.

Perhaps the most versatile new synthetic method developed in the 21st century is Huisgen's 1,3-dipolar cycloaddition of alkynes to azides, now commonly known as click chemistry, as first reported by Sharpless and coworkers.³³ The wide variety of molecular and solid state components that can be covalently tethered, often near room temperature with only inexpensive copper catalysts, has provided nearly limitless possibilities which have already been instituted into a number of research applications.³⁴⁻⁴⁰ For the development of photocatalytic systems with facile interchange of photosensitizer and catalyst components, click chemistry has the potential to provide the same limitless possibility. While preparing these systems still requires some synthetic work, the flexible requirements of simply needing alkyne and azide moieties on the components typically provides minimal complication in synthetic design. Research developing such systems on silicon surfaces has already made impressive strides towards photocatalytic systems for solar-to-fuel production.^{5,41,42} Here, we have developed a method to functionalize gallium-based semiconductors, which are known to exhibit an impressive driving force for proton reduction, with terminal azide moieties in only a few synthetic steps. These surfaces were then modified by two different types of alkyne-containing hydrogen production catalysts to confirm the success of the

click reaction and develop solar-to-fuel photocatalytic systems on gallium phosphide surfaces (Scheme 4.2). Preparation of azide-terminated gallium phosphide surfaces and analysis by GATR was performed by either Betsy Brown or Sabrina Peczonczyk as part of a collaborative study between the Lehnert and Maldonado groups.

Functionalization of GaP(111)A with Alkenyl Grignard Reagents.

GaP(111)A was reacted through a chlorination/Grignard sequence to form a monolayer of terminal olefins (C_3H_5- or C_5H_9-) as shown in Scheme 4.2, similar to previously described reactions.⁴³ Unless otherwise noted, data discussed throughout this section pertains to the reaction with C_5H_9MgBr . The water contact angle of C_5H_9 -GaP(111)A indicated the modified surface was moderately hydrophobic ($69 \pm 3^\circ$, $N=3$), which was similar to previously reported values for C_3H_5 -GaP(111)A ($73 \pm 2^\circ$, $N=3$) and CH_3 -terminated GaP(111)A ($67^\circ \pm 4^\circ$, $N = 3$) surfaces.⁴³

Electrophilic Bromination of C_5H_9 -GaP(111)A.

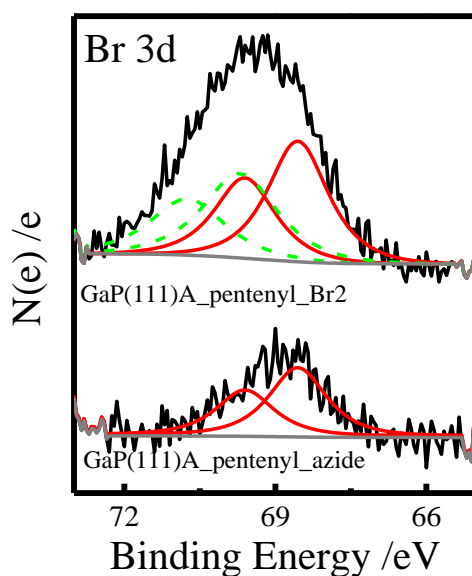


Figure 4.8. High-resolution Br 3d XP spectra of pentenyl-GaP(111)A (a) after the bromination step and (b) after the subsequent azide exchange. The doublet at 68.6 eV (red) was indicative of elemental Br while the doublet at 69.7 eV (green) is indicative of Br-C bonding. Spectra are offset for clarity. All spectra were collected at a pass energy of 160 eV.

Bromide functional groups were desired due to amenability to nucleophilic exchange with a wide variety of functional groups, such as $-\text{OH}$, $-\text{N}_3$, $-\text{CN}$, etc. Bromine addition across an olefin also affords two active bromine sites for further reaction. After bromination, high resolution Br 3d XP spectra exhibited a doublet at 69.7 eV and a doublet at 68.6 eV, corresponding to Br-C bonding and elemental Br, respectively (**Figure 4.8**).⁴⁴

Azide Exchange of Brominated GaP(111)A.

Azide-exchange was performed to probe further reactivity of bromine-modified GaP surfaces and for the variety of reaction opportunities afforded by a covalently bound azide on the GaP surface. Bromine-terminated GaP(111)A surfaces were reacted with NaN_3 in DMF for at least 3 days. No Br 3d signal at 69.7 eV from Br-C bonding was observed after the azide-exchange reaction, indicating a full conversion of the brominated monolayer. A small signal at 68.6 eV was observed (**Figure 4.8**). Elemental Br was previously shown to chemically attack underlying GaP substrates, regardless of the organic layer, with a corresponding binding energy of 68.5 eV.⁴³ After azide exchange, GATR-FTIR in **Figure 4.12** exhibited the N-N stretch of azide at 2156 cm^{-1} . High

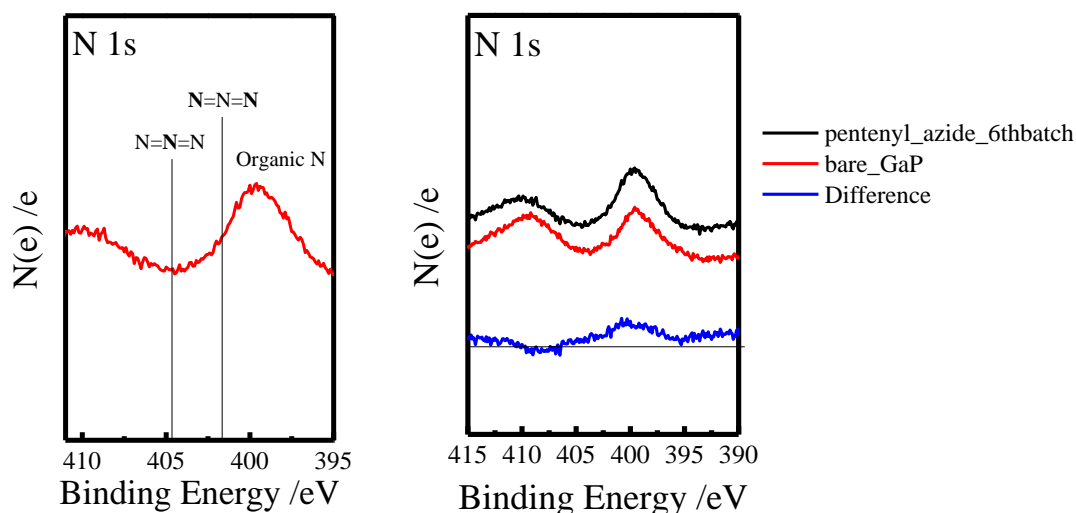


Figure 4.9. *Left:* XP spectra of the N 1s region of azide-terminated GaP(111)A, with the expected shifts for bound azides indicated at 405 and 402 eV. Organic nitrogen is observed in the range of 400.5-398.5 eV. *Right:* Difference XP spectra for N 1s showing a very low N 1s signal. All spectra were collected at a pass energy of 160 eV.

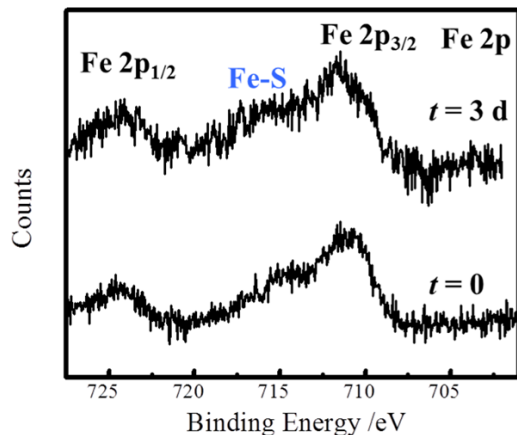


Figure 4.10. XP spectra of the Fe 2p region of $[\text{Fe}(\text{S}_2\text{C}_6\text{H}_4)((\text{C}_6\text{H}_5)_2\text{PN}((\text{CH}_2)_2\text{C}\equiv\text{CH})\text{P}(\text{C}_6\text{H}_5)_2\text{CO})]$ (**1**) modified GaP(111)A, obtained through the Click conversion of a pentenyl linker. Data were collected at a pass energy of 23.3 eV.

resolution N 1s XP spectra did not conclusively show discrete peaks corresponding to oxidation states of nitrogen in azides, commonly found at 405 and 400 eV.^{45,46} The broad signal observed at 399.5 eV (difference spectrum, **Figure 4.9**, right) is consistent with reports of azide, degraded by exposure to X-rays of high energy or for long periods of time (>10 minutes).⁴⁷

Click Reaction of Azide-Modified GaP(111)A with Alkyne-Modified Iron Catalyst

In chapter 2, we reported a series of pentacoordinate iron catalysts for hydrogen production with a highly functionalizable PNP ligand motif. In this study, we utilized one of the alkyne-functionalized catalyst derivatives, $[\text{Fe}(\text{S}_2\text{C}_6\text{H}_4)((\text{C}_6\text{H}_5)_2\text{PN}((\text{CH}_2)_2\text{C}\equiv\text{CH})\text{P}(\text{C}_6\text{H}_5)_2\text{CO})]$ (**1**), for attachment to the GaP surface via click chemistry. The azide-terminated GaP(111)A was reacted with the alkyne-derivatized iron complex in the presence of a Cu (I) catalyst for at least 3 days at room temperature. Afterwards, high resolution XPS analysis of the thoroughly rinsed surfaces shows new signals in the Fe 2p energy region (**Figure 4.10**). Analysis of the surface again after 3 days shows a negligible change in the Fe 2p signal, confirming the formation of a stable covalent bond to an iron species.

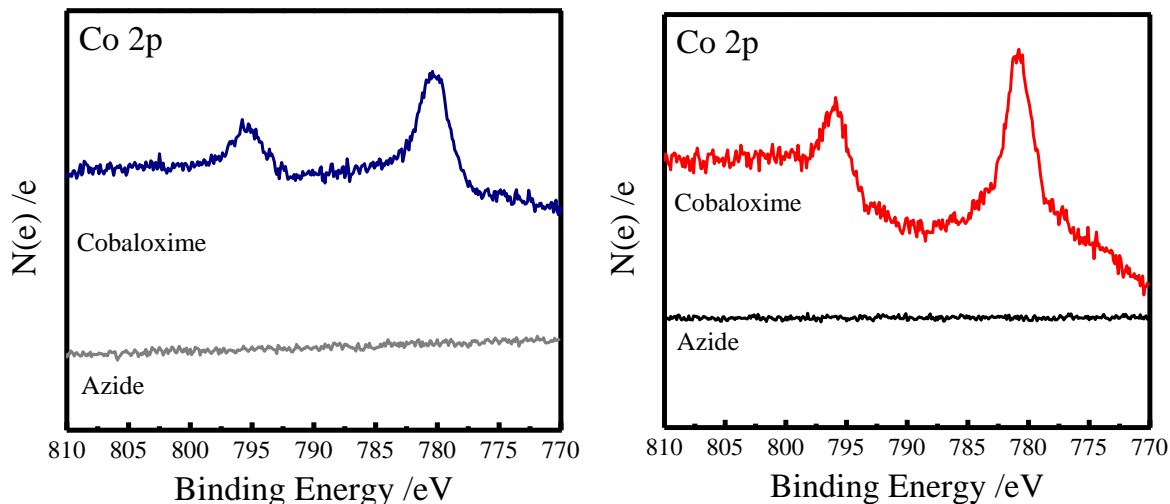


Figure 4.11. Left: Co 2p XP spectra of azide- (bottom) and cobaloxime-modified (top) GaP(111)A obtained through the Click conversion of an allyl linker. Right: P 2p XP spectra of azide- (bottom) and cobaloxime-modified (top) GaP(111)A obtained through the Click conversion of a pentenyl linker. All data were collected at a pass energy of 160 eV.

Click Reaction of Azide-Modified GaP(111)A with an Alkyne-Modified Cobaloxime Catalyst.

Cobaloxime catalysts are known for proton reduction from water under neutral conditions at high pH and are known to be active when attached to GaP.^{10,48} Azide-terminated GaP(111)A was reacted with the alkyne-derivatized cobaloxime complex in the presence of a Cu (I) catalyst

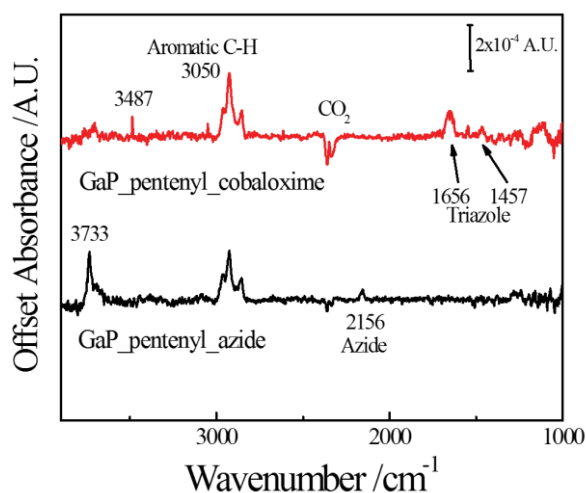


Figure 4.12. GATR-FTIR of azide-terminated (bottom) and cobaloxime-modified (top) GaP(111)A obtained through the Click conversion of a pentenyl-linker. Spectra are offset for clarity. The vertical scale bar = 2×10^{-4} A.U.

for at least 2 days at room temperature. High resolution Co 2p XP spectra show an increased signal after the Click reaction (**Figure 4.11**). Corresponding monolayer coverage was calculated to be 0.3 ± 0.1 monolayers. After the Click reaction, GATR-FTIR indicated no signal at 2156 cm^{-1} for azide and the appearance of peaks at 1656 and 1457 cm^{-1} corresponded to triazole stretching vibrations (**Figure 4.12**) is noted.

Reaction Sequence on $\text{C}_3\text{H}_5\text{-GaP(111)A}$.

The effect of linker length on the sequential reaction was probed by modifying the length of the linear olefin linker from $\text{C}_5\text{H}_9\text{-}$ to $\text{C}_3\text{H}_5\text{-}$. After chlorination and reaction with $\text{C}_3\text{H}_5\text{MgCl}$, surfaces were brominated, exchanged with sodium azide, and clicked with cobaloxime. High resolution Co 2p XP spectra in **Figure 4.11** indicate a monolayer coverage of 0.2 ± 0.1 .

Oxidation Resistance and Stability of Reacted Surfaces.

The stability of the clicked surfaces was tested by allowing samples to sit in ambient conditions for extended periods of time. In **Figure 4.13** (left), high resolution Co 2p XP spectra show a cobaloxime clicked to GaP(111)A immediately after the reaction and after sitting for 2

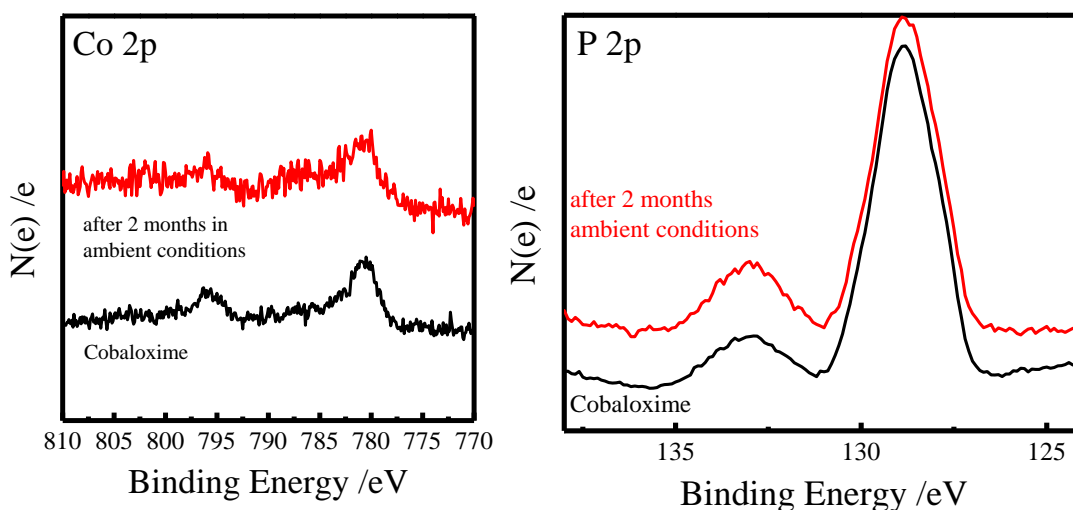


Figure 4.13. High-resolution XP spectra of Co 2p (*left*) and P 2p (*right*) of pristine cobaloxime-GaP(111)A obtained through Click conversion of a pentenyl-linker (bottom) and XP spectra of the same surfaces after two months in ambient conditions (top). Spectra offset for clarity. Data were collected at a pass energy of 160 eV.

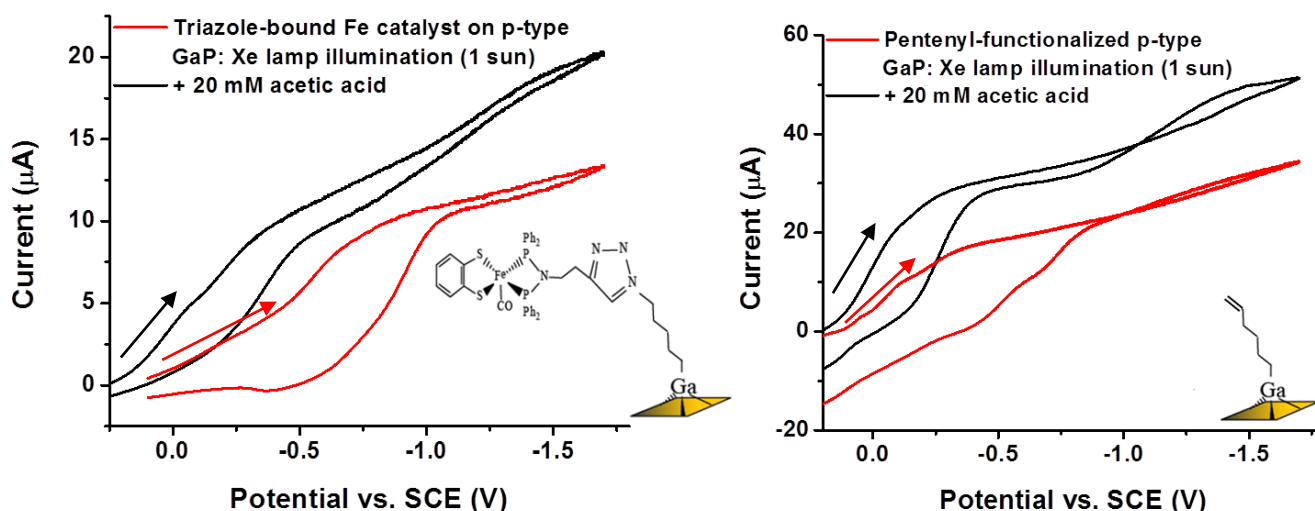


Figure 4.14. *Left:* Cyclic voltammetry of a [Fe(S₂C₆H₄)((C₆H₅)₂PN((CH₂)₂C≡CH)P(C₆H₅)₂CO) (**1**) modified GaP(111)A electrode in a 0.1 M KPF₆ aqueous solution under illumination before (red trace) and after (black trace) the addition of acetic acid. *Right:* Cyclic voltammetry of a pentenyl functionalized GaP(111)A electrode (prior to catalyst attachment) under the same conditions.

months in ambient conditions. The monolayer coverage was nominally unchanged at 0.3 ± 0.1 monolayers, though the XP signal exhibited a larger signal-to-noise ratio in the spectrum of the aged sample. P 2p XP spectra (**Figure 4.13**, right) indicate an increase in the PO_x signal at 133 eV after 2 months in ambient conditions, which corresponds to an increase in oxide thickness from 0.12 nm to 0.18 nm on the GaP surface.

Photoelectrochemical Catalyst Activity Tests

P-type GaP(111)A electrodes functionalized with the pentacoordinate iron catalyst **1** were submerged in a 0.1 M KPF₆ electrolyte solution (pH 7) and illuminated with white light at an intensity of 100 mW/cm². Analysis by cyclic voltammetry showed increasing photocurrent indicative of hydrogen production at potentials below the open circuit potential of 0 V vs. SCE, reaching a plateau current at approximately -0.6 V as seen in **Figure 4.14** (left). As the catalyst **1** was observed to only be active under acidic conditions (e.g., with addition of acetic acid in acetonitrile solution), 20 mM acetic acid was then added to the solution to assess catalyst activity. Subsequent scanning evidenced an increase in open circuit potential (and the coinciding onset of

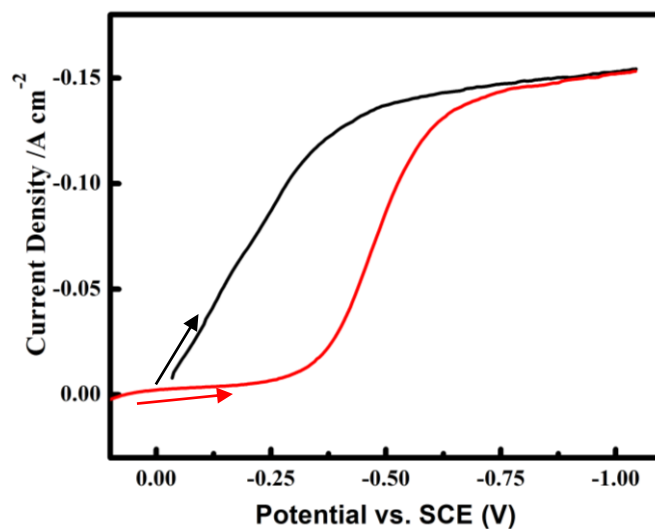


Figure 4.15. Cyclic voltammetry of a cobaloxime (**2**) modified GaP(111)A electrode (red trace) and a pentenyl-modified GaP(111)A control (black trace) in a pH 7 aqueous solution with 1 M potassium phosphate buffer and illuminated with white light at an intensity of 100 mW/cm². Return (anodic) scans are omitted for clarity.

the current wave) to 0.2 V, as well as a much earlier current plateau at -0.25 V with a steeper current incline. However, analysis of the pentenyl control surfaces (i.e., samples prior to catalyst functionalization) under identical conditions showed a nearly identical photocurrent response before and after addition of acetic acid (**Figure 4.14**, right), indicating no clear current enhancement due to the presence of the tethered iron catalysts.

For photoelectrochemical analysis of GaP electrodes functionalized with the cobaloxime catalyst **2**, the electrodes were submerged in a pH 7 aqueous solution with 1 M potassium phosphate buffer and illuminated with white light at an intensity of 100 mW/cm². Cyclic voltammetry of the electrodes under these conditions evidenced an increase in photocurrent at a potential of -0.25 V, with a plateau current that is reached at a potential of approximately -0.6 V (**Figure 4.15**). In comparison, cyclic voltammetry of a pentenyl control electrode under the same conditions showed an increase in photocurrent coinciding with the open circuit potential at 0 V, and a plateau current of equivalent current density to the cobaloxime-modified sample (~ -0.15

mA/cm²) was achieved at a potential of only -0.4 V. These results do not confirm an enhancement in activity for hydrogen production due to the tethered cobaloxime catalysts.

Discussion

The data presented herein elucidate a wet-chemical sequential reaction to impart a stable organic monolayer with terminal, reactive azide functionality to GaP(111)A surfaces. Azides have versatile reactivity through dipolar cycloaddition, or Click chemistry. Through this reaction strategy, a host of desired molecules can be attached to GaP(111)A and likely other Ga-containing III-V semiconductors.⁴⁹ In addition to reaction flexibility, chlorination/Grignard reaction sequences have shown mitigation of deleterious oxidation,^{31,43} extended stability against cathodic aging,²³ and lower surface state population²³ of GaP substrates through protective and stable Ga-C bonding.

Previously, C₁₈H₃₇-terminated GaP(111)A had shown an oxide thickness of 0.01 ± 0.04 nm over 7 weeks, though GaP substrates were shown to be more susceptible to oxide attack with shorter alkyl chain monolayers.³¹ Other contributing factors to the amount of oxide initially present include chemical attack by bromine on the underlying GaP substrate, which could facilitate oxidation under ambient conditions on newly exposed or roughened GaP, or the organic monolayer could direct oxide formation as previously described.^{50,51}

One notable aspect of the reaction sequence outlined in **Scheme 4.2** is the effect of linker length on total monolayer coverage of cobaloxime molecules. C₃H₅-terminated GaP has an effective length of approximately 7.3 Å between the GaP substrate and the reactive terminal group whereas C₅H₉-terminated GaP has approximately 10.3 Å, estimated from published bond length data and assuming *trans*- configuration for the olefin.⁵² The footprint of molecules larger than –CH₃ groups has been known to decrease monolayer coverage, due to the space required between

atop groups on planar, crystalline substrates. Here, the inter-atom distance of atop Ga atoms on GaP(111)A zincblende structure is 3.85Å.⁵³ Though -C₃H₅ groups are more similar in areal footprint to -CH₃ groups than -C₅H₉-groups, perhaps indicating higher initial monolayer coverage of -C₃H₅ molecules, the quantity of attached cobaloxime molecules is decreased in the latter case. One possible explanation is that molecules bound to C₅H₉-GaP(111)A have a greater degree of rotational freedom with a linker of longer length, and steric hindrance would therefore be reduced in this case compared to C₃H₅-GaP(111)A.

Attachment of both iron and cobalt catalysts, as evidenced by XPS and GATR data, confirm the success of the azide-functionalized gallium phosphide surfaces in facilitating triazole formation and successfully ‘clicking’ a molecular species onto the surface. For both compounds, the click reaction is facilitated under extremely mild conditions- at room temperature with minimal diffusion (i.e. no solution agitation). Further, in the instance of both catalysts, analysis of the surfaces by XPS after several days shows essentially no decrease in the Fe or Co 2p signals, further evidencing the stability of the covalent attachment through the chemically rugged triazole bond. The mild reaction conditions, high stability of the covalent attachment, and versatility in being able to bind any alkyne-appended molecule make the Click interface systems highly advantageous for use in the design of a wide variety of photocatalytic systems.

In both the pentacoordinate iron and cobaloxime catalyst-modified GaP systems, normal photocurrent responses were observed, evidencing that the GaP had not undergone significant degradation during the functionalization steps. However, comparison with the pentenyl modified GaP control surface (not functionalized with a catalyst) showed more negative onset potentials and potentials to reach plateau current than for the catalyst functionalized surfaces. Hence, the tethered catalysts do not provide a significant enhancement in hydrogen production activity compared to

the control. Given the inactivity observed for the pentacoordinate iron catalysts adsorbed to FTO/RGO electrodes, these results suggest that the iron catalysts are also not functional under heterogeneous conditions when bound to GaP, perhaps due to a bimolecular component in their mechanism (see **Scheme 2.3**). Curiously, photocathode systems reported by Moore and coworkers utilizing a polypyridine-linked cobaloxime on GaP surfaces show definitive activity over control surfaces, suggesting that the low activity in the systems tested here is likely due either to the method of attachment or the relative surface coverage of the two designs.^{10,54}

In summary, azide-functionalized gallium phosphide surfaces have been prepared, and the synthetic pathway has been monitored by XPS and GATR to give confirmation at each step. The resulting surfaces have been shown to react with two different alkyne-appended catalysts containing diverse chemical structures, and the reaction proceeds under very mild conditions. The presence and stability of the covalently-linked catalysts has been confirmed by XPS. Preliminary assessment of photocatalytic activity shows no substantial activity compared to control electrodes. The investigation of alternative catalysts with higher activity profiles in combination with this interface method is of great interest moving forward, and is likely the key in the development of stable and active photocatalytic systems based on the Click interface in the future.

Experimental.

Materials

All chemicals were purchased from Sigma-Aldrich unless otherwise noted. Methanol (anhydrous, 99.8%), tetrahydrofuran (anhydrous, $\geq 99.9\%$), CH_3MgCl (2.0 M solution in THF), $\text{C}_3\text{H}_5\text{MgCl}$ (2.0 M in THF), $\text{C}_5\text{H}_9\text{MgBr}$ (0.5 M in THF), PCl_5 (95%), chlorobenzene (anhydrous,

99.8%), dichloromethane (anhydrous, $\geq 98.7\%$), dimethylformamide (anhydrous, 99.8%), acetonitrile (anhydrous, 99.8%), doubly distilled H_2SO_4 (95-98%), bromine (99+%, Acros Organics), Cobalt chloride (97%), dimethylglyoxime ($>99\%$), and 3-ethynylpyridine (98%) were all used as purchased. Benzoyl peroxide ($\geq 97\%$, Fluka), copper (I) bromide (98%), sodium azide ($\geq 99\%$) were dried under a vacuum of <200 mTorr for at least 24 h. Chloroform and acetone were purchased from Fisher Scientific (ACS grade) and were used as received. Water with a resistivity of >18 $\text{M}\Omega$ cm (Barnsted Nanopure system) was used throughout. Polished n-type GaP(111)A wafers doped with sulfur at $1.6 \times 10^{18} \text{ cm}^{-3}$ with a thickness of $350 \pm 10 \mu\text{m}$ and p-type GaP(111)A wafers doped with zinc at $2.7 \times 10^{18} \text{ cm}^{-3}$ with a thickness of $350 \pm 25 \mu\text{m}$ were purchased from ITME. p-GaP(111)A was used exclusively for the photoelectrochemical studies, and all other characterization was performed on n-GaP(111)A.

Catalyst Preparation

Synthesis of $[\text{Fe}(\text{S}_2\text{C}_6\text{H}_4)((\text{C}_6\text{H}_5)_2\text{PN}((\text{CH}_2)_2\text{C}\equiv\text{CH})\text{P}(\text{C}_6\text{H}_5)_2)\text{CO}]$ (1)

The pentacoordinate iron hydrogen production catalyst with an alkyne-modified ligand framework was prepared as described in previous work⁵⁵ and was characterized by ^{31}P and ^1H NMR prior to use (see experimental section, **Chapter 2**).

Synthesis of Dichlorobis(dimethylglyoximate)cobalt

Cobaltous chloride hexahydrate (10.0 g, 42.2 mmol) and dimethylglyoxime (9.81g, 84.5mmol) were added to acetone (10mL) and stirred for 10 minutes, after which time the mixture was filtered. The filtrate was let to sit overnight and dark green crystals formed at the bottom of the flask. The crystals were filtered and washed with acetone to afford 10.68 g dichlorocobaloxime (70.6% yield). ^1H -NMR (400 MHz, DMF-d_7): $\delta_{\text{H}} = 2.15$ (s (broad), 12H) ppm.

Synthesis of Chloro(3-ethynylpyridine)bis(dimethylglyoximate)cobalt (2)

A solution of 3-ethynylpyridine (0.2 g, 2 mmol) in chloroform was added to dichlorocobaloxime (0.36 g, 1 mmol), and the mixture was stirred for 30 minutes. After this time 50 mL of water was added, creating a biphasic brown solution. The solution was allowed to stir for 3 hours, after which the organic layer was separated and washed with water and brine, then dried with sodium sulfate. The solution was dried to a light brown solid in vacuo, and recrystallized in hot acetone to afford 0.35 g (81%) of the titled compound as light brown block crystals. ¹H-NMR (400 MHz, CDCl₃): $\delta_{\text{H}} = 8.32$ (s, 1H), 8.25 (d, 1H), 7.7 (d, 1H), 7.15 (m, 1H), 3.34 (s, 1H), 2.42 (s (broad), 12H) ppm.

Semiconductor Surface Functionalization

Etching

GaP(111)A wafers were cut into ~ 0.5-1.5 cm² sections. Samples were first degreased by sequential sonication in water, methanol, and water for 2 minutes each. The samples were then etched in H₂SO₄ (aq) for 30 sec, rinsed with water and dried with a stream of N₂ (g).

Primary Functionalization

Alkylation of Gallium Phosphide Surface

Allyl or pentenyl groups were covalently bonded to GaP(111)A surfaces using the previously described chlorination/Grignard reaction sequence.³¹ Briefly, GaP(111)A samples were degreased and then etched with aqueous H₂SO₄ and introduced into a glovebox purged with dinitrogen gas where all subsequent reaction steps were carried out. GaP(111)A surfaces were chlorinated by immersion into a saturated solution of PCl₅ in chlorobenzene with a few grains of benzoyl peroxide for 50 min at 90°C. The samples were subsequently rinsed with fresh chlorobenzene and dried in the glovebox. The samples were then transferred into a pressure-tolerant glass reaction

vessel and immersed in the desired Grignard reagent. The vessel was then heated using a metal heating block to 110 -120°C for 12 -14 h. The samples were then rinsed with fresh THF and CH₃OH and dried in the glovebox. Samples were sonicated in methanol for 2 min before characterization.

Secondary Functionalization

Electrophilic Addition of Bromine

Functionalized GaP(111)A samples were immersed in a 2% solution of bromine in CH₂Cl₂ for 2 h at room temperature in a N₂ glovebox as previously described.⁴³ The samples were then rinsed with fresh CH₂Cl₂ and immediately characterized or further reacted.

Azide Exchange Reaction

Brominated samples were immersed in saturated sodium azide in dimethylformamide at room temperature in a glovebox for 3-5 days. The samples were rinsed with DMF and immediately characterized or further reacted.

Click Reaction With Alkyne-Ligated Catalysts.

In the glovebox, azide-terminated GaP(111)A was immersed in an acetonitrile solution with either 1 mM [Fe(S₂C₆H₄)((C₆H₅)₂PN((CH₂)₂C≡CH)P(C₆H₅)₂)CO] (**1**) or 2 mM chloro(3-ethynylpyridine)bis(dimethylglyoximate)cobalt (**2**) in addition to 20 mol % copper iodide, and reacted at room temperature for 2 days. Samples were rinsed with acetonitrile and allowed to dry in the glovebox.

X-ray Photoelectron Spectroscopy

X-ray photoelectron (XP) spectra were acquired with a Kratos Axis Ultra analyzer using a monochromated Al K α (1486.6 eV) source, or a Mg K α (1253.6 eV) source where noted. Spectra were acquired without charge neutralization at a base pressure of $\sim 1 \times 10^{-9}$ Torr and the source was operated at ~ 10 mA and ~ 15 kV with a pass energy of 160 eV. The spot size was 2 x 1 mm

with an energy resolution ~ 0.5 eV. Binding energy values of all spectra were corrected to the the peak energy of adventitious carbon (284.6 eV).^{56,57} Average acquisition times were 2-3 h per sample. The Br 3d spectra in **Figure 4.7** were acquired using a PHI 5400 analyzer equipped with an Al K α (1486.6 eV) source, without a monochromator or charge neutralization, with 6 mA current emission and a 12 kV anode high tension, and at a pass energy of 23.5 eV.

Spectra were fit using CASAXPS version 2.313 software using a Shirley type background. P 2p spectra were fit with a doublet using 80% Gaussian and 20% Lorentzian line shapes with an area ratio of 0.5, a full width at half maximum (fwhm) constrained within 0.8-1.5 eV, and a peak separation of 0.85 eV. Fractional monolayer coverage of oxidized GaP surfaces was calculated using the simplified substrate overlayer model (**Equation 1**).⁵⁸

$$d = \lambda_{ov} \sin\phi \left(1 + \frac{I_{overlayer}}{I_{substrate}} \frac{I_{substrate}^o}{I_{overlayer}^o} \right) \quad (1)$$

where d is the thickness of the oxide overlayer in nanometers, λ_{ov} is the escape depth of emitted electrons through the oxide layer, ϕ is the takeoff angle between the analyzer and the surface normal (54.6°), $I_{substrate}$ is the integrated area of the P 2p signal obtained from the bulk crystal, $I_{overlayer}$ is the integrated area of the oxide P 2p signals, $I_{substrate}^o$ is the integrated area of P 2p signal from the bulk crystal of a sample that was freshly etched with H_2SO_4 (aq) and $I_{overlayer}^o$ is the integrated area of the oxide P 2p signals from a GaP thermal oxide (heated in air). The escape depth of the P 2p electrons through the oxide overlayer was estimated using **Equation 2**:

$$\lambda_{ov} = 0.41A^{3/2}E^{1/2} \quad (2)$$

where A is the mean diameter of one unit in the overlayer in nanometers and E is the kinetic energy of the ejected core electron in (eV).⁵⁸ λ_{ov} was calculated to be 1.66 for P 2p core electrons assuming a surface oxide density equivalent to GaPO₄ (3.56 g cm⁻³).^{59,60}

The mean diameter of one unit (A) can be calculated:

$$A = \sqrt[3]{\frac{MW}{1000\rho N_A}} \quad (3)$$

where MW is mean atomic weight (g mol⁻¹), ρ is the density (kg m⁻³), and N_A is Avogadro's number.

Due to the larger size of all molecules tested here, the simple model of a three-layer structure was used here for monolayer coverage calculations.⁶¹ For coverage calculations for cobaloxime, the high resolution Co 2p XP spectrum was used. The density of the cobaloxime was calculated using the crystal packing density of a related cobaloxime structure and determined to be 1.5 g cm⁻³. Parameters of interest are listed in **Table 4.2**. In the model, the topmost layer included the cobaloxime (t_1), the GaP substrate served as the bottom layer (*sub*), and the linker in between t_1 and the substrate served as t_2 (**Chart 4.1**).

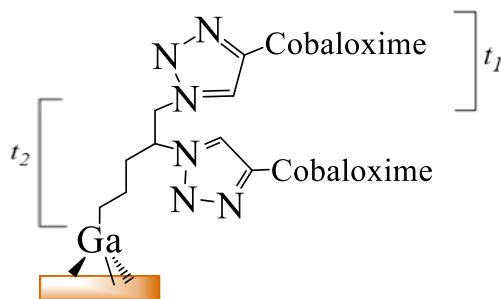


Chart 4.1. Cobaloxime-modified GaP(111)A surface labeled with t_1 and t_2 .

Table 4.2. Monolayer Coverage Calculation Parameters for Various Reactants

Surface (Element Measured)	Density (g cm ⁻³)	n	a _m (nm)	KE (eV)	λ _x (nm)	λ _{GaP} (nm)	SF	Length (nm) ^b	No. Density (atoms cm ⁻²)
Pentenyl-cobaloxime (Co 2p)	1.50	0.76	0.765	706.4	7.29	10.51	2.142	1.814	1.712 x 10 ¹⁴
Allyl-cobaloxime (Co 2p)	1.50	1.08	0.765	706.4	7.29	10.51	2.142	1.514	1.712 x 10 ¹⁴

^aMolecule lengths were estimated from reference 60 and 62.^{60,62}

To calculate the overlayer coverage using the simple three-layer model, **Equation 4** was adopted from Asami *et al.*:⁴

$$\frac{I_{ov}}{I_{sub}} = \left(\frac{SF_{ov}}{SF_{sub}} \right) \left(\frac{\rho_{ov}}{\rho_{sub}} \right) \left(\frac{1 - e^{\left[\frac{-t_1}{\lambda_{ov} \cos \varphi} \right]}}{e^{\left[\frac{-(t_1+t_2)}{\lambda_{sub} \cos \varphi} \right]}} \right) \quad (4)$$

where SF_{sub} is the sensitivity factor for the element of interest in the substrate, SF_{ov} is the instrument sensitivity factor for the element of interest in the overlayer, ρ_{ov} is the density of the element of interest in the overlayer, and ρ_{sub} is the density of the element of interest in the substrate. For GaP, ρ_{sub} is 4.14 g cm⁻³ and SF_{sub} is 0.412. Parameters referring to *ov* are referencing the topmost layer containing an N atom in this case. The variable *t*₁ is the thickness of the second layer and *t*₂ is the thickness of the intermediate layer. Values of *t*₁ and *t*₂ were approximated using crystallographic data of cobaloximes and bond length values of linkers, which are listed in **Table 4.2**, and using previously reported data on bond lengths and molecule size.^{60,62} The sum of the thicknesses is *d*, the total thickness of the organic overlayer. The following relationship also holds true:

$$t_1 = nt_2 \quad (5)$$

where n is the ratio of thicknesses of the two layers. The relationship was entered into the equation in place of t_2 and subsequently t_1 was solved for. Total thickness of the organic layer was calculated using **Equation 6**:

$$d = t_1 + t_2 \quad (6)$$

Monolayer coverage was calculated using **Equation 7**:

$$ML = \frac{d}{d_{lit}} \quad (7)$$

where d_{lit} is the sum of expected lengths t_1 and t_2 published in the literature.^{52,63} This value indicates the amount of total possible cobaloxime molecules on the surface. Fractional monolayer coverage, θ , was calculated to determine the number of cobaloxime molecules per atop Ga atom. Converting the density of cobaloxime to number density (atoms cm^{-2}) and multiplying this value by the monolayer coverage, we finally divide by the number of unreconstructed atop atoms on GaP(111)A (6.73×10^{14} atoms cm^{-2}) to obtain θ .⁶⁴

Infrared Spectroscopy

Infrared spectra were collected using a Thermo-Fisher 6700 FT-IR spectrometer with a deuterated triglycerine sulfate (DTGS) detector. The spectrometer was equipped with a grazing angle attenuated total reflectance (GATR) accessory with a Ge hemisphere. The incident light was p -polarized and fixed at an incident angle of 65° . All samples were approximately 1.2 cm x 1.2

cm, covering the majority of the Ge crystal. Reported spectra were recorded with 4 cm^{-1} resolution. All spectra were referenced to a background spectrum of the cleaned Ge hemisphere.

Photoelectrochemical Measurements

p-type GaP(111)A was diced into $0.5 \times 0.5\text{ cm}^2$ pieces. The backside was gently scratched with a diamond scribe. In:Zn was then soldered onto the back and annealed at 400°C for 10 min under flowing forming gas. Before chemical reactions, the In:Zn back contact was etched off by 30 second exposure to concentrated H_2SO_4 , using a razor blade to carefully remove excess In:Zn. After reactions were complete, In:Zn was soldered on the back again but not annealed. Samples were placed in a custom-made, Teflon o-ring cell, where back contact was made with a steel plate. A Pt counter and Ag/AgCl reference electrode were used. A Schlumberger SI 1286 Electrochemical Interface was used for potentiostatic control. Surfaces were illuminated using a tungsten white light lamp (ELH, Osram) with a quartz diffuser at an intensity of 100 mW cm^{-2} , measured by a thermopile (S302A, Thorlabs). Optical density filters (Newport) were used to achieve lower intensities.

References

- (1) McKone, J. R.; Lewis, N. S.; Gray, H. B. *Chem. Mater.* **2014**, *26*, 407.
- (2) Lewis, N. S.; Nocera, D. G. *Proceedings of the National Academy of Sciences* **2006**, *103*, 15729.
- (3) Reece, S. Y.; Hamel, J. A.; Sung, K.; Jarvi, T. D.; Esswein, A. J.; Pijpers, J. J. H.; Nocera, D. G. *Science* **2011**, *334*, 645.
- (4) Nocera, D. G. *Acc. Chem. Res.* **2012**, *45*, 767.

- (5) Stengel, I.; Mishra, A.; Pootrakulchote, N.; Moon, S.-J.; Zakeeruddin, S. M.; Gratzel, M.; Bauerle, P. *J. Mater. Chem.* **2011**, *21*, 3726.
- (6) Sano, Y.; Onoda, A.; Hayashi, T. *Chem. Commun.* **2011**, *47*, 8229.
- (7) Reisner, E.; Powell, D. J.; Cavazza, C.; Fontecilla-Camps, J. C.; Armstrong, F. A. *J. Am. Chem. Soc.* **2009**, *131*, 18457.
- (8) Downes, C. A.; Marinescu, S. C. *J. Am. Chem. Soc.* **2015**, *137*, 13740.
- (9) Trotochaud, L.; Mills, T. J.; Boettcher, S. W. *The Journal of Physical Chemistry Letters* **2013**, *4*, 931.
- (10) Krawicz, A.; Yang, J.; Anzenberg, E.; Yano, J.; Sharp, I. D.; Moore, G. F. *J. Am. Chem. Soc.* **2013**, *135*, 11861.
- (11) Lomoth, R.; Ott, S. *Dalton Trans.* **2009**, 9952.
- (12) Song, L.-C.; Wang, L.-X.; Tang, M.-Y.; Li, C.-G.; Song, H.-B.; Hu, Q.-M. *Organometallics* **2009**, *28*, 3834.
- (13) Min, Y.-L.; Zhang, K.; Chen, Y.-C.; Zhang, Y.-G. *Sep. Purif. Technol.* **2012**, *86*, 98.
- (14) Xiang, Q.; Yu, J. *The Journal of Physical Chemistry Letters* **2013**, *4*, 753.
- (15) Friedemann, M.; Pierz, K.; Stosch, R.; Ahlers, F. *J. Appl. Phys. Lett.* **2009**, *95*, 102103.
- (16) Sutter, E.; Albrecht, P.; Camino, F. E.; Sutter, P. *Carbon* **2010**, *48*, 4414.
- (17) Liu, B.; Huang, Y.; Wen, Y.; Du, L.; Zeng, W.; Shi, Y.; Zhang, F.; Zhu, G.; Xu, X.; Wang, Y. *J. Mater. Chem.* **2012**, *22*, 7484.
- (18) Cruz, R.; Pacheco Tanaka, D. A.; Mendes, A. *Solar Energy* **2012**, *86*, 716.
- (19) Wang, X.; Zhi, L.; Müllen, K. *Nano Lett.* **2008**, *8*, 323.
- (20) Standing, A.; Assali, S.; Gao, L.; Verheijen, M. A.; van Dam, D.; Cui, Y.; Notten, P. H. L.; Haverkort, J. E. M.; Bakkers, E. P. A. M. *Nat Commun* **2015**, *6*.

- (21) Sobon, G.; Sotor, J.; Jagiello, J.; Kozinski, R.; Zdrojek, M.; Holdynski, M.; Paletko, P.; Boguslawski, J.; Lipinska, L.; Abramski, K. M. *Opt. Express* **2012**, *20*, 19463.
- (22) Eady, S. C.; Peczonczyk, S. L.; Maldonado, S.; Lehnert, N. *Chem. Commun.* **2014**, *50*, 8065.
- (23) Brown, E. S.; Peczonczyk, S. L.; Wang, Z.; Maldonado, S. *The Journal of Physical Chemistry C* **2014**, *118*, 11593.
- (24) Frisch, M. J.; Trucks, G. W.; Schlegel, H. B.; Scuseria, G. E.; Robb, M. A.; Cheeseman, J. R.; Scalmani, G.; Barone, V.; Mennucci, B.; Petersson, G. A.; Nakatsuji, H.; Caricato, M.; Li, X.; Hratchian, H. P.; Izmaylov, A. F.; Bloino, J.; Zheng, G.; Sonnenberg, J. L.; Hada, M.; Ehara, M.; Toyota, K.; Fukuda, R.; Hasegawa, J.; Ishida, M.; Nakajima, T.; Honda, Y.; Kitao, O.; Nakai, H.; Vreven, T.; Montgomery Jr., J. A.; Peralta, J. E.; Ogliaro, F.; Bearpark, M. J.; Heyd, J.; Brothers, E. N.; Kudin, K. N.; Staroverov, V. N.; Kobayashi, R.; Normand, J.; Raghavachari, K.; Rendell, A. P.; Burant, J. C.; Iyengar, S. S.; Tomasi, J.; Cossi, M.; Rega, N.; Millam, N. J.; Klene, M.; Knox, J. E.; Cross, J. B.; Bakken, V.; Adamo, C.; Jaramillo, J.; Gomperts, R.; Stratmann, R. E.; Yazyev, O.; Austin, A. J.; Cammi, R.; Pomelli, C.; Ochterski, J. W.; Martin, R. L.; Morokuma, K.; Zakrzewski, V. G.; Voth, G. A.; Salvador, P.; Dannenberg, J. J.; Dapprich, S.; Daniels, A. D.; Farkas, Ö.; Foresman, J. B.; Ortiz, J. V.; Cioslowski, J.; Fox, D. J.; Gaussian, Inc.: Wallingford, CT, USA, 2009.
- (25) Baker-Hawkes, M. J.; Billig, E.; Gray, H. B. *J. Am. Chem. Soc.* **1966**, *88*, 4870.
- (26) Sproules, S.; Wieghardt, K. *Coord. Chem. Rev.* **2011**, *255*, 837.
- (27) Eisenberg, R.; Gray, H. B. *Inorg. Chem.* **2011**, *50*, 9741.
- (28) Clough, A. J.; Yoo, J. W.; Mecklenburg, M. H.; Marinescu, S. C. *J. Am. Chem. Soc.* **2015**, *137*, 118.
- (29) Dey, S.; Rana, A.; Dey, S. G.; Dey, A. *ACS Catalysis* **2013**, *3*, 429.
- (30) Tran, P. D.; Le Goff, A.; Heidkamp, J.; Jousset, B.; Guillet, N.; Palacin, S.; Dau, H.; Fontecave, M.; Artero, V. *Angew. Chem. Int. Ed.* **2011**, *50*, 1371.
- (31) Mukherjee, J.; Peczonczyk, S.; Maldonado, S. *Langmuir* **2010**, *26*, 10890.
- (32) Barr, T. L.; Seal, S. *Journal of Vacuum Science & Technology A* **1995**, *13*, 1239.
- (33) Kolb, H. C.; Finn, M. G.; Sharpless, K. B. *Angew. Chem. Int. Ed.* **2001**, *40*, 2004.

- (34) Ku, S.-Y.; Wong, K.-T.; Bard, A. J. *J. Am. Chem. Soc.* **2008**, *130*, 2392.
- (35) Voggu, R.; Suguna, P.; Chandrasekaran, S.; Rao, C. N. R. *Chem. Phys. Lett.* **2007**, *443*, 118.
- (36) Best, M. D. *Biochemistry* **2009**, *48*, 6571.
- (37) Vestberg, R.; Malkoch, M.; Kade, M.; Wu, P.; Fokin, V. V.; Barry Sharpless, K.; Drockenmuller, E.; Hawker, C. J. *J. Polym. Sci., Part A: Polym. Chem.* **2007**, *45*, 2835.
- (38) Paoprasert, P.; Spalenka, J. W.; Peterson, D. L.; Ruther, R. E.; Hamers, R. J.; Evans, P. G.; Gopalan, P. *J. Mater. Chem.* **2010**, *20*, 2651.
- (39) Bernardin, A.; Cazet, A.; Guyon, L.; Delannoy, P.; Vinet, F.; Bonnaffé, D.; Texier, I. *Bioconjugate Chem.* **2010**, *21*, 583.
- (40) Xu, X.; Daniel, W. L.; Wei, W.; Mirkin, C. A. *Small* **2010**, *6*, 623.
- (41) Seo, J.; Pekarek, R. T.; Rose, M. J. *Chem. Commun.* **2015**, *51*, 13264.
- (42) Campidelli, S.; Ballesteros, B.; Filoramo, A.; Díaz, D. D.; de la Torre, G.; Torres, T.; Rahman, G. M. A.; Ehli, C.; Kiessling, D.; Werner, F.; Sgobba, V.; Guldi, D. M.; Cioffi, C.; Prato, M.; Bourgoïn, J.-P. *J. Am. Chem. Soc.* **2008**, *130*, 11503.
- (43) Peczonczyk, S. L.; Brown, E. S.; Maldonado, S. *Langmuir* **2014**, *30*, 156.
- (44) Toledano, T.; Biller, A.; Bendikov, T.; Cohen, H.; Vilan, A.; Cahen, D. *The Journal of Physical Chemistry C* **2012**, *116*, 11434.
- (45) Daugaard, A. E.; Hvilsted, S.; Hansen, T. S.; Larsen, N. B. *Macromolecules* **2008**, *41*, 4321.
- (46) Prakash, S.; Long, T. M.; Selby, J. C.; Moore, J. S.; Shannon, M. A. *Anal. Chem.* **2007**, *79*, 1661.
- (47) Schulze, R. K.; Boyd, D. C.; Evans, J. F.; Gladfelter, W. L. *Journal of Vacuum Science & Technology A* **1990**, *8*, 2338.
- (48) Jing, D.; Guo, L.; Zhao, L.; Zhang, X.; Liu, H.; Li, M.; Shen, S.; Liu, G.; Hu, X.; Zhang, X.; Zhang, K.; Ma, L.; Guo, P. *Int. J. Hydrogen Energy* **2010**, *35*, 7087.

- (49) Peczonczyk, S. L.; Mukherjee, J.; Carim, A. I.; Maldonado, S. *Langmuir* **2012**, *28*, 4672.
- (50) Nemanick, E. J.; Hurley, P. T.; Brunschwig, B. S.; Lewis, N. S. *The Journal of Physical Chemistry B* **2006**, *110*, 14800.
- (51) Webb, L. J.; Lewis, N. S. *The Journal of Physical Chemistry B* **2003**, *107*, 5404.
- (52) Allen, F. H.; Kennard, O.; Watson, D. G.; Brammer, L.; Orpen, A. G.; Taylor, R. *Journal of the Chemical Society, Perkin Transactions 2* **1987**, S1.
- (53) Massa, W. *Crystal Structure Determination*; Springer Berlin Heidelberg, 2004.
- (54) Krawicz, A.; Cedeno, D.; Moore, G. F. *PCCP* **2014**, *16*, 15818.
- (55) Eady, S. C.; Breault, T.; Thompson, L.; Lehnert, N. *Dalton Transactions* **2016**.
- (56) Haber, J. A.; Lewis, N. S. *The Journal of Physical Chemistry B* **2002**, *106*, 3639.
- (57) Wagner, C. D.; Muilenberg, G. E. *Handbook of x-ray photoelectron spectroscopy : a reference book of standard data for use in x-ray photoelectron spectroscopy*; Physical Electronics Division, Perkin-Elmer Corp.: Eden Prairie, Minn., 1979.
- (58) Castle, J. E. *Practical surface analysis by Auger and X-ray photoelectron spectroscopy* John Wiley & Sons Limited: Chichester, 1983; Vol. 6.
- (59) Morota, H.; Adachi, S. *J. Appl. Phys.* **2007**, *101*, 113518.
- (60) W. Pies, A. W. *Crystal Structure Data of Inorganic Compounds · Key Elements: P, As, Sb, Bi*; 1st ed.; Springer-Verlag Berlin Heidelberg, 1979; Vol. 7.
- (61) Asami, K.; Hashimoto, K.; Shimodaira, S. *Corros. Sci.* **1977**, *17*, 713.
- (62) Laibinis, P. E.; Bain, C. D.; Whitesides, G. M. *The Journal of Physical Chemistry* **1991**, *95*, 7017.
- (63) Sturzenegger, M.; Prokopuk, N.; Kenyon, C. N.; Royea, W. J.; Lewis, N. S. *The Journal of Physical Chemistry B* **1999**, *103*, 10838.
- (64) O'Leary, L. E.; Rose, M. J.; Ding, T. X.; Johansson, E.; Brunschwig, B. S.; Lewis, N. S. *J. Am. Chem. Soc.* **2013**, *135*, 10081.

Chapter 5

Conclusions and Future Work

5.1. Conclusions

Solar-to-fuel conversion systems have the potential to meet the high global hydrogen demand, and comprise one of the most promising initiatives for replacement of fossil fuels as a primary energy source. Hydrogen is an exceptional candidate for the replacement of gasoline as an energy carrier. However, production methods are currently dominated by fossil fuel processing, which is not much more environmentally conscious than direct use of fossil fuels. The photocatalytic reduction of water constitutes a carbon free, renewable source of hydrogen which can be further coupled to water oxidation for recovery of proton and electron equivalents. Platinum, one of the most efficient materials for catalyzing proton reduction, is a limited resource with a high cost, and thus replacement by inexpensive yet efficient transition metal catalysts remains a major challenge in solar-to-hydrogen conversion. Another particularly complicated aspect of photocatalytic system design is the interface between the photosensitizer and the catalyst, which is often costly, ineffective, or overly selective and thus only compatible with distinct photosensitizer/catalyst couples. Such interfaces hinder customization and limit the scalability of photocatalytic devices.

Chapter 2 focuses on the design of inexpensive early transition metal catalysts for hydrogen production as alternatives to platinum. The prepared pentacoordinate iron complexes, partial

models of the [FeFe] hydrogenase active site, were observed to have high stability to air and contained an easily functionalizable PN(R)P ligand framework. Electrocatalytic analysis in acetonitrile solution found the complexes to be active catalysts for hydrogen production at very low overpotentials (<100 mV vs. platinum) exhibiting turnover frequencies as high as $\sim 3 \text{ s}^{-1}$ (**Section 2.1**). In comparing a series of compounds with aryl and aliphatic 'R' substitutions, use of more electron withdrawing substituents give a substantially lower overpotential ($\eta = 0.21$ vs. $\eta = 0.09$ for R = *i*-Pr vs. *p*-BrC₆H₄), showing a definitive effect of the PNP ligand properties on the metal's redox potential. In addition, trends toward higher activity are observed for derivatives with aliphatic compared to aryl substitutions, most notably in the case of R = C₆H₅ vs. (CH₂)₄C₆H₅ which are observed to have TOF values of 1.58 s^{-1} and 3.51 s^{-1} , respectively.

Comparison with similar pentacoordinate iron catalysts in the literature (**Section 2.2**) shows a distinct advantage of our rigid FePNP ring system in decreasing overpotential. However, a decrease in activity is observed which is likely due to the lower flexibility of the PNP unit. Such ligand flexibility has been reported to be critical to the activity of several hydrogen production catalyst systems.¹⁻⁵ Decreased stability under turnover conditions is also observed for the iron catalysts, and attempts to electrostatically adsorb derivatives with extended aromatic ligands to FTO/RGO electrodes were unsuccessful (**Section 2.3**).⁶

The results reported in Chapter 2 supplement a well-established literature base involving iron hydrogenase models for H₂ production.⁷⁻¹⁰ More specifically provide greater insight into the effect of the 'PNP' ligand structure and electronics on catalyst function in relation to other pentacoordinate iron hydrogenase models.^{6,11,12} The variable nature of the ligand design coupled with the high (solid state) stability of the iron complexes could allow for use in a variety of applications even outside of catalysis. Alkyne-functionalized derivatives have already provided

preliminary evidence of a successful Click reaction on gallium phosphide surfaces, as outline in **Section 4.2**.

In Chapter 3, interface designs comprised of graphitic supports, specifically reduced graphene oxide (RGO), were tested on metal oxide surfaces for the adsorption of cobalt bis(dithiolene) proton reduction catalysts. The studies in **Section 3.1** determined that the catalysts could be successfully adsorbed to both RGO and highly ordered graphite (HOPG) electrodes, exhibiting very similar cyclic voltammetry responses ($E_{1/2} = \sim -0.5$ V vs. SCE) to reports of the catalysts in solution. Surprisingly, while the overpotential and mechanism of the surface-adsorbed catalysts appear similar to reports of the catalysts in homogeneous phase, the observed activity is substantially higher, with estimated TOF values of over $6,000$ s⁻¹ (vs. < 1 s⁻¹ in solution) at overpotentials of ~ 0.5 V vs. platinum. Testing of catalysts on HOPG electrodes under turnover conditions showed an essentially quantitative Faradaic efficiency and sustained activity for over 10 hours.¹³⁻¹⁵ In **Section 3.2**, a series of cobalt bis(dithiolene) catalysts were studied on both RGO and graphite supports, allowing for a thorough analysis of how substitution on the dithiolate ring effects surface adsorption, TOF, and stability under turnover conditions. Some of the results highlight the benefits of an extended naphthalene ring in the ligand for decreasing overpotential ($\eta = 0.36$ V vs. -0.6 for naphthalene vs. benzene ligand systems, respectively) and increasing catalyst loading (~ 5 x higher loading for naphthalene vs. benzene ligand systems). However, overall the benefits of the halide-substituted ligand derivatives, most notably the fully substituted (TBA)[Co(S₂C₆Cl₄)₂], are seen to be most advantageous in terms of TOF (i_{cat}/i_p of over 400, TOF > 700 s⁻¹ under turnover conditions) and stability.

In **Section 3.3**, the activity of a cobalt bis(dithiolene) catalyst was studied across a series of graphitic supports to compare the effect of the support structure on the catalyst performance.

The catalyst was found to successfully adsorb to every tested support and display similar CV responses (~ -0.5 vs. SHE); however, desorption (evidenced by loss of the CV signal) was observed in the cases of graphene and glassy carbon, suggesting more layers and softer, more porous graphitic materials are beneficial for retaining adsorbed catalyst. The catalysts were also observed to adsorb on inexpensive bulk graphite electrodes, although they were seen to have somewhat lower TOF compared to previous reports ($i_{\text{cat}}/i_{\text{p}}$ of 50 vs. 176 on HOPG). While the same limited lifetime of ~ 8 hours is observed under turnover conditions, the electrodes could be reloaded simply by soaking in the same catalyst solution and regain the majority of the electrode's initial current density. The catalysts could also be adsorbed to graphite powder and embedded in a nafion film. When tested on glassy carbon electrodes, these films display a similar activity profile to the catalysts on bulk graphite with the added benefit of higher levels of sustained activity after 8 hours of electrolysis.

In summary, inexpensive graphite materials with electrostatically adsorbed cobalt bis(dithiolene) catalysts are of great interest for further study as renewable electrode systems for hydrogen production. With the low cost of both the catalyst and support materials, ease of preparation of the catalyst-loaded supports, and the relatively low overpotential for proton reduction, these systems could potentially serve as viable replacements for fossil fuel conversion to hydrogen, the current industry standard. With modifications to further lower overpotential and to improve the duration of function between catalyst reloading, these systems have a high potential for use at scale. In addition, use of graphite powder-embedded films has potential for longer term use in devices, as the catalytic activity is similar to bulk graphite with a higher catalyst retention time under turnover conditions. Analysis of film activity during extended time electrolysis (i.e.,

multiple days) and modifications in film design to retain more catalyst activity may provide excellent materials for use in scaled hydrogen production devices.

The results reported in this chapter comprise the first demonstrated example of metal bis(dithiolene) catalysts on graphitic supports as heterogeneous catalysts for hydrogen production from acidic aqueous solutions.¹³ The resulting heterogeneous manifolds are among the highest reported TOF values for cobalt proton reduction catalysts in literature, while preparation of the catalyst adsorbed-supports is far simpler than many of the published methods for heterogenization of catalysts.¹⁶⁻¹⁸ Further, the comparison of cobalt bis(dithiolene) derivatives with modified ligands is (to our knowledge) one of the most expansive comparisons of catalyst functionality across a derivative series on a graphitic support, and provides substantial insight into the benefits of ligand substitution for adsorption, activity and surface retention. In addition, the comparison of a cobalt bis(dithiolene) catalyst across a variety of graphitic supports is one of the first studies of its kind, allowing for an unprecedented look into the effect of the carbon ordering and density on cobalt bis(dithiolene) catalyst adsorption and retention.

Finally, in Chapter 4, two interface methods were tested for the development of photocathode hydrogen production systems with gallium phosphide (GaP) semiconductors. In **Section 4.1**, RGO and graphene were deposited on GaP surfaces to facilitate adsorption of cobalt bis(dithiolene) catalysts, as had been shown effective on various graphitic supports as described in Chapter 3. Graphene was determined to give significantly higher surface coverage and consistency on GaP electrodes compared to RGO, and is far more effective for catalyst adsorption as evidenced by XPS. Spectroscopic analysis of graphene-coated GaP electrodes by GATR and resonance Raman shows similar spectral features compared to the bulk catalyst material in the solid and solution state, providing evidence supporting preservation of the molecular structure of

the surface-adsorbed cobalt species. The low stability of these interface systems with applied potential, in combination with the results obtained for graphene-adsorbed catalysts in **Section 3.3**, suggests that the catalysts desorb, thus highlighting the need to develop ‘thicker’ graphitic interfaces for use on the GaP semiconductor surface. In **Section 4.2**, the covalent attachment of both pentacoordinate iron (reported in Chapter 2) and cobaloxime catalysts via click chemistry to azide-functionalized GaP surfaces is explored. While the successful preparation of the azide-terminated GaP surfaces and subsequent covalent attachment of the catalysts has been confirmed, neither catalyst system was seen to exhibit hydrogen production activity above control GaP levels, despite literature precedence for active surface-bound cobaloximes on GaP.^{19,20} This difference in activity is believed to be due to a comparatively lower catalyst loading in our system, in combination with the relatively low proton reduction activity for cobaloxime catalysts. A more successful direction therefore may be the use of more active catalysts in these GaP-click manifolds.

The results reported in Chapter 4 provide the first example of azide-functionalized gallium-based semiconductors, which have been subsequently shown to successfully undergo the Click reaction in the case of two distinct alkyne-modified proton reduction catalyst species. Studies of graphene-adsorbed cobalt bis(dithiolene) H₂ production catalysts have shown thin graphitic materials can successfully serve as a catalyst interface on semiconductor surfaces. This work is the first report of cobalt bis(dithiolene) catalysts immobilized on semiconductor surfaces by electrostatic adsorption. Both the Click and graphene interfaces developed here allow for a higher level of variability in the possible catalyst and semiconductor pairings, and have potential to be combined with a multitude of previous reported catalysts with aromatic ligand systems or alkyne functional groups.

Ideal semiconductor-catalyst interfaces should allow for facile connection of the catalyst and the photosensitizer to allow for fluent system optimization. The preparation should be simple and fast, allowing combination of the components in a minimal number of steps. In my thesis work, I have developed interface systems which address both of these needs- specifically, **graphitic interfaces** (e.g. reduced graphene oxide) which can easily be applied to a variety of substrates and can utilize any catalyst with an aromatic ligand system, and **click interfaces**, which can facilitate covalent attachment to an unlimited number of alkyne-modified catalysts/dye combinations. These two interface methods, when combined with modified versions of reported, highly active hydrogen production catalysts, provide a template for the design of extremely efficient photocathode systems for solar-to-fuel conversion in the future.

5.2. Future Work

To further improve upon the stability of and decrease overpotential for the cobalt bis(dithiolene) catalysts on graphitic supports reported in Chapter 3, more advanced ligand modification has the potential to be beneficial. Comparing catalyst derivatives reported in **Section 3.2** shows a significant decrease in overpotential both due to increased halide loading and use of an extended naphthalene ring system. If these overpotential shifts are in fact additive, synthesis of a fully halide-substituted naphthalene dithiolate may provide an unprecedented decrease in overpotential, which may allow for hydrogen productions at extremely low overpotentials. Similarly, if the catalyst loading effects of a large ligand ring system and halide substitution are additive, and the observed stability and activity increase with halide substitution is also observed in the naphthalene case, this ligand design could afford the most efficient cobalt bis(dithiolene) derivative observed yet in essentially every category of comparison (aside from ease of preparation). Alternatively, further tuning the overpotential of the catalyst system may be more

easily addressed by substituting the metal, thus drastically changing the redox properties of the overall complex and allowing for reduction at a more positive potential or activation via an alternative mechanism accessible closer to the thermodynamic limit for proton reduction. As extensive research has already been conducted on early transition metals in bis(dithiolene) ligand manifolds, future studies would largely involve second row transition metals and should consider not only the bis(dithiolene) species, but the potential formation of tris(dithiolene) and oligomeric species that may still serve as effective hydrogen production catalysts.

Further development of graphitic supports for catalyst adsorption should ideally follow two paths with distinct aims: first, the design of systems with incredibly low expense for the short-term production of hydrogen at scale, in which the graphitic support can be reloaded with catalyst after use, and second, the design of film systems that can be easily incorporated into a variety of devices for long-term hydrogen production applications. Following the results from studying various graphitic supports in **Section 3.3**, the most effective types of graphite for catalyst retention will likely be those with at least ~100 nm to micron thickness, as some insertion into the graphite edge is suggested by XPS analysis, and single-layer graphene has clearly been shown to have difficulty retaining catalyst. Catalyst adsorption is enhanced in more porous (less dense) graphitic materials. Based on these factors, to address the first aim, utilizing a relatively thin (micron scale) and porous graphitic material, such as a graphite paper or cloth, could be a way to increase catalyst loading while not increasing the difficulty of support preparation or sacrificing catalyst retention. Thus, cobalt bis(dithiolene) catalysts should be tested on such inexpensive graphitic materials to assure the same activity profile is maintained and to determine if catalyst ‘reloading’ can be continued indefinitely. Considering the low cost of these materials and the ease at which the components could be scaled and combined, they may provide a viable carbon emission-free alternative to

hydrogen production via fossil fuel conversion, especially if these scaled systems could be coupled to photovoltaics for the solar-driven production of hydrogen.

To address the second aim, while initial testing of graphite powder embedded in nafion films has shown that proton reduction activity seen for other graphite supports is conserved in the films (**Section 3.3**), relatively little is known about how the film design affects function. Future work will ideally address this issue by conducting experiments to determine the effect of increasing film thickness (but not exposed surface area to solution) on catalyst stability and activity. Further, testing of electronically conductive film materials, as opposed to the proton conductive but electronically insulating nafion used in initial studies, will provide an electronically unique environment for the catalyst, and therefore may give entirely new (and interesting) results. The information these studies will provide about the influence of mechanical and chemical components of film design on function will provide invaluable insight on how to create and apply these films in devices to attain maximum stability and activity in application.

To overcome the limitations in catalyst retention on single-layer graphene interfaces observed in **Sections 3.3** and **4.1**, mechanical deposition of RGO or exfoliated graphite on GaP to produce graphitic thin films is an attractive alternative to previously used reductive deposition techniques, which can reduce GaP to gallium metal and degrade the semiconductor material. In particular, spin coating of a graphene suspended in an organic solvent can provide flat, uniform films as thin as 10-100 nm.^{21,22} As film thickness can be controlled by modifying such experimental conditions as rotation rate and solvent viscosity, this method is ideal to test a variety of graphitic film thicknesses to design the optimal photocathode system capable retaining catalyst while effecting a minimal decrease in quantum yield.^{23,24} Alternatively, modification of the catalyst's ligand ring system to improve retention on graphene may be a viable alternative, as

would investigation of alternative hydrogen production catalysts. At the same time, due consideration should be given to the amount of effort being expended to give one particular catalyst system a slightly longer lifetime, when use of alternative proton reduction catalysts (particularly those shown in literature to remain adsorbed to graphitic surfaces indefinitely under turnover conditions) may ultimately provide a more efficient photocathode system.^{25,26}

The inconsistencies in azide surface coverage evidenced by XPS suggests that the chemical modification of Ga-based semiconductor surfaces is non-trivial, and requires further optimization to determine conditions for high loading. Considering XPS quantification is limited in terms of accuracy, use of an alkyne-modified fluorescent probe, such as commercially available uridine-based fluorescent dyes currently used in DNA imaging, may be highly beneficial not only to optimize the azide functionalization process, but to determine if both azides on the alkyl chain are truly capable of undergoing the Click reaction. The design of alternative alkyne-functionalized hydrogen production catalysts, such as derivatives of the cobalt bis(dithiolene) catalysts shown to be highly active on graphitic supports in Chapter 3, may also be highly beneficial for use in Click-modified semiconductor surfaces. While these modifications do require synthetic manipulation of the ligand manifold and thus introduce more costs, the development of cross coupling methods in the last decade may allow for facile introduction of alkynes into aromatic systems given the right conditions.²⁷

References

- (1) Stewart, M. P.; Ho, M.-H.; Wiese, S.; Lindstrom, M. L.; Thogerson, C. E.; Raugei, S.; Bullock, R. M.; Helm, M. L. *J. Am. Chem. Soc.* **2013**, *135*, 6033.

- (2) Wilson, A. D.; Shoemaker, R. K.; Miedaner, A.; Muckerman, J. T.; DuBois, D. L.; DuBois, M. R. *Proceedings of the National Academy of Sciences* **2007**, *104*, 6951.
- (3) Wilson, A. D.; Newell, R. H.; McNevin, M. J.; Muckerman, J. T.; Rakowski DuBois, M.; DuBois, D. L. *J. Am. Chem. Soc.* **2006**, *128*, 358.
- (4) Ezzaher, S.; Capon, J.-F.; Gloaguen, F.; Petillon, F. Y.; Schollhammer, P.; Talarmin, J. *Inorg. Chem.* **2009**, *48*, 2.
- (5) Rakowski DuBois, M.; DuBois, D. L. *Chem. Soc. Rev.* **2009**, *38*, 62.
- (6) Eady, S. C.; Breault, T.; Thompson, L.; Lehnert, N. *Dalton Transactions* **2016**.
- (7) Adam, F. I.; Hogarth, G.; Richards, I.; Sanchez, B. E. *J. Chem. Soc. Dalton Trans.* **2007**, 2495.
- (8) Yu, Z.; Wang, M.; Li, P.; Dong, W.; Wang, F.; Sun, L. *J. Chem. Soc. Dalton Trans.* **2008**, 2400.
- (9) Darensbourg, M. Y.; Lyon, E. J.; Zhao, X.; Georgakaki, I. P. *Proc. Natl. Acad. Sci. USA* **2003**, *100*, 3683.
- (10) Song, L.-C.; Wang, H.-T.; Ge, J.-H.; Mei, S.-Z.; Gao, J.; Wang, L.-X.; Gai, B.; Zhao, L.-Q.; Yan, J.; Wang, Y.-Z. *Organometallics* **2008**, *27*, 1409.
- (11) Beyler, M.; Ezzaher, S.; Karnahl, M.; Santoni, M.-P.; Lomoth, R.; Ott, S. *Chem. Commun.* **2011**, *47*, 11662.
- (12) Roy, S.; Mazinani, S. K. S.; Groy, T. L.; Gan, L.; Tarakeshwar, P.; Mujica, V.; Jones, A. K. *Inorg. Chem.* **2014**, *53*, 8919.
- (13) Eady, S. C.; Peczonczyk, S. L.; Maldonado, S.; Lehnert, N. *Chem. Commun.* **2014**, *50*, 8065.
- (14) McNamara, W. R.; Han, Z.; Alperin, P. J.; Brennessel, W. W.; Holland, P. L.; Eisenberg, R. *J. Am. Chem. Soc.* **2011**, *133*, 15368.
- (15) McNamara, W. R.; Han, Z.; Yin, C.-J.; Brennessel, W. W.; Holland, P. L.; Eisenberg, R. *Proc. Natl. Acad. Sci. USA* **2012**, *109*, 15594.
- (16) Losse, S.; Vos, J. G.; Rau, S. *Coord. Chem. Rev.* **2010**, *254*, 2492.

- (17) Le Goff, A.; Artero, V.; Jusselme, B.; Tran, P. D.; Guillet, N.; Métayé, R.; Fihri, A.; Palacin, S.; Fontecave, M. *Science* **2009**, *326*, 1384.
- (18) Seo, J.; Pekarek, R. T.; Rose, M. J. *Chem. Commun.* **2015**, *51*, 13264.
- (19) Krawicz, A.; Yang, J.; Anzenberg, E.; Yano, J.; Sharp, I. D.; Moore, G. F. *J. Am. Chem. Soc.* **2013**, *135*, 11861.
- (20) Krawicz, A.; Cedeno, D.; Moore, G. F. *PCCP* **2014**, *16*, 15818.
- (21) Chen, I. W. P.; Huang, C.-Y.; Jhou, S.-H. S.; Zhang, Y.-W. *Scientific Reports* **2014**, *4*, 3928.
- (22) Ricardo, K. B.; Sendeki, A.; Liu, H. *Chem. Commun.* **2014**, *50*, 2751.
- (23) Schubert, D. W.; Dunkel, T. *Mater. Res. Innovations* **2003**, *7*, 314.
- (24) Sahu, N.; Parija, B.; Panigrahi, S. *Indian Journal of Physics* **2009**, *83*, 493.
- (25) Dey, S.; Rana, A.; Dey, S. G.; Dey, A. *ACS Catalysis* **2013**, *3*, 429.
- (26) Tran, P. D.; Le Goff, A.; Heidkamp, J.; Jusselme, B.; Guillet, N.; Palacin, S.; Dau, H.; Fontecave, M.; Artero, V. *Angew. Chem. Int. Ed.* **2011**, *50*, 1371.
- (27) Chinchilla, R.; Nájera, C. *Chem. Rev.* **2007**, *107*, 874.